Resolving conformational changes

in FG nucleoporins due to multivalent

Karyopherin binding

Inauguraldissertation

zur

Erlangung der Würde eines Doktors der Philosophie

vorgelegt der

Philosophisch-Naturwissenschaftlichen Fakultät

der Universität Basel

von

Rafael L. Schoch

aus der Schweiz

Rehovot, 2017

Genehmigt von der Philisophisch-Naturwissenschaftlichen Fakultät

auf Antrag von

Dissertationsleiter: Prof. Roderick Lim

Korreferent: Prof. Andreas Dahlin

Basel, den 24.03.2015

Prof. Dr. Jörg Schibler

Dekanin/Dekan

Acknowledgment

Thesis Outline

This thesis is an investigation into the structure – function relationship of FG domains, which are located within the nuclear pore complex (NPC) and thus are fundamental to the NPC gating mechanism. The thesis is structured into topical chapters that build on each other, starting with an „Introduction" that familiarizes the reader with the biological background and the scientific framework of this thesis. It then continues rather technical in the chapter „Non-interacting molecules as innate structural probes in surface plasmon resonance" and "BSA penetration into strongly stretched PEG brushes". Those chapters are not directly related to the NPC but introduce an important novel technique that is key to many of the following chapters as well: „Conformational characterization of FG domains", „Kinetic analysis of multivalent Kapβ1 binding". Those chapters are certainly more appealing to the reader with interest in the NPC. In the chapter „Model of Kap-centric NPC control" the main findings are resumed and applied to the NPC in a more presumptive manner. The „Basics & Theory" sections within the chapters are rather comprehensive, introducing many of the theories and publications I was dealing with in order to receive a full understanding of the matter. Finally in „Outlook & Conclusions" the main findings are summarized and a meaningful continuation of this project is outlined. This thesis is ought to reflect the spirit of a holistic approach to science and thus connects theory with experiments and is subject to topics ranging from biology to physics, in favor of a profound biophysical understanding. As such this thesis is covering a multitude of scientific branches, that is in well tradition of the wonderful Nanosciences Curriculum at the University of Basel that I had the honor to attend.

Table of content (TOC) image from Schoch & Lim, 2013, giving the reader a quick visual impression of the techniques and methods involved in a rather symbolic fashion. The image shows a polymer brush and cantilevers that symbolize height measurements. The heights are, however, accessed using „non-interacting probes" in solution and using surface plasmon resonance (SPR), as indicated by the electric field color and vector field representation.

Contents

Chapter 1

Introduction

1.1 Motivation

The nuclear pore complex (NPC) is a large macromolecular assembly that exclusively regulates the exchange between the nuclear genetic material and the cytoplasmic protein machinery (Stewart, 2007; Terry et al., 2007; Peters, 2009). The different nuclear transport pathways, such as the nuclear localization signal (NLS) import pathway, and the nuclear transport receptors (NTR's) as well as other regulatory proteins involved therein have been well described. It is also well established that the transport of cargo is mediated by NTR's via interacting with NPC proteins (Nucleoporins or Nups) containing highly disordered FG domains that otherwise form a barrier to inert molecules with a size greater than about 40 kDa. However, the biophysical nature of the permeability barrier and the mechanism of transport remain poorly understood. While low-affinity interactions are thought to enable the NTR's to transiently „hop" between binding sites, the disordered FG domains would impose an entropic barrier for passive diffusion. As far as this notion is valid in rationalizing the *in vitro* observations regarding nucleo-cytoplasmic transport (NCT), it is lacking the molecular foundation due to limitations in resolving those highly dynamic processes *in vivo* as well as *in vitro*. Moreover, the rapid *in vivo* dwell times of NTR's ($\sim 5\ ms$) (Ma & Yang, 2010) obviously contradict the apparent avidity of highly multivalent NTR − FG domain interactions and high affinities measured *in vitro* thus far (Tetenbaum-Novatt et al., 2012). However, an *in vitro* investigation carefully considering the environment of such an interaction may still converge in a realistic picture of the overall process. In the context of the NPC there are several environmental constraints that are likely to influence NTR − FG domain interactions.

This includes closely tethered FG domains that display collective functional characteristics (Atkinson et al., 2013) (albeit their exact numbers and locations are uncertain), the presence of high concentrations of NTR's (Paradise et al., 2007), as well as their confinement within a cylindrical geometry. The thesis thus mainly focuses on the structure – function relationship of diverse FG domains using surface plasmon resonance (SPR), a technique that is commonly used for biomolecular binding studies. The FG domains are end-tethered to the SPR sensor surface at high densities in order to mimic one of their main structural characteristics within the NPC, and NTR's are applied at concentrations that are considered physiological. SPR is a straightforward technique in quantifying protein adsorption to the sensor surface, however, it is unfavorable in determining the overall conformation of the FG domains. For SPR to contribute structural information, it requires knowledge about the dielectric properties (i.e. refractive index) of such an interfacial molecular assembly (De Bruijn et al., 1991). Demanding an integral conformational and functional characterization of the FG domains, thus a novel SPR based method is applied to overcome those limitations *in situ*, using „non-interacting molecules as innate structural probes".

1.2 The nuclear pore complex (NPC)

The nuclear pore complex (NPC) enables the bidirectional exchange of macromolecules across the nuclear envelope (Stewart, 2007). The main NPC features shall be introduced in the following sections in regard of nuclear localization signal (NLS) mediated transport. Main focus is thereby applied to the vertebrate NPC, although many basic features were first discovered in the yeast NPC that is expected to share a common structure and transport functionality (Yang et al., 1998).

1.2.1 Structure of the NPC

Structural characterization of the entire vertebrate NPC by cryo-electron microscopy (EM) revealed a triple ring model of the NPC that consist of a central ring of massive spokes, framed top and bottom by two thin coaxial rings (Akey, 1989; Reichelt et al., 1990). These cytoplasmic and nucleoplasmic coaxial rings as well as the central spoke assembly have an eightfold rotational symmetry axis in respect to the central axis that is perpendicular to the nuclear membrane plane (Franke, 1974; Akey, 1989; Reichelt et al., 1990). The spoke-ring complex additionally anchors more peripherally associated components, including the cytoplasmic filaments and the nuclear basket (Jarnik & Aebi, 1991). The minimum inner diameter of the complex defined by the spokes assembly is $\sim 50\ nm$ whereas the effective total diameter of the NPC is ~ 150 nm in vertebrates (Akey, 1989). Mass determination by scanning transmission EM revealed a total mass of 125 MDa for intact NPC's from Xenopus laevis oocyte (Reichelt et al., 1990). Even tough it was already known that nucleo-cytoplasmic transport is taking place through the center of the pore (Feldherr et al., 1984; Richardson et al., 1988; Askey & Goldfarb, 1989), the constitution of the pore interior remained largely unclear. It was initially described as electron-opaque granule, the 'central granule' (Franke, 1974), a relatively labile structure with mass density typical for proteins, the 'central plug' (Reichelt et al., 1990), or a low density channel-like feature, the 'transporter' (Askey, 1989), that can have open or closed conformation (Askey & Goldfarb, 1989). However, a variety of pore-traversing filaments have been noted (Franke, 1974) and detergent isolated spoke complexes unveiled fine-spun material arranged in a ring that were attributed to "inner pore filaments" (Reichelt et al., 1990).
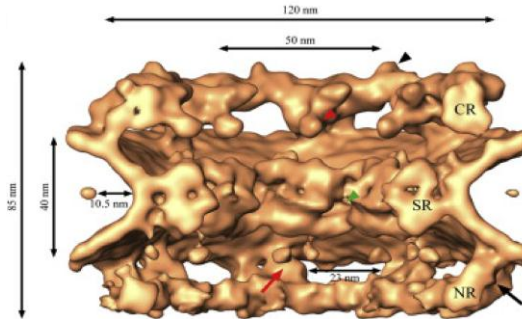
Fig. 1.1. Recent cross-section from cryo-electron tomography of the human NPC (taken from Maimon et al., 2012) revealing the hourglass morphology of the hNPC and its key dimensions. The abbreviations stand for: cytoplasmic ring (CR), nuclear ring (NR), and spoke ring (SR), respectively.

1.2.2 Transport receptors and transport mechanisms

1.2.2.1 The molecular foundation of nuclear import

The majority of nuclear proteins contain a nuclear localization sequence (NLS) that is necessary for nuclear import (Forbes, 1992). The NLS receptors Kapα1 and Kapα2 (Adam & Gerace, 1991) where identified and in combination with Kapβ1 (importin-β) to stimulate binding of the import substrate at the nuclear envelope (Adam & Adam, 1994). Additionally, for translocation of a docked substrate into the Nucleus (Moore & Blobel, 1992) a small GTPase Ran was identified (Moore & Blobel, 1993). In solution binding assays using yeast homologs of RanGTP, Kapα and Kapβ further revealed RanGTP to disrupt the karyopherin heterodimer by binding directly to Kapβ1 (Rexach & Blobel, 1995). Although there was evidence for proteins containing FXFG motifs to function in nuclear import of proteins, they were first identified as docking sites using overlay plots (Radu et al., 1995a, 1995b) and it was already proposed that the movement of cargo across the nuclear pore is a stochastic process that operates via „repeated association-dissociation reactions of karyopherin-NLS protein complexes" (Radu et al., 1995a) or „stochastic karyopherin-mediated binding and release of NLS proteins", as binding of the karyopherin-NLS protein complex to a FXFG region lowers the affinity of the NLS protein for karyopherin

(Rexach & Blobel, 1995). Additionally, karyopherin subunits were attributed to have lower affinity for FXFG regions than a karyopherin heterodimer. FG repeats consist of hydrophobic amino acid motifs such as FG, FXFG, or GLFG and hydrophilic linkers of 5-50 amino acid residues (Peters, 2009). The FG repeat regions of yeast nucleoporins have been shown to exhibit structural characteristics typical for intrinsically disordered proteins (IDP's) by predictive amino acid sequence analysis and biophysical characterization (Denning et al., 2003). The biophysical characterization revealed small sedimentation coefficients, large Stokes radii typical of non-globular structures with low compactness, as well as a low content of secondary structure. Finally, hypersensitivity of nuclei-associated FG Nups to the small proteinase K, suggests that the FG regions retain considerable disorder and flexibility at the NPC.

Nature Reviews | Molecular Cell Biology
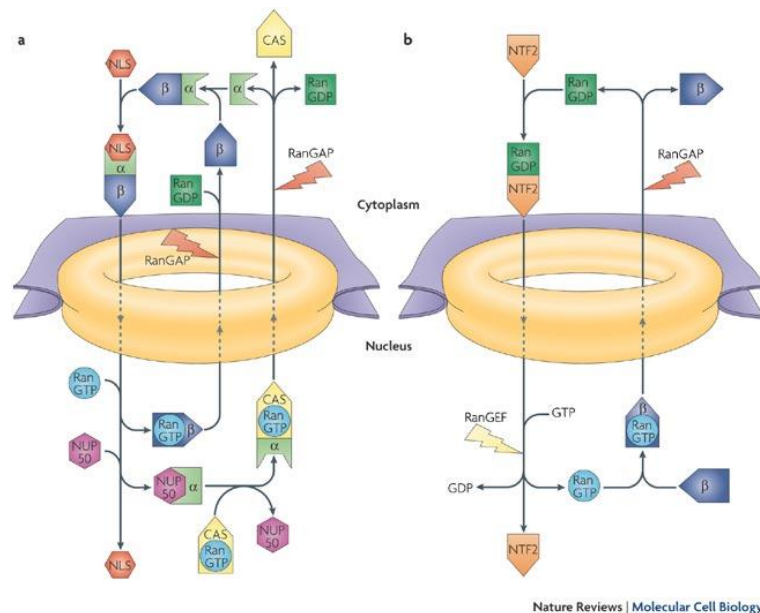
Fig. 1.2. NLS cargo import cycle (picture taken from Stewart, 2007). Proteins containing an NLS are recognized by Kapα in complex with Kapβ, where Kapβ mediates binding of the import complex to FG nucleoporins located at the NPC. In the nucleus RanGTP disrupts the karyopherin heterodimer by binding directly to Kapβ which releases the cargo from the pore. Kapβ in complex with RanGTP shuttles back into the cytoplasm, whereas Kapα is recycled to the cytoplasm by its nuclear export factor CAS. In the cytoplasm the GTPase activation protein RanGAP stimulates GTP hydrolysis and release of Kapβ. RanGDP is then shuttled to the nucleus by its transport factor NTF2 where the nucleotide exchange factor RanGEF catalyzes nucleotide exchange and generates RanGTP.

1.2.2.2 The transport models

The yeast FG Nups are found throughout the NPC from its cytoplasmic to the nuclear extremities with an estimated number of 160 copies per NPC from immuno-gold labeling, where most of the FG Nups are symmetrically distributed from the NPC mirror plane (Rout et al., 2000). Given the number and disposition of FG Nups the authors propose a *Brownian Affinity Gating model*: While Brownian diffusion accounts for translocation, the confined channel together with the "filamentous" FG Nups presents a significant entropic barrier for passive diffusion. Macromolecules that bind to Nups increase their residence time at the entrance of the pore, and so their diffusion across the NPC is greatly facilitated. Hence, translocation of cargo does not require conventional mechanical gating by providing a "virtual gate" that "opens" if signal mediated transport is active. Rapid and reversible binding to symmetrically distributed Nups would promote a fast diffusional exchange of transport factors between the two faces of the NPC. Vectorial transport may arise from the asymmetry of a minority of FG Nups and the asymmetric distribution of Ran-GTP (Mattaj and Englmeier, 1998), where RanGTP is essential for release of the import substrate into the nucleoplasm (Görlich et al., 1996). However, the direction of transport through the NPC can be inverted in the presence of high concentrations of cytoplasmic RanGTP (Nachury & Weis, 1999), contradicting the *hypothesis of an affinity gradient* responsible for directionality of transport (Ben-Efraim & Gerace, 2001), suggesting that the directionality is determined mainly by the compartmentalized distribution of RanGTP. Similar reasoning is implied from deletion studies were all asymmetrically localized FG domains together were non-essential and except for specific combinations of symmetrically localized FG domains half of the total mass of FG domains could be deleted without loss of viability or the NPC's normal permeability barrier in yeast (Strawn et al., 2004). The homodimers of nuclear transport factor-2 (NTF2), a RanGDP import receptor (Ribbeck et al., 1998; Smith et al., 1998), is of similar size to GFP and below the passive diffusion limit of ~40 kDa (Macara, 2001), still NTF2 passes the NPC about 120 times faster than GFP does (Ribbeck & Görlich, 2001). The authors thus propose the *"selective phase" hypothesis*: FG repeats attract

each other to form a rather homogeneous meshwork that restricts the passage of inert objects. Transport receptors on the other hand compete locally with the repeat-repeat interactions via direct binding to the repeats, increasing their "solubility" in the central plug. The FG domains thus form a semi-liquid phase that transport receptors can easily partition but inert molecules above a certain size cannot. The *oily-spaghetti model* assumes the nuclear pore to have a central open tube and the nucleporin "spaghetti" would form a layer around this tube (Macara, 2001). Carrier proteins bind weakly and transiently and the nucleoporins are flexible and freely moving such that the carriers can diffuse from one binding site to the other relatively unhindered, stochastically back and forth across the pore. The cytoplasmic and nucleoplasmic nucleoporins would serve as docking sites, facilitating complex assembly and disassembly, rather than sites involved directly in translocation. The *reduction-of-dimensionality model* assumes that the filaments and the central channel of the NPC are lined by a coherent FG surface, whereas a loose network of hydrophilic peptide chains extend from the channel forming a selectivity filter (Peters, 2005). Neutral molecules would permeate the NPC only by diffusing through a narrow open tube in the channel center, whereas transport receptors attaching to the FG surface remain bound but can rapidly move around on the surface by a two-dimensional random walk. The filament sections would serve as antennas collecting transport receptors from the aqueous phase. Extensive characterization of yeast FG domains such as Stokes radii determination and protein composition analysis revealed two distinct categories of IDP structures in FG nucleoporins (Yamada et al., 2010). The ratio of charged to hydrophobic AAs could best predict the different structural categories ranging from collapsed coil (low ratio) to extended coil (high ratio) conformations, where some Nups display a bimodal distribution resembling the canopy and trunk of a "tree", respectively. These findings were rationalized in the *forest model* where collapsed "shrubs" and extended "threes" form two distinct transport zones: Zone 1 is the open central channel flanked by self-interacting hydrophobic canopies of the "threes". This central transporter structure could easily deform and expand in diameter to accommodate large cargo's without breaking the hydrophobic network maintained by the canopies. Zone 2 is defined by the space of the extended stalks,

that is lined by the hydrophobic domains in shrub configuration and the exterior surface of the transporter structure. Unloaded Kaps and Kaps loaded with small cargo's could move across the NPC via Zone 2. The different models for nucleo-cytoplasmic transport (NCT) are summarized in Fig. 1.3.
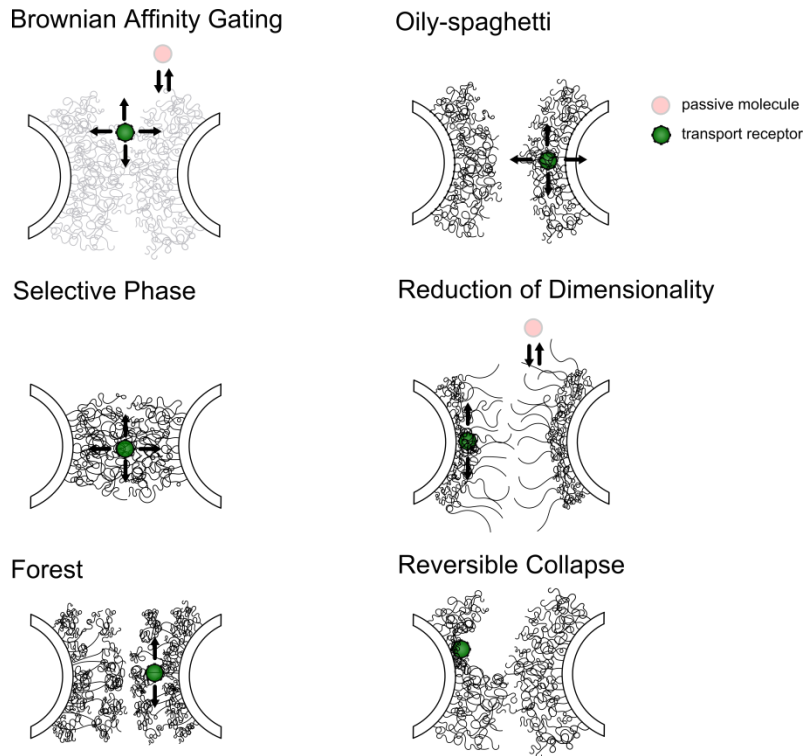
Fig. 1.3. Models for nucleo-cytoplasmic transport including the proposed arrangement of „filamentous" FG Nups and the expected movement of a transport receptor inside the NPC. See text for a detailed explanation of the models.

1.2.3 Transport receptors and their interactions with FG nucleoporins

1.2.3.1 Molecular recognition and affinity

The crystal structures of Kapβ1 (importin-β) bound to RanGTP and the Kapα1 IBB (importin-β binding) domain have been determined (Vetter et al., 1999; Cingolani et

al., 1999). Kapβ1 is an all-helical protein composed of 19 tandem heat repeats, arranged in a right handed superhelix, each containing an A and a B helix connected by a short turn. Repeats are arranged within the molecule to produce an outer layer of A helices defining the convex surface and an inner layer of B helices defining the concave surface. RanGTP and the Kapα1 IBB domain are bound to the inner (concave) surface of Kapβ1, although RanGTP binding involves the N-terminal half whereas IBB domain binding involves mainly the C-terminal half, the latter complex having a highly compact, essentially globular shape, with Kapβ1 in a spiral conformation. SAXS data of Kapβ1 in its unbound state suggest a less compact S-like appearance with $D_{max} = 15 \pm 1$ nm and $R_g = 4.6 \pm 0.1$ nm. In comparison the RanGTP / Kapβ1 complex has structural parameters $D_{max} = 11 \pm 1$ nm and $R_g = 3.6 \pm 1$ nm (Fukuhara et al., 2004). These results indicate that the global conformation of Kapβ1 is ligand dependent with a closed conformation in the presence of either an IBB cargo or RanGTP and a highly flexible conformation of the free, ligand unbound, molecule in solution (Forwood et al., 2010). The crystal structure of a complex formed between residues 1-442 of Kapβ1 and a construct containing five tandem FXFG repeats from yeast nucleoporin Nsp1 reveals the FXFG cores to bind on the convex face of Kapβ1 at a primary site located between the A helices of HEAT repeat 5 and 6, respectively, and at a secondary site between the A helices of HEAT repeat 6 and 7, respectively (Bayliss et al., 2000). The interactions involve almost exclusively the two Phe's of the FXFG core that are buried in a hydrophobic pocket generated by side chains of the A helices of Kapβ1. Additionally it was shown that GLFG repeats bind to the same hydrophobic site on Kapβ1 previously identified as the principal FXFG binding site (Bayliss et al., 2002). The molecular recognition of FG repeats by Kapβ1 appears to involve primarily the FG dipeptide (**XXFG**) where L (**G**LFG) and F1 (**F**XFG) form a cap that further shields it from solvent, although some contribution to the hydrophobic interface is also made by F1 and to a lower extent by L. For the yeast homolog of Kapβ1, Kap95p, a third FG binding pocket was discovered when in complex with yeast Nup1p and the interaction interface involved substantial contributions from hydrophobic residues located in the linker between Phe residues (Liu & Stewart, 2005). Two additional

weak binding pockets were predicted using structural alignment of the N- and C-terminal halves combined with site-directed mutageneisis in the A helices of heat repeats 14 and 16 (Bednenko et al., 2003). Molecular dynamic simulations could successfully reproduce the three binding spots uncovered by X-ray crystallography as well as one of the two spots discovered experimentally by site-directed mutagenesis (Isgro & Schulten, 2005). Additionally five novel sites were discovered in the simulations, suggesting that Kapβ1 features many more binding spots than suspected so far. Analogous to interactions between hydrophobic batches on NTR's and FG Nups it was shown using modified BSA that surface hydrophobicity is sufficient to provide access to the NPC (Naim et al., 2009). NTF2 on the other hand forms a homodimer, where two identical FXFG binding sites (hydrophobic depressions) on the dimeric molecule are formed by residues from each chain of NTF2 (Bayliss et al., 2002). Interestingly NTR's are not only hydrophobic but also highly negatively charged, whereas many nucleoporins that constitute the selectivity barrier are positively charged, suggesting that electrostatic interactions are an essential part of the selective filtering mechanism (Colwell et al., 2010). Since NTR's and FG domains have multiple binding sites, where the binding strength is the product, not the sum of individual equilibrium dissociation constants (avidity), they show high binding affinities with nano-molar dissociation constants K_D in various binding assays. As the free concentration of NTR's in living cells is in the micro-molar range (Paradise, 2007), and thus well above the effective K_D values measured for FG-NTR complexes, the FG domains of the NPC seem to be saturated with NTR's (Peters, 2009). This is in agreement with quantitative fluorescent microscopy analysis revealing over 100 Kapβ1 molecules bound to a single NPC (Tokunaga et al., 2008). Detailed characteristics of the FG domains relevant to this study are listed in table 1.1.

Receptor	Nup	K_D	Method	Publication
Kapβ1	Nup62	8.04 ± 0.2 nM	SPR	Lott et al., 2010
Kapβ1	Nup62	73.3 ± 11.6 nM	ELISA	Bednenko et al., 2003
Kapβ1	Nup153	1.1 ± 0.1 nM	ELISA	Bednenko et al., 2003
Kapβ1	Nup62	100 ± 8 nM	ELISA	Ben-Efraim & Gerace, 2001
Kapβ1	Nup153	9 ± 2.5 nM	ELISA	Ben-Efraim & Gerace, 2001
Kap95	Nsp1	0.32 ± 0.04 / 5.3 ± 1.7 μM	QCM-D	Eisele et al., 2010
Kapβ1	Nsp1	0.11 ± 0.03 μM	ELISA	Bayliss et al., 2002
Kap95	Nsp1	0.16 ± 0.04 μM	ELISA	Bayliss et al., 2002
Kapβ1	Nup100	0.18 ± 0.01 μM	ELISA	Bayliss et al., 2002
Kap95	Nup100	0.11 ± 0.01 μM	ELISA	Bayliss et al., 2002
Kapβ1	Nup116	0.19 ± 0.01 μM	ELISA	Bayliss et al., 2002
Kap95	Nup116	0.11 ± 0.03 μM	ELISA	Bayliss et al., 2002
Kapβ1	Nup1	0.14 μM	ELISA	Bayliss et al., 2002
Kap95	Nup1	0.35 μM	ELISA	Bayliss et al., 2002
Kap95	Nup42	1500 ± 200 nM	Bead assay	Pyhtila & Rexach 2003
Kap95	Nup100	223 ± 38 nM	Bead assay	Pyhtila & Rexach 2003
Kap95	Nup1	7.9 ± 1.7 nM	Bead assay	Pyhtila & Rexach 2003

Table 1.1. Literature collection of binding affinities for FG domain – karyopherin interactions from various types of binding assays.

1.2.3.2 Number and localization of FG nucleoporins in vertebrates

From quantification of SDS-PAGE band intensities the copy number of FG domains in the mammalian NPC was estimated based on the assumption that nucleoporins would be present at a copy number of 8 or multiples of 8, owing to the rotational symmetry of the NPC (Cronshaw et al., 2002). About one third of Nups contain FG domains yielding together ~200 FG domains and ~3000 FG motifs per NPC. The estimated copy numbers of the FG repeat containing Nup153 (FXFG), Nup98 (GLFG), Nup214 (FXFG) and Nup62 (FXFG) are 8, 8, 8, and 16 respectively. However, recent crystallographic studies suggest that Nup62-Nup54-Nup58 together form the mid-plane ring of the transport channel with 128 molecules of Nup62, where the FG regions of Nup62 point symmetrically towards the peripheries of the transport channel (Solmaz et al., 2011). Immuno-gold labeling shows Nup98 localized in the center of the NPC (Krull et al., 2004; Chatel et al., 2012) and is considered to be essential for maintaining the passive permeability barrier as well as active nuclear transport (Hülsmann et al., 2012). Nup153 is located at the nuclear ring as well via its zinc-finger domain to the distal ring from where the highly flexible and mobile FG domain protrudes (Fahrenkrog et al., 2002). The FG domains of Nup62 are located close to the entry and exit side of the NPC's central pore, whereas the anchorage site was located at the cytoplasmic entry site of the central pore (Schwarz-Herion et al., 2007). Nup214 is anchored to the cytoplasmic side of the NPC and its FG domain appears highly flexible (Paulillo et al., 2005).
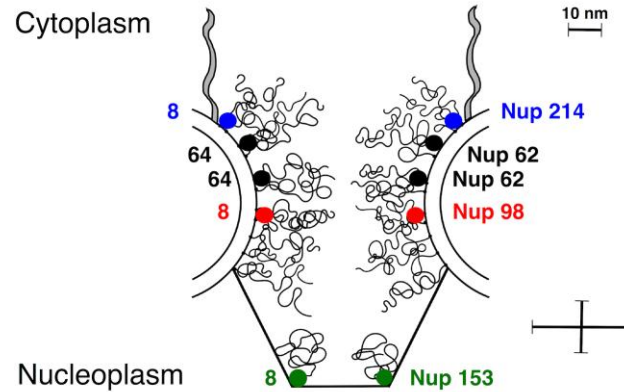
Fig. 1.4. Localization of the FG nucleoporins in the NPC from immunogold-labeling (Nup214, Nup62, Nup98, Nup62) and estimated copy number from SDS-PAGE band intensities (Nup214, Nup62, Nup98) and crystallography (Nup62). However, the same crystallographic studies suggest Nup62 to be symmetrically distributed towards the peripheries of the NPC.

1.2.4 Nuclear transport studies: In vivo, in vitro & in silico

1.2.4.1 „in vivo"

From nuclear accumulation of fluorescent transport receptors it was shown that a single NPC is able to translocate 800 transportin molecules (100 kDa) or 2500 NTF2 homodimers (29.5 kDa) per second and approaches rates of purely diffusion controlled processes (Ribbeck & Görlich, 2001). The initial transport rates for transportin molecules into the nucleus at low concentrations reveal a Michaelis–Menten constant $K_M = 4\,\mu M$, consistent with weak and thus transient interactions, whereas at higher transportin concentrations the translocation rates deviate from an ideal Michaelis-Menten curve. The transport rates do not saturate at increasing transportin concentrations, apparently because cooperativity in NPC passage becomes significant at higher transportin concentrations. The dominant-negative Kapβ1 45-462 mutant lacking the Ran / Kapα binding residues, which binds virtually irreversibly to

NPC's, imposes a very tight block on facilitated translocation events. The inactivation of the Ran binding site in Kapβ1 prevents termination but not translocation, suggesting that RanGTP binding to Kapβ1 releases Kapβ1 from the NPC. Interaction times of various transport substrates and transport receptors with the NPC were obtained by tracking the process of transit by using single-molecule fluorescence (SMF) microscopy (Yang et al., 2004). Transport time and rates are summarized in table 1.2. The transport rates vary from *ms* to *s* depending on the substrate, where each NPC is capable of transporting several substrate molecules simultaneously. Molecular tracking further reveals that substrate molecules spend most of their transit time randomly moving in the central pore of the NPC and that the rate-limiting step is escape from the central pore requiring RanGTP for rapid release (Yang et al., 2004). Similar measurements suggest that translocation is accelerated for loaded receptor molecules (Kubitscheck et al., 2005) and that for large cargo's efficient transport requires multiple NTR's with non-substantial increase in residence time, i.e. by only ∼2-fold between low and high NTR:cargo conditions (Tu et al., 2013). However, multivalency is expected to increase the residence time due to a lower rate of release from the FG network. The authors thus speculate that multivalency enthalpically decreases the entropic permeability barrier located in the center of the pore, thus enhancing transport efficiency, while most of the transport time is spent in the low FG density cytoplasmic and nucleoplasmic periphery respectively. Interestingly, the transport times for import complexes consisting of NLS-2xGFP, Kapα1, and Kapβ1 are dropping from 8.6 ± 0.4 to 2.2 ± 0.1 ms when the concentration of the complex is increased from 0.1 nM to 15 μM (Yang & Musser, 2006). Similarly, the import efficiency increases from 51 ± 5 to 77 ± 5 % over the same concentration range. The same modulation was achieved when the Kapβ1 concentration alone was increased to 15 μM at a fixed cargo concentration of 0.1 nM showing that transport times are dropping to 1.4 ± 0.1 ms. This drop in transport times has a transition point consistent with K_D∼1 μM for the binding of Kapβ1 molecules/complexes to the NPC. The authors thus introduce the term "pore occupancy" to explain for the observed changes in interaction time, in a sense that NPC transport properties can vary significantly depending on the particular molecules bound to it any given moment in time. In a

single molecule study with high spatiotemporal resolution of 10 nm and 400 μs the 3D spatial density maps for transient interaction sites of Kapβ1 and Kapβ1-cargo complexes were obtained (Ma & Yang, 2010). In the central pore region Kapβ1 rarely occupies an approximately 15-nm-diameter axial channel and instead primarily locates at the periphery of the channel. Transiting cargo in complex with Kapβ1 reveals a similar pathway but occupies more space of the central channel in the central pore region than Kapβ1 alone. In a proceeding study it was shown in addition that small molecules (0.3 – 29 kDa) smoothly diffuse trough a single axial central channel with a cut-off size of approximately 40-60 kDa for passive diffusion (Ma et al., 2012). Even though facilitated and passive transport pathways show partial overlap, the results seem in agreement with a single channel configuration in the NPC as proposed in the oily-spaghetti and the ROD models but do not support the selective phase model where multiple holes and pathways are predicted. Remarkably, the diameter of the Kapβ1 unoccupied central channel in the middle plane of the NPC reversibly increases as the Kapβ1 concentration is increased, indicating "self-regulated" conformational changes of the FG Nup barrier to occur in intact NPC's. For quantum dots (QD's) functionalized with multiple covalently coupled Kapβ1 binding (IBB) domains as a mimic of large cargo's the mean square displacements along the transport axis are sub-diffusive and QD's with higher receptor density translocate faster (Lowe et al., 2010).

Substrate	Size	Transport Mechanism	Transport Time	Publication
NLS-2xGFP		Facilitated transport	10 ± 1 ms	Yang et al., 2004
NTF2	29.5 kDa	Transport receptor	5.8 ± 0.2 ms	Kubitscheck et al., 2005
NTF2-RanGDP	83.6 kDa	Loaded Transport receptor	5.2 ± 0.2 ms	Kubitscheck et al., 2005

Transportin	97 kDa	Transport receptor	7.2 ± 0.25 ms	Kubitscheck et al., 2005
Transportin-M3-GST	179 kDa	Loaded Transport receptor	5.6 ± 0.2 ms	Kubitscheck et al., 2005
NLS-2xGFP		Facilitated transport	1.4 ± 0.1 ms	Yang & Musser, 2006
BSA-NLS		Facilitated transport	6.2 ± 0.3 ms	Dange et al., 2008
Kapβ1		Transport receptor	6.6 ± 0.2 ms	Dange et al., 2008
Kapβ2		Transport receptor	4.6 ± 0.1 / 103 ± 6 ms	Dange et al., 2008
Kapβ1		Transport receptor	4.9 ± 1.9 ms	Ma & Yang., 2010
Dextran	10 kDa	Passive diffusion	1.7 ± 0. ms	Ma et al., 2012
QD's	18 ± 4 nm	Facilitated transport	Median: 34 s	Lowe et al., 2010
mRNA		Facilitated transport	65 ± 5 / 350 ± 25 ms	Siebrasse et al., 2012
M9-βGal-8C	~500 kDa	Facilitated transport	8.7 ± 0.8 ms	Tu et al., 2013
M9-2xGFP	~60 kDa	Facilitated transport	6.8 ± 0.9 ms	Tu et al., 2013

Table 1.2. Literature collection of dwell times for various transport substrates within the NPC.

Cryo-electron tomography was used to take snapshots of cargo-trajectories inside the NPC and superimposed to obtain three-dimensional probability density maps of cargo

localization (Beck et al., 2007). For the gold-labeled fusion protein NLS-2xGFP the density was relatively low in a region with a maximum diameter of 20 nm in the middle of the central channel, even though the corresponding region exhibits a high electron microscopy density from uncertain origin.
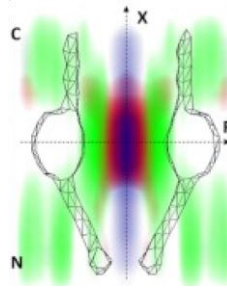
Fig. 1.5. Superimposed transport routes of passive diffusion and facilitated translocation (taken from Ma et al., 2012). Central slice showing probability density of Kapβ1 (green), 0.3 kDa fluorescein (red), and 29 kDa GFP (blue), respectively, superimposed to the NPC structure (grey).

1.2.4.2 „in vitro"

Artificial systems can mimic the transport selectivity of NPC's. For instance a polycarbonate membrane perforated by ∼30-nm-diameter nanopores coated with a thin gold layer was modified with yeast Nsp1 or Nup100 FG domains and the flux of fluorescently labeled proteins across the membrane was measured (Jovanovic-Talisman et al., 2009). Membranes functionalized with Nsp1-FG behave as a selective filter with a strong preference for the transport receptors NTF2, Kap95 and Kap121, as well as respective transporter-cargo-complexes, while significantly inhibiting the passage of control proteins that do not interact with FG domains. Interestingly, a significant reduction in flux of control proteins occurs only in the presence of transport factors that bind FG domains efficiently, such that transport factors may be considered transient components of the NPC that help to discriminate against the passage of nonspecific materials. In a similar study, the *in vitro* reconstitution of a biomimetic 'minimalist NPC' provided a platform for studying

nucleo-cytoplasmic transport phenomena at the single molecule level (Kowalczyk et al., 2011). Therefore nanopores of ~40 nm diameter were drilled in a thin free-standing silicon nitride membrane and subsequently functionalized with FG domains of either Nup98 or Nup153. Spikes in the ion current measurements at physiological salt concentration could then be related to the translocation of individual proteins after adding either 2.9 μM of Kapβ1 or 4.2 μM of BSA. The FG domain coated pores very effectively block the passage of BSA, whereas Kapβ1 selectively proceeds with a dwell time of ~2.5 ms for both Nup98- and Nup153-coated pores, this is more than a 10-fold increase in dwell time compared to the bare pore.

1.2.4.3 „in silico"

Computational approaches to nucleo-cytoplasmic transport are limited to coarse grained model systems in which the atomic details are lost in order to obtain computational feasibility (Moussavi-Baygi et al., 2011a & 2011b). The NPC main scaffold is elastic and discretized into linear springs where FG repeat axial extension is modeled by discrete worm-like chains (WLC) and inter-FG as well as Kap-FG hydrophobic affinity is modeled by a long-range potential energy. The complex of NLS-cargo and Kapβ is considered as a solid sphere with Kapβ as a half-circle on the cargo-complex with eight binding spots of equal affinity for FG repeats ($2\,k_BT$) that is slightly stronger than that of FG-FG binding ($1.5\,k_BT$). In the absence of any molecular traffic and competing factors this leads to a mean passage time for transport of 2.6 ± 0.13 ms for a 15 nm cargo-complex and reflects the stochastic nature of nucleo-cytoplasmic transport. The cargo-complex is most likely found near the wall, where it hydrophobically interacts with the FG repeat layer near the wall ($r = 17.8 \pm 2.6$ nm for a channel radius of 30 nm). Within the central channel the cargo-complex is attached to the FG layer for > 95 % of time whereas it detaches more often within the NPC peripheries. The average lifetime of a hydrophobic bond between a single binding spot on the Kapβ and an FG motif during transport is approximately 1.5 ns with a standard deviation of about 17 ns. Once the cargo is

hydrophobically engaged, on average about 7.89 of eight binding spots are interacting simultaneously with FG repeats. In simulations where there are too many binding spots (high avidity) the cargo-complex becomes trapped within the pore and the cytoplasmic filaments play an important role in selectivity by repelling inert cargo's.

For solute-specific protein channels that span biological membranes there is accumulating evidence that corresponding channels display pronounced binding to the solute that transits the channel. Several theoretical studies thus rationalize the effect of particle-channel interactions on transit probability of the particle trough the channel (Berezhkovskii et al., 2002 & 2005). These studies assume that particle diffusion occurs in the potential $U(x)$ and the diffusion coefficient $D(x)$ depends on particle position x. The translocation probabilities for single particles reach their maximum values when a deep potential well occupies the entire channel or when intra-channel equilibration occurs much faster than all other processes, i.e., when $D(x) \rightarrow \infty$. However, the translocation probability is not the only factor that determines the efficiency of transport. The residence time is an important factor since particles sitting in the channel block the entry of other particles (i.e., the channel can be occupied by only one particle). It follows that there is an optimum in potential depth that makes channel transport most efficient as a trade-off in transport probability and residence time. This result holds for a diffusion based model as well as for a model of N identical binding sites (in analogy to SFD), where the average lifetime τ of the molecule inside the channel can be expressed as

$$\tau = \frac{N}{2k_{off}} \qquad (1.1)$$

and k_{off} is the rate constant for escape from the channel. The diffusion in an effective potential was also addressed consistent with functional properties of the NPC for karyopherin-mediated import resulting from interactions with flexible FG

nucleoporins and RanGTP release (Zilman et al., 2007). The transport receptors are thus considered to stochastically hop back and forth inside the channel via binding and unbinding to FG repeats and spatial diffusion. The results are similar to single particle channels. If the model accounts for limited space inside the channel, there is an optimal binding strength that balances increased transport probability with increased time spent within the NPC. The authors reason that optimal interaction strength with FG repeat regions provides a mechanism for selectivity of NPC-mediated transport. However, in a situation where optimally binding karyopherins compete for space and binding sites with others, weakly binding macromolecules, the selectivity for optimal binding is even enhanced. This follows from the relatively short residence time of the weak binders that increases the probability of return to the cytoplasm if binding sites are occupied by karyopherins. Crucially, the authors also show with their model that the transport properties of the NPC are not very sensitive to the number of FG repeat regions as long as they are flexible enough for their fluctuation regions to overlap, accounting for the robustness of transport upon deletion of FG repeat regions (Strawn et al., 2004). For their numerical studies they find essentially identical transport efficiencies in a multiwell potential and a corresponding single well potential. The results were obtained by assuming the unbinding and rebinding to occur faster than the lateral diffusion of karyopherin-cargo complexes such that possible differences in the diffusion coefficient outside and inside the NPC are neglected. For a diffusion coefficient of $D = 1 - 10 \mu m^2/s$ typical for protein diffusion in the crowded environment of the cytoplasm they calculate residence times of $0.01 - 1$ s and optimal interaction strengths of 5 - 15 $k_B T$ for a flux of $10 - 1000$ molecules/s trough the NPC.

1.3 Structure and function of end-tethered FG domains

1.3.1 Studies on FG domain structure

AFM studies on FG domains of Nup153 tethered via terminal cysteines to gold nanodots ~100 nm in diameter exhibit a long-range steric repulsive force, featuring a polymer brush-like, entropic barrier conformation (Lim et al., 2006; Lim et al., 2007). The brush-like conformation collapsed into a more compact state upon the addition of nano-molar concentrations of Kapβ1 and was restored upon addition of RanGTP. Yeast nucleoporins containing GLFG domains weakly interact with each other (K_D~mM) and this cohesion requires Phe residues in GLFG motifs (Patel et al., 2007). Contrary the FXFG domains are not cohesive supporting the notion that some FG Nups function exclusively as repulsive bristles under physiological conditions. Recent Molecular dynamics simulations of various initial conformations of the FG domain of Nsp1, a key yeast central channel Nup, were performed to access information about structure and interactions of FG domain assemblies (Gamini et al., 2014). The initial conformation comprise fully extended Nsp1 FG domains tethered to a gold ring, Nsp1 FG domains tethered to a flat gold surface in a random polymer conformation as well as untethered Nsp1 FG domains in bulk solvent in a random polymer conformation. At the end of the simulation the initially fully stretched Nsp1 FG domains formed brush like bundle structures, where the bundles are interconnected via single Nsp1 FG chains crosslinking adjacent bundles (see Fig. 1.6). Interestingly the structure of a mutant FG domain of Nsp1 where all its phenylalanines and glycines are replaced by alanines is very similar to wild-type Nsp1 FG domains, suggesting that FG motifs are not particularly critical for the formation of these structures. Similar to the stretched Nups, the FG domains tethered to a flat surface in a random conformation revealed a brush-like structure of bundles, whereas the freely floating Nsp1 FG domains formed again bundles but with many more links between them resulting in a mesh-like structure. The pore size in the

resulting Nsp1-FG assemblies were computed, where large pores of radius ~77 Å for bundles with few crosslinks (6 nm grafting distance) and relatively small pores of radius 43-50 Å for mesh-like bundles are available for diffusive passage of molecules, respectively. Since tethering effects should be minimal in the central region of the pore, the authors argue, that the structure found in this region should be similar to the mesh-like bundles. In a very similar study it was observed that the Nsp1 brush spots many surface exposed FG repeats and that more than half of the FG repeats are available at the bundle surface (Miao & Schulten, 2009). In an atomistic simulation on the aggregation behavior of FG repeat motifs it was shown that Hydrogen bonding is the most important structural determinant in the aggregates (with some β-sheet content), but interactions between polar side chains dominated the intermolecular energetics (Dölker et al., 2010). The authors conclude from their results that interactions between FG repeats are determined by hydrogen bonding and electrostatic interactions rather than $\pi - \pi$ bonding, and that hydrophilic linkers play a much larger role in the formation of the permeability barrier than previously thought.
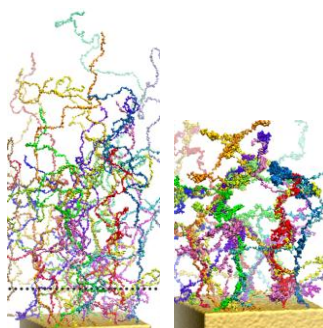
Fig. 1.6. Initial random array configuration of Nsp1 FG domains (left). Formation of cross-linked Nsp1 FG domain bundles after a simulation time of 1 us (right) (taken from Gamini et al., 2014).

A coarse grained molecular dynamics study was used to investigate the distribution of FG Nups inside the NPC (Ghavami et al., 2014). Here, a one-bead-per-amino-acid model takes into account hydrophobic (attractive), hydrophilic (repulsive), and electrostatic interactions, whereas hydrogen bonding is not incorporated. The model reveals a relatively low density region observed along the central axis of the NPC,

which is surrounded by a coherent hydrophobic doughnut-like structure, rich in FG repeats. The accumulation of charged residues is higher near the scaffold where the FG Nups are anchored, i.e. the charged residues form a bumper to push the dense FG cluster towards the center. Most intriguing is their finding from the comparison between viable and inviable NPC's. When modeling the deletion studies of Strawn et al. *in silico*, they find that the formation of a high-density hydrophobic structure, rich in FG repeats, is a characteristic feature of viable NPC's. The maximum density of the FG Nups inside the pore does not exceed 185 mg/ml in the inviable NPC's, whereas for the wild-type and viable NPC's, this value increases to 300 mg/ml within the FG doughnut.

1.3.2 Challenges in resolving FG domain structure and function

Due to the intrinsic disorder in FG domains neither crystallography nor tomography are constructive in resolving their structure (Maimon et al., 2012). Most „*in vitro*" assays have so far been limited to either biophysical in solution characterization (Denning et al., 2003) or surface based binding assays neglecting the structural scaffolding of FG domains (Bayliss et al., 2002; Pyhtila & Rexach, 2003; Lott et al., 2010). Structural characterization of densely-packed surface-tethered FG domains has so far most elaborately been performed using atomic force microscopy (AFM), revealing a long-range steric repulsive force, featuring a polymer brush-like conformation (Lim et al., 2006; Lim et al., 2007). However, AFM does not feature molecular quantification and thus the structural characterization is incomplete and the functional component is missing at all. Even though quartz crystal microbalance (QCM) has functional and structural detection capabilities and was used to study end-tethered FG domains (Eisele et al., 2010), structural determination relies on model constraints (Voinova et al., 2002; Hook et al., 2001) and molecular quantification is less accurate compared to optical techniques (Voros, 2004). Here surface plasmon resonance (SPR) is used due to the high mass sensitivity (Homola, 2006), however structural characterization using SPR has been formidable because of the requirement

of having to ascertain the refractive index (RI) of the layer itself, which is non-trivial (Koutsioubas et al., 2007; Debruijin et al., 1991). To overcome those limitations I have therefore innovated a novel technique that diminishes the refractive index constraint in SPR by using „non-interacting particles as innate structural probes". Because mass of surface-bound molecules can easily be quantified using SPR, conformational changes together with binding affinities can now be correlated *in situ* with respect to the relative spatial arrangements of ligand – receptor molecules

Chapter 2

Non-interacting molecules as innate structural probes in surface plasmon resonance

Parts of this chapter were published in Schoch & Lim., 2013.

Direct SPR-based quantification of molecular layer thickness has been ambitious because of the requirement of having to ascertain the refractive index (RI) of the layer itself, which is nontrivial (see section 2.1.1.6). Resolving the thickness of a molecular layer, combined with SPR-obtained estimates of surface density/grafting distance, this would provide an overall three-dimensional description of how ligand and analyte molecules are spatially distributed within such a layer. Complementing the routinely obtained ligand – analyte binding information in SPR (i.e. affinity and kinetics) this would allow to evaluate the structure – function relationship of a molecular layer *in situ*.

In this chapter the basic formalism is introduced for measuring the thickness of a surface adsorbed layer (adlayer) using non-interacting molecules, which minimizes the RI constraint. In addition, the section provides results of the evanescent field calculations that elucidate the accuracy of the method with respect to the RI constraint. By simulating the SPR response the appropriate decay length l_d, the only

parameter that is still sensitive to the adlayer RI in the formalism, for a given molecular layer can be estimated. This simulation was first based on various approximations on the SPR response and thus only holds for low refractive index layers. For a broader spectrum of layers the simulation has to be corrected using Fresnel reflectivity derived factors. However, most straightforward is a simulation based on Fresnel reflectivity calculations only. The theoretical treatments indicate that the method is most appropriate for low refractive index (RI) layers with an estimated maximal error of $\pm$ 15 % in the thickness. Most of the methods presented here have been published previously in Schoch & Lim, 2013. A key aspect of the presented formalism is its ease-of-use and direct applicability in conventional SPR flow cell systems.

This chapter additionally provides experimental validation for the concept of non-interacting molecules as structural probes that „feel" the exclusion volume of a surface tethered molecular layer. Bovine serum albumin (BSA) was used as non-interacting molecules in the height measurements of polyethylene glycol (PEG) molecular brushes, where the reference layer consists of a short self-assembling thiol, i.e. $HS\text{-}(CH_2)_{11}\text{-}(OCH_2CH_2)_3\text{-}OH$ (henceforth $C_{17}H_{36}O_4S$), of known layer thickness $d_1 = 2\ nm$ and refractive index $n_a = 1.45$ (Palegrosdemange et al., 1991). The SPR acquired PEG brush thicknesses scale with PEG hydrodynamic diameter and are in good agreement with atomic force microscopy (AFM) force-distance measurements. Most of the results in this section were published in Schoch & Lim, 2013.

2.1 Basics & Theory

2.1.1 Surface plasmon resonance (SPR)

The following subchapters shall briefly introduce the phenomena of surface plasmon resonance. If not stated otherwise the aspects covered here are adapted from "Modern

Introduction to Surface Plamons" by Dror Sarid and William Challener.

2.1.1.1 Maxwell's equations and boundary conditions

The two Maxwell's vector equations in terms of the curl ($\nabla \times$) operator can be written as

$$\nabla \times \boldsymbol{E} = i\mu\omega\boldsymbol{H} \tag{2.1}$$

and

$$\nabla \times \boldsymbol{H} = -i\varepsilon\omega\boldsymbol{E} \tag{2.2}$$

where μ and ε are the magnetic permeability and electric permittivity respectively. From the latter equation the three components of $\boldsymbol{E}$ are derived

$$E_x = \frac{i}{\varepsilon\omega}\left(\frac{\partial}{\partial y}H_z - \frac{\partial}{\partial y}H_y\right) \tag{2.3}$$

$$E_y = \frac{i}{\varepsilon\omega}\left(\frac{\partial}{\partial x}H_z - \frac{\partial}{\partial z}H_x\right) \tag{2.4}$$

$$E_z = \frac{i}{\varepsilon\omega}\left(\frac{\partial}{\partial x}H_y - \frac{\partial}{\partial y}H_x\right) \tag{2.5}$$

Here, another important set of equations are the boundary conditions imposing restrictions on the electromagnetic fields at an abrupt interface separating two media. For the electric field they are given as

$$\boldsymbol{n}_{12} \times \left(\boldsymbol{E}^{(2)} - \boldsymbol{E}^{(1)} \right) = 0 \tag{2.6}$$

and

$$\boldsymbol{n}_{12} \cdot \left(\boldsymbol{D}^{(2)} - \boldsymbol{D}^{(1)} \right) = \rho \tag{2.7}$$

respectively, where $\boldsymbol{n}_{12}$ is the unit vector pointing from media 1 to media 2 that is perpendicular to an infinitesimal area of this interface, ρ is the surface charge density across the interface and $\boldsymbol{D} = \varepsilon\boldsymbol{E}$ is the electric displacement.

2.1.1.2 Surface plasmon electric fields
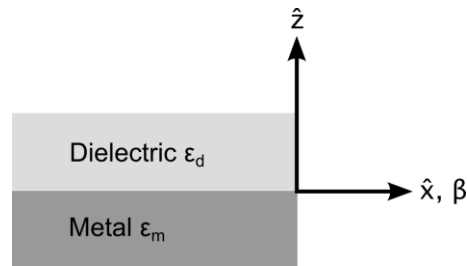
Fig. 2.1. Single interface in the *y-x* plane composed of a thick planar metallic gold substrate and a thick planar dielectric cover, that can support a transverse magnetic (TM) or p-polarized mode with the propagation constant, β, pointing into the *x*-direction.

As depicted in Fig. 2.1, a single interface in the *y-x* plane composed of a thick planar metallic gold substrate and a thick planar dielectric cover can support a transverse magnetic (TM) or p-polarized mode whose propagation constant, β, points in the *x*-direction and the normal to the interface points in the *z*-direction. A TM mode is characterized by having a single magnetic field component H_y oriented along the *y*-direction. Using a time-independent vector field, H_y can be written explicitly as

$$H_y = b e^{i(k_z z + k_0 \beta x)} \tag{2.8}$$

where b is a normalization constant and we have used $k_{sp} = k_0 \beta$ with $k_0 = 2\pi/\lambda$ and λ is the free space wavelength. Similar we can introduce $k_{z,m} = i k_0 \gamma$ and $k_{z,d} = i k_0 \delta$ to be the transverse wave vectors in the metal and cover respectively. Here γ and δ denote the decay constants and the factor i accounts for the fact that these transverse wave vectors are imaginary, as expected from evanescent fields. Using Maxwell's equations (Eqs. 2.3 and 2.5) we can easily derive the electric fields of a TM mode from H_y

$$E_z(z) = b e^{(i k_0 \beta x)} \frac{k_0 \beta}{\omega} \begin{pmatrix} \frac{1}{\varepsilon_d} e^{-k_0 \delta z} \; z > 0 \\ \frac{1}{\varepsilon_m} e^{k_0 \gamma z} \; z < 0 \end{pmatrix} \tag{2.9}$$

$$E_x(z) = b e^{(i k_0 \beta x)} \frac{i k_0}{\omega} \begin{pmatrix} \frac{-\delta}{\varepsilon_d} e^{-k_0 \delta z} \; z > 0 \\ \frac{\gamma}{\varepsilon_m} e^{k_0 \gamma z} \; z < 0 \end{pmatrix} \tag{2.10}$$

where we have used ε_j with the subscript $j = m$ for metal and $j = d$ for dielectric, respectively.

2.1.1.3 TM mode solution

The boundary conditions dictate the continuity of E_x in Eq. 2.10 giving

$$\frac{\delta}{\varepsilon_d} = \frac{-\gamma}{\varepsilon_m} \tag{2.11}$$

Since both γ and δ are mainly real and positive, we find that the relative values of ε belonging to the substrate and cover must have opposite signs, namely

$$\frac{\varepsilon_d}{\varepsilon_m} < 0 \tag{2.12}$$

One can express the γ and δ in the substrate and cover, respectively, by

$$\gamma^2 = \beta^2 - \varepsilon_m \mu_m \tag{2.13}$$

and

$$\delta^2 = \beta^2 - \varepsilon_d \mu_d \tag{2.14}$$

Rewriting Eq. 2.12 in terms of β yields the well-known solution for a propagating surface plasmon mode

$$\beta = \sqrt{\frac{\varepsilon_m \varepsilon_d}{\varepsilon_m + \varepsilon_d}} \tag{2.15}$$

where we have used $\mu_m = \mu_d = 1$ for non-magnetic media. The decay length l_d of the evanescent field in the dielectric according to Eqs. 2.9 and 2.10 is thus given as

$$l_d = \frac{1}{k_0 \delta} = \frac{\lambda}{2\pi} \left(\frac{-\varepsilon_d^2}{\varepsilon_d + \varepsilon_m} \right)^{-1/2} \tag{2.16}$$

2.1.1.4 Prism coupling
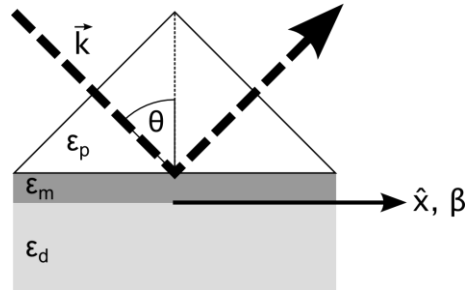
Fig. 2.2. Kretschmann configuration: the photons undergo total internal reflection (TIR) at the base of a high refractive index prism where they couple evanescently trough a very thin metal layer to the surface plamon mode.

In the frequency range of interest we find for the propagation constant β (Knoll, 1998)

$$\beta = \sqrt{\frac{\varepsilon_m \cdot \varepsilon_d}{(\varepsilon_m + \varepsilon_d)}} \geqslant \sqrt{\varepsilon_d} \qquad (2.17)$$

which has the important consequence that the momentum of a free photon k_{ph} propagating in a dielectric medium is always smaller than the momentum of a surface plasmon mode k_{sp}. To overcome this problem, in the common Kretschmann configuration, the photons are not coupled directly to the metal/dielectric interface, but undergo total internal reflection (TIR) at the base of a high refractive index prism where they couple evanescently trough a very thin metal layer to the surface plamon mode (see Fig. 2.2). This light traveling the prism is characterized by a higher momentum as $\varepsilon_p > \varepsilon_d$. Although, as a result of the finite thickness of the metal film evanescent leakage causes some modifications $\Delta\beta$ to the surface plasmon mode in contrast to a freely propagating mode β (Homola, 2006). For the excitation of surface plasmons the projection of the photon wavevector to the *x*-direction at the base of the

prism is the relevant parameter (Ekgasit et al., 2004)

$$k_{xP} = (2\,\pi/\lambda)\left[\varepsilon_p sin^2\theta\right]^{1/2} \tag{2.18}$$

where ε_p is the permittivity of the prism. For the coupling between the TIR evanescent wave and the surface plasmon to occur the propagation constant of the photon k_{xP} and the plasmon k_{sp} (see Eq. 2.15) have to be equal, yielding

$$\theta_{SPR} \approx arcsin\left(\left[\frac{\varepsilon_d\varepsilon_m}{(\varepsilon_m+\varepsilon_d)\varepsilon_p}\right]^{1/2}\right) \tag{2.19}$$

for the resonance angle. The angle θ_{SPR} is commonly recorded in SPR measurements and changes with the optical properties ε_d of the substrate within the penetration depth l_d of the plasmon evanescent field.

2.1.1.5 Fresnel calculations

One can describe the angular dependence of the reflectivity by solving Fresnel's equations for the layer architecture, which for the Kretschmann configuration comprises a stratified medium with plane boundaries enclosed by a prism of dielectric constant ε_p and a substrate with complex dielectric constant ε_d. For N isotropic layer with thickness d_j and dielectric constant ε_j placed between the prism and the dielectric substrate the Fresnel reflection coeffiecients for parallel polarized radiation are given by (Ekgasit et al., 2004)

$$r_\parallel = \frac{(M_{11}+M_{12}q_D)q_P-(M_{21}+M_{22}q_D)}{(M_{11}+M_{12}q_D)q_P+(M_{21}+M_{22}q_D)} \tag{2.20}$$

where M_{mn} is an element of the characteristic matrix $M(2 \times 2)$ of the plane boundary stratified layers

$$M = \Pi_{j=1}^{N} \begin{bmatrix} cos(k_{zj}d_j) & \frac{-i}{q_j}sin(k_{zj}d_j) \\ -iq_jsin(k_{zj}d_j) & cos(k_{zj}d_j) \end{bmatrix} \tag{2.21}$$

where $q_j = k_{zj}/\varepsilon_j$, and k_{zj} is the z-component of the wavevector in the jth layer given by

$$k_{zj} = \left[(2\pi/\lambda)^2\varepsilon_j - k_{xP}^2\right]^{1/2} \tag{2.22}$$

where k_{xP} is the x-component of the wavevector in the prism.

2.1.1.6 Thickness measurements with SPR
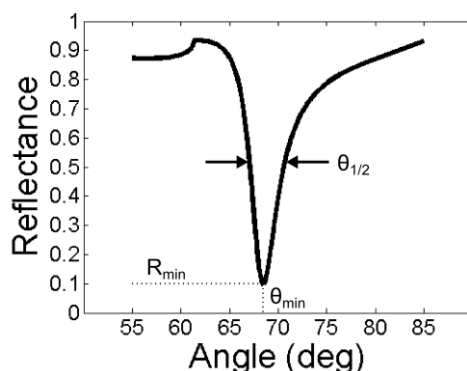
Fig. 2.3. A SPR reflectivity curve and the parameters that describe it: the position of the minimum θ_{min}, the minimum reflectance R_{min} and the half-width $\theta_{1/2}$.

A SPR reflection curve can be described by three parameters: the position of the minimum θ_{min}, the minimum reflectance R_{min} and the half-width $\theta_{1/2}$ (De Bruijn et al., 1991; see Fig 2.3). If an adlayer with dielectric constant ε_a and thickness d_a adsorbs to the metal surface the reflection curve changes. For adsorption of a thin and transparent layer R_{min} does not change, whereas $\theta_{1/2}$ appears to change in a similar way with ε_a and d_a as the minimum position θ_{min}, such that there is commonly only one observable θ_{min}. However, the minimum position θ_{min} depends on both the dielectric constant ε_a and thickness d_a of an adlayer and therefore there is no unique solution for d_a. Apart from ε_a and d_a the change in θ_{min} depends on λ, ε_m and ε_s, the dielectric constant of the metal and the solvent respectively. One can therefore vary one of these parameters to obtain more than one set of solutions for ε_a, d_a.

Although, it is impossible to obtain an exact analytical expression for θ_{min}, one can derive an approximate solution for a small shift $\Delta\theta_{min}(\varepsilon_a, d_a)$ in the minimum position from the Fresnel reflection coefficient $r_\parallel$ (De Bruijn et al., 1991). Plotting each set of solutions ε_a vs d_a for $\Delta\theta_{min}$ measured in two different bulk solvents ε_s,

yields an intercept that identifies the pair ε_a, d_a with an estimated accuracy of ± 6 Å for either sputtered PTFE layers or adsorption of αHSA.

For varying the wavelength λ, in a two-color approach, the thickness of an *n*-alkane thiol self-assembled monolayer has been determined in dichloromethane solvent (Peterlinz & Georgiadis, 1996). This approach requires an educated estimate for the dispersion relation of the layer, where a 10% error in the estimate leads to a 2% error in the thickness for this particular system.

The SPR reflection curve can be evaluated by solving Fresnel's equations for direct comparison. Although $\theta_{1/2}$ and θ_{min} depend on both the refractive index n_a and thickness d_a, depending on the thickness of the metal layer changes in n_a or d_a for a non-adsorbing adlayer may cause different dependencies $\Delta\theta_{1/2}/\Delta\theta_{min}$ that can assist the evaluation of these parameter (Salamon et al., 1997a). However, when the adlayer is light-adsorbing the separation of the parameters is simpler and much more accurate and may be used to study structural changes in proteolipid films using SPR angular spectroscopy (Salamon et al., 1997b).

For self-assembled polystyrene molecular brushes on aluminum the thickness was determined from SPR reflection curves (Koutsioubas et al., 2007). The dependency of $\Delta\theta_{1/2}/\Delta\theta_{min}$ on d_a and ε_a of the non-adsorbing layer was shown to allow for a determination of the thickness d_a for either thick layers or with a high optical contrast only, given the limited resolution of the SPR apparatus. The polymer brush thickness was determined using a parabolic functional dependence approximated by ten layers of varying polymer fractional volume. These values are inserted in the Fresnel equations and produce a reflectivity curve, which is in turn compared to the experimental one using a least squares fitting algorithm to extract the brush thickness.

The exponential decay of the evanescent electromegnetic field intensity in z-direction $|E_z(z)|^2 \propto exp(-2z/l_d)$ was shown to be a good approximation for the SPR response versus distance for a thin organic plug at different distances from the metal surface (Liedberg et al., 1993). Based on this dependence, and given the linear response regime with thickness for thin layers (i.e. $d_a \ll l_d$), a simple formalism to estimate the thickness d_a of an adlayer was introduced (Jung et al., 1998)

$$d = -\frac{l_d}{2} \frac{\Delta RU}{m \cdot (n_a - n_s)}$$ (2.23)

where n_a and n_s are the refractive indices of the adlayer and the solvent, respectively, and ΔRU represents the immobilization SPR signal. The constant m is the sensitivity factor of the sensor for bulk changes in refractive index.

2.1.2 Atomic force microscopy (AFM) – force distance curves

Atomic force microscopy (AFM) is a technique to measure small forces between a sample and a tip attached to a cantilever beam (Binnig et al., 1986). It is not only a tool to image the topography of a solid surface at high resolution, but can also be used to measure fore-versus-distance curves (i.e. „*force curves*") (Butt et al., 2005). In AFM the force between the tip and the sample is measured by monitoring the deflection of the cantilever. The deflection of the cantilever (in V) is measured using a beam from a laser diode. The beam is focused on the end of the cantilever where it is reflected and monitored using a split photodiode detector. The *deflection sensitivity* (in nm/V) converts the signal from the photodiode (in V) into the cantilever deflection Z_c (in nm) and can be obtained from the slope of the hard wall contact, i.e. the linear portion of the contact region of the deflection (in V) versus position of the

z-piezo Z_p curve. Thus in a force measurement the chip to which the cantilever is attached is moved up and down by applying a voltage to the piezoelectric translator, while measuring the cantilever deflection Z_c versus position of the z-piezo Z_p. To obtain the final force-versus-distance curve, the cantilever deflection Z_c and z-piezo position Z_p have to be converted into force F and distance D. The tip-sample separation D („distance") is simply the sum of Z_c and Z_p:

$$D = Z_p + Z_c \tag{2.24}$$

This conversion is shown in Fig. 2.4.
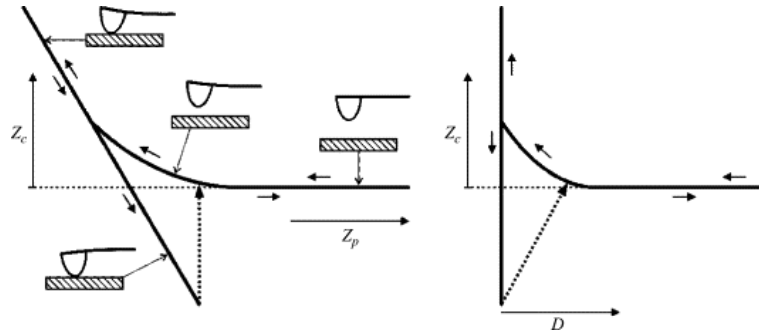
Fig. 2.4. Approach-retract cycle of the AFM tip normal to the surface (from Butt et al., 2005). Left side: cantilever deflection Z_c versus position of the piezo Z_p. Right side: cantilever deflection Z_c versus tip-sample distance D.

To obtain the force F the deflection of the cantilever Z_c is multiplied with the *spring constant* of the cantilever k_c:

$$F = k_c Z_c \tag{2.25}$$

where the spring constant of the cantilever k_c can be obtained from a thermal tune procedure. After constructing the „force curves", they can then be used to characterize the medium in between the tip and the sample.

2.1.3 Polymer physics & polymer brush

The concept of polymer brushes shall briefly be introduced in this section. Therefore some basic principles of polymer physics need to be addressed first that are valid for polymer brushes as well. What is a polymer brush? In the diluted regime of non-interacting coils, the end-grafted polymers form halfspheres with radius similar to the Flory radius and often are referred to as *„mushrooms"*. In contrast a *„polymer brush"* is formed when densely grafted polymer chains start to interact with each other and stretch away from the grafting plane due to excluded volume effects (De Gennes, 1980).

2.1.3.1 The polymer end-to-end distance

An *ideal chain* is considered to perform a random-flight with mean square end-to-end distance (Rubinstein & Colby, 2003)

$$\langle R^2 \rangle = Nb^2 \tag{2.26}$$

where N is the number of monomers each of length b. However, random-flight behavior applies only to a limited class of solvent and temperature conditions called θ-conditions, whereas for most real chains interactions with both their solvent and themselves need to be considered. Thus the *excluded volume v* is introduced to describe the effective two-body (pairwise) monomer-monomer interaction in solution.

At low polymer concentration the interaction part of the free energy density F_{int}/V can be written as a virial expansion in powers of the monomer number density c_n

$$\frac{F_{int}}{V} = \frac{kT}{2}(vc_n^2 + wc_n^3 + \ldots) \approx kT\left(v\frac{N^2}{R^6} + w\frac{N^3}{R^9} + \ldots\right) \qquad (2.27)$$

where we have used the *mean field approximation*, that assumes the monomers to distribute uniformly within a coil. The total free energy of a real chain in the Flory approximation (good solvent, i.e. $v > 0$) is then given by

$$F = F_{int} + F_{ent} \approx kT\left(v\frac{N^2}{R^3} + \frac{R^2}{Nb^2}\right) \qquad (2.28)$$

where the purely entropic contribution F_{ent} is the energy required to stretch an ideal chain to end-to-end distance R. Minimizing the free energy F this gives the end-to-end distance (Flory radius)

$$R_F \approx v^{1/5}b^{2/5}N^{3/5} \qquad (2.29)$$

For a poor solvent, the excluded volume is negative ($v < 0$) and the minimum of the free energy corresponds to $R = 0$. Such strong collapse of a polymer is unphysical and we need to add a stabilizing term to the free energy. At low concentration, the two-body term v dominates the interaction, whereas the *three-body term* w gets important at higher concentrations and can stabilize the collapse of a globule (since $w > 0$). The total free energy is dominated by the interaction terms at higher densities

$$F \approx kT \left(v \frac{N^2}{R^3} + w \frac{N^3}{R^6} \right)$$
(2.30)

and the globule size is

$$R_{gl} \approx \left(\frac{wN}{|v|} \right)^{1/3}$$
(2.31)

a typical value of the three-body interaction coefficient for almost symmetric monomers is $w \approx b^6$. Thus the end-to-end distance R scales with $N^{1/3}$ for $v < 0$, $N^{1/2}$ for $v = 0$, and $N^{3/5}$ for $v > 0$, respectively.

2.1.3.2 The neutral polymer brush

Polymer brushes can be treated similar to a coil in solution (see section 2.1.3.2) using Flory arguments of global energy balance, i.e. excluded volume interactions vs. free energy to stretch a chain away from the grafting surface. For the polymer brush we then use the end-to-end distance H and introducing a constant monomer concentration $\phi_n \approx N b^3/\sigma H$ in the layer to get for the brush free energy in good solvent (Zhulina et al., 1991)

$$F \approx \frac{H^2}{Nb^2} + \frac{N^2 v b^3}{\sigma H}$$
(2.32)

where σ is the surface area per chain and v is the excluded volume. Differentiating and solving for the value that minimizes F, we get for the equilibrium brush height

$$H \approx \left(\frac{vb^2}{\sigma}\right)^{1/3} bN, \quad v > 0 \tag{2.33}$$

In a similar fashion one could obtain the equilibrium brush height H in theta and poor solvent, respectively. These models are considered as decent approximations in the strongly stretched limit, however, they assume a step-function for the monomer density profile which is a serious simplification.

A more realistic monomer density profile can be obtained from the self-consistent field (SCF) theory, a technique to calculate probability distributions of chain conformation within the mean-field approximation (Kawakatsu, 2004). In the limit of strong stretching the *mean-field approximation* is valid and each chain interacts with itself and the others only through the average concentration $\langle \phi(\vec{r}) \rangle$. The free energy for K chains can be expressed directly in continuum language using a stretch free energy term and an excluded volume energy term (Milner et al., 1988)

$$F = \sum_{i=1}^{K} \int dn \left[\frac{1}{2} \left(\frac{d\vec{r_i}}{dn} \right)^2 \right] + \frac{1}{2} v \int dV \, \phi^2(\vec{r}) \tag{2.34}$$

The density profile that minimizes the free energy is parabolic $\phi(z) = (A - Bz^2)/v$. The parabolic profile leads to the layer height in good solvent (Zhulina et al., 1991)

$$H \approx \left(\frac{8}{\pi^2}\right)^{1/3} \left(\frac{vb^2}{\sigma}\right)^{1/3} bN, v > 0 \tag{2.35}$$

Note that the scaling for N, b, v and σ is the same as for the step-function profile (Eq.

2.33). The prefactor varies depending on the source considered but remains generally close to one, i.e. the ratio between the parabolic and step-profile brush height is 0.9 – 1.3 (Zhulina et al., 1991; Kawakatsu, 2004; Milner et al., 1988). The major difference are the density profile and the distribution of chain ends which spread through the entire height of the brush in the parabolic configuration. With decreasing solvent quality the layer contracts as a whole and the average segment density increases. In this case the decrease of density in the periphery becomes more abrupt, i.e. the density tends to the stepwise shape (Zhulina et al., 1991).

Numerical approaches to SCF theory can be used for any type of chain architecture and solvent environment, respectively (Carignano & Szleifer, 1993). Here, the mean-field can be described through the condition of volume filling, where the polymer-solvent layer is treated as an incompressible fluid. Therefore, a lateral pressure profile $\pi(z)$ is introduced that takes into account all the energies of repulsive interactions of the central chain with the other molecules in the system. The lateral pressure $\pi(z)$ represents the osmotic pressure of the solvent which is needed in order to keep the chemical potential constant throughout the system. However, in the absence of solvent $\pi(z)$ cannot represent osmotic pressure, but is the result of the repulsive interactions between the chain molecules in order to achieve volume filling. Therefore another way of looking at it is that $\pi(z)$ is the average repulsive interaction felt by a monomer.

2.2 A novel approach for measuring polymer brush thickness in SPR

2.2.1 Formalism

The effective RI n_{eff} of the dielectric in SPR can be described by the weighted sum of local indices at the metal-dielectric interface (Jung et. al., 1998)

$$n_{eff} = \frac{2}{l_d} \int n(z) exp(-2z/l_d) dz \tag{2.36}$$

where $n(z)$ is the RI at height z perpendicular to the sensor surface and l_d is the characteristic evanescent field decay length. For a molecular layer of mean thickness d, $n(z) = n_a$ for $0 \leq z \leq d$ and $n(z) = n_s$, for $d < z \leq \infty$ where the subscripts a and s correspond to "adlayer" and "solvent", respectively. By this definition, Eq. 2.36 becomes

$$n_{eff} = n_a + (n_s - n_a) exp(-2d/l_d) \tag{2.37}$$

and in the presence of noninteracting molecules, n_s is replaced by n_p giving

$$n_{eff} = n_a + (n_p - n_a) exp(-2d/l_d) \tag{2.38}$$

assuming (i) the layer is unaffected by the particles (i.e., by definition of noninteracting), and (ii) the non-interacting molecules are distributed homogeneously

in solvent. By subtracting Eqs. 2.37 and 2.38, n_a is now eliminated giving

$$\Delta n_{eff} = (n_p - n_s) exp(-2d/l_d) \tag{2.39}$$

where Δn_{eff} denotes the overall change in the effective RI. In the absence of adsorption from solution, Δn_{eff} can be replaced by the term R/m because the SPR response to changes in the bulk solution RI (where $n_{PBS} = 1.33411$ and $n_{BSA} = 1.33567$, for PBS and PBS/BSA respectively) is approximately linear over a restricted range (i.e., $\Delta n = 0.01$ (Jung et al., 1998)). Here, R and m correspond to the SPR response resulting from the non-interacting molecules and the slope relating the change in the SPR response to changes Δn_{eff} in bulk solution, respectively. If a reference cell is implemented in addition to the sample cell (with respective parameters defined by subscripts 1 and 2), $d_2 - d_1$ can then be calculated using a single decay length l_d giving

$$d_2 = \frac{l_d}{2} ln \left(\frac{R_1}{R_2} \frac{m_2}{m_1} \right) + d_1 \tag{2.40}$$

where noticeably all RI's are eliminated. Here, d_1 corresponds to a passivation layer in the reference cell of known thickness (i.e., $HS\text{-}(CH_2)_{11}\text{-}(OCH_2CH_2)_3\text{-}OH$; henceforth $C_{17}H_{36}O_4S$). Eq. 2.40 then provides the mathematical basis by which the thickness of a molecular layer can be assessed without requiring the RI (except for its contribution to l_d; see later).
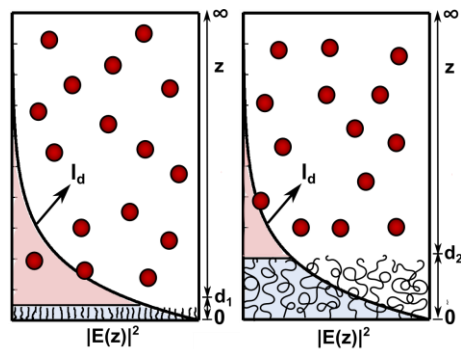
Fig. 2.5. Schematic illustration of how the SPR response (red shaded area) from the noninteracting molecules (red filled circles) varies with distance. In the reference cell (left) the molecules approach more closely to the gold sensor surface giving rise to a higher SPR response, whereas in the samples cell (right) the molecules have a limited approach distance and a lower SPR response is obtained. According the formalism of Eq. 2.40, a single constant l_d describes the exponential decay of the evanescent field for both cells.

2.2.2 Simulations - SPR evanescent field

2.2.2.1 Simulating the SPR response
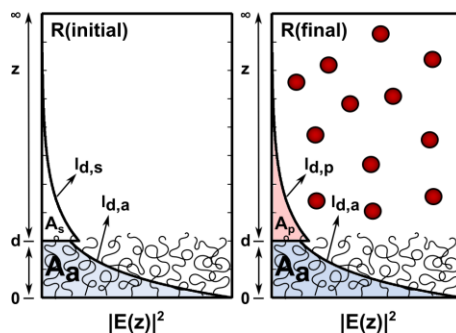
Fig. 2.6. The SPR responses $R(initial)$ and $R(final)$ differ by the presence of the non-interacting molecules. A_a, A_s, and A_p correspond to the areas defined by the electric field $|E(z)|^2$ and bounded by $l_{d,a}$, $l_{d,s}$, and $l_{d,p}$, respectively.

Within the general formalism of Eq. 2.40 the RI constraint is diminished but not entirely eliminated because of its contribution to l_d, which defines the distance from the metal-dielectric interface at which the electric field amplitude decreases by a

factor $1/e$. Moreover, note that l_d is taken as a single decay length whereas in real physical terms the "adlayer" decay length $l_{d,a}$ is different from the "solvent" decay length in the absence ($l_{d,s}$) and in the presence of BSA ($l_{d,p}$) as shown in Fig. 2.6. Therefore, Eq. 2.16 only represents a rough estimate of l_d. Nevertheless, l_d can be further refined by simulating the BSA-SPR response for a given adlayer as defined by its thickness d and refractive index n_a. In an initial attempt this follows the same "area" analysis from Fig. 2.6 with the aim of finding a single decay length l_d that accounts for $l_{d,a}$, $l_{d,s}$, and $l_{d,p}$. Toward this goal, one has to distinguish and determine the areas bounded by the evanescent field in the adlayer A_a as well as in the absence (A_s) and presence of BSA (A_p), respectively, such that a single decay length l_d satisfies $d = d_2$ (where d is the input adlayer thickness).
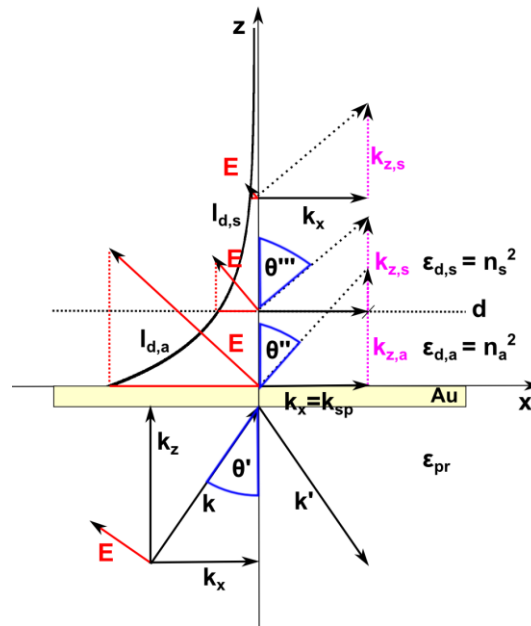
Fig. 2.7. Excitation of surface plasmons by means of a prism coupler (Kretschmann configuration). In order for the incident light to couple to plasmons the propagation constant of the evanescent wave k_x and the surface plasmons k_{sp} have to be equal. This occurs at the SPR angle θ_{min} in air that accordingly refracts into angles θ', θ'' and θ''' in the different dielectric media of the multilayer structure, where ε_{pr}, $\varepsilon_{d,a}$ and $\varepsilon_{d,s}$ are the dielectric constants of prism, adlayer and solvent respectively. The electric field E of the surface plasmons decays exponentially into the dielectric media and can be characterized by the decay length $l_{d,j}$ ($j = a$ for adlayer, $j = s$ for solvent) that defines the distance from the interface at which the amplitude of the electric field decreases by a factor $1/e$. The decay length $l_{d,j}$ is inherently coupled to the propagation constant $k_{z,j}$. The electric field component E_x is continuous at the dielectric boundary between adlayer and solvent.

Fig. 2.7 illustrates how $l_{d,a}$ and $l_{d,s}$ emerge from a transparent two-layer dielectric where each respective dielectric constant adjacent to the Au sensor surface is denoted by $\epsilon_{d,j} = n_j^2$ (as usual $j = a$ denotes "adlayer" and $j = s$ denotes "solvent", respectively). Since no simple analytical solution exists for obtaining $l_{d,a}$, $l_{d,p}$ and $l_{d,s}$, the aim of this section is to numerically refine $l_{d,j}$ using an approximation for small changes in k_{sp}. Here, we relate each individual $l_{d,j}$ to its respective wavevector via $l_{d,j} = 1/Re(k_{z,j})$ (Homola, 2006), where the wavevector $k_{z,j}$ in the jth layer of a multilayer dielectric substrate is given by Eq. 2.22 and the x-component of the incident p-polarized wave-vector k_x is given by Eq. 2.18. According to Eq. 2.19, the SPR angle θ_{min} responds approximately linear to small changes in the bulk dielectric constant $\Delta\varepsilon_d$ of the medium, i.e., $\theta_{min} \approx a \cdot \Delta\varepsilon_d + b$ (see Fig. 2.8).
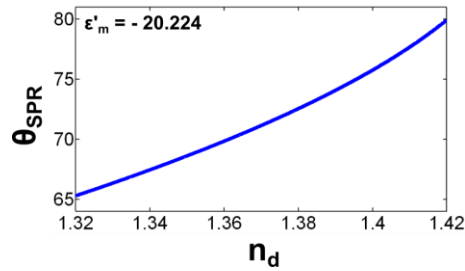
Fig. 2.8. Plot of Eq. 2.19. The change in the SPR angle θ_{SPR} is approximately linear for small changes in the RI Δn_d.

At SPR, the incident light wavevector in the prism k_x equals the wavevector of the surface plasmons k_{sp} i.e., $k_x = k_{sp}$, where from Eq. 2.18 we now write $k_{sp} \approx (2\pi/\lambda)\left(\varepsilon_{pr}sin^2(a \cdot \Delta\varepsilon_d + b)\right)^{1/2}$. By further replacing k_x for k_{sp} in Eq. 2.22 and recalling the relation $l_{d,j} = 1/Re(k_{z,j})$ the decay length inside a lossless semi-infinite bulk medium is now defined by

$$l_d \approx (\lambda/2\pi)\left[\varepsilon_{d,0} + \Delta\varepsilon_d - \varepsilon_{pr}\sin(a \cdot \Delta\varepsilon_d + b)^2\right]^{-1/2} \qquad (2.41)$$

By comparing Eq. 2.41 to Eq. 2.16, we can easily solve for the linear parameters a and b. Given that Eq. 2.38 uses a simple exponential factor to describe the angular SPR response of a two-layer structure, analogously we use the exponential factor $\left[1 - \exp(-2d/l_d) \cdot \Delta\varepsilon_{s,a}\right]$ for a perturbation $\Delta\varepsilon_d$ in Eq. 2.41 to get

$$l_{d,j} \approx \frac{\lambda}{2\pi}\left(\varepsilon_{d,j} - \varepsilon_{pr}\sin\left(a \cdot \Delta\varepsilon_{j,a} \cdot \left[1 - \exp\left(-\frac{2d}{l_d}\right)\right] + b\right)^2\right)^{-1/2} \tag{2.42}$$

where $\Delta\varepsilon_{j,a}$ describes the change in the dielectric constant of the adlayer with respect to the solvent (i.e., $j = s$) as well as the change in the dielectric media for the adlayer with respect to the solvent/BSA solution (i.e., $j = p$), respectively.

Following the "area" analysis of Eq. 2.36, the SPR response for BSA injection is given by $R = R(final) - R(initial)$ as shown in Fig. 2.6, which provides the analytical form

$$R = \left(\frac{A_a}{A_a+A_p} - \frac{A_a}{A_a+A_s}\right) \cdot n_a + \frac{A_p}{A_a+A_p} \cdot n_p - \frac{A_s}{A_a+A_s} \cdot n_s \tag{2.43}$$

where A_a, A_p and A_s corresponds to the area given by the electric field strength $|E(z)|^2$ bounded by the decay length $l_{d,a}$, $l_{d,p}$ and $l_{d,s}$ respectively. Each area term is obtained by integrating Eq. 2.36 omitting the normalization factor $2/l_d$ and refractive index $n(z)$

$$A_{z1,z2} = \int_{z1}^{z2} \exp\left(\frac{-2\cdot z}{l_{d,j}}\right) \cdot dz \tag{2.44}$$

By defining the boundaries z_1 and z_2 we obtain for the area $A_a(z_1 = 0, z_2 = d)$

$$A_a = \frac{l_{d,a}}{2}\left(1 - \exp\left(\frac{-2 \cdot d}{l_{d,a}}\right)\right)$$ (2.45)

and the area $A_s(z_1 = d, z_2 = \infty)$

$$A_s = \frac{l_{d,s}}{2}\exp\left(\frac{-2 \cdot d}{l_{d,a}}\right)\frac{n_a^2}{n_s^2}$$ (2.46)

where in Eq. 2.46 at height d the field strength $|E(z)|^2$ is corrected by a factor $\exp\left(-2d/l_{d,a}\right)/\exp\left(-2d/l_{d,s}\right)$ to account for the weakening of the electric field, i.e., due to its evanescent character, as it traverses the first layer (i.e., adlayer) of the dielectric media. Along these lines, one also needs to consider the dielectric boundary conditions at the adlayer-solvent interface arising from Maxwell equations i.e., $E_{x,a} = E_{x,s}$ (in the xy plane) and $n_a^2 \cdot E_{z,a} = n_s^2 \cdot E_{z,s}$ (normal to the surface). This gives rise to a discontinuity in the total electric field strength $|E(z)|^2$ as illustrated in Fig. 2.6. The resonance angle obtained from the Fresnel calculations is $\theta_{SPR} \approx 70°$ (in air; $n = 1$) (using *Winspall* Software, Max Plank Institute for Polymer Research, Mainz, Germany; see table 2.1) and considering Snell's law, i.e., $sin\left(\theta_{SPR}\right)/sin\left(\theta'''\right) = n_s/n_{air}$, this is $sin(\theta''') \approx 45°$ in the solvent media where, n is the RI of the corresponding media (i.e., $n_s = 1.33411$ and $n_{air} = 1.0$). The electric field $E(z)$ therefore is considered with equal contributions from x- and z-components and we thus correct the electric field strength $|E(z)|^2$ by a factor (n_a^2/n_s^2) at the interface, comprising x- (continuous) and z- (n_a^4/n_s^4) components. This is shown in Fig. 2.9 where the jump in the electric field strength $|E_s(z)|^2/|E_a(z)|^2$ is shown for the SPR angle $\theta_{min} \approx 70°$ giving $\theta''' \approx 45°$ in PBS,

i.e., $\left(\varepsilon_{d,a}/\varepsilon_{d,s}\right)^2 \cdot cos(45°) + 1 \cdot sin(45°)$,   together   with   the   approximations $\varepsilon_{d,a}/\varepsilon_{d,s}$ and $\left(\varepsilon_{d,a}/\varepsilon_{d,s}\right)^{1.1}$.
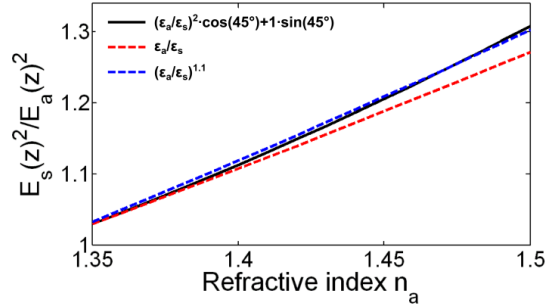
Fig. 2.9. Jump in the electric field strength $|E_s(z)|^2/|E_a(z)|^2$ is shown for the SPR angle $\theta_{SPR} \approx 70°$ giving $\theta''' \approx 45°$ in PBS, i.e. $\left(\varepsilon_{d,a}/\varepsilon_{d,s}\right)^2 \cdot cos(45°) + 1 \cdot sin(45°)$, together with the approximations $\varepsilon_{d,a}/\varepsilon_{d,s}$ and $\left(\varepsilon_{d,a}/\varepsilon_{d,s}\right)^{1.1}$.

Analogous to A_s we obtain for the area A_p $(z_1 = d, z_2 = \infty)$

$$A_p = \frac{l_{d,p}}{2} \exp\left(\frac{-2d}{l_{d,a}}\right)\left(\frac{n_a^2}{n_p^2}\right) \tag{2.47}$$

The simulation of the SPR response for BSA probe measurements is summarized in the algorithm shown in Fig. 2.11. First, an initial value is provided for d and n_a of the layer in cell2 i.e., $\varepsilon_{d,j} = n_j^2$. For the current experiments, the experimentally obtained values of n_s (1.33411) and n_p (1.33567) for PBS and BSA/PBS solution respectively are used in the simulation (see Fig. 2.16). An initial value l_d is required (e.g. such as from Eq. 2.16) to calculate $l_{d,j}$ from Eq. 2.42 which provides the means to compute the areas A_a, A_s and A_p and the corresponding SPR response R (Eq. 2.43). The SPR response R_1 for cell1 is calculated only once using $d = 2\ nm$ and $l_{d,a}$ is obtained from $n_a = 1.45$ (Palegrosdemange et al., 1991) for $C_{17}H_{36}O_4S$ (not shown in Fig. 2.11). For simplicity l_d in the reference cell was set $l_d = 300\ nm$ in Eq. 2.42, but this

influence is insignificant in the outcome of the simulation (see Fig. 2.10).
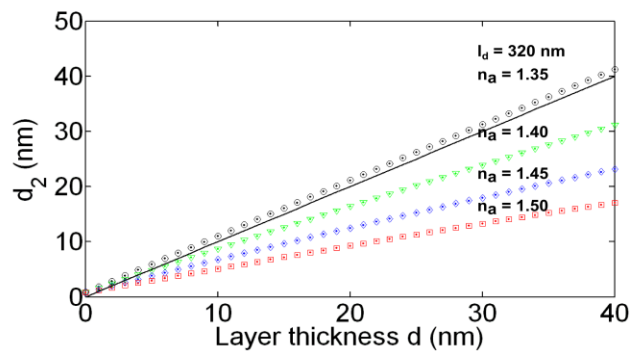
Fig. 2.10. The simulation is barely influenced by the decay length l_d set for the reference cell in Eq. 2.42 as shown for $l_d = 300\ nm$ (symbols) as well as $l_d = 600\ nm$ (points).

The values calculated for the BSA-SPR response R_1 and R_2 are then inserted into Eq. 2.40 and the output d_2 is compared to the input d.

start
$n_s = 1.33411$
$n_p = 1.33567$

$n_a = X \quad d = Y$

set layer characteristics:
- refractive index (n_a)
- thickness (d)

$l_d = Z$

set single decay length

$l_{d,j} = \lambda/(2\pi)\cdot(\varepsilon_{d,j}-\varepsilon_{pr}\sin^2(a\cdot\Delta\varepsilon_{d,a}\cdot[1-\exp(-2d/l_d)]+b))^{-1/2}$
(j = a,s,p)

calculate decay length for
adlayer ($l_{d,a}$), solvent ($l_{d,s}$)
and BSA in solvent ($l_{d,p}$)

$A_a = l_{d,a}/2*(1-\exp(-2d/l_{d,a}))$

$A_s = l_{d,s}/2*(1-\exp(-2d/l_{d,a}))\cdot(n_a/n_s)^2$

$A_p = l_{d,p}/2*(1-\exp(-2d/l_{d,a}))\cdot(n_a/n_p)^2$

calculate areas bound by $l_{d,a}$
$l_{d,s}$ and $l_{d,p}$ respectively

$n_a = X+\Delta X$
or
$d = Y+\Delta Y$

$l_d = Z+\Delta Z$

loop: alter decay length l_d or
layer chracteristics (n_a,d)

$R_j = [A_a/(A_a+A_p)-A_a/(A_a+A_s))\cdot n_a+A_p/(A_a+A_p)\cdot n_p-A_s/(A_a+A_s)\cdot n_s$
j=1,2   (for cell1,cell2)

calculate SPR response for
BSA injection

$d_2 = l_d/2\cdot\ln(R_1/R_2\cdot m_2/m_1)+d_1$

calculate thickness d_2

$d_2 - d = 0$?

NO

check if the thickness d_2
matches the input thickness d

YES

$\frac{y_s}{y_f}$ correction factor obtained
from Fresnel calculations

$l_d(n_a,d) = l_d$

end
decay length map

if all layer chracteristics are
sampled the decay length map
is printed

Fig. 2.11. Flow chart depicting the principle of the simulation. The algorithm consists of two loops where the first defines the layer characteristics $(n_{a,d})$ and the second samples the decay length l_d, which results in a decay length map where every layer can be attributed a single value l_d.

In this manner the single decay length l_d is selected iteratively to minimize the absolute difference in d_2 and d for cell2. The simulation thus refines the decay length l_d such that a single decay length l_d satisfies $d = d_2$ as illustrated in Fig. 2.12.
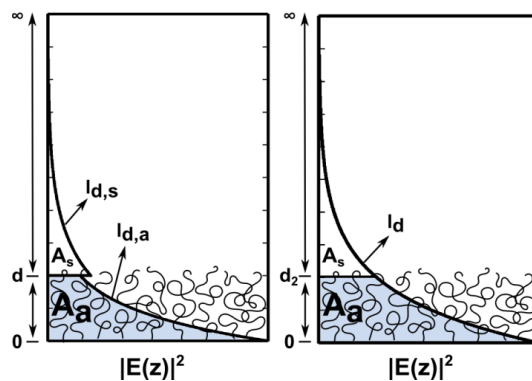
Fig. 2.12. A proper physical description of the electric field $|E(z)|^2$ where the areas A_a and A_s are bound by distinct decay lengths $l_{d,a}$ and $l_{d,s}$ respectively (left). The objective of the simulation is to provide a single value l_d (right) that satisfies $d = d_2$.

Fig. 2.13A shows the simulation results for the input parameters $l_d = 320\ nm$ for $n_a = 1.35,\ 1.4,\ 1.45$ and 1.5 respectively. After several iterations, a refined value of $l_d = 300\ nm$ provides an accurate measure for $n_a = 1.35$ where we obtain $d_2 = d = 20\ nm$ (inset). However, due to the various simplifications in the simulation the outcome was checked against Fresnel equations to calculate the reflectivity curve $R_p(\theta)$. Table 2.1 summarizes the parameters used for the multilayer stack to calculate the reflection of the incident light using *Winspall* Software. A regression was fitted to each reflectivity curve $R_p(\theta)$ to obtain the SPR angle θ_{min} (i.e. minimum in $R_p(\theta)$) for a given adlayer with and without BSA in the solvent. In analogy to the simulation, the SPR angle shift $\Delta\theta_{SPR}$ that describes the BSA response R_1 and R_2, respectively, was then inserted into Eq. 2.40 for both reference and sample cells. Figure 2.13B shows the calculated d_2 values for BSA injections obtained from the Fresnel equations with the same input parameters $l_d = 320\ nm$ for $n_a = 1.35,\ 1.4,\ 1.45$ and 1.5 respectively (the line fits are fixed to $d = d_2 = 0$). Comparing between Fig. 2.13A and 2.13B we find good agreement between the Fresnel calculated values and the output values from the simulation for small changes in the dielectric profile (i.e., $n_a \approx 1.35 - 1.4$) even though the Fresnel derived thickness is more sensitive to increasing adlayer RI. For instance, the simulation fails to predict the Fresnel results at $n_a = 1.4 - 1.5$. This is likely related to simplifications in the simulation such as

the linear dependence of SPR response on n_{eff} and the constant weighting of electric field components E_x and E_z. Nevertheless, we can derive a factor y_s/y_f to correct for the deviation in the simulated decay length from the Fresnel-derived thickness at high layer RI values as shown in Fig. 2.13C.
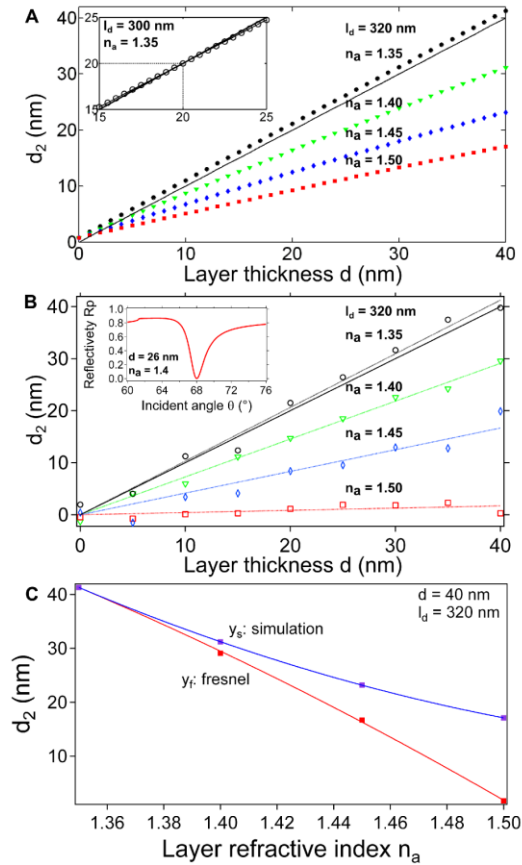
Fig. 2.13. (A) Simulation results showing d_2 for $l_d = 320\ nm$ over a simulated range of n_a and d. Inset: $l_d = 300\ nm$ provides an accurate layer thickness for $d = 20\ nm$ and $n_a = 1.35$. **(B)** Results of d_2 for $l_d = 320\ nm$ using the SPR response R obtained from reflectivity calculations (i.e., Fresnel equations). The values of d_2 from the Fresnel equations are in good agreement for $n_a \approx 1.35 - 1.4$ with the simulated values. Inset: Representative reflectivity curve $R_p(\theta)$ from Fresnel calculations. **(C)** The correction factor y_s/y_f is obtained by comparing d_2 obtained from the simulation and from the Fresnel calculations for $d = 40\ nm$ and $l_d = 320\ nm$, respectively.

	prism	Au	adlayer	solvent	BSA	$C_{17}H_{36}O_4S$
n	1.52	0.16	1.35 - 1.45	1.33411	1.33567	1.45
k	0	4.5	0	0	0	0
d (nm)	∞	50	0 - 40	∞	∞	2

Table 2.1. Summary of the parameters used for the Fresnel reflectivity calculations. Each layer is represented by the RI n, the imaginary part of the RI k and the layer thickness d. In the reflectivity simulation a half-cylinder prism and $\lambda = 760\ nm$ for the p-polarized incident light were used. The simulations were performed using *Winspall* Software (Max Planck Institute for Polymer Research, Mainz, Germany).

The reflectivity curve $R_p(\theta)$ can also be calculated using the Fresnel equations introduced in section 2.1.1.5. From the reflectivity curve $R_p(\theta)$, the minimum of the dip θ_{min} was then read out by using a regression fit. This can be done for any given layer characteristics (i.e. d_a, n_a) and solvent type (i.e. n_s, n_p). The SPR angular response $\Delta\theta_{SPR}$ that is analog to the BSA response R_1 and R_2, respectively, is then inserted into Eq. 2.40 using an arbitrary decay length $l_{d,arb}$ to obtain d_2. The decay length l_d is then simply derived from calculating $l_d = ((d_2 - d_1)/(d_a - d_1)) \cdot l_{d,arb}$. The matlab function *l_d_calc.m* to be found in the appendix is a simple routine that enables to calculate l_d for a given input of layer thickness d_a and refractive index n_a. The matlab function *fresnel.m* does the same for an entire decay length map. Similarly, the decay length l_d can be optimized for a SPR experiment using the immobilization response ΔRU and is based on calculating the refractive index of the layer as will be introduced in section 2.2.3. The matlab function *l_d_opt.m* in the appendix is then optimizing via finding the decay length l_d that matches with n_a and d_2 for a given immobilization response ΔRU.

2.2.2.2 Decay length maps

The outcome of the simulation over the range $n_a = 1.35 - 1.45$ and $d = 0 - 40\ nm$ is summarized in the decay length map shown in Fig. 2.14. The color codes denote the appropriate decay lengths to measure the thickness of a molecular layer at each characteristic value of d and n_a respectively. The singularity of l_d at $d = 2\ nm$ is due to the presence of the $C_{17}H_{36}O_4S$ layer in the reference cell with a node at $n_a = 1.45$, i.e., the RI defined for the reference layer. Thus, the method may cause errors for very thin (i.e. $d < 5\ nm$) layers that are optically different from $C_{17}H_{36}O_4S$. Generally, molecular layers with $n_a \approx 1.35 - 1.4$ and $d > 5\ nm$ can be optimally measured using Eq. 2.40 by invoking $l_d \approx 300 - 400\ nm$ (cyan in Fig. 2.14). Therefore, taking $l_d = 300\ nm$, a conservative estimate for the average maximal error in the thickness is ±15%. Still, for higher RI layers ($n_a > 1.4$) l_d is more sensitive to n_a reaching 800 nm for a layer RI of $n_a = 1.45$ at $d = 40\ nm$. When Fig. 2.14 is used as a reference to select l_d, it is important to note that the decay length map was calculated for $\lambda = 760\ nm$, which can differ with SPR instrumentation.

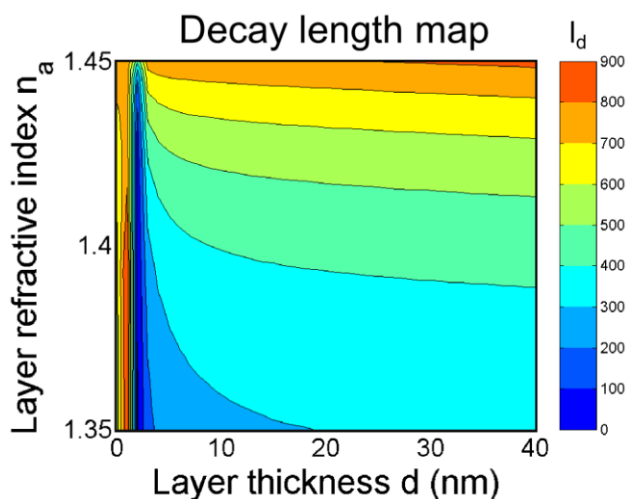**Fig. 2.14.** Color-coded decay length map that identifies the appropriate l_d for a given layer characteristic (for $\lambda = 760\ nm$). For a layer with $n_a \approx 1.35 - 1.4$ the thickness can be accessed using $l_d = 350\ nm$ which minimizes the RI constraint to an estimated average error of ±15% in d_2 (cyan area). Note that for higher RI layers l_d is more sensitive to n_a.

The decay length map can as well be calculated in a straight forward manner from the angular reflectance using the Fresnel reflection coefficients (see section 2.1.1.5). Here the minimum position of the angular reflection θ_{min} was read out from the calculated reflectance R_p from a parabolic around its minimum. The shift in the minimum position $\Delta\theta_{min}$ due to BSA injections can be used to calculate the thickness d_2 from Eq. 2.40 and l_d can be evaluated such that the input thickness d matches the output thickness d_2. The layer characteristics here are the same as used in the simulation and summarized in table 2.1. The resulting sensitivity of l_d to the layer characteristics (see Fig. 2.15) is very similar as in Fig. 2.14 even though the bending of the areas is slightly different. The cyan area with mean $l_d = 350\ nm$ now covers a range of $n_a \approx 1.37 - 1.41$ such that it is located slightly higher than before (i.e. $n_a \approx 1.35 - 1.4$). Also there are high l_d states at $n_a \approx 1.45$ and $d \approx 5nm$ with $l_d > 900nm$.
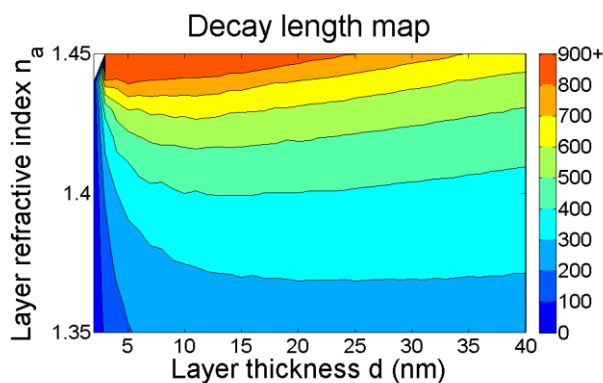
Fig. 2.15. Decay length map directly obtained from Fresnel calulations. The appropriate l_d for a given layer characteristic (for $\lambda = 760\ nm$) is shown using the same color-code as for Fig. 2.14.

2.2.3 Calculating the grafting distance

To estimate the ligand/analyte grafting distance g, the shift in the immobilization baseline ΔRU (RU = resonance units) has to be related to the amount of molecules adsorbed onto the sensor surface. This was shown for proteins immobilized in a 100 nm dextran hydrogel layer to be $0.10° \pm 0.01° = 1\ ng/mm^2$ which is equivalent to $1000\ RU = 1ng/mm^2$ (Lofas et al., 1991; Stenberg et al., 1991). However, this

relation has to be refined because it overestimates the adsorbate mass due to the strength of the evanescent field being larger at the gold surface than in a thicker dextran layer. An analytical expression for the average evanescent field strength within an adlayer of thickness d and RI n_a can be derived starting from a similar scenario to that of Fig. 2.12. The contribution of the adlayer R_a over the total SPR response can be expressed as

$$R_a = \frac{A_a}{A_a + A_s} \cdot n_a \tag{2.48}$$

To calculate the areas A_a and A_s see section 2.2.2.1. The average field strength I_{av} inside a homogeneous layer is then proportional to R_a/n_a divided by the thickness d of the layer

$$I_{av} \propto \frac{A_a}{A_a + A_s} / d \tag{2.49}$$

By comparing two situations with layers of distinct thickness d_1 and d_2 where in both situations the solvent RI is $n_s = 1.33411$, we can calculate a factor f that correlates the average field strength inside the two layers

$$f = \frac{I_{av1}}{I_{av2}} = \frac{A_{a1} \cdot (A_{a2} + A_{a2})}{A_{a2} \cdot (A_{a1} + A_{s1})} \cdot \frac{d_2}{d_1} \tag{2.50}$$

where the subscripts 1 and 2 correspond to layer1 and layer2 respectively. For a typical layer with $d_1 = 20 \, nm$ ($n_a = 1.35$) and for a dextran hydrogel layer with $d_2 = 100 \, nm$ ($n_a = 1.35$) we get a factor $f = 1.3$. This means that the average field strength inside the $d_1 = 20 \, nm$ layer is 1.3 times higher than inside the $d_2 = $

$100\ nm$ dextran hydrogel layer. Thus, a more suitable relation is $1300\ RU = 1\ ng/mm^2$ for proteins directly tethered to the gold surface. This relation has to be further corrected for using PEG (instead of proteins) by identifying the proportional increment for PEG in PBS (0.1203 cm^3/g) over BSA in PBS (0.1554 cm^3/g) from refractometry (i.e., the slope in Fig. 2.16 converted to cm^3/g) according to de Feijter's formula (De Feijter et al., 1978). This gives a new relation $1000\ RU = 1\ ng/mm^2$ for PEG adsorption.
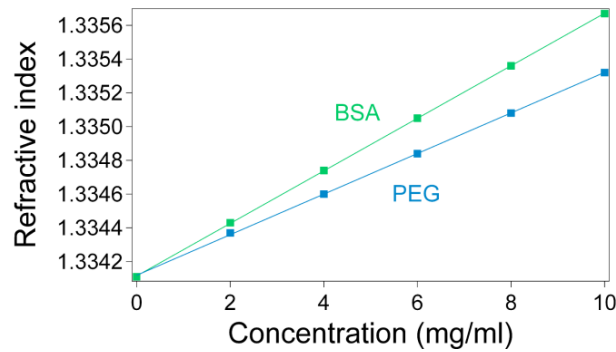
Fig. 2.16. Refractive index increment for PEG ($M_w = 20'000\ Da$) in PBS (lower line) as well as BSA in PBS (upper line).

It is then possible to calculate the grafting distance g_{PEG} (for a square lattice in nm) between PEG molecules once the mass adsorbed per unit area is known for a given molecular weight M_w

$$g_{PEG}(nm) = \sqrt{\frac{1000 \cdot M_w \cdot 10^{21}}{N_A \cdot \Delta RU}}$$
(2.51)

as well as the grafting distance g_{prot} for proteins

$$g_{prot}(nm) = \sqrt{\frac{1300 \cdot M_w \cdot 10^{21}}{N_A \cdot \Delta RU}}$$
(2.52)

where N_A is the Avogadro constant. Notably, the height of a grafted molecular layer can now be correlated to the intermolecular grafting distance of its constituent molecules.

To calculate the RI of the PEG brush n_{PEG} in PBS we consider again the relation $1000\ RU = 1\ ng/mm^2$ as well as d_2 (i.e. to calculate the adlayer mass per volume) and relate it to the RI increment for PEG in PBS (0.1203 cm^3/g) measured by refractometry giving

$$n_{PEG} = \frac{\Delta RU \cdot 0.12}{1000 \cdot d_s} + n_s \tag{2.53}$$

as well as the refractive index n_{prot} for a protein layer

$$n_{prot} = \frac{\Delta RU \cdot 0.1554}{1300 \cdot d_s} + n_s \tag{2.54}$$

2.2.4 Materials & Methods
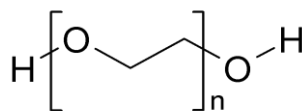
Fig. 2.17. Structure of polyethylene glycol (PEG), where n is the number of monomers in a polymer.

Materials

10 mg/ml BSA ($\geq$ 98%, Sigma-Aldrich) was carefully dissolved in phosphate

buffered saline (PBS) pH 7.2 (Invitrogen). HS-$(CH_2)_{11}$-$(OCH_2CH_2)_3$-OH (abbreviated as $C_{17}H_{36}O_4S$) (nanoScience Instruments, US) was dissolved until reaching 10 mM in ethanol and diluted with PBS to 1 mM before experimentation. Thiolated PEG molecules of 5 different molecular weights M_W were used: SH-PEG 2'100 Da (Polymer Source Inc.), SH-PEG 5'000 Da (Nektar), SH-PEG 10'000 Da (Iris Biotech), SH-PEG 20'000 Da (Laysan Bio Inc.), and SH-PEG 54'000 (Polymer Source Inc.).

SPR Measurements PEG

All SPR measurements were performed at 25°C in a four flow cell Biacore T100 instrument (GE Healthcare) where the standard deviation in the output signal is typically $S = 0.1\ RU$ (RU = resonance units) at a detection frequency of 10 Hz, which corresponds to $\Delta d \gg 0.01\ nm$ in the measured thickness. In all experiments, one flow cell was used as reference and the remaining three flow cells as sample cells. All flow cells are independent of each other with no leakage occurring between them. Thus three separate experiments could be conducted in parallel on a single gold sensor surface. SPR bare gold sensor chips 'SIA Kit Au' were from GE Healthcare. Upon removal from storage in an argon atmosphere, gold sensor surfaces were ultra-sonicated in acetone and high purity ethanol (Merck) for 15 min respectively and dried in a nitrogen gas stream followed by 60 min UVO cleaning (Jelight Company Inc., Model 42A-220). The gold sensor surfaces were then ultra-sonicated for another 15 min in ethanol, dried in a nitrogen gas stream and mounted on the sample holder for immediate SPR/AFM usage. A clean gold sensor surface was incubated with 1 mM SH-PEG in PBS in flow cell 3-4 for 10 min, then in flow cell 2 for 10 min each at 2 µl/min. Flow cell 1 was incubated with 1 mM $C_{17}H_{36}O_4S$ for 20 min. This was followed by another 50 min of SH-PEG incubation in flow cells 3-4 and flow cell 2, respectively. The second immobilization did not alter the PEG surface concentration significantly. After 1h of PBS baseline, BSA titrations (5 x 30 sec with 60 sec interval) followed at a flow rate of 10 µl/min with each injection passing all cells

sequentially and average R_1 and R_2 values of the three last injections were measured relative to the PBS baseline obtained 30 sec later. The PBS running buffer was filtered and degassed using filterware (Techno Plastic Products AG) of 0.2 μm pore size. In total 5, 5, 4, 23, and 6 thickness measurements were performed for PEG 2, 5, 10, 20, and 54 kDa respectively.

Dynamic light scattering PEG

The SH-PEG hydrodynamic diameter was measured at 10 mg/ml in PBS upon addition of 1 mM TCEP (Sigma) using a Zetasizer Nano instrument (Malvern). This gave s_{PEG} = 2.3 ± 0.3 nm, 4.05 ± 0.5 nm, 4.8 ± 0.5 nm, 6.6 ± 0.7 nm, and 10.1 ± 1.0 nm for PEG 2, 5, 10, 20, and 54 kDa, respectively, using $n = 1.40$ and $n = 1.330$ as the refractive index for PEG and dispersant (i.e., water; $T = 25.0°C$, viscosity = 0.8872 cP) respectively.

Polydispersity measurements PEG

10 mg/ml PEG solutions were analysed by size exclusion chromatography (Wyatt 4.6x300 mm, 5 μm bead, 300 angstrom pore, silica SEC column, 10 mM Tris-HCl pH 7.2, 100 mM NaCl and 2 mM TCEP) interfaced with a Wyatt miniDawn Tristar multi-angle light scattering detector and a Wyatt Optilab rEX refractive index detector. The instruments were calibrated according to the manufacturer's protocol and the polydispersity index (M_w/M_n) was calculated in the ASTRA 5 software. This gave M_w/M_n = 1.089, 1.046, 1.016, 1.016, and 1.068 for PEG 2, 5, 10, 20, and 54 kDa respectively.

AFM measurements PEG:

SPR bare gold sensor chips 'SIA Kit Au' were from GE Healthcare. Upon removal

from storage in an argon atmosphere, gold sensor surfaces were ultra-sonicated in acetone and high purity ethanol (Merck) for 15 min respectively and dried in a nitrogen gas stream followed by 60 min UVO cleaning (Jelight Company Inc., Model 42A-220). The gold sensor surfaces were then ultra-sonicated for another 15 min in ethanol, dried in a nitrogen gas stream and mounted on the sample holder for immediate SPR/AFM usage. The clean gold sensor surface was incubated for 1h with 1 mM SH-PEG in PBS. The SPR sensor was then immersed in PBS for 1h, rinsed with Milli-Q water and dried in a nitrogen gas stream. A Bioscope II instrument (Bruker, USA) using OBL-10 cantilevers (Bruker, USA) with spring constant $k_c{\sim}0.006 - 0.009 \, N/m$ was used to record force volume maps of the modified substrate. Before use the cantilevers were passivated using droplet incubation of 1 mM $C_{17}H_{36}O_4S$ in PBS for 10 min and rinsed with PBS. Each 5 x 5 μm^2 force volume map was recorded with 32 x 32 data points or 1024 force curves in PBS. The ramp size was 500 nm and the maximum (trigger) force applied was 500 pN. After the measurement additional force curves were obtained on a clean glass substrate in PBS as a control for tip contamination. Baseline corrected force-distance curves were fitted with an exponential curve using an *Igor* script (WaveMetrics). The contact point was obtained by setting a threshold of 1.5 pN for the fit to the experimental data.

2.2.5 Experimental proof of concept using PEG and BSA

The sensitivity factor m_2/m_1 in Eq. 2.40 describes the difference in bulk sensitivities for cell1 and cell2. Thus, m_2/m_1 approaches unity when such differences are negligible. To establish that $m_2/m_1 \approx 1$, the simultaneous immobilization of $C_{17}H_{36}O_4S$ (1 mM) in four flow cells gives a SPR response of $\Delta RU = 2189 \pm 149 \, RU$, which indicates that the layers are similar (Fig. 2.18A). The calculated thickness from the BSA-SPR responses (Fig. 2.18B) for $C_{17}H_{36}O_4S$ is $d_2 = 2.5724 \pm 0.4145 \, nm$ with the layer in cell1 set to $d_1 = 2.0 \, nm$. If we assume the $C_{17}H_{36}O_4S$ layers to be equal (i.e., $R_1 = R_2$), we can interpret the standard deviation $\sigma_X =$

$\pm\, 0.4145\ nm$ of the thickness d_2 as a measure for the difference in the sensitivity of the cells, using Eq. 2.40 to get a value for m_2/m_1

$$\sigma_X = \frac{l_d}{2}\ln\left(\frac{m_2}{m_1}\right) \tag{2.55}$$

which gives

$$\frac{m_2}{m_1} = e^{\frac{2\sigma_X}{l_d}} \tag{2.56}$$

with $l_d = 320\ nm$ and $\sigma_X = 0.4145\ nm$ we find $m_2/m_1 = 1.003 \approx 1$. In comparison, the ratio R_1/R_2 for a $d_2 = 20\ nm$ thick molecular layer using a $d_1 = 2\ nm$ thick reference layer is $1.119 \gg 1.003$. It is therefore justifiable for m_2/m_1 to be set to unity for all thickness measurements performed with the same instrumentation and Eq. 2.40 consequently reduces to

$$d_2 = \frac{l_d}{2}\ln\left(\frac{R_1}{R_2}\right) + d_1 \tag{2.57}$$

Eq. 2.57 is sufficient to calculate the thickness of a molecular layer if an appropriate decay length is used.
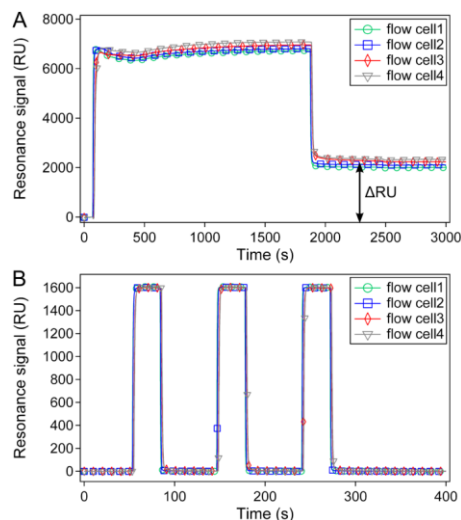
Fig. 2.18. (A) Simultaneous immobilization of $C_{17}H_{36}O_4S$ in flow cells 1-4 giving $\Delta RU = 2189 \pm 149\ RU$ (overlay plot) and (B) simultaneous BSA injections for flow cells 1-4 showing a congruent SPR response (overlay plot).

Fig. 2.19 describes the experimental application of non-interacting BSA molecules to measure the thickness of a SH-PEG molecular layer. First, $C_{17}H_{36}O_4S$ and the SH-PEG molecules are covalently grafted via thiol-binding to cell1 (reference) and cell2 (sample) in the SPR system, respectively. Injecting BSA into cell1 and cell2 then results in the SPR response signals (in resonance units or RU) R_1 and R_2, respectively. Here, the lack of binding reflects the ability of PEG to sterically repel BSA from the surface (Norde & Gage, 2004). Thus, using Eq. 2.57, d_2 can be computed for SH-PEG using the known value of $d_1 = 2\ nm$ for the $C_{17}H_{36}O_4S$ layer (Palegrosdemange et al., 1991)
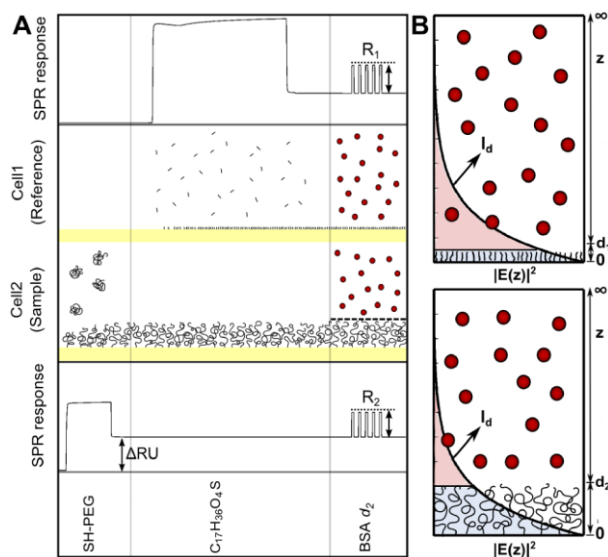
Fig. 2.19. Measuring the thickness of a molecular layer. (A) Covalently grafting of $C_{17}H_{36}O_4S$ and SH-PEG to cell1 (reference) and cell2 (sample) respectively. R_1 and R_2 are the SPR signals obtained upon injecting noninteracting BSA molecules in order to measure the PEG layer thickness in the sample cell. (B) Schematic illustration of how the SPR response (red shaded area) from the BSA molecules (red filled circles) varies inversely with distance (z). In cell 1, BSA molecules approach more closely to the $C_{17}H_{36}O_4S$-grafted (d_1) gold sensor surface giving rise to a higher SPR response. In cell2, the BSA molecules have a limited approach distance because of the surface-grafted PEG layer (d_2) and a smaller response is obtained.

The SPR sensogram responses ΔRU for representative brushes comprised of SH-PEG 2'100, 5'000, 10'000, 20'000, and 54'000 Da, respectively are shown in Fig. 2.20A. The respective BSA responses R_1 and R_2 are shown in Fig. 2.20B. Variations in R_2 indicate to height differences in the various PEG layers as compared to R_1 for the $C_{17}H_{36}O_4S$ reference layer. Note that d_2 scales inversely with the SPR response R_2, (i.e., see Eq. 2.57) where the BSA responses indicate that brush layer thickness scales with the molecular weight M_w of PEG. By invoking Eq. 2.16 this gives $l_d \approx 292\ nm$ where $\lambda = 760\ nm$, $\varepsilon'_m = -20.224$ (Schulz, 1954a & 1954b), and $n_{PBS} = 1.33411$ using $\varepsilon_d = n_d^2$ for the non-adsorbing bulk solvent. This then gives d_2 values of 5.3 nm, 9.1 nm, 11.6 nm, 19.2 nm, and 37.0 nm for PEG 2'100 Da, 5'000 Da, 10'000 Da, 20'000 Da, and 54'000 Da, respectively as shown in Fig. 2.20C. These values scale in agreement with known polymer layer thickness of similar molecular weight and accordingly conform to the scaling law for brushes in good solvents $H \propto M_w$ (De Gennes, 1980).

From Fig. 2.20A, it is noteworthy that the immobilization signal ΔRU does not scale with the size of the PEG molecules, which underscores the relevance of the proposed methodology. This indicates that the RI of each PEG brush is distinct depending on molecular size and grafting distance. It is obvious that this constitutes a major source of error in the formalism of Jung *et al.* (i.e., Eq. 2.23), where the layer thickness d_{jung} is computed from measuring ΔRU and assuming a value of n_a for the molecular layer. This error is illustrated in Fig. 2.20C when plotting layer thickness against the hydrodynamic diameter σ_{hyd} where we use $n_a = 1.36$ (i.e., $n_{PEG} \approx 1.35 - 1.4$ (Heuberger et al., 2005) for all the PEG brushes due to the lack of *ad hoc* estimates for their respective RI. For ease of comparison, we have arbitrarily set the sensitivity factor m in Eq 2.23 to match the BSA-obtained values for PEG 10'000 Da. In this way, we obtain d_{jung} values of 9.3 nm, 6.9 nm, 11.6 nm, 9.5 nm, and 11.9 nm for PEG 2'100 Da, 5'000 Da, 10'000 Da, 20'000 Da, and 54'000 Da, respectively. As seen in Fig. 2.20C, the marked difference in the BSA measurements as compared to the formalism of Jung *et al.* indicates that the latter is severely limited in predicting the scaling behavior of different PEG brushes.
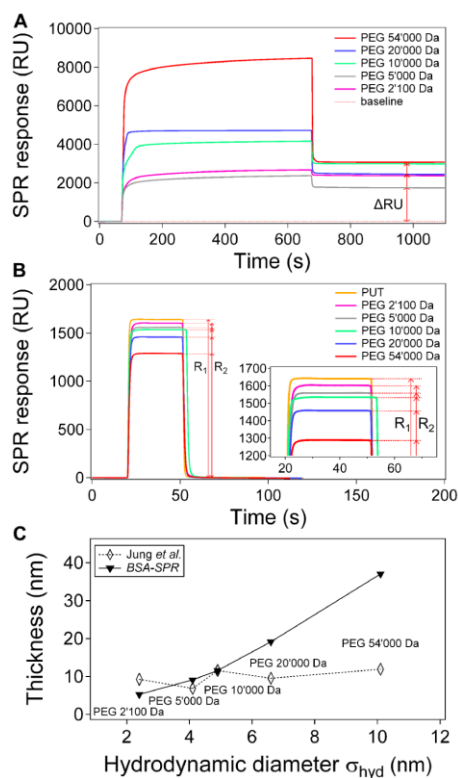
Fig. 2.20. (A) Immobilization (ΔRU) of the different SH-PEG molecules on the SPR sensor surface. **(B)** Variations in the BSA-SPR response R_2 as compared to a $C_{17}H_{36}O_4S$ reference layer R_1 ($d_1 = 2\ nm$). As from Eq. 2.57, the thickness scales inversely with the BSA-SPR response indicating to the increase in brush height with respect to PEG molecular weight M_w. **(C)** Comparison of the BSA-SPR method with the Jung *et al.* formalism (see text). The thickness of each layer scales with the PEG hydrodynamic diameter σ_{hyd} from the BSA-SPR response whereas the Jung *et al.* formalism leads to errors in the calculated thickness when using a common refractive index for all PEG brushes (i.e., $n_a = 1.36$).

As an external measure of brush thickness, AFM force measurements were obtained (Fig. 2.21A) and analyzed (Fig. 2.21B) on each respective PEG-grafted Au sensor surface (see Methods). This gives 5.1 ± 0.8 nm, 9.3 ± 0.7 nm, 11.9 ± 1.2 nm, 19.2 ± 1.1 nm, and 40.8 ± 5.1 nm for the average thickness values of PEG 2'100 Da, 5'000 Da, 10'000 Da, 20'000 Da, and 54'000 Da, respectively. Compared against the AFM measurements, it is shown in Fig. 2.21C that using Eq. 2.57 with $l_d = 300\ nm$ provides very reasonable BSA-SPR brush thicknesses where $d_2 = 5.7 \pm 0.9$ nm, 9.7 ± 0.6 nm, 11.8 ± 1.9 nm, 18.7 ± 2.9 nm, and 38.4 ± 1.2 nm for PEG 2'100 Da, 5'000 Da, 10'000 Da, 20'000 Da, and 54'000 Da respectively. Thus, the scaling law of

brush height with molecular weight $H \propto M_w$ validated. Here the error margin in the AFM measurements is defined by the width at half height of the Gaussian distribution of brush heights, whereas the error for SPR is the standard deviation for multiple measurements.
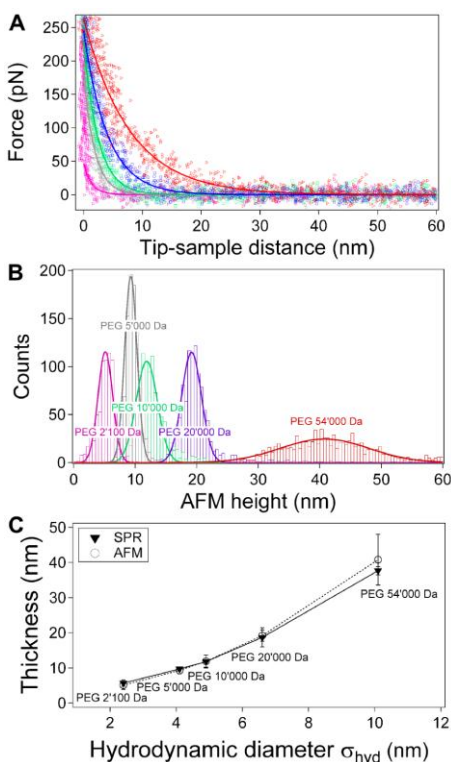
Fig. 2.21. (A) PEG layer height obtained from AFM force-distance curves. The z range of steric repulsion exerted on the tip increases with increasing PEG molecular weight M_w. **(B)** Gaussian analysis of PEG brush heights for different molecular weights M_w. **(C)** A comparison of AFM and BSA-SPR (Eq. 2.57 with $l_d = 300\ nm$) derived PEG brush heights shows close agreement.

It is further useful to correlate d_2 to the mean PEG grafting distance g_{PEG}, which is estimated from the shift in the immobilization baseline ΔRU (Fig. 2.20A). Assuming a square lattice of grafting points, g_{PEG} can be calculated using the relation $1000\ RU = 1\ ng/mm^2$ and using d_2 (measured by BSA) the refractive index of each PEG layer can be calculated (see section 2.2.3). This gives $g_{PEG} = 1.4 \pm 0.3$ nm, 2.2 $\pm$ 0.1 nm, 2.5 $\pm$ 0.1 nm, 3.9 $\pm$ 0.4 nm, and 5.4 $\pm$ 0.1 nm as well as $n_{PEG} = 1.372$,

1.355, 1.361, 1.348, and 1.344 for the brushes of PEG 2'100 Da, 5'000 Da, 10'000 Da, 20'000 Da, and 54'000 Da respectively. From these measurements, $g_{PEG} < \sigma_{PEG}$ and $d_2 > \sigma_{PEG}$ for all PEG sizes thereby confirming that the surface grafted layers indeed form molecular brushes. These parameters are summarized in table 2.1 together with the AFM measurements. Given n_{PEG} and d_2, the decay length map predicts that the optimal decay lengths would be $l_d = 294$ nm, 291 nm, 309 nm, 297 nm, and 299 nm for the molecular brushes of PEG 2'100 Da, 5'000 Da, 10'000 Da, 20'000 Da, and 54'000 Da respectively and thus are in good agreement with $l_d = 300\ nm$ as shown in Fig. 2.22.

	PEG 2'100 Da	PEG 5'000 Da	PEG 10'000 Da	PEG 20'000 Da	PEG 54'000 Da
σ_{PEG} (DLS)	2.3 ± 0.3 nm	4.1 ± 0.6 nm	4.8 ± 0.5 nm	6.6 ± 0.7 nm	**10.1 ± 1.0 nm**
g_{PEG} (SPR)	1.4 ± 0.3 nm	2.2 ± 0.1 nm	2.5 ± 0.1 nm	3.9 ± 0.4 nm	5.4 ± 0.1 nm
d (AFM)	5.1 ± 0.8 nm	9.3 ± 0.7 nm	11.9 ± 1.2 nm	19.2 ± 1.1 nm	40.8 ± 5.1 nm
d_2 (SPR)	5.7 ± 0.9 nm	9.7 ± 0.6 nm	11.8 ± 1.9 nm	18.7 ± 2.9 nm	38.4 ± 1.2 nm

Table 2.2. Structural parameters describing each PEG brush. Hydrodynamic diameter σ_{PEG}, grafting distance g_{PEG}, thickness d and d_2, respectively.
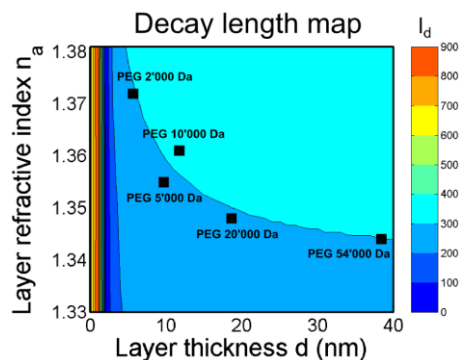
Fig. 2.22. The values (n_{PEG}, d_2) obtained from the SPR measurements are plotted into the decay length map confirming $l_d = 300\ nm$ as an appropriate decay length to measure the thickness of a PEG polymer brush. Specifically, $n_{PEG} = 1.372$, 1.355, 1.361, 1.348, and 1.344 and $l_d = 294$ nm, 291 nm, 309 nm, 297 nm, and 299 nm for the brushes of PEG 2'100 Da, 5'000 Da, 10'000 Da, 20'000 Da, and 54'000 Da respectively.

It was tested if the thickness measurements are influenced by the concentration of non-interacting molecules. The effect of BSA concentration on the measured thickness was examined for SH-PEG 5'000 Da. Fig. 2.23 shows the shift in the SPR response upon immobilization of PEG 5'000 Da in cells 2-4. The grafting distance can be calculated from the shift in the baseline ΔRU and using Eq. 2.51 giving $g_{PEG} = 2.33$ nm, 2.16 nm and 2.18 nm.
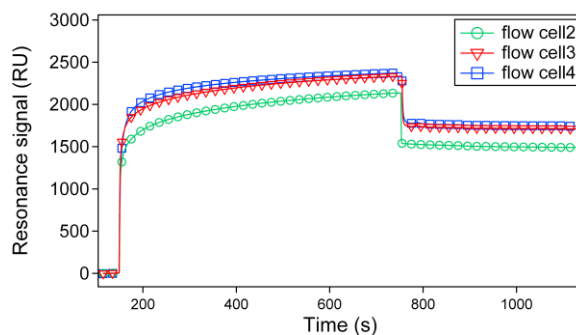
Fig. 2.23. Immobilization of SH-PEG 5'000 Da in cells 2-4. The grafting distance is calculated from the shift in the baseline ΔRU giving $g_{PEG} = 2.33$ nm, 2.16 nm and 2.18 nm.
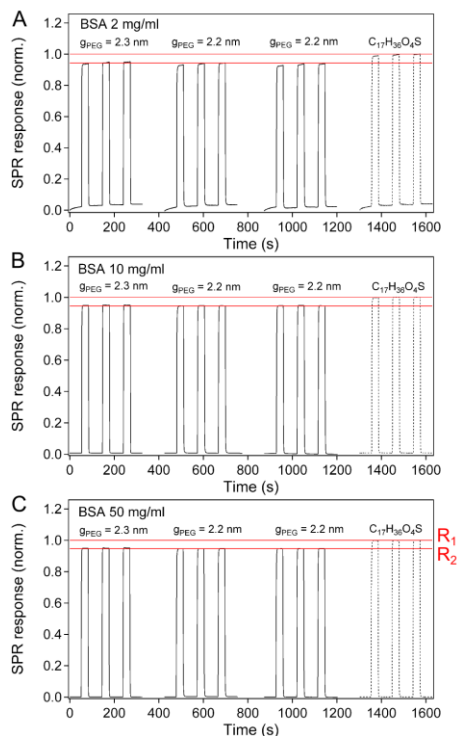
Fig. 2.24. BSA-SPR response for cells 2-4 with PEG 5'000 Da immobilized and for cell1 with $C_{17}H_{36}O_4S$. The SPR response in the PEG cells is normalized to the SPR response in the $C_{17}H_{36}O_4S$ cell (----) for BSA concentrations **(A)** 2 mg/ml, **(B)** 10 mg/ml and **(C)** 50 mg/ml respectively. The ratio R_1/R_2 is constant over the range of applied concentrations as indicated by the red lines.

Fig. 2.24 shows the BSA-SPR response that was obtained for $C_{17}H_{36}O_4S$ in cell1 and PEG 5'000 Da in cells 2-4 respectively (immobilization shown in Fig. 2.23). The BSA-SPR response in cells 2-4 is normalized relative to the BSA-SPR response in cell1 (i.e., with $C_{17}H_{36}O_4S$ immobilized). The BSA concentrations are (A) 2 mg/ml, (B) 10 mg/ml and (C) 50 mg/ml from top to bottom in Fig. 2.24. The absolute SPR response is increasing with bulk BSA concentration but the relative response R_1/R_2 does not change with BSA concentration and we get $d_2 = 9.9 \pm 0.7\ nm$ for 2 mg/ml, $d_2 = 9.8 \pm 0.4\ nm$ for 10 mg/ml, and $d_2 = 9.8 \pm 0.5\ nm$ for 50 mg/ml BSA. These values are averaged over the three PEG layers with $g_{PEG} = 2.22 \pm 0.09\ nm$ as shown in table 2.3. The thickness is $d_2 = 9.8 \pm 0.5\ nm$ when averaged over all layers and BSA concentrations.

	d_2 (2 mg/ml)	d_2 (10 mg/ml)	d_2 (50 mg/ml)	grafting distance g_{PEG}
PEG 5'000 Da	9.7 nm	9.6 nm	9.4 nm	2.33 nm
PEG 5'000 Da	10.7 nm	10.3 nm	10.3 nm	2.16 nm
PEG 5'000 Da	9.3 nm	9.5 nm	9.8 nm	2.18 nm
Mean values	9.9 ± 0.7 nm	9.8 ± 0.5 nm	9.8 ± 0.5 nm	2.22 ± 0.09 nm

Table 2.3. The measured thickness d_2 for similar SH-PEG 5'000 Da layers (i.e. similar grafting distance $g_{PEG} = 2.22 \pm 0.09 \ nm$). The mean values for the thickness d_2 are similar over the applied BSA concentrations 2 mg/ml, 10 mg/ml and 50 mg/ml, respectively, with $d_2 = 9.8 \pm 0.5 \ nm$ when averaged over all SH-PEG 5kDa layers and BSA concentrations.

2.3 Discussion

The conundrum in determining thickness measurements in SPR lies in having to deconvolve the RI from thickness for a transparent molecular layer as both evoke similar changes in the resonance spectral response (Salamon et al., 1997). This is evident in Fig. 2.20A where the PEG immobilization signal does not scale with brush height due to the distinct RI of each layer. It is for this exact reason that large errors emerge from the Jung *et al.* formalism when a common RI is assumed for each of the different PEG layers (Fig. 2.20C) (Jung et al., 1998). As demonstrated here, such pitfalls can be avoided by monitoring the SPR response of non-interacting molecules (e.g., BSA) that naturally "sense" the intrinsic exclusion volume of the PEG brush (i.e., the steric repulsive barrier). In this manner, the BSA molecules function as innate non-invasive probes that provide conformational height information with respect to an interfacial molecular layer. It is evident R_2 in Fig. 2.20B does scale with the height of the PEG brush. The method is further strengthened by computing the optimal decay lengths l_d (Fig. 2.14) that correspond to an approximate refractive index of a molecular layer for use in Eq. 2.57. As explained in a previous section, using $l_d = 350 \ nm$ generates a maximal error of ±15% (due to the RI constraint) in

the thickness of molecular layers with refractive indices ranging from $n_a \approx 1.35$ to 1.4 (e.g., highly solvated molecular brushes). Regardless, from Fig. 2.22 one will find that variations in l_d have a much smaller effect on calculating d_2 (using Eq. 2.57) than variations in the RI (relative to the solvent $n_a - n_s$) on calculating d_{jung} (using Eq. 2.23) for the different PEG layers. For this reason, the presented methodology provides a powerful means to overcome the RI constraint in SPR.

When considered in a broader context, the proposed SPR method does not require a preconceived notion regarding the structure of the underlying molecular layer, which is advantageous over other surface-based techniques. These include both optical and mechanical techniques such as ellipsometry (Arwin, 2011), dual polarization interferometry (DPI) (Lukosz, 1997), quartz crystal microbalance with dissipation monitoring (QCM-D) (Voros, 2004; Voinova et al., 2002) and atomic force microscopy (AFM) (Hyotyla et al., 2011; Butt et al., 2005). Briefly, the main challenge for ellipsometry is similar to SPR and resides in separating the RI and thickness for a thin and transparent molecular layer. Although DPI and QCM-D are non-invasive techniques, data fitting and analysis usually involve models that assume well-defined homogeneous and isotropic layers (Lukosz, 1997; Voinova et al., 2002; Eisele et al., 2012). The latter is a serious simplification since a majority of molecular layers deviate from a simple step function profile and for polymer brushes a parabolic density profile is expected from theory (Milner et al., 1988) as well as experiments (Karim et al., 1994). Additionally, in QCM-D solvent may couple via viscous drag or entrapment in cavities in the adsorbed film (Hook et al., 2001) thereby rendering the technique insensitive to small changes in surface corrugations. Similarly, conventional optical approaches are potentially insensitive to surface corrugations with a dimension smaller than the wavelength λ of the incident light (Lukosz, 1997). As for AFM, height determination usually depends on the force resolution of the cantilever in identifying the "true" contact point between the tip and the layer (Melzak et al., 2010). As a further advantage over AFM, the BSA molecules probe surface corrugations with minimal "mechanical" force at a resolution that is defined

by their molecular size. This is also similar to the plasmonic ruler approach (Mock et al., 2012), where the signal that determines the layer thickness emerges from "particles" above the layer and not the signal from the layer itself.

In terms of its limitations, the SPR method likely depends on geometric factors such as the intrinsic shape and size of the non-interacting particles as well as the grafting distance between neighboring polymer chains (Kim & O'Shaughnessy, 2002; Lee & Penn, 2009). For instance, large particles experiencing enhanced van der Waals attraction to the grafting surface (Jeon & Andrade, 1991) can lead to thickness underestimates by affecting (i) the conformation of the layer, and (ii) particle distribution in solution. On the other hand, underestimates can also result from the penetration of BSA molecules into a layer, which increases in likelihood for layers exhibiting larger grafting distances (e.g., "mushrooms"). Indeed, the slight reduction in SPR-measured thickness of PEG 54'000 Da (which exhibits the largest grafting distance of $g_{PEG} = 5.4 \pm 0.1 \, nm$) as compared to AFM-obtained values may arise from a small degree of BSA ($\sigma_{BSA} = 7.4 \, nm$) penetrating the layer (Fig. 2.21C). This also correlates to a decrease in layer density as a function of increasing PEG size (and grafting distance) as inferred from their characteristic RI's (Eq. 2.53; Fig. 2.22). Interestingly, control experiments at increased BSA concentrations (max. 50 mg/ml) did not reveal any significant influence of osmotic pressure on the measured thickness for PEG 5'000 Da nor did any BSA adsorption occur on the PEG or the $C_{17}H_{36}O_4S$ (i.e., the BSA injections are rectangular).

Chapter 3

PEG brush height decreases smoothly with temperature

This chapter is so far unpublished

In this chapter we show experimentally that the height of strongly stretched PEG polymer brushes is decreasing smoothly with temperature already around room temperature. Far from the lower critical solution temperature (LCST) the PEG brush thus undergoes a smooth conformational transition in agreement with the classical polymer brush, however, with a transition to good solvent when temperature is lowered. In our experiments we use bovine serum albumin (BSA) monomers as well as cross-linked BSA dimers to probe the excluded volume of strongly stretched PEG polymer brushes using surface plasmon resonance (SPR). As the difference in the brush height measured from BSA monomer and BSA dimer $\Delta d \approx 1\,\mathrm{nm}$ is in agreement with the difference $\Delta R_h \approx 1\,\mathrm{nm}$ in their hydrodynamic radii, this suggests that BSA only probes the edge of the brush and that the BSA-PEG interaction is weak. This view is supported by extensive SPR reflectivity calculations.

3.1 Basics & Theory

3.1.1 Background

Polymer brushes of poly(ethylene glycol) (PEG) represent a widely used standard in

preventing undesired protein adsorption to surfaces from aqueous solution (Norde & Gage, 2004; Emilsson et al., 2014; Currie et al., 1999; Currie et al., 2003). The underlying barrier mechanism emerges from steric repulsion between the proteins and the polymer brush (Szleifer 1997; Satulovsky et al., 1999; Halperin et al., 2007; Halperin & Kröger 2009; Halperin 1999; Jeon et al., 1991; Jönsson & Johansson, 2004). Additional functionality emerges for thermo-responsive polymers such as poly(N-isopropylacrylamide) (PNIPAM) that allow for the switching between repulsive and attractive states (Halperin & Kröger, 2011). Accordingly the polymer brushes of PNIPAM reveal a narrow collapse transition at $T \approx 30°C$ (Yim et al., 2004; Plunkett et al., 2006; Yim et al., 2004) that enables to control surface adhesion of cells and proteins (Gil & Hudson, 2004). This collapse transition is associated to a lower critical solution temperature (LCST) that is very common to the phase behavior of water soluble polymers (Bekiranov et al., 1997). The PEG-water system has a phase diagram of the closed-loop type with a LCST at $T \approx 100°C$ (Bae et al., 1991; Saeki et al., 1976). Several attempts to explain the LCST of PEG have been commenced. Especially they consider the loss of hydrogen bonds with temperature (Matsuyama & Tanaka, 1990; Bekiranov et al., 1997), such as describing solvent quality with temperature via the entropic loss for PEG-water hydrogen bond formation (see section 3.1.2.3) (Dormidontova, 2002). Other models are the so called two state models, here, the change in solvent quality would emanate due to changes in the gauch-trans equilibrium in the PEG chain with temperature (Karlström, 1985) as well as the n-cluster model, where it is possible for the polymer chains to exhibit attractive n-body interactions (Halperin, 1998; de Gennes, 1991). Attractive n-body

interactions allow for LCST behavior and vertical phase separation within the brush, whereas for the classical polymer brush the swelling or collapse with temperature is considered a much smoother conformational transition due to stabilizing ternary interactions (Zhulina et al., 1991, Halperin & Kröger, 2011).

The behavior of PEG polymer brushes around room temperature is experimentally unresolved. In the present work we aim to determine the thickness of strongly stretched PEG polymer brushes at different temperatures using bovine serum albumin (BSA) as molecular probes. The temperature range probed (i.e. 5°C to 35°C) is important for biologically-related applications that typically span a range of 4°C to 37°C. The measurements are based on our surface plasmon resonance (SPR) based technique for probing the intrinsic excluded volume of polymer brushes using non-interacting particles (Schoch & Lim., 2013). Questions arise to the extent of BSA penetration into the polymer brush, in order to verify that the BSA exclusion properly reflects the PEG brush height. Experimental data on particle penetration in case of non-adsorbing particles is however scarce. Only one study, to our knowledge, ascertains colloidal penetration for thick and poly-disperse polystyrene brushes to depend on colloid size and solvent quality (Filippidi et al., 2007). For intermediate sized proteins the penetration of polymer brushes has been treated mainly in a polymer-theoretical context (Halperin et al., 2011; Egorov, 2012; Szleifer 1997; Kim & O'Shaughnessy, 2006; Steels et al., 2000; Chen & Chen; 2012) as well as using simulation techniques (Milchev et al., 2008; Ermilov et al., 2010; Merlitz et al., 2012; Yaneva et al., 2009).

Qualitatively, the free energy $F_{ins}(z)$ for inserting a non-interacting particle at height z from the grafting plane increases with particle radius R and monomer volume fraction $\phi(z)$. In a self-consistent field (SCF) theory based study a thorough description of particle penetration depending on solvent quality was given (Halperin et al., 2011). It considers the insertive limit $R \ll H$, where H is the unperturbed brush height, such that the insertion into the brush perturbs the monomer concentration profile only locally (Steels et al., 2000). In this case $F_{ins}(z)$ of a non-interacting particle is related to the osmotic pressure $\Pi(z)$ of the brush and the scaling $F_{ins} \propto (\Phi^2, R^3)$ for good solvent and $F_{ins} \propto (\Phi^3, R^3)$ for theta solvent, respectively, is obtained (Halperin et al., 2011). For shallow insertions surface tension contributions $F_{ins} \propto (\Phi, R^2)$ may be considered crucial as well (Milchev et al., 2008, Egorov et al., 2012, Ermilov et al., 2010, Wang et al., 2001; Halperin & Kröger, 2009, Halperin et al., 2011). To compare with the theoretically established size-dependence of particle penetration into a polymer brush we measure the exclusion of BSA monomer d_{mono} as well as cross-linked BSA dimer d_{dimer} for a PEG polymer brush at different temperatures. In case of substantial BSA penetration this would lead to diverging brush heights $\Delta d = d_{dimer} - d_{mono}$ as measured from BSA monomers and the bigger BSA dimers, respectiely. Thus the meaning of BSA is twofold: 1) BSA acts as an intrinsic probe to measure brush height; 2) BSA is a model protein to test penetration into the PEG brush. An advantage of our approach is that by the use of BSA monomer and BSA dimer, respectively, the particle-monomer interactions may be considered identical in both cases. Thus we would expect Δd to diverge as well for substantial particle-monomer interactions at the edge of the brush due to the bigger

surface area of the BSA dimer.

It was shown previously (Emilsson et al., 2015) that using cloud point grafting for SH-PEG, the layer satisfies the scaling $H \propto N$, where N is the number of monomers per chain, as obtained from a mean-field treatment for polymer brushes at moderate high density (Milner et al., 1988; Zhulina et al., 1991). SH-PEG 20kDa is the largest PEG that still follows this trend. Therefore our analysis can benefit from analytical SCF solutions based on the mean-field approximation (Milner et al., 1988; Zhulina et al., 1991; Halperin et al., 2011) as well as from the insertive limit of particle penetration (i.e. $R \ll H$) (Halperin et al., 2011). Importantly, we measure a smooth decrease in brush height with temperature already around room temperature. For the BSA dimer we consistently measure increased brush heights when compared to the BSA monomer (i.e., $d_{dimer} > d_{mono}$), where the measured difference in height is $\Delta d \approx 1$ nm in agreement with the difference in hydrodynamic radii $\Delta R_h \approx 1$ nm of the BSA monomer and the BSA dimer. It follows that the molecules only probe the edge of the PEG polymer brush as supported by reflectivity calculations (Ekgasit et al., 2004) using SCF monomer density profiles for theta as well as good solvent and osmotic exclusion $F_{osm}(z) \approx \Pi(z)R^3$ (Halperin et al., 2011). When additionally including an attractive term $F_{att}(z) \approx -\epsilon \Phi(z)(R/a)^2$ (Halperin et al., 2011), where a is the PEG monomer size, the measured $\Delta d \approx 1$ nm is however only compatible with the literature value $\epsilon = 0.05 \, k_B T$ (Abott et al., 1992) when considering a brush monomer profile for good solvent. In this case the measured brush height is underestimated due to the accumulation of BSA molecules at the edge of the brush,

whereas the trend in brush height with temperature is persistent. The reflectivity calculations thus strongly support the experimental evidence of a decrease in PEG brush height with increasing temperature.

3.1.2 Polymer physics

3.1.2.1 Polymer scaling with temperature

To understand theoretically how polymer chain size changes with temperature, we need to consider the temperature dependence of the excluded volume (Rubinstein & Colby, 2003). The monomer-monomer pair interaction is described by short-range repulsion for $r < b$ and long-range attraction for $r > b$ as described by the Lennard-Jones potential $U(r)$. The excluded volume is then defined as minus the integral of the Meyer f-function $f(r)$

$$v = -\int f(r)d^3r = \int (1 - \exp[-U(r)/(kT)])d^3r \tag{3.1}$$

the Meyer f-function for $r < b$ is $f(r) \approx -1$ and for $r > b$ is $f(r) \approx -U(r)/k_B T$. With these two parts we get for the excluded volume

$$v \approx \left(1 - \frac{\theta}{T}\right)b^3 \tag{3.2}$$

The first term is the contribution of the hard-core repulsion and is of the order of the monomer volume b^3. The second term contains the temperature dependence, for $T < \theta$ the excluded volume is negative ($v < 0$), indicating a net attraction between

monomers (*poor solvent*). For $T > \theta$ this leads to a positive excluded volume ($v > 0$) resulting in swelling of the coil (*good solvent*). For $T = \theta$ the excluded volume vanishes ($v = 0$) and the chain scales such as an ideal chain (*θ-solvent*).

For the next section it is important to be aware of the relation between the exclusion parameter v and the Flory interaction parameter χ

$$v = b^3(1 - \chi) \tag{3.3}$$

The interaction parameter χ accounts for the difference in solvent-solvent, segment-segment and solvent-segment interactions. In principle, the interaction parameter χ describes the energy of solvating a segment and is inversely proportional to the temperature. However, the temperature dependence of real χ-parameters is more complex due to internal structure and degrees of freedom of an actual segment.

3.1.2.2 Polymer phase behavior

By considering the temperature dependence of the free energy of mixing, a phase diagram can be constructed to summarize the phase behavior of the mixture (Rubinstein & Colby, 2003). The binodal χ_b defines the coexistence of compositions Φ' and Φ'' for a given interaction parameter χ. The binodal line thus separates the phase diagram into a single-phase region and a two-phase region. Using the phenomenological temperature dependence of the interaction parameter $\chi(T) \simeq A + B/T$, this relation can be transformed to the binodal of the phase diagram in the space of temperature and composition $T_b(\varphi)$. In a binary blend the point on the binodal curve corresponds to the critical point if $\delta T_b/\delta \varphi = 0$ and this point determines the critical composition Φ_c, the critical temperature T_c and the critical interaction

parameter χ_c. In the common case where $B > 0$, then χ decreases as temperature is lowered and for interaction parameters χ and temperatures T above the critical point only a single phase exists that is stable at any composition $0 \leq \varphi \leq 1$. The highest temperature in the two phase region is called the *upper critical solution temperature* (UCST) and defines the well understood text book polymer behaviour. However, there are also cases where $B < 0$ for a binary blend. It follows that χ decreases as temperature is lowered and we find that the lowest temperature of the two-phase region is the *lower critical solution temperature* (LCST). Consequently those polymer blends phase separate when temperature is raised. Additionally there are also examples where B varies with temperature, changing sign as temperature is changed and resulting in both UCST and LCST (*closed loop behavior*).

3.1.2.3 Polymer hydrogen bonding

Polyethylene glycol shows closed loop behavior of phase coexistence in aqueous solutions. The closed loop behavior can be reproduced by applying a mean field approach which includes the effect of competition of PEG and water as proton acceptors in hydrogen bond formation (Dormidontova, 2002). The specificities of the PEG and water molecules in hydrogen bond formation can be captured via the characteristic energetic and entropic change upon hydrogen bond formation. Thus we get an additional term in the free energy

$$F = F_{ent} + F_{int} + F_{assoc} \qquad\qquad (3.4)$$

As introduced in section 2.1.3.1, F_{ent} has purely entropic character and F_{int} describes the interactions between monomers except from the hydrogen bonding ones. F_{assoc} is the part of the free energy due to PEG-water and water-water hydrogen bonding that combines the contributions for the energetic gain and entropic loss for hydrogen

bonding

$$\frac{\Delta F_i}{kT} \equiv \frac{\Delta E_i}{kT} - \Delta S_i \qquad\qquad (3.5)$$

where $i = p$ for PEG-water and $i = w$ for water-water hydrogen bonds and the entropic loss is connected with the loss of orientational entropy for the donor and acceptor groups which have to keep the correct orientation inside the characteristic space angle Δ for the hydrogen bond to remain stable

$$\Delta S_i = -\ln\left(\frac{1-\cos\Delta_i}{2}\right) \qquad\qquad (3.6)$$

The average fraction of hydrogen bond formation between PEG and water, and between water molecules decreases rapidly with temperature increase because the relative energetic gain for hydrogen bond formation decreases compared with kT. As the entropic loss for PEG-water hydrogen bond formation is assumed to be larger ($\Delta_p < \Delta_w$) the fraction of hydrogen bond formation between PEG and water decreases relative to water-water association. Instead of a linear increase of the χ parameter with inverse temperature as expected for polymers without specific interactions, aqueous solutions of PEG exhibit the opposite tendency: a decrease in χ and thus an increase in the excluded volume v (see Eq. 3.3) with a decrease in temperature.

3.2 Temperature dependence of SPR response

One can describe the angular dependence of the reflectivity $R_p(\theta)$ in SPR by solving Fresnel's equations for the layer architecture (see section 2.1.1.5). The parameters

used for the reflectivity calculations at $T = 25°C$ are summarized in Table 3.1. The Au refractive index (RI) is from Schulz, 1954, the $C_{17}H_{36}O_4S$ refractive index n and layer thickness d is taken from Palegrosdemange et al., 1991.

	Prism	Au	PEG	PBS	BSA	$C_{17}H_{36}O_4S$
n	1.52	0.16	~ 1.35	1.33411	1.33489	1.45
k	0	4.5	0	0	0	0
d (nm)	∞	50	several	∞	∞	2

Table 3.1. Summary of the parameters used for the reflectivity calculations at $T = 25°C$. Each layer is represented by the RI n, the imaginary part of the RI k and the layer thickness d.

The solvent (PBS) and BSA (in PBS) refractive indices were measured at $T = 25°C$ and a wavelength of $\lambda = 589\ nm$ using a Reichert AR7 Series Automatic Refractometer. They were therefore corrected in wavelength and temperature using a model for water. The water refractive index in dependence of temperature and wavelength can be described using the Cauchy formula with temperature-dependent coefficients (Bashkatov & Genina, 2003)

$$n(\lambda, t) = A(t) + \frac{B(t)}{\lambda^2} + \frac{C(t)}{\lambda^4} + \frac{D(t)}{\lambda^6} \tag{3.7}$$

where λ is the wavelength [nm] and $A(t)$, $B(t)$, $C(t)$, $D(t)$ are the Cauchy coefficients as a function of temperature t [°C]

$$A(t) = 1.3208 - 1.2325 \cdot 10^{-5}t - 1.8674 \cdot 10^{-6}t^2 + 5.0233 \cdot 10^{-9}t^3 \quad (3.8)$$

$$B(t) = 5208.2413 - 0.5179t - 2.284 \cdot 10^{-2}t^2 + 6.9608 \cdot 10^{-5}t^3 \quad (3.9)$$

$$C(t) = -2.5551 \cdot 10^8 - 18341.336t - 917.2319t^2 + 2.7729t^3 \quad (3.10)$$

$$D(t) = 9.3495 + 1.7855 \cdot 10^{-3}t + 3.6733 \cdot 10^{-5}t^2 - 1.2932 \cdot 10^{-7}t^3 \quad (3.11)$$

For the glass prism the Sellmeier dispersion formula can be used to describe the refractive index for any wavelength λ [μm] from the near UV to 2.3 μm (Schott, Optical Glass Data Sheet, 2013)

$$n^2(\lambda) - 1 = \frac{B_1\lambda^2}{\lambda^2 - C_1} + \frac{B_2\lambda^2}{\lambda^2 - C_2} + \frac{B_3\lambda^2}{\lambda^2 - C_3} \quad (3.12)$$

With $B_1 = 1.03961212$, $B_2 = 0.231792344$, $B_3 = 1.01046945$, $C_1 = 0.00600069867$, $C_2 = 0.0200179144$, $C_3 = 103.560653$ for N-BK7HT glass. The temperature dependence of the refractive index can then be calculated using the formula

$$\frac{dn(\lambda,T)}{dT} = \frac{n^2(\lambda,T_0) - 1}{2n(\lambda,T_0)}\left(D_0 + 2D_1\Delta T + 3D_2\Delta T^2 + \frac{E_0 + 2E_1\Delta T}{\lambda^2 - \lambda_{TK}^2}\right) \quad (3.13)$$

with $D_0 = 1.86 \cdot 10^{-6}$, $D_1 = 1.31 \cdot 10^{-8}$, $D_2 = -1.37 \cdot 10^{-11}$, $E_0 = 4.34 \cdot 10^{-7}$, $E_1 = 6.27 \cdot 10^{-10}$ and $\lambda_{TK} = 0.17\ \mu m$ for N-BK7HT glass. The constants are valid for a temperature range from -100°C to +140°C and a wavelength range from 0.365 μm to 1.041 μm.

The temperature dependence of the optical constants of gold in the red and infrared part of the spectrum, i.e. in the absence of adsorption bands, can be described in good approximation on the basis of the Drude theory and the theory of electron-phonon scattering (Ujihara, 1972). The Drude result for the dielectric constant is given by (Johnson & Christy, 1972)

$$\varepsilon = \varepsilon_1 + j\varepsilon_2 = 1 - \frac{\omega_p^2}{\omega^2 + \omega_c^2} + j\frac{\omega_p^2\omega_c}{(\omega^2 + \omega_c^2)\omega} \tag{3.14}$$

where ω is the photon frequency, ω_p is the electron plasma frequency and ω_c is the average collision frequency. The electron-phonon collision frequency increases with temperature (Ujihara, 1972)

$$\omega_c = K'T^5 \int_0^{\vartheta/T} \frac{z^4 dz}{e^z - 1} \tag{3.15}$$

where K' is a constant (approximation), T is the temperature and ϑ is the Debye temperature. Physically this means that with increasing temperature the phonon population increases and thus the probability of electron-phonon scattering increases. The constant K' can be obtained from

$$K' = \omega_{c,0}\left(T_0^5 \int_0^{\vartheta/T_0} \frac{z^4 dz}{e^z - 1}\right)^{-1} \tag{3.16}$$

where $\omega_{c,0}$ is the collision frequency at temperature T_0

$$\omega_{c,0} = \frac{\omega_p^2 - \left(\omega_p^2 - 16n^2k^2\omega^4\right)^{1/2}}{4nk\omega} \tag{3.17}$$

with known n and k parameters of the complex index of refraction at T_0 and ω, using

$$\omega_p = \sqrt{\frac{Ne^2}{\varepsilon_0 m^*}} \tag{3.18}$$

where N is the electron density, ε_0 is the vacuum permittivity, e is the elementary charge and m^* is the effective electron mass.

Experimentally defined refractive indices at $\lambda = 589\ nm$ for n_{PBS} and n_{BSA} (i.e. BSA in PBS) define offsets relative to water at $\lambda = 589\ nm$ (from the Cauchy formula) that are added to the refractive index of water at $\lambda = 760\ nm$ (from the Cauchy formula) and any temperature T from 5°C to 35°C to approximate the refractive index of n_{PBS} and n_{BSA} at these temperatures

$$n_{BSA}(\lambda_1, T_1) = n_{H_2O}(\lambda_1, T_1) + \left[n_{BSA}(\lambda_2, T_2) - n_{H_2O}(\lambda_2, T_2)\right] \tag{3.19}$$

$$n_{PBS}(\lambda_1, T_1) = n_{H_2O}(\lambda_1, T_1) + \left[n_{PBS}(\lambda_2, T_2) - n_{H_2O}(\lambda_2, T_2)\right] \tag{3.20}$$

The refractive index of the prism at temperature T and $\lambda = 760\ nm$ is directly calculated from the equations for BK7 glass. For the gold layer the equations introduced were applied using $n = 0.16$ and $k = 4.5$ at $T_0 = 25°C$ (Schulz, 1954), the electron density $N = 5.9 \times 10^{22}\ cm^{-3}$ (Ujihara, 1972), the Debye temperature

$\vartheta = 164°K$ and an effective electron mass $m^* = 0.99\, m$ (Johnson & Christy, 1972), where m is the free electron mass.
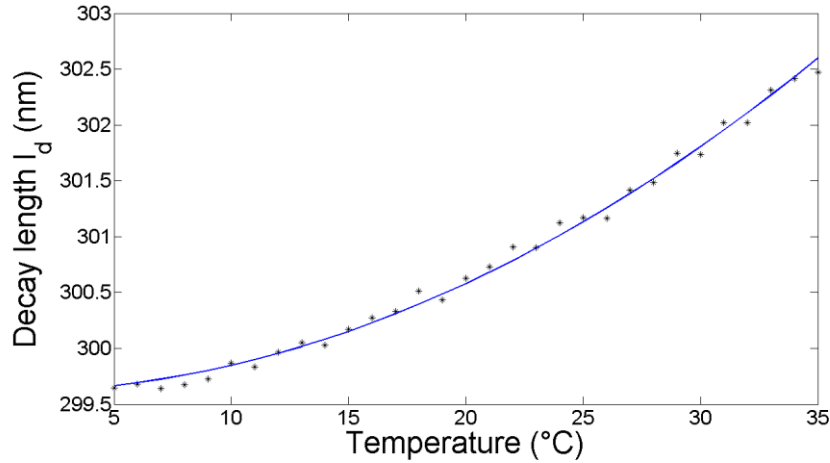
Fig. 3.1. Temperature dependence of the optimal evanescent field decay length l_d for a brush with refractive index $n_0 = 1.36$ at $z = 0$ and height $H = 40\, nm$. The blue line is a quadratic least square fit: $y = 299.6 + 0.00245 \cdot x^2$. Here, the temperature dependence of the PEG was ignored due to an unknown temperature behavior.

The temperature dependence of the decay length l_d was calculated using the Fresnel matrix formalism (Eqs. 2.20-2.22), representative of a molecular brush with refractive index $n_0 = 1.36$ at $z = 0$ and height $H = 40\, nm$ (see below). The blue line is a quadratic least square fit to the computed decay lengths. Accordingly, the decay length l_d to be used for the height measurements needs to be adjusted for temperature. From the fit parameter we can estimate the relative error due to temperature if a constant decay length is used. For going from 5°C to 35°C the measured thickness would increase by only $\approx 1\%$ due to temperature effects on the decay length. Nevertheless, the temperature dependence of the individual layers was incorporated into the reflectivity calculations.

3.3 Calculating the SPR response for BSA injection

From the matrix formalism (Eqs. 2.20-2.22) the reflectivity arrays $R_p(\theta)$ were calculated over a range $\theta = 64° - 74°$ at an angular resolution of $\Delta\theta = 0.001°$. The minimum position was then read out from the array and used as an initial guess to position a parabolic least square fit around the minimum, yielding an improved angular positioning of the minimum θ_{min}. The change in the minimum position $\Delta\theta_{min}$ was calculated for BSA injections in both the reference and the sample cells. In the reference cell a single isotropic layer of $C_{17}H_{36}O_4S$ between the Au layer and the infinite dielectric medium is used, whereas in the sample layer due to the non-isotropy of a polymer brush the layer was divided into isotropic $d_j = 0.2\ nm$ slices. The monomer volume fraction $\phi(z)$ was constructed according to the self-consistent field (SCF) theory for strongly stretched polymer brushes (Halperin et al., 2011)

$$\Phi(z) = \Phi_0(1 - z^2/H^2)^m \tag{3.21}$$

Here, H is the brush height, z is the distance from the sensor surface and $\phi(z = 0) = \phi_0$. For a good solvent $m = 1$ and for a theta solvent $m = 0.5$. To obtain information about the free energy F_{ins} of inserting BSA monomers and dimers, respectively, into a polymer brush, it is important to model the distribution of BSA molecules within the brush. We were using different model assumptions from literature. For small spherical particles with radius $R \ll H$, where the particle is small enough to allow polymer chain trajectories to circumvent it (Halperin et al., 2011)

$$F_{osm}(z) = \int_{z-R}^{z+R} \Pi\ (z')A(z, z')dz' \tag{3.22}$$

where $A(z, z')dz$ is the cross sectional volume at z' of the particle whose geometrical

center is at altitude z, and $\Pi(z')$ is the osmotic pressure given as (Halperin et al., 2011)

$$\Pi(z) = \Pi_0(1 - z^2/H^2)^{(m+1)} \tag{3.23}$$

where Π_0 is the osmotic pressure at the at $z = 0$. We were using the hydrodanamic radius R_h of BSA, i.e. $R_{h,mono} = 3.125\ nm$ and $R_{h,dimer} = 4.13\ nm$, as measured by DLS and assuming a spherical shape to calcualte $F_{ins} = F_{osm}$. The BSA molecules then distribute within the brush according the Boltzman distribution law (Halperin et al., 2011)

$$c_{BSA}(z) \approx c_0 exp\left[\frac{-F_{ins}(z)}{k_B T}\right] \tag{3.24}$$

where c_0 is the injected bulk BSA concentration. However, as we are interested in optical indeces for the refelctivity calculations rather than concentrations, we use for the polymer brush in solvent

$$\varepsilon_{PEG,solvent} = (1 - z^2/H^2)^m \cdot \varepsilon_{PEG} + (z^2/H^2) \cdot \varepsilon_{solvent} \quad for\ 0 \leqslant z \leqslant H \tag{3.25}$$

and for the polymer brush with particles

$$\varepsilon_{PEG,BSA} = (1 - z^2/H^2)^m \cdot \varepsilon_{PEG} + (z^2/H^2) \cdot \varepsilon_{solvent} + exp(-F_{ins}/k_B T)$$
$$\cdot (\varepsilon_{BSA} - \varepsilon_{solvent})$$
$$for\ 0 \leqslant z \leqslant H \tag{3.26}$$

Where $\varepsilon_{solvent} = n_{PBS}^2$, $\varepsilon_{BSA} = n_{BSA}^2$, and $\varepsilon_{PEG} = n_0^2 = 1.36^2$ is the dielectric costant of the brush at $z = 0$. This estimate comes from $n_{PEG} \approx 1.35$ when assuming a step profile for the polymer brush as well as a decay length $l_d = 300 \, nm$ optimal for PEG polymer brushes in our setup (Schoch & Lim, 2013).

Additionally we were using an attractive term that scales with the particle surface area (Halperin et al., 2011; Halperin & Kröger, 2009)

$$F_{att}(z) = -\frac{\epsilon k_B T}{a^2} \Phi_0 \int_{z-R}^{z+R} \left(1 - \frac{z^2}{H^2}\right) ds(z, z', dz') \tag{3.37}$$

where ds is a strip on the sphere's surface and ϵ defines the adsorption free energy per monomer in contact with the protein surface. Note that in this case $F_{ins}(z) = F_{osm}(z) + F_{att}(z)$.

In the calculations Π_0 was varied from $2 \cdot 10^{25} k_B T$ to $240 \cdot 10^{25} k_B T$ in steps of $2 \cdot 10^{25} k_B T$, H was varied from 5 nm below the height d_{mono} measured with the BSA dimers at each temperature up to $d_{mono} + 10 \, nm$ in steps of 0.5 nm, and the scaling factor m was fixed at $m = 0.5$ for theta conditions or $m = 1$ for good conditions, respectively. For each brush scenario the shift in the reflectivity dip $\Delta\theta_{PEG}$ due to the BSA injections was calculated for both monomer and dimer (i.e. by using $R_{h,mono}$ and $R_{h,dimer}$ respectively) at all temperatures T, and can be used to obtain a calculated layer height d_{calc} in each scenario

$$d_{calc} = l_d/2 \cdot \ln\left(\Delta\theta_{PEG}/\Delta\theta_{ref}\right) \tag{3.28}$$

d_{calc} can then be compared to the actually measured value d_{mono} using a decay length $l_d = 300\ nm$. Here $\Delta\theta_{ref}$ is the shift in the reference cell (i.e. $C_{17}H_{36}O_4S$) and only changes with temperature, as no penetration into the reference layer is assumed for either BSA species.

3.4 Materials & Methods

BSA dimer purification

20 mg/ml of bovine serum albumin (BSA) ($\geq$ 98%, Sigma Aldrich) was disolved in 20 ml of 0.1 M MES, 0.5 M NaCl, pH 5.5 using a magnetic stirrer and 20x molar excess of 1-ethyl-3-(3-dimethylaminopropyl) carbodiimide HCl (EDC) (Thermo Scientific) as well as 40 x molar excess of N-Hydroxysuccinimide (NHS) (Sigma Aldrich) were added while stirring. Therefore 200 mM EDC and 400 mM NHS where each dissolved in 0.1 M MES buffer at pH 5.5 just before mixing them with BSA. The reaction mixture was then incubated over night at 4°C while stirring. Purification of the reaction mixture was done using a HiLoad 16/600 Superdex 200 column (GE Healthcare) in phosphate buffered saline (PBS) (gibco by life technologies). Therefore 3 ml of BSA mixture was loaded to the column at 1 ml/min and the BSA dimer and BSA monomer peak elution fractions were collected (1 ml fractions) according to the 280 nm absorbance (see Fig. 3.2). Only the fractions closest to the peak maximum were kept (4 fractions of dimer and 3 fractions of monomer). After the entire BSA mixture was separated, all the monomer as well as the dimer peak fractions were pooled and concentrated to 4 ml using centrifugal filter units (Amicon Ultra – 15 10K, Millipore). The concentrated dimer and monomer fractions were then

again purified as described above. The dimer did not separate between the two purification steps, even when stored for several days at 4°C, neither did the monomers aggregate. Again only the fractions closest to the peak maximum (5 fractions each) were pooled and used for the SPR experiments within a few days. Dynamic light scattering measurements were performed for additional characterisation of the BSA species using a Zetasizer Nano instrument (Malvern).
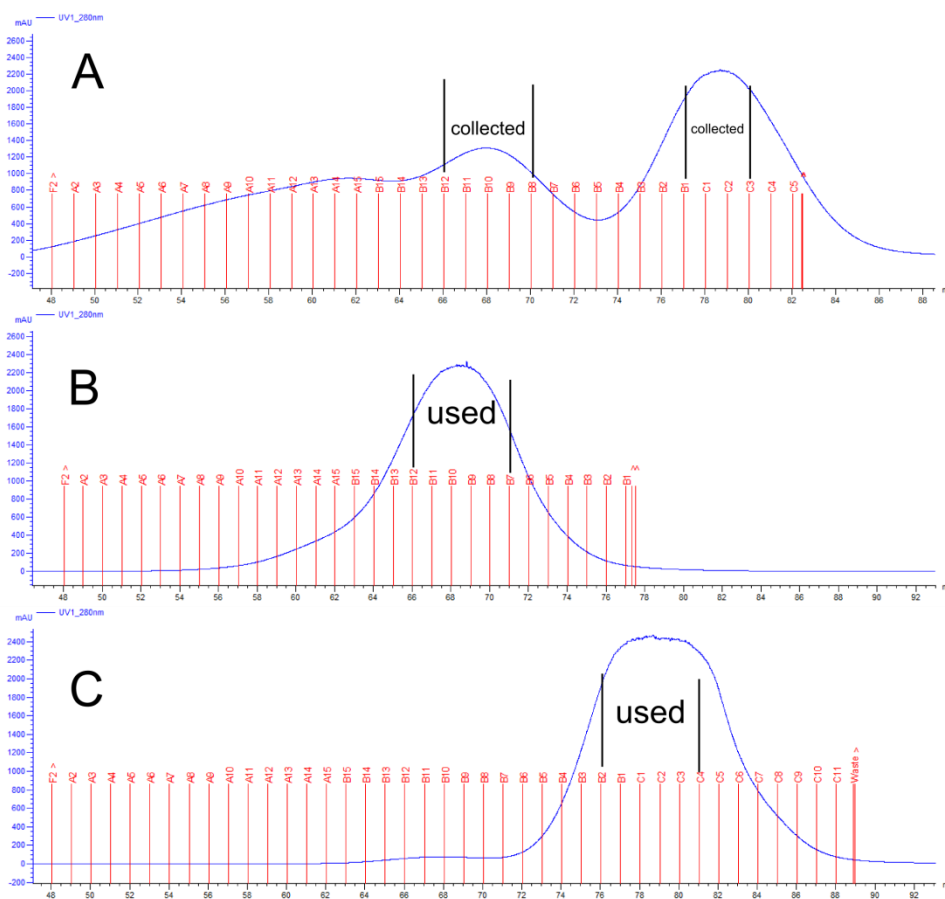

Fig. 3.2. Purification of BSA monomer as well as crosslinked BSA dimer using a Hiload 16/600 superdex 200 column (GE Healthcare). **(A)** First purification step after crosslinking. The fractions that were collected are indicated in the figure. **(B),(C)** Second purification step. The fractions used as BSA dimer **(B)** and BSA monomer **(C)** are indicated in the figure.

SPR measurements

All surface plasmon resonance (SPR) measurements were performed in a four flow cell Biacore T100 instrument (GE Healthcare). SPR bare gold sensor chips „SIA Kit Au" were from GE Healthcare. Upon removal from storage in an argon atmosphere, gold sensor surfaces were ultrasonicated in aceton and high purity ethanol (Merck) for 15 min, respectively, and dried in a nitrogen gas stream followed by 60 min UVO cleaning (Jelight Company Inc., Model 42A-220). The gold sensor surfaces were then ultrasonicated for another 15 min in ethanol, dried in a nitrogen gas stream an mounted on the sample holder for immediate SPR usage. The PBS running buffer was filtred and degased using filterware (Techno Plastic Products AG) of 0.2 um pore size. Immobilization of the molecular layers and initial BSA height measurements in the SPR instrument were performed at 35°C. For cloud point grafting (Emilsson et al., 2015) 0.6 mg of SH-PEG 20kDa ($M_w = 19$kDa according the manufacturer) (Laysan Bio Inc.) was dissolved in 50 ml of 0.9 M Na2SO4. The clean gold sensor surface was incubated with SH-PEG in flow cells 3-4 for 3h at 1 μl/min, then in flow cells 1-2 with 1mM of HS-$(CH_2)_{11}$-$(OCH_2CH_2)_3$-OH (Nanoscience) in PBS, 10% ethanol, for 20 min. This was followed by another 3 x 3h of SH-PEG incubation in flow cells 3-4, 3h of rinsing of all flow cells with PBS and 3 short injection of 5 mg/ml BSA in PBS. The flow was then increased to 10 μl/min and BSA titrations (3 x 30s with 60s interval) of BSA monomer and BSA dimer, respectively, were performed with each injection passing all cells sequentially. The average BSA response values where measured relative to PBS baseline obtained 30 s later for BSA monomer and BSA dimer, respectively. The initial injections at 35°C were then

followed by injetions of BSA monomer and BSA dimer at 25°C, 15°C, and 5°C, respectively. During the entire measurement the sample compartment temperature was kept at 15°C.

3.5 Results & Discussion

In Fig. 3.3A, triplet injections of BSA monomer and BSA dimer are shown for the sample cell (i.e. HS-PEG 20kDa) and the reference cell (i.e. HS-$(CH_2)_{11}$-$(OCH_2CH_2)_3$-OH), respectively. The relative decrease of the BSA response in the sample cell with respect to the reference cell allows us to determine the height of the PEG polymer brush in the sample cell (Schoch & Lim, 2013). The PEG molecules were immobilized prior to the BSA injections using the cloud-point grafting technique (Emilsson et al., 2015) at 35°C. The BSA dimer and BSA monomer species are injected at temperatures 35°C, 25°C, 15°C and 5°C, respectively, where each temperature change causes a shift in the baseline as seen in Figure 3.3A. At 35°C there is a slight but steady loss of PEG molecules over time. We can however minimize the effects of material loss when starting the height measurements at 35°C, such that all subsequent height measurements will involve approximately the same amount of PEG immobilized on the sensor surface. Figure 3.3B shows the measured thicknesses for a single sample cell using a single reference cell and a decay length $l_d = 300\ nm$ of the evanescent field suitable for PEG polymer brushes in our SPR setup (Schoch & Lim, 2013). This follows from $d = l_d/2 \times \ln(R1/R2) + d_{ref}$, where $R1$ and $R2$ are the BSA responses from the reference and sample cell,

respectively, d_{ref} is the height of the reference layer (i.e. $d_{ref} = 2\,nm$) (Palegrosdemange et al., 1991), and l_d is the decay length of the SPR evanescent field. As can be seen, the measured PEG brush height d decreases with temperature and increased heights are measured when using the BSA dimer d_{dimer} instead of the BSA monomer d_{mono}.
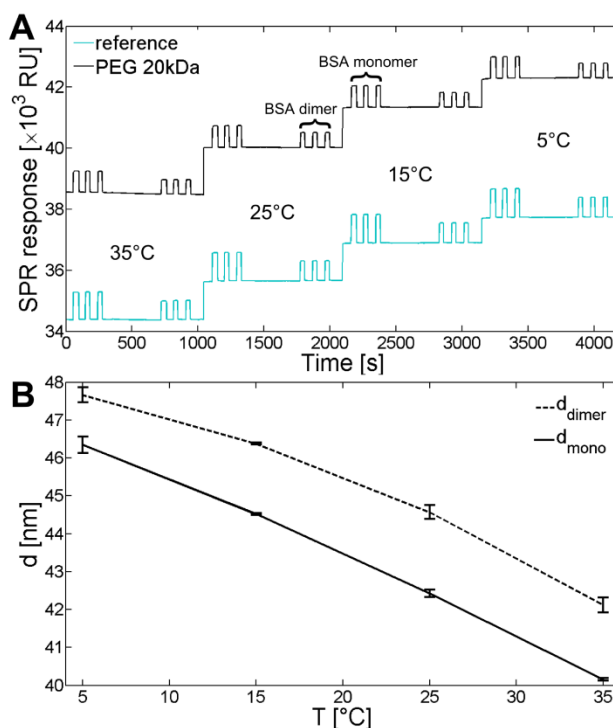
Fig. 3.3. (**A**) Exemplary SPR sensograms showing the injection of BSA monomer and BSA dimer triplets at temperatures 35°C, 25°C, 15°C and 5°C for a sample cell (i.e. HS-PEG 20kDa) (black) and a reference cell (i.e. HS-(CH₂)₁₁-(OCH₂CH₂)₃-OH) (gray), respectively. A decrease in temperature causes an upward shift in the SPR baseline. (**B**) Measured brush heights d from BSA monomer d_{mono} (solid line) and BSA dimer d_{dimer} (dashed line) injections, respectively, evaluated for the single sample cell and the single reference cell shown in figure (A).

The averaged thicknesses obtained for PEG 20kDa brushes from a total of 12 samples are shown in Figure 3.4A. The thicknesses were as well averaged over the two reference cells available per measurement. The average PEG grafting distance g_{PEG}

estimated from the immobilization responses is $g_{PEG} = 2.17 \pm 0.04 \, nm$ (see section 2.2.3). For the BSA monomer the measured height is $d_{mono} = 43.7 \pm 2.2$ nm at 5°C and monotonically decreases with temperature to $d_{mono} = 38.5 \pm 2.0$ nm at 35°C. The measured brush heights are in good agreement with previous measurements (both AFM and SPR) for cloud point grafting of HS-PEG 20kDa (Emilsson et al., 2015). Similarly for the BSA dimer, where however the measured brush heights d_{dimer} are slightly higher, indicating that the dimer is "penetrating" to a lower extent into the polymer brush. This trend is as expected from theory where the energetic penalty for inserting a non-interacting particle into a polymer brush F_{ins} is considered to scale with the size of the particle (Halperin et al., 2011; Egorov, 2012; Milchev et al., 2008; Ermilov et al., 2010; Merlitz et al., 2012; Yaneva et al., 2009). The average difference in the measured heights Δd (i.e., $\Delta d = d_{dimer} - d_{mono}$) is shown in Figure 3.4B. The difference is 0.70 ± 0.36 nm at 5°C and increases to 1.39 ± 0.73 nm at 35°C.
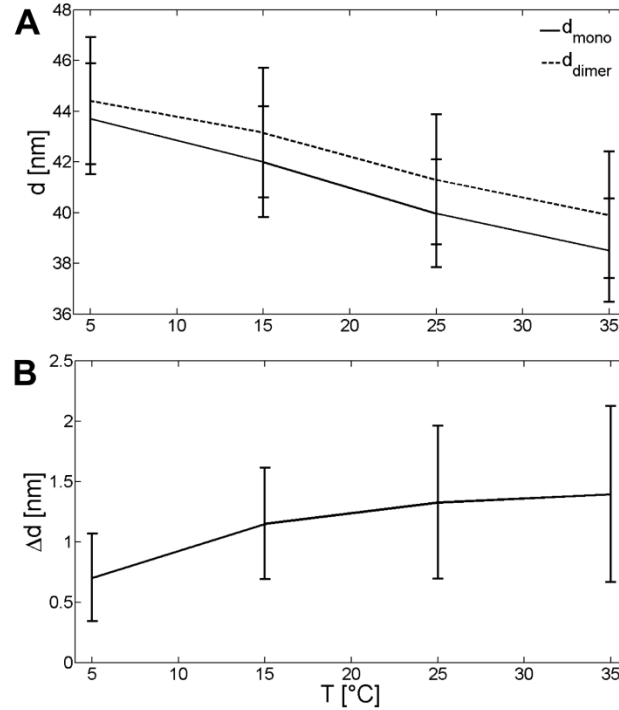
Fig. 3.4. (A) Measured brush heights d from BSA monomer d_{mono} (solid line) and BSA dimer d_{dimer} (dashed line), respectively. The heights are averaged over 12 samples and the two reference cells available per measurement, respectively. The measured brush height is decreasing with increasing temperature for both BSA monomer and BSA dimer, respectively. The decrease is about 5 nm or 10 % over the evaluated temperature range. **(B)** The BSA dimer injections yield consistently higher brush heights d where $\Delta d \approx 1\ nm$ (i.e. $\Delta d = d_{dimer} - d_{mono}$).

All measurements consistently reveal an increase in measured brush height when using the BSA dimer compared to the BSA monomer. No matter, the difference Δd is small for monomer and dimer species over the entire temperature range, i.e. $\Delta d \approx 1\ nm$, suggesting that the edge of the brush (as seen by the particles) is relatively abrupt such that both species are not penetrating much into the brush. Even though the temperature changes the optical constants and thus the decay length l_d of the evanescent field (i.e., here a constant $l_d = 300\ nm$ was used), this effect is minor over the temperature range investigated (see section 3.2). Nevertheless, the temperature effects are included into the reflectivity calculations in order to validate

the measured trend in brush height (see below). It is not entirely clear to us why Δd is increasing with temperature – most probably it is due to surface effects in the reference cell. The reference layer may lose part of its protein resistance below 11°C (Schwendel at al., 2001), however, for BSA molecules this effect is small at 5°C (Skoda et al., 2009). Such effects could cause a decrease of Δd at 5°C, whereas Δd is relatively stable when going from 15°C up to 35°C. Additionally, a decrease in the osmotic pressure of the polymer brush with temperature might contribute to the observed increase in Δd.

The decrease in brush height with temperature is rather surprising as PEG has an LCST above 100°C (Bae et al., 1991; Saeki et al., 1976). It seems however that already in the temperature range investigated (i.e. far off the LCST) the PEG brush undergoes a smooth conformational transition. This is in agreement with the classical polymer brush (in one dimension) where temperature sensitive binary interactions are stabilized by repulsive ternary interactions (Zhulina et al., 1991, Halperin & Kröger, 2011), and consistent with a steady loss in solvent quality with increasing temperature for PEG in aqueous solution (Dormidontova, 2002, Matsuyama & Tanaka, 1990). The decrease in brush height is also compatible with the shrinking of PEG polymer coils observed in dilute water solutions over a similar temperature range (Hammouda & Ho, 2007).

To further validate the measured trend in brush height with temperature we have

performed reflectivity calculations (Egkasit et al., 2004). In our reflectivity calculations (see sections 3.2 and 3.3) we use analytical polymer brush density profiles from SCF theory (Halperin et al., 2011) $\Phi(z) = \Phi_0(1 - z^2/H^2)^m$ where H is the unperturbed brush height and Φ_0 is the monomer volume fraction at $z = 0$. Solvent quality for PEG in bulk aqueous solution is reported to be at moderate good conditions (i.e. "marginal solvent") (Haynes et al., 1993; Edmond & Ogston, 1968; Rogers & Tam, 1977; Venohr et al., 1998; Eliassi et al., 1999). However, a recent study reports poor solvent conditions for PEG polymer brushes (Lee et al., 2015). We thus use $m = 1$ for good solvent and additionally we also investigate $m = 0.5$ for theta solvent in our calculations. The osmotic pressure then scales as $\Pi(z) \propto \Phi(z)^2$ for good solvent and $\Pi(z) \propto \Phi(z)^3$ for theta solvent, respectively, and the free energy $F_{osm}(z) \approx \Pi(z)R^3$ estimates the work expended upon inserting a particle against the osmotic pressure of the brush (Halperin et al., 2011). To avoid over-parametrization the m value is fixed, whereas we vary H and/or the osmotic pressure Π_0 at z = 0. For the size of the penetrating particles we use the hydrodynamic radii determined from dynamic light scattering, i.e. $R_{h,mono} = 3.13 \pm 0.32\,nm$ and $R_{h,dimer} = 4.13 \pm 0.19\,nm$, and spherical shape for simplicity. The corresponding hydrodynamic volumes are in well agreement with the more realistic ellipsoidal volume that was used to describe BSA (Abbott et al., 1992). The osmotic pressure Π_0 can be estimated from $\Pi = \alpha(k_B T/a^3)\Phi^{(9/4)}$ for bulk PEG where $\alpha = 0.8$ and $a = 0.35\,nm$ (Hansen et al., 2003). Taking Π_0 within the brush as it applies to bulk solutions is valid for theta solvents or marginal solvents at sufficiently high monomer densities, i.e. when the chains exhibit near ideal conformations (Rubinstein & Colby,

2003; Halperin & Kröger, 2009; Milner et al., 1988). For the monomer volume

fraction we use $\Phi_0 \approx 0.23$ obtained experimentally for PEG at similar grafting

density to ours (Schneck et al., 2015), this gives an estimated $\Pi_0 \approx 70 \cdot$

$10^{25} k_B T$ (J/m^3). Multiplied by the hydrodynamic volume of "spherical" BSA V_{BSA}

this gives an osmotic free energy penalty $F_{osm}(0) \approx V_{BSA} \cdot \Pi_0 \approx 90 k_B T$, which we

shall take as a reference value for deep BSA monomer insertion. In the case of non-

interacting particles the free energy for particle insertion is simply $F_{ins}(z) = F_{osm}(z)$.

In the calculations we then use $c_{BSA}(z) = c_0 \cdot exp[-F_{ins}(z)/k_B T]$, where c_0 is the

injected bulk BSA concentration, to obtain the BSA distribution within the brush

(Halperin & Kröger, 2011; Halperin et al., 2011) and simulate the respective SPR

response for injecting BSA. Via varying the osmotic pressure Π_0 and/or the brush

height H we can accordingly obtain the measured d_{mono} from the distribution of BSA

monomers. In Figure 3.5 (A) the insertion penalty $F_{ins}(0)$ is shown that is required to

obtain Δd (i.e., $\Delta d = d_{dimer} - d_{mono}$) in the measured brush height at $T = 25°C$.

The osmotic scaling $F_{ins} \propto (\Phi^3, R^3)$ for our assumed theta conditions is in agreement

within the uncertainty of our experimental data (dashed line in Fig. 3.5A). It suggests

$\Delta d \approx 1.45\ nm$ at the reference value, which is within the errorbars for $T = 15 -$

$35°C$ and is about the average measured at 35°C. However similar values are also

obtained for good solvent conditions, where $F_{ins} \propto (\Phi^2, R^3)$ and $\Delta d \approx 1.6$ at the

reference value (solid line in Fig. 3.5A). Both scalings reveal a sharp increase of

$F_{ins}(0)$ already above $\Delta d \approx 1\ nm$ consistent with experimental data and the

difference $\Delta R_h \approx 1\ nm$ in the BSA hydrodynamic radii. All together the measured

exclusion of BSA monomer and BSA dimer is in agreement with simple SCF scaling

theory (Halperin et al., 2011) for proteins of the size investigated and the osmotic approximation in either good or theta solvent. For PEG in aqueous solution it is reasonable to assume attractive BSA surface contributions $F_{ins} \propto (\Phi, R^2)$ as well (Steels et al., 2000). The adsorption free energy of $-\epsilon k_B T$ for a monomer in contact with the protein surface is however weak with a positive $\epsilon \ll 1$ (Halperin & Kröger 2009). In Figure 3.5B we therefore also consider attractive surface contributions $F_{att}(z) \approx -\epsilon \Phi(z)(R/a)^2$ with $\epsilon \approx 0.001 - 0.05 \ k_B T$ additionally to an osmotic contribution with $F_{osm}(0) = 90 k_B T$. The free energy for particle insertion is then defined as $F_{ins}(z) = F_{osm}(z) + F_{att}(z)$. The attractive term depends on the monomer size a for PEG about which there is no consensus in literature (Halperin & Kröger, 2009). Here we use $a = 0.41$ nm (Schneck et al., 2013) to stay in agreement with $\phi_0 \approx 0.23$ (Schneck et al., 2015) and $\epsilon = 0.05 \ k_B T$ determined for the BSA – PEG interaction (Abbott et al., 1992). The calculations reveal that Δd decreases with increasing ϵ due to the larger surface area of the BSA dimer. The value of $\epsilon = 0.05 \ k_B T$ measured for the BSA – PEG interaction in bulk solution (Abbott et al., 1992) is still compatible with the experimental $\Delta d \approx 1 \ nm$ for good solvent conditions (i.e. when $m = 1$). On the other hand for theta solvent conditions (i.e. when $m = 0.5$) the reference value $\epsilon = 0.05 \ k_B T$ would lead to a negative Δd, though it is possible that the interaction term ϵ is different for a polymer brush than in a bulk dilute polymer solution (Abbott et al., 1992). The negative Δd obtained for theta solvent results from an increase in PEG monomer density at the edge of the brush with respect to good solvent conditions. The brush heights H that lead to d_{mono} are shown in Figure 3.5C for the repulsive case $F_{ins}(0) = 90 k_B T$ (for good and theta

solvent) as well when including an attractive term $\epsilon = 0.05 \, k_B T$ (for good solvent).

Importantly, this also takes into account temperature corrections to the SPR dielectric

constants (except for the unknown behavior of PEG) (see section 3.2). The calculated

brush heights H are consistently decreasing in each scenario, whereas BSA

monomers and dimers are almost entirely excluded from the brush as seen by the

values of d_{mono} and d_{dimer}, respectively. This is in agreement with the adsorption of

IgG to the edge of dense PEG brushes as measured by neutron reflectometry

(Schneck et al., 2015). In the presence of an attractive term $\epsilon = 0.05 \, k_B T$ the brush

height H increases. This is due to the accumulation of BSA molecules at the edge of

the brush rather than BSA penetration (see Figs. 3.6 and 3.7). Importantly the

measured decrease in brush height with temperature can not be explained from

particle penetration due to a decrease in osmotic pressure with temperature, as this

would necessitate a dramatic decrease in Π_0 and would cause a pronounced increase

in Δd that is inconsistent with our measurements (see below). The true scaling at the

edge of the brush may involve additional unknown scaling laws (Ermilov et al.,

2010). It is however not within the scope of the experimental precision for making a

more accurate prediction about the scaling laws. Neither does our analysis include

polymer brush tail effects (Currie et al., 2003) and polydispersity as encountered in

real brushes as well as the non-spherical shape of the BSA molecules (Abbott et al.,

1992). We also note that the measured smooth conformational transition in brush

height with temperature does not exclude the possibility of a narrow collapse

transition at higher monomer concentrations and/or temperatures due to attractive n-

body interactions (Hu & Wu, 1999).
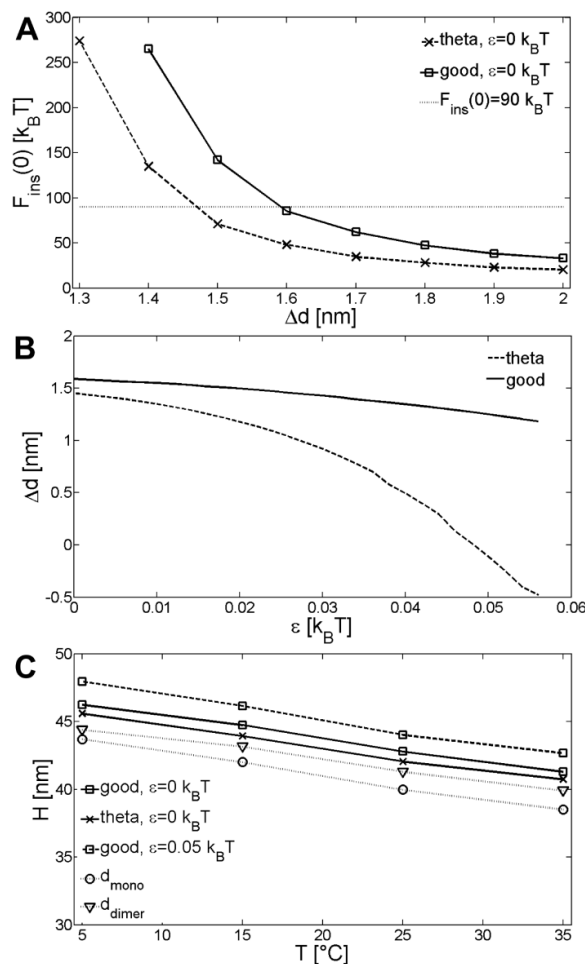
Figure 3.5. (A) Calculated Δd at $T = 25°C$ for the osmotic term $F_{osm}(z) \approx \Pi(z)R^3$ for good ($\Pi(z) \propto \Phi(z)^2$) (solid line) and theta ($\Pi(z) \propto \Phi(z)^3$) (dashed line) solvent conditions. The reference value $F_{ins}(0) = F_{osm}(0) = 90 k_B T$ for BSA monomer insertion is indicated by the dotted line. The calculations are performed using SCF monomer density profiles. The reference value $F_{ins}(0) = 90 k_B T$ leads to $\Delta d \approx 1.45 \ nm$ in theta solvent and $\Delta d \approx 1.6 \ nm$ in good solvent, respectively, in agreement with experimental results. **(B)** Calculated Δd for a brush with $F_{osm}(0) = 90 k_B T$ and an attractive surface term $F_{att}(z) \approx -\epsilon\phi(z)(R/a)^2$ where now $F_{ins} = F_{osm} + F_{att}$. Theta solvent conditions (dashed line) are not compatible with the literature value $\epsilon = 0.05 \ k_B \ T$ as this leads to a negative Δd. **(C)** Brush height H obtained for the SCF density profile with $F_{osm}(0) = 90 k_B T$ for conditions $\epsilon = 0.05 \ k_B \ T$ (dashed lines) and $\epsilon = 0 \ k_B \ T$ (solid lines) as well as good and theta solvent, respectively. The BSA monomer and BSA dimer (shown as d_{mono} and d_{dimer} (dotted lines)) are almost entirely excluded from the brush. Using an attractive surface term the brush height H however increases relative to the measured values d_{mono} and d_{dimer}, respectively, due to the accumulation of BSA molecules at the edge of the brush. The calculations include corrections in the SPR layer dielectric constants with temperature.
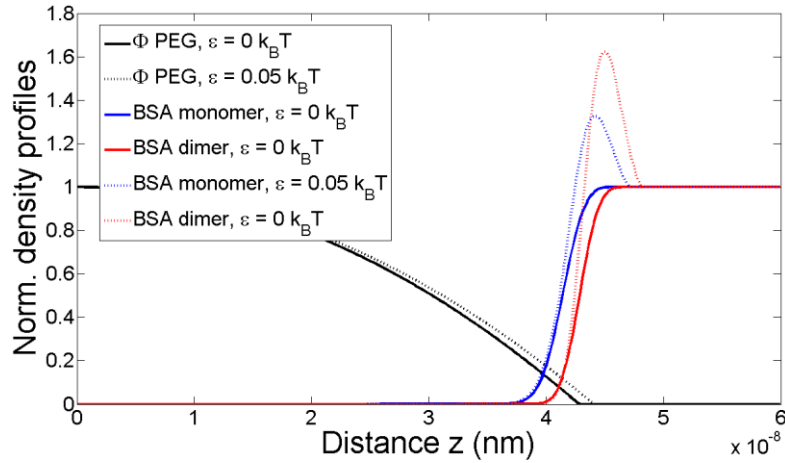
Fig. 3.6. BSA distribution in *good solvent* for the brush heights shown in Fig. 3.5C at $T = 25°C$. Here the two conditions $\epsilon = 0\ k_BT$ and $\epsilon = 0.05\ k_BT$ lead to the same d_{mono} and only slightly different Δd. The attractive term $\epsilon = 0.05\ k_BT$ however leads to a redistribution of BSA molecules at the edge of the brush and thus the brush height H is slightly higher in order to obtain the same d_{mono} as for $\epsilon = 0\ k_BT$.
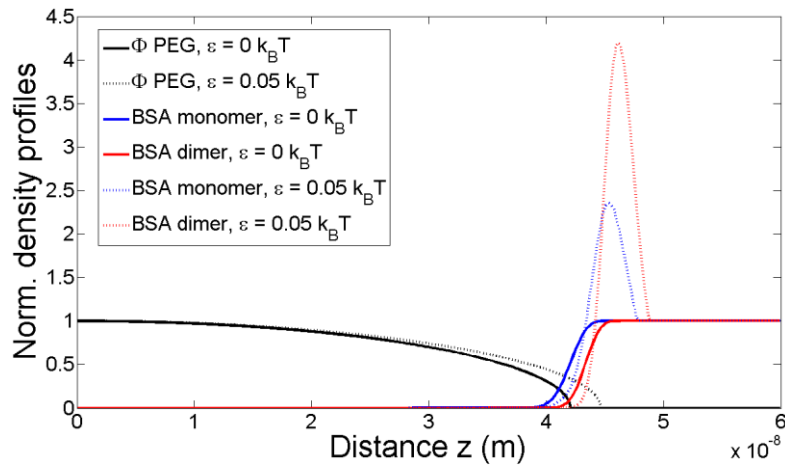
Fig. 3.7. BSA distribution in *theta solvent* for the brush heights shown in Fig. 3.5C at $T = 25°C$. Here the two conditions $\epsilon = 0\ k_BT$ and $\epsilon = 0.05\ k_BT$ lead to the same d_{mono} but different Δd values, i.e. Δd for the attractive $\epsilon = 0.05\ k_BT$ is even negative. The attractive term $\epsilon = 0.05\ k_BT$ leads to a pronounced redistribution of BSA molecules (especially the dimers) at the edge of the brush and thus the brush height H is higher in order to obtain the same d_{mono} as for $\epsilon = 0\ k_BT$.

Instead of fixing the osmotic pressure at the reference value $\Pi_0 = 70 \cdot 10^{25}(J/m^3)$ we also fixed the brush height in the calculations to clarify if the reduction in d_{mono}

could be explained by a decrase in osmotic pressure alone and thus an increase in BSA penetration with temperature. Here the brush height is fixed to $H = 46.25\ nm$, i.e. the brush height determined for $\Pi_0 = 70 \cdot 10^{25}(J/m^3)$ at $T = 5°C$ (see Fig. 3.8A). In the calculations the osmotic pressure Π_0 was then varied in order to obtain d_{mono} for each temperature. As shown in Fig. 3.8B for good solvent conditions this would necessitate a drastic decrease in the osmotic pressure of the brush, which is not compatible with a constant brush height. Additionally this would lead to an increase in Δd that is not compatible with our experimental results (see Fig. 3.8C).
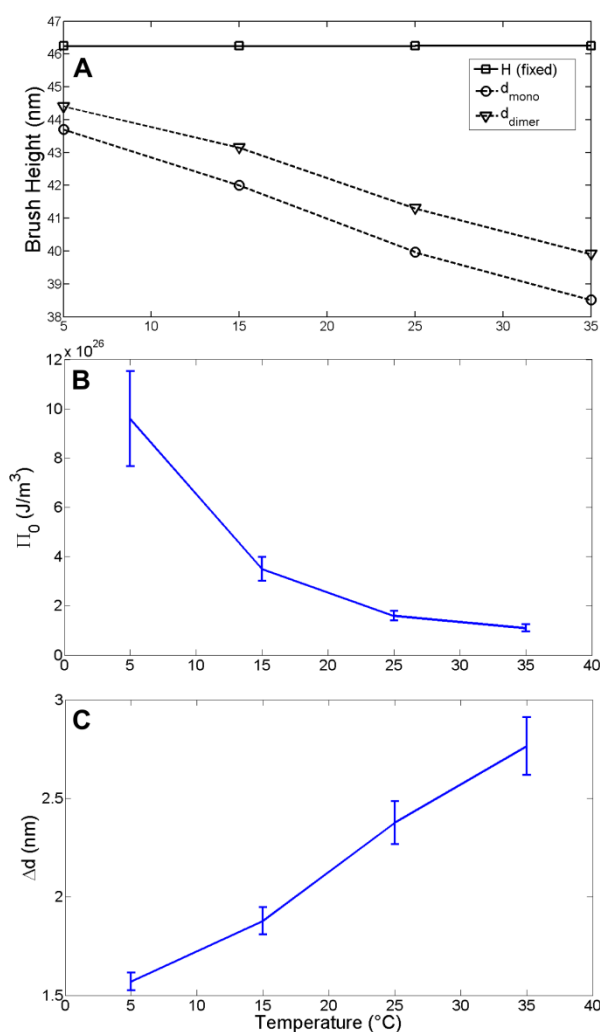
Fig. 3.8. (A) Brush height measured for BSA monomers d_{mono} and BSA dimers d_{dimer} as well as assuming a fixed brush height H in the calculations. **(B)** Osmotic pressure Π_0 used in the calculation to obtain d_{mono} from the BSA distribution for good solvent. **(C)** Resulting Δd from the calculations, for good solvent.

Chapter 4

Conformational characterization of FG domains

Parts of this chapter were published in Schoch et al., 2012, and Kapinos & Schoch et al., 2014.

In this chapter the technique of noninteracting molecules is extended to probe stepwise conformational changes in FG nucleoporins upon binding of karyopherin-β1 (Kapβ1). It is divided into two parts. The first part is dedicated to surface-tethered Nup62 FG domains. Here, BSA titrations are revealing a collapse caused by Kapβ1 binding at low concentrations, that gradually transitions into a reextension at higher Kapβ1 concentrations. This ability to self-heal is directly coupled to Kapβ1-FG binding avidity that promotes the maximal incorporation of Kapβ1 into the FG domain layer. At physiological concentrations of Kapβ1, the „pile-up" of Kapβ1 molecules in the extended layer is supporting weak binding to unoccupied FG repeats at the periphery of the layer. Thus for surface-tethered Nup62 FG domains, binding avidity does not hinder fast transport *per se*. These results were previously published in Schoch et al., 2012.

In the second part of this chapter the same analysis is extended to the FXFG domains of Nup214, and Nup153 as well as the GLFG domain of Nup98. While the FXFG domains have the capacity to extend and accommodate large numbers of Kapβ1 molecules, the more cohesive GLFG domain of Nup98 forms a cohesive layer that is

only partially penetrable by Kapβ1 and thus unable to extend and form Kapβ1 multilayers. These results were previously published in Kapinos & Schoch et al., 2014. At the end of this chapter, implications of the results are discussed on the molecular and NPC level and limitations as well as possible error sources of the SPR technique are analyzed.

4.1 Basics & Theory

4.1.1 The polyelectrolyte polymer brush

For polyelectrolyte brushes the picture is more complex as brush height needs to be linked to the fraction of charged monomers α and the ionic strength of the solution φ_s (Pincus, 1991; Tran et al., 1999; Bright et al., 2001). In the osmotic regime that is predicted for dense and strongly charged brushes, the brush height H does not depend on the grafting density, but rather on the osmotic pressure of counterions confined inside the brush. For a low degree of charges and sparse grafting as well as in the "weak screening" limit the brush height is given by

$$H \approx 2\pi l_B \alpha^2 \sigma^{-1} b^2 N^3 \tag{4.1}$$

where l_B is the Bjerrum length. With addition of salts the regime changes due to a reduction in counterion osmotic pressure. In the "strong screening" regime the equilibrium condition gives

$$H \approx \left(\frac{\alpha^2 b^2}{\varphi_s \sigma}\right)^{1/3} bN \tag{4.2}$$

The scaling expression for the brush height $H \sim N\sigma^{-1/3}$ is again the same as for the neutral brush and the salt concentration φ_s has inverse influences on the brush height.

4.1.2 Polymer brush morphology and particle binding

Recent theoretical studies consider the attractive-binding of particles to a polymer brush. If the particles are attracted to the polymers the presence of nanoparticles can induce large morphological transitions of the layer (Opferman et al., 2011). For small particles of size of a monomer the brush morphology changes as a function of particle concentration in solution c_0 and interaction energy $\chi(\varepsilon_b)$ between nanoparticles and the polymers. For very weak interaction energies at high particle concentrations the brush height is increasing. For sufficiently strong interactions and at moderate concentrations a decrease in brush height occurs via a smooth decrease (for weaker binding) or a first-order phase transition, i.e. collapse (for stronger binding), followed by a swelling at higher concentrations. If the size of the particles increases the effects are very similar, with compression and recovery of the brush height at increasing concentrations (Opferman et al., 2013). The compression of the brush allows for an increase in monomer particle contacts, whereas the swelling at high concentrations allows the layer to accommodate additional nanoparticles. The SCF calculations, in contrast to the simpler mean-field analogon, do not predict a phase transition but a rapid and continuous decrease of layer height for small particles of monomer size, and if the nanoparticle size increases to a larger volume, the transition region of brush height compression becomes broader. The layer density profiles for high binding strength also show distinct regimes depending on concentration and size of the nanoparticles. For small particle size at low solution concentrations the particles infiltrate the layer but cause only a small perturbation to the parabolic density profile of the monomers, whereas for high particle concentrations, in the compressed state, the density of both monomers and particles are close to a step function. The formation of the dense state typically starts with the formation of a thin band of high density near the grafting surface. The behavior of the system changes for large particles

and/or low grafting distance of the polymers. Then the energy penalty for penetration is not compensated via the binding interactions and as a consequence the particles only penetrate the top most, diluted region of the brush. At high concentrations the particles progressively infiltrate the layer but the profile shows increasing nanoparticle density towards the top of the brush. In this regime the height of the layer as well as the monomer density profile do not change much as a result.

4.1.3. Equilibrium constant & Langmuir isotherm

In case of an interaction taking place at the sensor surface one has to distinguish between the immobilized ligand L and the analyte in solution A. Complex formation LA can then be described in a second order reaction model:

$$L + A \underset{k_d}{\overset{k_a}{\rightleftarrows}} LA \tag{4.3}$$

were the time dependence of the complex concentration $[LA]$ can be expressed as the summed effects of complex formation and dissociation

$$\frac{d[LA]}{dt} = k_a[L][A] - k_d[LA] \tag{4.4}$$

where k_a is called the association rate constant and k_d is called the dissociation rate constant. In terms of SPR, the complex concentration $[LA]$ equals the measured binding response R (in RU) and the free ligand concentration $[L]$ can be replaced by $(R_{max} - R)$, where R_{max} is the response at full saturation of the sensor surface (Sundberg et al., 2007). Additionally, due to the replenishing analyte flow and the

high number of analyte molecules in solution compared to the amount of ligand at the surface, the analyte concentration is technically held constant, i.e. $[A] = c$, and we obtain for Eq. 3.4

$$\frac{dR}{dt} = k_a c (R_{max} - R) - k_d R \tag{4.5}$$

Eq. 3.5 is formally identical to the equation describing a first order reaction in solution and is therefore usually referred to as pseudo first-order reaction in solution (Stepanek et al., 2006). After a sufficiently long time dR/dt becomes zero and an equilibrium response $R = R_{eq}$ is achieved. Thus rewriting Eq. 3.5 gives the Langmuir isotherm

$$R_{eq} = \frac{c \cdot R_{max}}{K_D + c} \tag{4.6}$$

where

$$K_D = \frac{k_d}{k_a} = \frac{[L][A]}{[LA]} \tag{4.7}$$

is the equilibrium dissociation constant and can be determined by measuring the dependence of the sensor equilibrium response R_{eq} on the injected analyte concentration c. K_D is often also referred to as the binding affinity.

4.2 Quantifying Kapβ1 binding

For the binding of Kapβ1 to the FG domains using SPR, the quantification of bound Kapβ1 molecules is based on the relation $1300\ RU = 1\ ng/mm^2$ for protein binding

to a planar sensor surface (see section 2.2.3). The hydrodynamic diameter of Kapβ1 measured in PBS is $\sigma_{Kap\beta1} = 12.06 \pm 2.09\ nm$. This is in agreement with SAXS data where maximal dimension of a Kapβ1 molecule in aqueous solution is $D_{max} = 12\ nm$ and the radius of gyration $R_g = 3.9\ nm$, respectively (Forwood et al., 2010). Since Kapβ1 can be approximated as a homogeneous ellipsoid, its semi-minor axis can be evaluated from SAXS data according to $R_g = [a^2 + b^2 + c^2]/5$, where a, b, and c correspond to the two semi-minor axes and the semi-major axis of an ellipsoid, respectively (Feigin & Svergun, 1987). With $c = 6\ nm$, $R_g = 3.9\ nm$ and assuming a and b to be of equal width, this gives 4.5 nm for each semi-minor axis, respectively. From these values the volume occupied by such an ellipsoid is $V \approx 500\ nm^3$, which is equivalent to a sphere with a diameter $d \approx 10\ nm$. If the Kapβ1 spheres arrange in a square lattice, the surface density $\rho_{Kap\beta1}$ in Da/nm^2 is

$$\rho_{imp\beta} = M_w / \left(g_{Kap\beta1}\right)^2 \tag{4.8}$$

and with $M_w = 98'000\ Da$ for Kapβ1, and $g_{Kap\beta1} = 10\ nm$ (equal to the sphere diameter), this gives $\rho_{Kap\beta1} \approx 1000\ Da/nm^2$ for a Kapβ1 monolayer. If we sum up the masses for a Kapβ1 monolayer to $1\ mm^2$ this gives $1 \times 10^{15}\ Da$ or $1.66\ ng$, and using the relation $1300\ RU = 1\ ng/mm^2$ we find that a monolayer of Kapβ1 equals a sensor response of approximately $2200\ RU$.

4.3 Materials & Methods

The cysteine-modified FG domain constructs used in this chapter are: Nup214 (aa 1809-2090; partial FXFG domain), Nup62 (aa 1-240; full length FXFG domain), Nup98 (aa 1-498; full length GLFG domain), and Nup153 (aa 874–1475; full length FXFG domain). For clarity, these are termed cNup214, cNup62, cNup98 and

cNup153, respectively. From dynamic light scattering (DLS) analysis, their measured hydrodynamic radii (r_h) are 3.4 ± 1.5 nm (cNup214), 3.7 ± 1.7 nm (cNup62), 5.6 ± 1.6 nm (cNup98) and 5.1 ± 3.2 nm (cNup153).

Briefly, the SPR experiments use BSA molecules, which act as inert *non-interacting* probes that naturally "feel" the intrinsic exclusion volume of the FG domains (i.e., thickness) (Fig. 4.1A). A comprehensive description of the method and related calculations can be found in chapter 2. A first BSA injection provides the initial FG domain layer thickness (d_{cNup}; Fig.4.1B), using the expression

$$d_{cNup} = \frac{l_d}{2} ln \left(\frac{R_{ref}}{R_{BSA}} \frac{m_{BSA}}{m_{ref}} \right) + d_{ref} \qquad (4.9)$$

where $l_d = 350 \, nm$ is the characteristic evanescent field decay length, R_{BSA} is the BSA-SPR response from the FG domain measurement cell where m_{BSA} is a calibration constant, R_{ref} is the BSA-SPR response for a reference cell (not shown) where m_{ref} is a calibration constant, and $d_{ref} = 2 \, nm$ is the thickness of a 1-Mercapto-11-undecyltetra(ethyleneglycol) (i.e., HS-$(CH_2)_{11}$-$(OCH_2CH_2)_3$-OH) passivating layer in the reference cell. To calculate the inter-FG domain grafting distance from the SPR response (R_{cNup}), Eq. 2.54 is applied. In this manner, we are able to determine how the grafting distance between FG domains (g_{cNup}) affects d_{cNup}.

Once d_{cNup} and g_{cNup} are established, subsequent BSA injections are used to monitor *in situ* changes in the layer thickness as caused by Kapβ1-FG binding interactions at increasing Kapβ1 concentrations. This is defined as $d_{cNup \cdot Kap}$ and follows directly from Eq. 3.9 (replacing d_{cNup}) by measuring R_{BSA} after each consecutive Kapβ1 injection (Fig. 4.1C). Likewise, the average distance between

bound Kapβ1 molecules g_{Kap} at each respective Kapβ1 concentration can be obtained using Eq. 3.9 (using R_{Kap} instead of R_{cNup}).
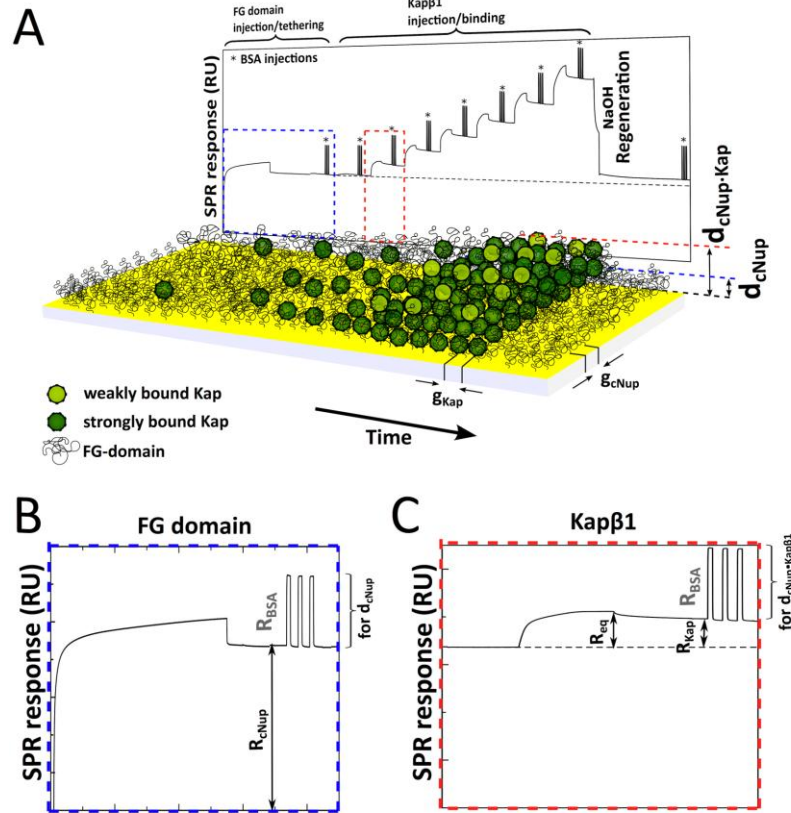
Fig. 4.1. SPR methodology and measured parameters. **(A)** A typical experimental sequence starts with the surface tethering of the FG domains followed by titrations of increasing Kapβ1 concentrations. Triple BSA injections (*) are used to determine FG domain layer thickness prior to (d_{cNup}) and after each Kapβ1 injection ($d_{cNup \cdot Kap}$). An increase in RU corresponds to increased Kapβ1-FG domain binding as depicted. A terminal NaOH "regeneration" step ensures that Kapβ1 is biochemically bound to the FG domains. **(B)** Zoom-in of the dotted box in (A). R_{cNup} corresponds to the surface tethered FG domains and is used to calculate the inter-FG domain grafting distance (g_{cNup}). d_{cNup} is calculated from the BSA response (R_{BSA}). **(C)** Zoom-in of the dashed box in (A). R_{eq} corresponds to Kapβ1-FG domain binding equilibrium at each respective Kapβ1 injection concentration. R_{Kap} is used to extract the next-neighbor distance of bound Kapβ1 molecules (g_{Kap}) prior to the BSA injections (R_{BSA}), which is then correlated to $d_{cNup \cdot Kap}$.

Sequence of FG domain fragments and purity of expressed proteins
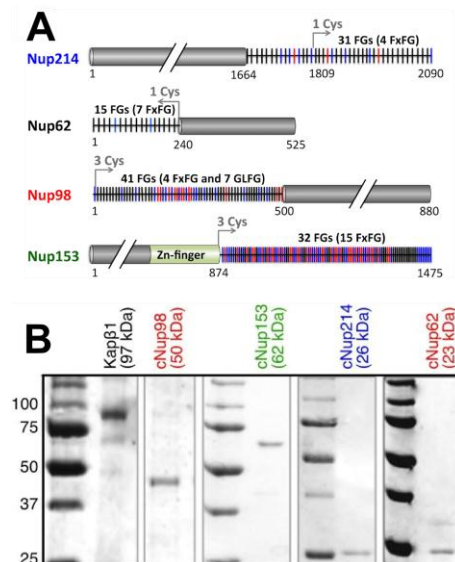
Fig. 4.2. (A) FG domain fragments used in this study. **(B)** 12 % PAGE (0.1 % SDS) of Kapβ1 and vertebrate FG domain fragments (cNups).
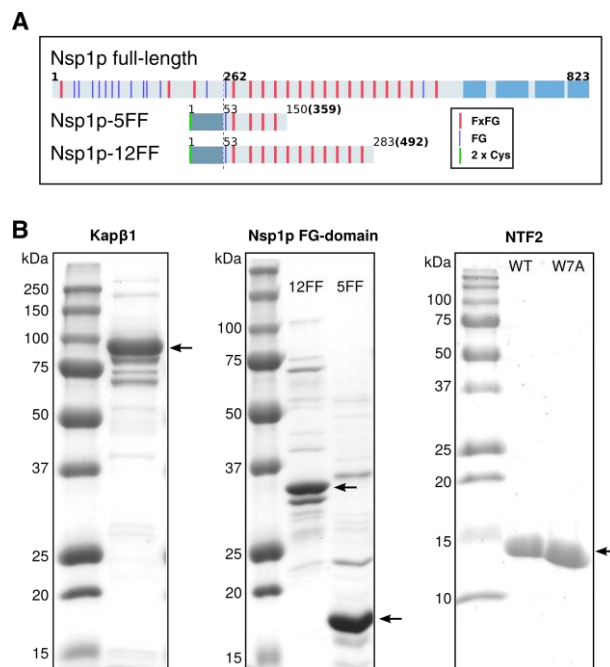
Fig. 4.3. (A) Nsp1 FG domain fragments, fragment 12 FF was used in this study. Residue numbers in bold correspond to full-length Nsp1p. The fragments contain a 52-residue 2xCys-/6xHis-/S-tag at their N-termini. **(B)** 6% PAGE (0.1% SDS) of Kapβ1, 15% PAGE (0.1% SDS) of Nsp1p FG domain fragments Nsp1p-12FF and Nsp1p-5FF, and 15% PAGE (0.1% SDS) of NTF2 and W7A-NTF2, respectively.

Materials

10 mg/ml BSA ($\geq$ 98%, Sigma-Aldrich) was carefully dissolved in phosphate buffered saline (PBS) pH 7.2 (Invitrogen). $HS\text{-}(CH_2)_{11}\text{-}(OCH_2CH_2)_3\text{-}OH$ (abbreviated as $C_{17}H_{36}O_4S$) (nanoScience Instruments, US) was dissolved until reaching 10 mM in ethanol and diluted with PBS to 1 mM before experimentation.

SPR Measurement Protocol

All SPR measurements were performed at 25°C in a four flow cell Biacore T100 instrument (GE Healthcare) where two flow cells were used as reference and the remaining two flow cells as sample cells. SPR bare gold sensor chips 'SIA Kit Au' were from GE Healthcare. Upon removal from storage in an argon atmosphere, gold sensor surfaces were ultra-sonicated in acetone and high purity ethanol (Merck) for 15 min respectively and dried in a nitrogen gas stream followed by 60 min UVO cleaning (Jelight Company Inc., Model 42A-220). The gold sensor surfaces were then ultra-sonicated for another 15 min in ethanol, dried in a nitrogen gas stream and mounted on the sample holder for immediate SPR usage. The clean gold sensor surface was incubated with cNup62, cNup153, cNup98, or cNup214 in PBS in flow cell 3-4, respectively. The incubation time was varied from 10 min up to 1 h at a flow rate of 2 μl/min to obtain different cNup grafting distances g_{cNup} (i.e., surface density). This was followed by a 120 s exposure to 1 mM $C_{17}H_{36}O_4S$ (nanoScience Instruments, US) to prevent unspecific binding to gold. Flow cell 1-2 was incubated with 1 mM $C_{17}H_{36}O_4S$ for 30 min at a flow rate of 2 μl/min. BSA titrations (3 x 30 sec with 60 s interval) after each Kapβ1 concentration followed at a flow rate of 10 μl/min with each injection passing all cells sequentially (6 min after each Kapβ1 injection). Average R_1 and R_2 values were measured at the end of each BSA injection cycle relative to the PBS baseline obtained 30 s later. The PBS running buffer was filtered and degassed using filterware (Techno Plastic Products AG) of 0.2 μm pore size. Kapβ1 was injected for 10 min at a flow rate of 10 μl/min at concentrations of

0.0001/ 0.0005/ 0.001/ 0.01/ 0.02/ 0.03/ 0.04/ 0.0625/ 0.125/ 0.25/ 0.5/ 1/ 2/ 4/ 8/ 13.4 µM although this could vary for different experiments.

4.4 Surface tethered FG domain characterization

Summarized in Fig. 4.4 is the dependence of d_{cNup} on g_{cNup}. A general feature found for all four FG domains is that their layer thicknesses increase as g_{cNup} decreases. For brevity, the analysis considers two regimes: (i) "brush" where $g_{cNup} < r_h$; and (ii) "mushroom" where $g_{cNup} > r_h$. In the brush regime, the FG domains have a tendency to extend from the surface obeying the scaling behavior of polyelectrolytic intrinsically disordered proteins (Solmaz et al., 2011). By definition, brush formation occurs when surface-tethered polymeric chains stretch away from their anchoring sites due to lateral crowding. This does not mean to preclude the existence of intra- or inter-FG domain interactions, which depends on the intrinsic physicochemical properties of each FG domain (e.g., hydrophobicity and charge (Yamada et al., 2010)). Brush formation in the close-packed regime is apparent for the non-cohesive FXFG domains of cNup214, cNup62 and cNup153, which reach maximal thicknesses of $d_{cNup} \sim 20\,nm$ respectively, at the smallest obtainable grafting distances. In contrast, cNup98 exhibits a limited extension in the close-packed regime in spite of its relatively large amino acid composition (498 aa) and r_h, which come closest to cNup153 (602 aa). Yet, cNup98 exhibits a maximum thickness of ~11 nm when $g_{cNup} = 4\,nm$, which is approximately half the thickness of cNup153 at the same grafting distance. This indicates that cNup98 is inherently more compact and cohesive in comparison to the other FXFG domains (Xu et al., 2013; Labokha et al., 2013).
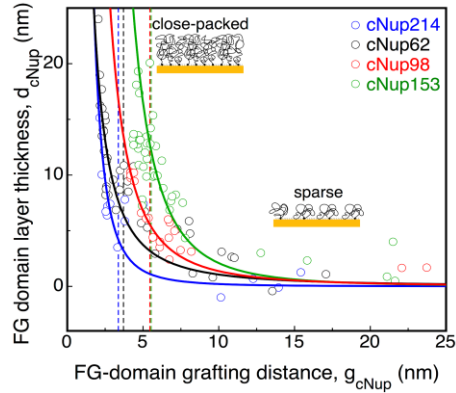
Fig. 4.4. Dependence of layer thickness (d_{cNup}) on FG domain grafting distance (g_{cNup}) for cNup214, cNup62, cNup98 and cNup153. Dashed lines that follow below each respective symbol correspond to the measured hydrodynamic radius (r_h) of each FG domain (see Methods).

4.5 Conformational changes in FG domains and Kapβ1 avidity

3.5.1 A case study: Non-monotonic cNup62 behavior

Shown in Fig. 4.5A is a representative SPR measurement where $d_2(initial) = 14.1\,nm$ for $g_{cNup} = 2.4\,nm$. Given that $d_2(initial) > \sigma_{cNup62}$ and $g_{cNup62} < \sigma_{cNup62}$, where σ_{cNup62} (= 8.5 nm) is the hydrodynamic size of cNup62, indicates that the FG domains form an extended molecular brush (Lim et al., 2006). For calculating Δd, $\rho_{Kap\beta1}$ and $g_{Kap\beta1}$ for sixteen titrations of $c_{Kap\beta1}$ increasing from 0.1 nM to 13.4 µM, striking non-monotonic phase behavior emerges when Δd is plot against $\rho_{Kap\beta1}$ (Fig. 4.5B): (1) up to $c_{Kap\beta1} = 40\,nM$, Δd declines sharply (i.e., negative height change) reaching a minimum at $\rho_{Kap\beta1} = 29.9\,Da/nm^2$ ($g_{Kap\beta1} = 55.5\,nm$); (2) Δd undergoes a gradual increase that crosses over $\Delta d = 0$ at $\rho_{Kap\beta1} = 1010\,Da/nm^2$ ($g_{Kap\beta1} = 9.8\,nm$) at $c_{Kap\beta1} = 4\,\mu M$; and (3) Δd increases steadily (i.e., positive height change) till $\rho_{Kap\beta1} = 1443.6\,Da/nm^2$ ($g_{Kap\beta1} = 8.2\,nm$) at the maximum $c_{Kap\beta1} = 13.4\,\mu M$. Further evidence of these transitions can be drawn

from correlations with Kapβ1-FG binding activity. In Fig. 4.5C, the quality of a single component Langmuir isotherm fit (χ^2) to R_{eq} deteriorates once $c_{Kap\beta1}$ is increased past 4 μM, where $K_D \sim 400\,nM$. Conversely, χ^2 is minimized by a two component fit over the entire $c_{Kap\beta1}$ range giving $K_{D1} = 347\,nM$ and $K_{D2} = 95.9\,\mu M$, which suggests that a low affinity-binding phase emerges at higher $c_{Kap\beta1}$ values. For comparison, a single component fit giving $K_D = 1.28\,\mu M$ appropriately describes Kapβ1-FG binding to sparse non-brush-like cNup62 "mushrooms" (Fig. 4.5C inset; $g_{cNup62} = 11.0\,nm$ and $d_2(initial) = 2.5\,nm$). As depicted in Fig. 4.6, the steep negative decline ($\Delta d < 0$) is most likely caused by a local collapse of cNup62 around Kapβ1 due to multivalent Kapβ1-FG interactions. In Phase 2, the "recovery" in Δd is a consequence of in-layer steric crowding as caused by a further addition of Kapβ1, which rearranges the FG domains into more entropy-favoring conformations. Subsequent crossover occurs ($\Delta d \to 0$; $c_{Kap\beta1} = 4\,\mu M$) when $\rho_{Kap\beta1} = 1010\,Da/mm^2$ which closely approximates the expected surface density of a packed Kapβ1 monolayer ($\sim$ 1000 Da/nm^2) (see section 4.2). Referring to Fig. 4.5C, $K_{D1} = 347\,nM$ is relatively strong up till this point owing to maximal Kapβ1-FG binding within the cNup62 layer. However, correlating $\Delta d > 0$ and $K_{D2} = 95.9\,\mu M$ in Phase 3 indicates the formation of a weakly bound secondary "pile up" layer when excess Kapβ1 binds to unoccupied FG domain regions that protrude from the cNup62 layer.
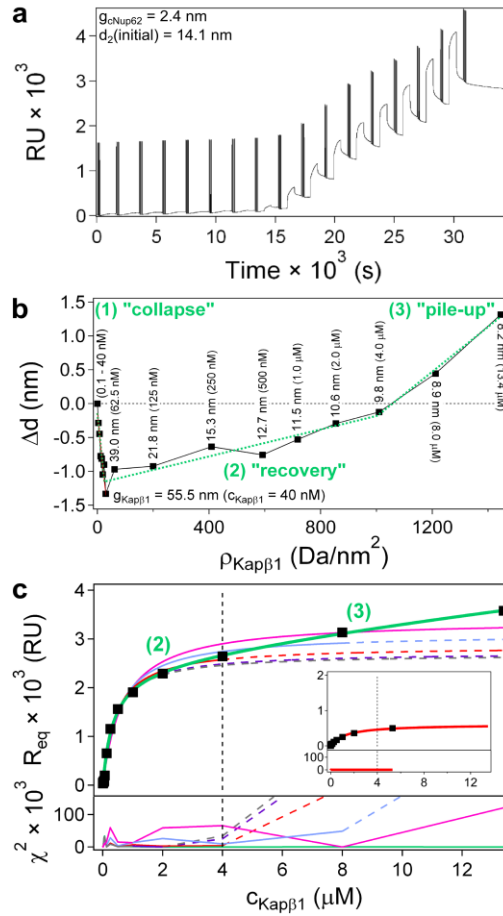
Fig. 4.5. Non-monotonic behavior in a cNup62 brush due to Kapβ1-FG binding. **(A),** Successive 3 x 30s BSA injections follow sixteen $c_{Kap\beta1}$ titrations ranging from 0.1 nM to 13.4 μM on a cNup62 brush characterized by $g_{cNup62} = 2.4\, nm$ and $d_{2(initial)} = 14.1\, nm$. **(B),** The cNup62 brush undergoes (1) collapse at low $\rho_{Kap\beta1}$ followed by (2) "recovery" that reaches (3) "pile-up" upon crossing $\Delta d \approx 0$. $g_{Kap\beta1}$ and $c_{Kap\beta1}$ (in parentheses) correspond to individual Δd measurements. **(C),** The steady state (R_{eq}) SPR response across the entire $c_{Kap\beta1}$ range (from a; 0.1 nM to 13.4 μM) is optimally fit using two Langmuir isotherms (green) giving $K_{D1} = 347\, nM$ and $K_{D2} = 95.9\, \mu M$. For single fits (K_D of approximately 400 nM), χ^2 is minimized at low terminal $c_{Kap\beta1}$ values (grey, purple and red) but deviates past $c_{Kap\beta1} > 4\, \mu M$ (blue and pink) for single fits. Solid and dashed lines denote the actual fitted $c_{Kap\beta1}$ range and the predicted K_D behavior, respectively. (inset) A single $K_D = 1.28\, \mu M$ is found for Kapβ1 binding to sparse cNup62 "mushrooms" (where $g_{cNup62} = 11.0\, nm$ and $d_{2(initial)} = 2.5\, nm$).
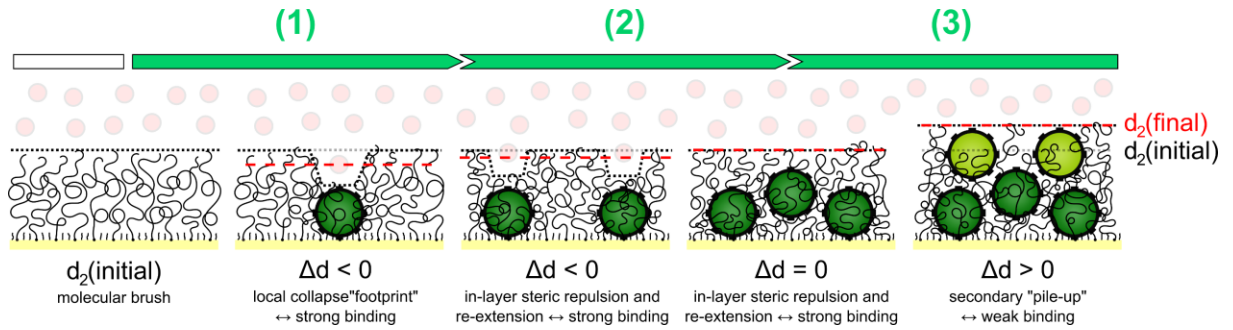
Fig. 4.6. Kapβ1-FG binding activity and cNup62 form-function are intimately coupled. (1) A local collapse of cNup62 occurs around Kapβ1 due to strong multivalent Kapβ1 (dark green)-FG binding at low $\rho_{Kap\beta1}$. (2) Additional Kapβ1 molecules bind tightly in the cNup62 layer driving unoccupied FG domains to extend or "recover" due to increasing in-layer steric repulsion whereupon the layer self-heals reaching $\Delta d = 0$. (3) At high $\rho_{Kap\beta1}$, a secondary layer of Kapβ1 (light green) binds weakly to unoccupied FG domain protrusions giving $\Delta d > 0$. Red dashed lines (**---**) correspond to the cNup62 layer height as measured by BSA (red watermarked).

The results of Δd vs. $\rho_{Kap\beta1}$ in Fig. 4.7A obtained from cNup62 brushes with different g_{cNup62} and $d_2(initial)$ indicate that the collapse transition is a common feature during initial Kapβ1-binding. This is followed by a recovery phase with taller brushes requiring more Kapβ1 molecules (higher $\rho_{Kap\beta1}$) to reach "pile-up". Recalling that $\rho_{Kap\beta1} \sim 1000 \, Da/nm^2$ approximates a packed Kapβ1 monolayer indicates that taller brushes $(d_2(initial) > 14.1 \, nm)$ accommodate a secondary Kapβ1 layer to recover. For comparison, sparser mushroom-like cNup62 layers undergo a negligible collapse and reach "pile up" without recovering. A three-dimensional spatial description is shown in Fig. 4.7B where the change in total mass-volume density Δv (i.e., cNup62 and Kapβ1) is plot against relative height change $\Delta d/d_2(initial)$. During collapse, the linear increase in Δv is dominated by a compaction of cNup62 since only small amounts of Kapβ1 are bound. Interestingly, the overlap indicates that Δv scales with $\Delta d/d_2(initial)$, that is, the total amount of space occupied is equally optimized within different cNup62 layers regardless of their initial brush conformation or amount of bound Kapβ1. During the initial stages of recovery, Δv increases at constant $\Delta d/d_2(initial)$ where the void volume of each layer is being filled with additional Kapβ1. Upon reaching "pile-up", Δv approaches a saturated critical capacity that is maintained by increasing $\Delta d/d_2(initial)$ (i.e., *via*

FG domain re-arrangements). While this interpretation is consistent with theoretical predictions (Kim & O'Shaughnessy, 2002), it shows that "pile-up" commences sooner for sparse cNup62 layers because of their isolation and lower capacity to bind Kapβ1.
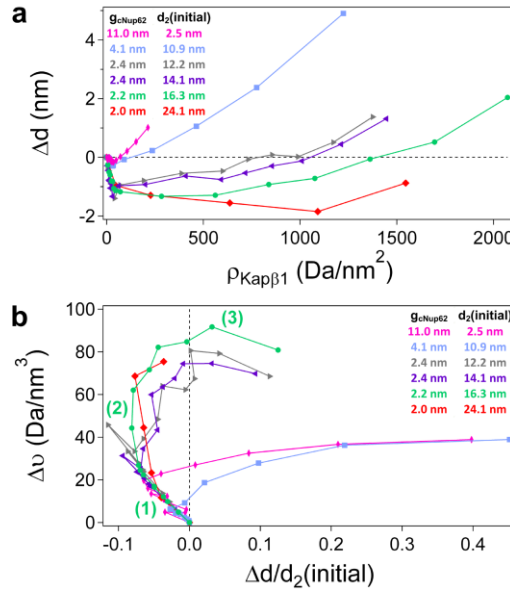
Fig. 4.7. Brushes collapse sparse layers do not. **(A)**, Plot of Δd vs. $\rho_{Kap\beta1}$ where the extent of collapse increases for taller cNup62 brushes (red > green > purple > grey) as compared to sparser layers (blue, pink). A greater amount of bound Kapβ1 is also required for taller brushes to recover before reaching "pile up" (red > green > purple > grey). Sparse cNup62 layers exhibit a negligible collapse followed by an immediate "pile up" without recovering (blue, pink). **(B)**, Plot of the total (Kapβ1 and cNup62) mass density change Δv vs. relative height change $\Delta d/d_2(initial)$. (1) For brushes (red, green, purple, grey), a linear increase in Δv accompanies a 10% reduction in $\Delta d/d_2(initial)$ due to cNup62 compaction upon collapse. Their overlap reveals that the total space occupied scales with the extent of collapse and is conserved. (2) The transition into "recovery" at $\Delta v \sim 20\ Da/nm^3$ proceeds with additional Kapβ1 binding without changing $\Delta d/d_2(initial)$. Saturation at $\Delta v \sim 70\ Da/nm^3$ denotes FG domain re-extension to maintain its capacity to accommodate more Kapβ1 marking the commencement of (3) "pile-up". Sparser conformations (blue, pink) have a low Kapβ1 capacity and "pile-up" at low Δv without recovering.

Fig. 4.8A summarizes the dependence of $d_2(initial)$ on g_{cNup62}. Clearly, extended molecular brushes form at small g_{cNup62} and transition into sparser layers or mushrooms at large g_{cNup62}. Since cNup62 ($pI = 9.31$) is net positively charged at pH 7.2, it follows that this behavior is polyelectrolytic in nature (i.e., forming polyelectrolyte brushes) as suggested by Flory-Huggins theory (Bright et al., 2001). The corresponding plot of K_D versus g_{cNup62} in Fig. 4.8B reveals how non-

monotonic behavior is linked to Kapβ1-FG binding avidity. When $g_{cNup62} >$ σ_{cNup62}, single K_D values of̃ ~10 μM reflect the limited propensity of individual cNup62 mushrooms to bind Kapβ1. This appears to split at $g_{cNup62} < \sigma_{cNup62}$ where two binding constants K_{D1} and K_{D2} emerge and become more apparent at low g_{cNup62} (Fig. 4.8C) due to the onset of brush formation. At low to moderate $c_{Kap\beta1}$, strong binding ($K_{D1} \sim 0.2\,\mu M$) accompanies collapse and recovery where Kapβ1 has access to FG repeats residing amongst neighboring FG domains, thereby reaching a maximum (K_{D1} decreases) at small g_{cNup62}. This is consistent with prevailing sub-μM K_D values noting that the highest Kap concentrations tested were below 1 μM (Ben-Efraim & Gerace, 2001; Bednenko et al., 2003; Lott et al., 2010). Whereas at large $c_{Kap\beta1}$, in-layer steric crowding and a reduction of unoccupied FG repeats give rise to weaker binding (K_{D2} ranging from 10 μM to 1 mM) that is associated with "pile-up". The large variation in K_D is therefore a hallmark of binding avidity that emerges from the myriad of Kapβ1-FG binding possibilities that derive from the inherent flexibility and conformational susceptibility of surface-tethered FG domains.
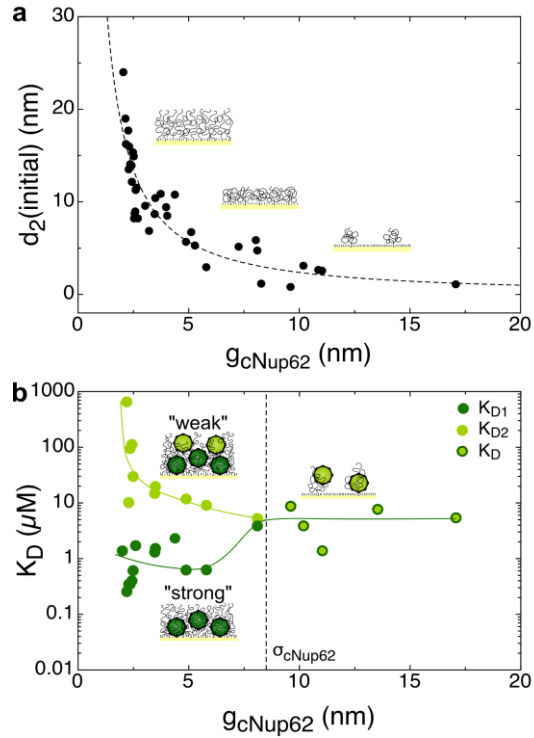
Fig. 4.8. Brush height and Kapβ1 binding avidity are correlated via cNup62 grafting distance. **(A)**, Dependence of $d_2(initial)$ on g_{cNup62} showing that cNup62 forms a molecular brush at low g_{cNup62} (i.e., high surface grafting density) and transitions towards sparse mushrooms at high g_{cNup62}. A fit of the Flory-Huggins equation to $d_2(initial)$ suggests that cNup62 is polyelectrolytic in nature (*SI Appendix 9*). **(B)**, Kapβ1 binding affinity to cNup62 is modulated by g_{cNup62}. An intermediate single binding phase occurs at g_{cNup62} larger than σ_{cNup62} (= 8.5 nm; dotted line) due to the limited Kapβ1-binding capacity of sparse mushrooms. This is splits at low g_{cNup62} (i.e., in the brush regime) where strong binding to cNup62 (K_{D1}; dark green) occurs at low to moderate $c_{Kap\beta1}$ (collapse and recovery) whereas weak binding (K_{D2}; light green) occurs at large $c_{Kap\beta1}$ ("pile up").

4.5.2 Conformational changes and molecular occupancy
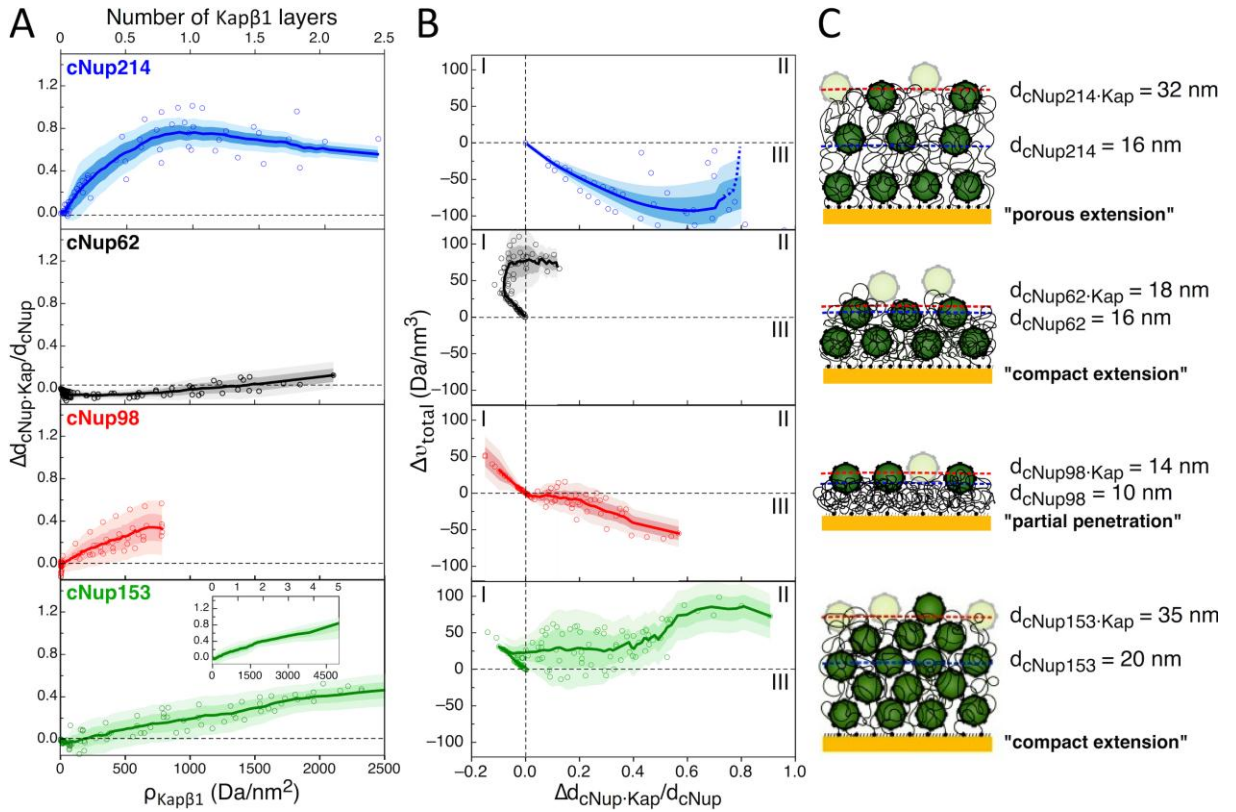
Fig. 4.9. Different close-packed FG domains respond to Kapβ1-binding differently. **(A)** Relative changes in FG domain layer thickness ($\Delta d_{cNup \cdot Kap}/d_{cNup}$) plotted as a function of Kapβ1 surface concentration ($\rho_{Kap\beta1}$) for cNup214, cNup62, cNup98 and cNup153. $\rho_{Kap\beta1} = 1000\ Da/nm^2$ for a single Kapβ1 layer. The data accounts for the full range of Kapβ1 injections (0 to 13.6 μM) except for cNup153, which is shown in the inset. **(B)** Corresponding changes in total protein density (Kapβ1 and FG domains; Δv_{total}) plotted as a function of $\Delta d_{cNup \cdot Kap}/d_{cNup}$. Three characteristic responses are: (I) "compaction", (II) "compact extension", and (III) "porous extension". See text for details. **(C)** Sketch of Kapβ1 occupancy within each FG domain layer prior to BSA injection (dark) and at equilibrium in the presence of physiological Kapβ1 concentration (light and dark). Values d_{cNup} and $d_{cNup \cdot Kap}$ highlight the change in thickness before and after Kapβ1 binding. Note: The dark and light shaded areas in (A) and (B) correspond to one and two standard deviations (SD), respectively.

Subsequent changes in FG domain brush thickness due to Kapβ1-binding ($d_{cNup \cdot Kap}$) can be correlated to the relative arrangement of Kapβ1 molecules bound within the layer (see section 4.2). This was monitored by titrating Kapβ1 in the following sequence: 0.1, 0.5, 1.0, 10, 20, 30, 40, 62.5, 125 nM, and 0.25, 0.5, 1, 2, 4, 6 to 13.6

µM. Fig. 4.9 summarizes the Kapβ1-binding response across all experiments for each close-packed FG domain (5 to 10 experiments per FG domain), which may be described in three ways. First, the relative change in layer thickness ($\Delta d_{cNup \cdot Kap}/d_{cNup}$) is shown as a function of surface density of bound Kapβ1 ($\rho_{Kap\beta1}$), which is related to the number of Kapβ1 layers formed (Fig. 4.9A). This relation is given as 2200 RU or 1000 Da/nm^2 based on the amount of material that corresponds to the equivalent of 1 (net) Kapβ1 layer (see section 4.2). Second, the change in the total protein mass density within the layer (Δv_{total} in Da/nm^3; that accounts for both Kapβ1 and the FG domain mass per unit volume) is plot as a function of $\Delta d_{cNup \cdot Kap}/d_{cNup}$ (Fig. 4.9B). Based on this plot, three different conformational responses can be distinguished: (I) "compaction" where Δv_{total} is positive and $\Delta d_{cNup \cdot Kap}/d_{cNup}$ is negative, (II) "compact extension" where Δv_{total} and $\Delta d_{cNup \cdot Kap}/d_{cNup}$ are positive, and (III) "porous extension" where Δv_{total} is negative while $\Delta d_{cNup \cdot Kap}/d_{cNup}$ is positive (i.e., the layer becomes more porous). Third, the representative molecular occupancy of Kapβ1 that is reached is illustrated within each close-packed FG domain layer at the highest applied Kapβ1 concentrations (Fig. 4.9C).

Overall, each FG domain exhibits its own characteristic response upon binding Kapβ1. cNup214 almost doubles its initial thickness value ($\Delta d_{cNup214 \cdot Kap}/d_{cNup214} = 0.8$) at the point where one Kapβ1 layer is bound. From here, Kapβ1 occupancy increases up to 2.5 layers (at maximum titration) without any further increase in thickness. We find from Δv_{total} that cNup214 reaches a maximum porous extension after initial Kapβ1-binding followed by a filling of the layer as subsequent Kapβ1 molecules bind. In comparison, cNup62 collapses into a more compact layer upon initial Kapβ1-binding as indicated by the decrease in $\Delta d_{cNup62 \cdot Kap}/d_{cNup62}$ with increasing Δv_{total}. This is followed by a recovery phase and a compact extension that accommodates a maximum of two Kapβ1 layers (Schoch et al., 2012). Similarly, cNup153 first undergoes a reversible collapse transition (Lim et al., 2007) (Kapβ1 < 60 nM) before exhibiting compact extension at higher Kapβ1

concentrations. Indeed, this reaches 1.75 $d_{cNup153}$ (~ 35 nm), which accommodates at least 5 Kapβ1 layers at 13.6 μM Kapβ1.

Interestingly, cNup98 undergoes a compaction at very low Kapβ1 concentrations (< 30 nM) followed by a small increase in thickness incorporating less than one Kapβ1 layer at physiological Kapβ1 concentration. Given that $d_{cNup98 \cdot Kap}$ reaches a maximum of 14 nm and that Kapβ1 can be approximated as a sphere with a diameter of 9.9 nm, the decrease in Δv_{total} likely results from a partial (i.e., incomplete) penetration of Kapβ1 into the compact cNup98 layer, which cannot extend further due to intrinsic cohesion. Based on the above analysis, the differing extensibilities upon Kapβ1 binding of each close-packed FG domain is given as cNup214 > cNup153 > cNup62 > cNup98 and the capacity for Kapβ1binding as cNup153 > cNup214 > cNup62 > cNup98.
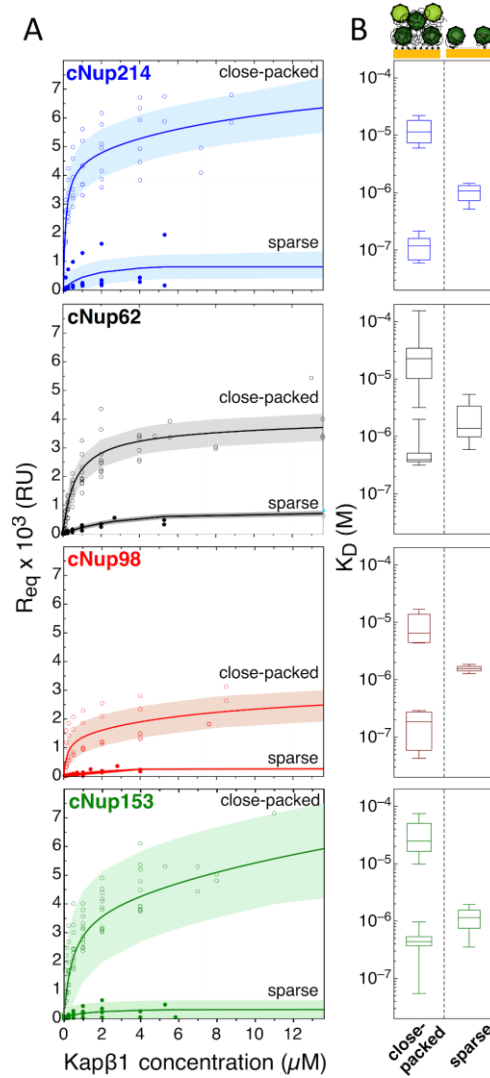
Fig. 4.10. Equilibrium analysis of Kapβ1-FG domain binding. **(A)** Dependence of Kapβ1-FG domain equilibrium binding response (R_{eq}) on the bulk Kapβ1 concentration for cNup214, cNup62, cNup98 and cNup153 in the close-packed ($g_{cNup} < r_h$) and sparse ($g_{cNup} > 2r_h$) regimes. Solid lines represent a two-component Langmuir isotherm fit in the close-packed regime, and a one-component Langmuir isotherm fit in the sparse regime, respectively. The shaded area corresponds to one standard deviation in both cases. **(B)** Equilibrium dissociation constants (K_D) obtained from (A) in the close-packed and sparse regimes. Box plots show the median, first and third quartiles (values greater then six standard deviations are considered as outliers and are not shown).

In terms of Kapβ1-FG domain binding equilibria, the results of Langmuir isotherm analysis vary widely depending on FG domain surface density (Fig. 4.10A). The resulting equilibrium dissociation constants (K_D) (Fig. 4.10B) show that Kapβ1 binds

moderately at ~1 µM K_D for all FG domains in a sparse configuration where a single isolated FG domain molecule effectively binds one Kapβ1 molecule. In comparison, the experimental Kapβ1 binding data obtained in the close-packed FG domain regime requires a two-component Langmuir isotherm fit. Here, a high affinity species (K_D ~ 100 nM to 1 µM) represents tight Kapβ1 binding given the high FG repeat density in each close-packed FG domain layer. The increase in Kapβ1 occupancy at higher concentrations leads to a reduction of free FG repeats within the layer, which results in a second low affinity species (K_D ~ 10 µM). Importantly, this increase in K_D represents a general hallmark of binding avidity that reflects a reduction of multivalent interactions when a close packed FG domain layer becomes saturated with Kapβ1. At that stage fewer FG repeats are available and subsequent Kapβ1 binding becomes weak as avidity is diminished.

4.6 Discussion

The results from SPR reveal non-monotonic FG domain behavior that is most pronounced for the central Nup62. This transition is also visible for Nup153 as well as marginally visible for Nup98, but lacking the FG domain of Nup214. A collapse upon addition of Kapβ1 was previously observed for Nup153 using AFM force-distance curves at pico-molar Kapβ1 concentrations (Lim et al. 2006; Lim et al., 2007), whereas in vivo a reversible condensation of Kapβ1 at the NPC wall was observed with increasing Kapβ1 concentration, indicating „self-regulated" conformational changes of the FG Nup barrier to occur in intact NPC's (Ma et al., 2012). However, in the planar system used here, at elevated concentrations of Kapβ1, the FG domains re-extend, which maximizes their capacity to bind more Kapβ1. The extensibilities upon Kapβ1 binding of the individual FG domains are given as cNup214 > cNup153 > cNup62 > cNup98. It can now be speculated that the extensibilities depend on location, such that FG domains located closer to the periphery are more prone to extension in agreement with space that is available and/or their functional disposition, where the FG domain of Nup98 (i.e., GLFG)

would form a cohesive annular ring around the central plane. In the same direction it was already reasoned that the cytoplasmic and nucleoplasmic nucleoporins (such as Nup214 and Nup153) would serve as docking sites (Macara, 2011) and antennas collecting transport receptors from the aqueous phase (Peters, 2005), rather than sites involved directly in translocation.

A key finding here is the high molecular occupancy of tightly bound Kapβ1 in the FxFG domains of cNup214, cNup62, and cNup153 at physiological Kapβ1 concentrations due to binding avidity. Paradoxically, most of the in vitro affinity assays predict strong binding of Kapβ1 in the low or medium nanomolar range (see table 1.1), that cannot account for the rapid ~5 ms NPC translocation times (Ma & Yang, 2010), given a diffusion based on rate (Tetenbaum-Novatt et al., 2012). Here, the SPR results show that end-tethered FG domain conformation is intimately coupled to Kapβ1-FG binding activity as defined by their relative spatial arrangements (i.e., g_{cNup} and $g_{Kap\beta1}$). Thus the results support a view where crowding and conformational changes are important in promoting weak binding and fast Kapβ1 transport in the NPC. Indeed, the binding activity in the close-packed regime changes with Kapβ1 occupancy. The Langmuir isotherm analysis predicts that at least two Kapβ1 binding phases exist at physiological concentrations, (i) strong binding (K_D ~ 100 nM) to a population of semi-collapsed FG domains and (ii) weak binding to the protrusions of a preoccupied FG domain layer (K_D ~ 10 μM). The weak binding equilibrium is thus an emergent property of the FG domain layer due to Kapβ1 binding. Thus, binding avidity need not hinder fast transport *per se*.

In contrast to the in-solution behavior of non-tethered FG domains, the NPC interior presents many closely tethered FG domains that display collective functional characteristics *in vivo* (Atkinson et al., 2013). Here, our work indicates that FG domain surface tethering is an essential contextual consideration for the NPC because it defines the pore boundary, establishes FG domain orientation with respect to an interface, and enforces a limit on Kap occupancy (and how far FG domains can

extend). In the close-packed regime, all the FXFG domains studied here (cNup214, cNup62 and cNup153) exhibit molecular brush behavior, and have a large capacity to incorporate up to 2 layers or more of Kapβ1 molecules at physiological Kapβ1 concentrations, albeit with varying degrees of extensibility. On the other hand, cNup98 forms a short compact GLFG domain layer that is only partially penetrable to Kapβ1. This suggests that the close-packed, surface tethered form of cNup98 may cohere more strongly than pure Nup98 hydrogels, where Kapβ1 penetrated a depth of a few micrometers (Labokha et al., 2013). Further functional correlations are difficult to establish because a hydrogel can comprise of fibrous meshworks and sub-micrometer-sized porous channels with unique morphological and sieving properties (Strawn et al., 2004).

Our results reveal that a low affinity fraction of Kapβ1 dominates at physiological concentrations once a FG domain layer is saturated and preoccupied with Kapβ1. This low affinity species experiences hindered penetration due to increased steric effects arising from FG domain layer extension and saturation to promote a fast phase with limited access to FG repeats at the layer periphery.

4.7 Error analysis

The accuracy of the height measurements may be affected by the following sources and parameters:

    1) Physical interactions of BSA at the interface

    2) Penetration of BSA into cNup62

    3) Osmotic pressure of BSA molecules

    4) Elution of ligand molecule

    5) Changes of refractive index within the molecular layer

    6) Decay length of evanescent field

7) $C_{17}H_{36}O_4S$ layer height

8) Analyte binding in reference cell

9) Sensitivity of SPR instrument

10) Baseline drift (e.g. analyte dissociation)

11) Statistical fluctuations for individual BSA injections

12) Distinct sensitivities of flow cells

13) Error Summary

Note: The error analysis in this section is discussed in the context of the measurement shown in Fig. 4.5.

1) Physical interactions of BSA at the interface

Overall it is difficult to quantify this source of error arising from physical (non-chemical) interactions including van der Waals, electrostatic and hydrophobic interactions (Norde, 2008). Nevertheless, control experiments can be carried out on molecular layers that are unlikely to collapse to check if the negative Δd values are artifacts caused by physical interactions between BSA and Kapβ1. Here, BSA is applied to measure the $C_{17}H_{36}O_4S$ heights in flow cell1-4, where $C_{17}H_{36}O_4S$ is considered non-collapsible and $C_{17}H_{36}O_4S$ in cell1 was set $d_1 = 2.0\ nm$. Next, cell3 and cell4 were incubated with 2 µM Kapβ1 for 12 min and the heights were measured again. In cell3-4, small amounts of Kapβ1 ($\approx$ 100 RU) adsorb nonspecifically to $C_{17}H_{36}O_4S$, which results in $\Delta d = 0.4435 \pm 0.0107\ nm$. This provides evidence that negative Δd values are not artifacts that result from weak non-specific BSA - Kapβ1 interactions.

2) Penetration of BSA into cNup62

Although BSA (hydrodynamic diameter $\sigma_{BSA} = 7.4\ nm$) does not bind cNup62, there is a possibility that it can penetrate into the cNup62 layer. If so, this would bring

about underestimates in the d_2 measurements and underestimates in the measured collapse.

3) Osmotic pressure of BSA molecules

This error is difficult to quantify as well. Osmotic pressure may trigger FG domain self-interaction due to a modified chemical potential of water in solution. However, a meaningful quantification of osmotic effects could only be obtained from a comprehensive experimental study where similar cNup62 layers are evaluated for their height response by either injecting Kapβ1 or buffer only in a statistically relevant amount of probings.

4) Elution of ligand molecule

Removal of cNup62 from the layer with BSA/Kapβ1 injection is unlikely. This was validated in a measurement where Kapβ1 binding causes cNup62 to collapse following the removal of non-covalently attached cNup62 chains by washing with 0.2 M NaOH (see Fig. 4.11C).
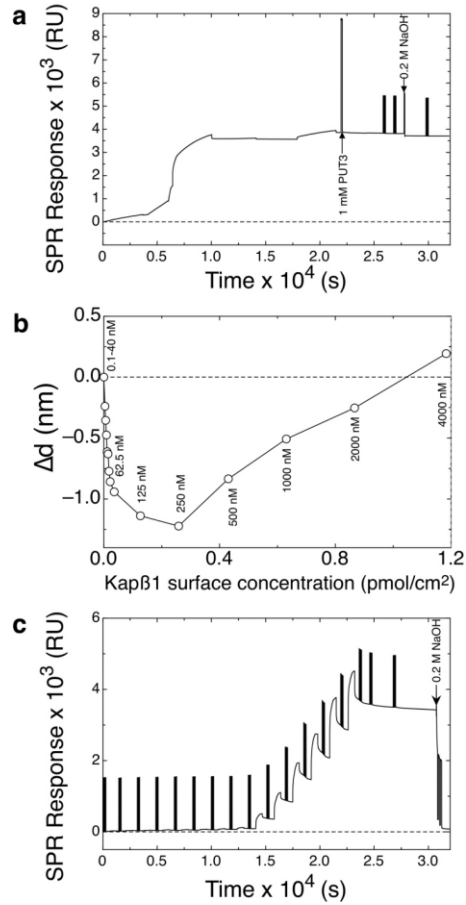
Fig. 4.11. (A) cNup62 is covalently tethered to the gold sensor surface where less than 3% of the FG domains are removed upon washing with 0.2 M NaOH. **(B)** Non-monotonic behavior as caused by Kapβ1-binding after treatment with 0.2 M NaOH. **(C)** Almost 100% removal of Kapβ1 from cNup62 layer after 3 short injections of 0.2 M NaOH (black arrow) for $d_2(initial) = 17\ nm$.

5) Changes of refractive index within the molecular layer

This error decreases for smaller layer thickness and changes in the refractive index. As n_a may vary within an experiment (e.g., due to receptor binding) one would accordingly have to correct for the optimal decay length l_d in Eq. 3.9 for an accurate determination of Δd. Here its shown as an example how this error is estimated for $\Delta d = -1.4\ nm$ at $c_{Kap\beta1} = 40\ nM$ from Fig. 4.5B. At $\Delta d = -1.4\ nm$ the grafting distance of Kapβ1 is $g_{Kap\beta1} = 55.5\ nm$. Considering the dimension of Kapβ1 ≈ 10.0 nm (see section 4.2) we can estimate the fraction of a monolayer Kapβ1 bound at $\Delta d = -1.4\ nm$, giving 0.032 times a monolayer. Taking $n = 1.45$ for a layer of proteins (Voros, 2004) we can calculate $\Delta n \approx 0.0037$ for Kapβ1 binding at $\Delta d =$

$-1.4\ nm$.

From the decay length map in section 2.2.2.2, for $l_d = 350\ nm$ and $d = 14.1\ nm$, the refractive index of the layer is $n_a = 1.3759$. We can now calculate from the decay length map the decay length to be expected for a layer with $d = 14.1\ nm$ and $n_a = 1.3759 + \Delta n = 1.3796$, this gives $l_d = 358.5\ nm$. Thus the estimated error that would emerge from choosing a wrong decay length is roughly $14.1nm - 350/358.5 \cdot 14.1nm = -0.33nm$ which is smaller than $\Delta d = -1.4\ nm$. Thus, the negative trend in Δd at small $c_{Kap\beta1}$ cannot be explained by the change in the refractive index Δn_a due to Kapβ1 binding. One has to consider that with ongoing binding of Kapβ1 to the surface this error is increasing and this would enhance the "pile-up" phase in Fig. 4.5B. Thus we can summarize that the qualitatively observed phases "collapse", "recovery" and "pile-up" are not an artifact of a constant decay length l_d in Eq. 3.9.

6) Decay length of evanescent field

As seen from Eq. 3.9 the measured absolute thickness d_2 linearly depends on the decay length l_d. A common $l_d = 350\ nm$ in the measurements as used as an appropriate average for the cyan area in the decay length map ($n_a \approx 1.35 - 1.4$; $d_a \approx 10 - 40\ nm$) thus for deviations in n_a *one* would have to correct the decay length in Eq. 3.9. For the measurement with $d_2(initial) = 14.1\ nm$ (for $l_d = 350\ nm$) and $g_{cNup62} = 2.4\ nm$ we can run an optimization procedure for the decay length using $1300\ RU = 1\ ng/mm^2$ (see section 2.2.3) and a refractive index increment of $0.1554\ cm^3/g$ for proteins (see section 2.2.3). This leads to an optimized decay length $l_d = 417\ nm$, layer refractive index $n_a = 1.396$, and initial height $d_2(initial) = 16.4\ nm$, respectively. From this analysis the cNup62 layers seem to have a refractive index of $n_a \approx 1.36 - 1.41$ rather than $n_a \approx 1.35 - 1.4$ for the cyan area and the error in the initial height can be as much as 20 % of the initial height for using $ld = 350\ nm$. However, the optimization procedure described in

appendix X is a meaningful path to keep this error as narrow as possible.

7) $C_{17}H_{36}O_4S$ layer height

For simplicity the reference $C_{17}H_{36}O_4S$ layer height was set to $d_1 = 2.0\ nm$ in agreement with the ellipsometric measured thickness $d = 2.01\ nm$ for the same molecule (Palegrosdemange et al., 1991) and its methoxy-terminated analog that was experimentally determined using X-ray photoelectron spectroscopy ($d_1 = 2.0\ nm$) (Harder et al., 1998). Bearing in mind the consistency of the reference heights to model estimates (Kankate et al., 2010) ($d \sim 2.3\ nm$), the absolute error in the method due to the $C_{17}H_{36}O_4S$ thickness d_1 in Eq. 3.9 is in the sub-nanometer range (< 0.3 nm).

8) Analyte (Kapβ1) binding in reference cell

Unspecific binding of analyte molecules in the reference cell *underestimates* the measured thickness in the sample cell. The error is different for each measurement depending on the as-formed passivation layer but the error can be estimated for a particular measurement using the characteristic dimension of the analyte molecule. In the titration experiment in Fig. 4.5, at $c_{Kap\beta1} = 40\ nM$, we obtain a grafting distance $g_{Kap\beta1} = 79.3\ nm$ in the reference cell and $g_{Kap\beta1} = 55.5\ nm$ in the sample cell. Recalling that Kapβ1 monolayer formation occurs at $g_{Kap\beta1} = 10\ nm$ (see section 4.2), we have 1.5 % of a layer formed in the reference cell and 3.2 % of a layer in the sample cell. By multiplying the number of layers with the dimension of Kapβ1 (10.0 nm) we get a layer height of $0.015 \times 10\ nm = 0.15\ nm$ in the reference cell. This is a small error for the reference layer height compared to the change in the height in the sample cell and we can write $\Delta d = -1.22 + 0.15\ nm$ for the collapse (positive error). Typically, the error increases at higher bulk Kapβ1 concentrations due to nonspecific Kapβ1 binding in the reference cell (see also error source 1). For instance, in the final titration at $c_{Kap\beta1} = 13.4\ \mu M$ (see Fig. 4.5), this error would be

0.9 nm (corresponding to a 9% layer of Kapβ1 in the reference cell). If this error was accounted for, the final Δd_2 would be 2.1 nm instead of the reported value 1.2 nm (i.e., 1.2 nm+0.9 nm). Thus, this error is negligible when non-specific binding in the reference cell is low. Further, the same error has to be considered in absolute height measurements.

9) Sensitivity of SPR instrument

The height measurements may be influenced by fluctuations in the SPR response. The root mean square noise in the sensogram of the titration measurement is $N_{rms} = 0.12\ RU$. The BSA signals have an intensity of about 1550 RU and a deviation in the signal of 0.12 RU gives an error of nm in the height.

10) Baseline Drift

A drift in the baseline (e.g., caused by analyte dissociation) would influence the measured BSA response. As the BSA response is never perfectly rectangular but ends with a tail, the baseline value is taken 30 seconds after the end of the BSA injection. In the titration experiment of Fig. 4.5 the drift in the baseline due to analyte dissociation is up to 0.12 RU/s. This gives an error in ΔRU of $30\ s\ \times 0.12\ RU/s = 3.6\ RU$ or $\approx 0.38\ nm$ from Eq. 3.9.

11) Statistical fluctuations for individual BSA injections

The measured thickness deviates slightly for individual BSA injections. For the triplet of the most collapsed state $(c_{Kap\beta1} = 40\ nM)$ the standard deviation for the three injections is 0.1641 nm, which is smaller than the measured collapse. The average standard deviation for all BSA triplets for all titrations is 0.0746 nm.

12) Distinct sensitivities of flow cells

In the calculations from above we obtained a standard deviation $\sigma_X = \pm 0.4145\ nm$ of the thickness d_2 measured for 4 equal $C_{17}H_{36}O_4S$ layers. This error is influencing the absolute values of the thickness measurements.

13) Error Summary

All error sources are summarized in table 3.1 based on the quantities obtained above. The estimated error ε is then the weighted average

$$\varepsilon = \frac{\sum_{i=1}^{n} g_i x_i}{\sum_{i=1}^{n} g_i}\ with\ g_i = \frac{x_i^2}{\sigma^2} \tag{4.10}$$

of each element (source of error) x_i where σ is the smallest element (error) in the set. The elements are weighted by the size of the element as they do not belong to a common distribution of random numbers. Negative and positive error terms, respectively, were summed up in each column to form a new error term. This error analysis then gives accuracies of $d_2 \pm 2.25\ nm$ for measurements of absolute thickness and $\Delta d \pm 0.22\ nm$ for the change in thickness of the collapse.

Error source	Estimated absolute error in measured thickness d_2 for the cNup62 layer	Estimated error in measured collapse Δd = -1.22 nm for the cNup62 layer
1) BSA – substrate interactions.	unknown	unknown
2) BSA penetration into cNup62	unknown (underestimates d_2)	unknown
3) Osmotic pressure of BSA molecules	unknown	unknown
4) Elution of ligand molecules	unknown	unknown

5) Change in the refractive index	----	± 0.33 nm
6) Decay length of the evanescent field	± 2.26 nm	---
7) Reference SAM height	± 0.3 nm	---
8) Binding in reference cell	± 0.9 nm	± 0.15 nm
9) Sensitivity of SPR instrument	± 0.012 nm	± 0.012 nm
10) Drift in baseline (i.e. analyte dissociation)	+ 0.38 nm	---
11) Statistical fluctuations for individual BSA injections	± 0.0746 nm	± 0.1641 nm
12) Sensitivities of the flow cells	± 0.4145 nm	---
13) **Estimated Error e:**	**± 1.96 nm**	**± 0.28 nm**

Table 4.1. From the error analysis the estimated accuracy of the relative collapse is within $\Delta d \pm 0.22\ nm$ whereas the accuracy of the absolute thickness of the molecular layer is within $d_2 \pm 2.25\ nm$. This proves that the qualitatively observed phases "collapse", "recovery" and "pile-up" are not artifacts due to a constant decay length l_d in Eq. 3.9 or of any other error sources as discussed above.

Chapter 5

Kinetic analysis of multivalent Kapβ1 binding

Parts of this chapter were published in Schoch et al., 2012, and Kapinos & Schoch et al., 2014.

The following chapter incorporates a kinetic analysis of multivalent Kapβ1 – FG domain binding. While a slowly exchanging Kapβ1 phase forms an integral constituent within the FG domain layer, kinetic analysis shows that for all close-packed FG domains a fast phase exists that is most pronounced at high Kapβ1 concentrations. It is reasonable that this fast phase dominates NPC transport characteristics due to limited binding with the pre-occupied FG Nups at physiological Kapβ1 concentrations. These results were previously published in Kapinos & Schoch et al., 2014. Additionally, an alternative analysis exemplifies how entropic constraints due to layer extension influences the binding kinetics. At the end of this chapter, implications of the results are discussed on the molecular and NPC level and limitations as well as possible error sources of the SPR technique are analyzed.

5.1 Basics & Theory

5.1.1 Polymer brush and particle binding

When a polymer brush is compressed or otherwise deformed from its equilibrium

structure it responds with a restoring force (Currie et al., 2003). For particles attracted towards a brush coated surface, compression of the brush leads to an increase in osmotic interactions that counteract attractive interactions and thus suppress the adsorption of particles to the surface. It has been shown experimentally that for a polymer brush this suppression is most effective when the grafting distance is less than the dimension of the particles (Norde & Gage, 2003).

Numerical SCF theory was applied to protein adsorption on surfaces with polymer brushes (Szleifer, 1997). As introduced in section 5.11 the repulsive interactions between molecules, the hard-core repulsion, are taken into account by packing constraints, i.e. the sum of the volumes occupied by protein, polymer and solvent must be equal to or smaller than the available volume. The effective potential of the protein with the polymer modified surface, assuming all the components of the system are the same, simply is

$$U(z) = \int_z^\infty \pi(z') v_p(z') dz' + U_{ps}(z) \qquad\qquad (5.1)$$

where z' is to account for the overall size of the protein, $v_p(z')dz'$ is the volume that the proteins at distance z' from the surface contribute to z, $\pi(z')$ is the lateral pressure profile, and $U_{ps}(z)$ is the interaction of the protein with the solid surface. The first term represents the average repulsions felt by the protein molecule due to the grafted polymers and other protein molecules, and the second term is the bare surface-protein attractive interaction. If the proteins start to adsorb there will be a additional repulsion near the surface due to the presence of the protein molecules. Moreover the average configurational properties of the grafted chains will be modified by the presence of the protein molecules. Therefore, as proteins adsorb, the effective potential changes a complete description of kinetic behavior must consider the varying potential as a function of adsorbed protein, i.e. the effective potential is time dependent (Satulovsky

et al., 2000).

5.1.2 Mass transport effects

For typical flow cell dimension used in SPR the flow characteristics is laminar. This implies that the velocity profile in the flow cell is parabolic with the maximum velocity in the midpoint of flow cell height and zero velocity at the sensor surface (Štěpánek et al., 2006). Translational diffusion therefore becomes important close to the sensor surface to achieve concentration uniformity and the SPR signal is not a simple result of biochemical processes at the sensor surface. In the full model of mass transport one needs to solve numerically the fundamental partial differential describing analyte distribution in the flow cell due to laminar flow and translational diffusion coupled with the relevant kinetic equations. However, the full model calculations are time-consuming and thus not suitable for practical use in experimental evaluation. Therefore simpler models were developed to estimate mass transport limitation and validated using full numerical calculations of analyte distribution within the flow cell (Myszka et al. 1998, Štěpánek et al., 2006). Transport effects will influence the kinetics of binding when the reaction rate is fast compared to the rate of transport, i.e., when $k_a R_T \geq k_{tr}$, where R_T is the total receptor (i.e. ligand in our notation) concentration and k_{tr} is the diffusion limited rate constant (Lok et al., 1998; Sjölander & Urbaniczky, 1991)

$$k_{tr} \approx 1.282 \left(\frac{v_{max} D^2}{hl} \right)^{1/3} \tag{5.2}$$

where h is the height of the flow cell, l is the length of the flow cell, D is the analyte diffusion coefficient and v_{max} is the maximum velocity in the center of the flow cell

$$v_{max} = \frac{3}{2}\frac{\Phi}{hw} \tag{5.3}$$

where Φ is the flow rate and w is the width of the flow cell. In the two-compartment model the variation in analyte concentration in the flow cell is considered by dividing the flow cell chamber into two compartments (Myska et al., 1998). In each compartment the concentrations are uniform in space but may change in time. The analyte concentration in the outer compartment (i.e., far from the surface) agrees with the injected bulk concentration c, whereas for the inner compartment (i.e., close to the surface) the concentration c_{surf} changes because analyte is transported between the compartments and analyte binds to and dissociates from the surface. This gives the combined equation for compartment-like binding and transport:

$$\frac{dc_{surf}}{dt} = k_{tr}\left(c - c_{surf}\right) - \frac{ds}{dt} \tag{5.4}$$

$$\frac{ds}{dt} = k_{on}c_{surf}(s_{max} - s) - k_{off}s \tag{5.5}$$

where s are the occupied surface sites and s_{max} is the total number of surface sites.

5.1.3 Molecular reaction dynamics

This section is a brief summary of concepts taken from the book *Theories of Molecular Reaction Dynamics* by Niels E. Henriksen and Flemming Y. Hansen.

5.1.3.1 Transition state theory

In conventional transition-state theory the main focus is on the activated complex

with the reaction scheme in the form

$$A + B \rightarrow (AB)^{\ddagger} \rightarrow products \tag{5.6}$$

and for assuming equilibrium between the transition state $(AB)^{\ddagger}$ and the reactants A and B, the rate of the reaction in thermodynamic terms gets

$$k_{TST}(T) = \frac{k_B T}{h} \frac{e^2}{c^0} exp\left(\Delta S_{\ddagger}^0 / R\right) exp(-E_a / RT) \tag{5.7}$$

where $c^0 = N/V$ is a concentration, typically chosen as 1 mole/liter and standard changes indicated by the symbol ^{0}. From this expression originates the idea that the pre-exponential factor in the Arrhenius expression $k(T) = A exp(-E_a / k_B T)$ is due to 'entropy effects'. Note that the activation energy E_a refers to the difference in the average internal energy at a given temperature. To derive Eq. 5.7 the approximation has to be taken that the motion along the reaction coordinate can be separated from the other degrees of freedom and treated classically as a free translation along the minimum energy path.

5.1.3.2 Potential of mean force (PMF)

Denoting the reaction coordinate by q_1 and the TS by $q^{\ddagger}$ and asserting that the reactants are 'to the left' of the TS ($q_1 < q^{\ddagger}$), we find that the TST rate constant can be expressed as

$$k_{TST}(T) = V \sqrt{\frac{k_B T}{2\pi\mu_1}} \frac{e^{-w(q^{\ddagger})/k_B T}}{\int_{-\infty}^{q^{\ddagger}} e^{-w(q_1)/k_B T} dq_1} \tag{5.8}$$

where a potential $w(q_1)$ was introduced

$$-w(q_1)/k_B T = ln\{\int \ldots \int e^{-U_N(q_1, q_2, \ldots)/k_B T} dq_2 dq_3\} + const \tag{5.9}$$

The potential of mean force $w(q_1)$ is the potential that gives the mean force acting on the reaction coordinate, averaged over all other coordinates. For the average speed along the reaction coordinate the reduced mass μ_1 was used.

5.1.3.3 Brownian motion

The problem of Brownian motion relates to the motion of a heavy colloidal particle immersed in a fluid made up of light particles. The *Langevin equation* is a so-called stochastic equation of motion

$$\frac{dv}{dt} = -\gamma v + F(t) \tag{5.10}$$

where γ is defined as the friction constant divided by the mass M and $F(t)$ is a random function describing the action of all individual solvent molecules on the Brownian particles. Using the condition $\langle F(t) \rangle = 0$ we can find for the solution of the Langevin equation

$$\langle v^2 \rangle = v_0^2 \cdot exp(-2\gamma t) + \frac{f}{2\gamma}\left(1 - exp(-2\gamma t)\right) \qquad (5.11)$$

This shows us how the square of the velocity of the particle, on the average, develops in time given that it had at time $t = 0$ the value v_0^2. The expression shows that for short times, where $t \ll (2\gamma)^{-1}$, the velocity fluctuations are mainly determined by the initial value v_0^2. Only for larger times the initial value is progressively forgotten and the average square of the velocity approaches the value of $f/2\gamma$, which is solely determined by collisions and is independent of the initial velocity. The factor f can be determined from the fluctuation-dissipation theorem

$$\lim_{t\to\infty}\langle v^2 \rangle = \frac{f}{2\gamma} = \frac{k_B T}{M} \qquad (5.12)$$

and one can rewrite Eq. 5.22 as

$$\langle v^2 \rangle = \frac{k_B T}{M} + \left[v_0^2 - \frac{k_B T}{M}\right] exp(-2\gamma t) \qquad (5.13)$$

5.1.3.4 Kramers Theory

Kramer proposed a stochastic description of the dynamics in the reaction coordinate similar to that of the Brownian motion of a heavy particle in a solvent. The influence of the solvent may be described by the *Langevin equation* where the one dimensional motion takes place in the potential $U(r)$, and the well at r_a refers to the reactants, r_b to the transition state, and r_c to the products (see Fig. 5.1).

Further, the shape of the external potential near the transition state

$$U(r) = U(r_b) - \frac{1}{2}M\omega_b^2(r - r_b)^2 \tag{5.14}$$

and at the reactant well

$$U(r) = U(r_a) + \frac{1}{2}M\omega_a^2(r - r_a)^2 \tag{5.15}$$

is approximated by a parabolic shape. The Kramers equation for the rate constant of a chemical reaction in solution then gets

$$k_s = \frac{\omega_a}{2\pi\omega_b}\left(\sqrt{\frac{\gamma^2}{4} + \omega_b^2} - \frac{\gamma}{2}\right)exp\big(-\big(U(r_b) - U(r_a)\big)/k_B T\big) \tag{5.16}$$

The influence of the solvent is represented by the friction coefficient, which may be directly related to the viscosity η of the Solvent via Stokes law:

$$\gamma = \frac{6\pi\eta R}{M} \tag{5.17}$$

where R is the hydrodynamic radius of the particle.

For $\gamma/2 \gg \omega_b$ we find that

$$k_s = \frac{\omega_a}{2\pi} \frac{\omega_b}{\gamma} exp\big(-\big(U(r_b) - U(r_a)\big)/k_B T\big) \qquad (5.18)$$

which is the high friction limit. It shows that the rate constant goes towards zero for an infinite friction constant. In the other limit, where $\gamma/2 \ll \omega_b$, we find

$$k_s = \frac{\omega_a}{2\pi} exp\big(-\big(U(r_b) - U(r_a)\big)/k_B T\big) \qquad (5.19)$$

which is the ordinary (gas-phase) transition-state theory result for a one dimensional oscillator.
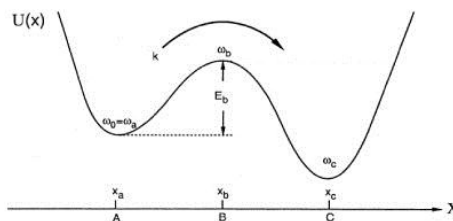
Fig. 5.1. Sketch of the potential energy U as a function of reaction coordinates x (r in the text). The state around (a) represents the reaction state, (b) the transition state and (c) the product state, respectively.

5.1.4 Regularization of discrete ill-posed problems

Regularization theory aims to provide efficient and numerically stable methods for including proper side constraints that lead to useful stabilized solutions to discrete ill-posed problems such that the regularized solution is a good approximation to the desired unknown solution (Per Christian Hansen, 2007). For a linear system of equations

$$Ax = b, A \in \mathbb{R}^{n \times n} \tag{5.20}$$

and linear least square problem

$$\min_{x} \|Ax - b\|_2, A \in \mathbb{R}^{m \times n}, m > n \tag{5.21}$$

the matrix A is called ill-conditioned if the solution $\boldsymbol{x}$ is potentially very sensitive to perturbations in $\boldsymbol{b}$ and implies that the columns in A are nearly linear dependent. The most common and well-known form of regularization is the one known as *Tikhonov regularization*. Here, the idea is to define the regularized solution $\boldsymbol{x}_\lambda$ as the minimizer of the following weighted combination of the residual norm and the side constraints

$$x_\lambda = argmin\{\|Ax - b\|_2^2 + \lambda^2 \|L(x - x^*)\|_2^2\} \tag{5.22}$$

where the regularization parameter λ controls the weight given to minimization of the side constraint relative to the minimization of the residual norm $\|Ax - b\|_2$. For L the identity matrix I_n is a typical choice and x^* may be an initial estimate of the desired solution. The singular value decomposition (SVD) of A for the analysis of discrete ill-posed problems has the form

$$A = U\Sigma V^T = \sum_{i=1}^{n} u_i \sigma_i v_i^T \tag{5.23}$$

where $U = (\boldsymbol{u}_1, ..., \boldsymbol{u}_n)$ and $V = (\boldsymbol{v}_1, ..., \boldsymbol{v}_n)$ are matrices with orthonormal columns, $U^T U = V^T V = I_n$, and where $\Sigma = \text{diag}(\sigma_1, ..., \sigma_n)$ has non-negative diagonal

elements appearing in non-increasing order such that

$$\sigma_1 \geqslant \ldots \geqslant \sigma_0 \geqslant 0 \tag{5.24}$$

The numbers σ_1 are the singular values of A while u_i and v_i are the left and right singular vectors of A, respectively. The generalized singular value decomposition (GSVD) of a matrix pair (A, L), uses a slightly more complex formalism. However, as for now we consider only the case where L is the identity matrix I_n, and then U, V and the singular values of the GSVD are identical to the ones obtained from SVD except for the ordering of the singular values and vectors. The regularized solution x_{reg} for the least square problem (Eq. 5.21) are then given by

$$x_{reg} = \sum_{i=1}^{n} f_i \frac{u_i^T b}{\sigma_i} v_i \tag{5.25}$$

Here, the numbers f_i are filter factors for the particular regularization method. For Tikhonov regularization the filter factors are

$$f_i = \frac{\sigma_i^2}{\sigma_i^2 + \lambda^2} \tag{5.26}$$

and the filtering effectively sets in for $\sigma_i < \lambda$. The purpose of a regularization method is thus to dampen or filter out the contributions corresponding to the smallest singular values σ_i, that destabilize the solution of the least square problem and involves choosing an appropriate regularization parameter λ.

5.2 Data analysis

5.2.1 Kinetic interaction maps

The following section deals with the analysis of FG domain – Kapβ1 binding kinetics. The term "interaction map" is to denote a two-dimensional distribution of rate and/or affinity constants, and is pertinent to the analysis of heterogeneous ligand populations (Svitel et al., 2003). Here, the analysis is based on a singular value decomposition, and Tikhonov regularization is used to favor the most parsimonious distribution of binding states (see section 5.1.4). Each binding state is descried as a pseudo-first-order reaction, while the kinetic model mimics multilayer formation. To evaluate the kinetic analysis for its usefulness to resolve FG domain – Kapβ1 binding kinetics, the analysis is applied on a simulated data set describing a more complex reaction than pseudo-first-order. The matlab code is available in the script *kinetic_analysis.m* in the appendix.

5.2.1.1 Implementation of the kinetic analysis

The analysis of the Kapβ1 - FG domain binding kinetics follows the basic idea of surface heterogeneity introduced by (Svitel et al., 2003). For this purpose the binding sites are modeled as a discrete set $P_i(k_{on}, k_{off})$ of totally $N = N_{kon} \times N_{koff}$ (i.e., 36 x 36) binding states

$$s_{total}(c,t) = \sum_{i=1}^{N} P_i(k_{off}, k_{on}) s_i(k_{off}, k_{on}, c, t) \Delta k_{off} \Delta k_{on} \qquad (5.27)$$

where the binding states can be represented in form of a grid of $N\ (k_{on}, k_{off})$-pairs
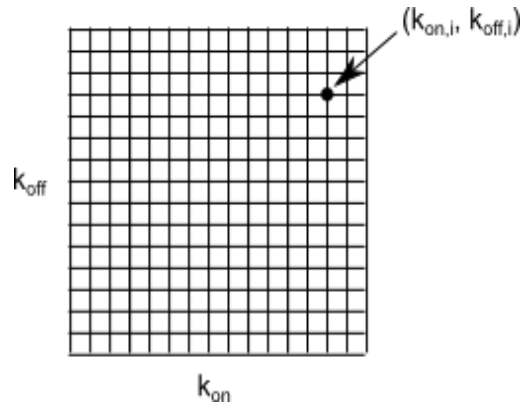
Fig. 5.2. Grid representation of the total $N = N_{kon} \times N_{koff}$ binding states. For each grid point i a binding sensogram $s_i(k_{on}, k_{off}, c, t)$ with $i = 1 \dots N$ is constructed and weighed by a factor $P_i(k_{on}, k_{off})$ represented as a contour plot of colors in the final interaction map.

and each grid point shall be weighed by a factor $P_i(k_{on}, k_{off})$ describing the fractional abundance. The weightings can be visualized in the 3rd dimension using a contour plot of colors. To do so for each grid point a full sensogram $s_i(k_{on}, k_{off}, c, t)$ is constructed that shows the characteristics in agreement with the experimentally obtained sensogram, e.g. for the dissociation phases $c = 0$. The kinetic model for the sensograms is defined by single (k_{on}, k_{off})-pairs assuming pseudo first order kinetics and was extended to the experimentally observed multilayer formation

$$L + A_s \underset{k_{off,i}}{\overset{k_{on,i}}{\rightleftarrows}} LA_1 + A_s \underset{k_{off,i}}{\overset{k_{on,i}}{\rightleftarrows}} LA_2 + A_s \underset{k_{off,i}}{\overset{k_{on,i}}{\rightleftarrows}} \dots \underset{k_{off,i}}{\overset{k_{on,i}}{\rightleftarrows}} LA_n \qquad (5.28)$$
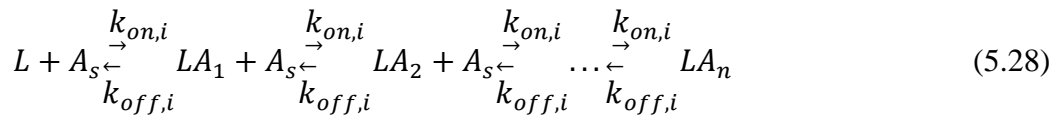
Here, L are the free binding sites, A_s is the analyte concentration in solution and LA_n are the occupied binding sites in each layer n. A set of ordinary differential equations arising from the kinetic model was solved numerically using the matlab function **ode15s**. The sensogram $s_i(k_{on}, k_{off}, c, t)$ is then calculated by linearly superimposing the concentrations $LA_1 + 2 \times LA_2 + 3 \times LA_3$, where the free ligand

concentration L is modeled as binding sites per surface area given by the size of the analyte ($10 \times 10 \ nm^2$ for Kapβ1). This simplification arises due to the fact that in the multivalent system 'Kapβ1 - FG domains' the distance of ligand sites on the surface is much smaller than the dimension of the analyte such that the analyte size is limiting the number of surface sites. This gives a total number of 1×10^{10} surface sites per mm^2 and each of them can accommodate up to n Kapβ1 molecules, according the multilayer extension. The concentration of occupied sites LA_n can be written as fractions of the initial ligand concentration L and for comparison the experimental sensogram can be transformed to number of layers by dividing through 2200 RU (see section 4.2). The sensograms $s_i(k_{on}, k_{off}, c, t)$ can now be arranged into a matrix $A = [s_1, s_2, \dots s_i, \dots s_N]$ to solve the following minimization problem, that was stabilized using Tikhonov regularization:

$$p_\lambda = argmin\{\|Ap - b\|_2^2 + \lambda^2 \|L(p - p*)\|_2^2\} \qquad (5.29)$$

where p is a vector with $N = N_{kon} \times N_{koff}$ elements for the set of discrete binding states, b is a vector of N_{dat} experimental data points and A is a matrix of $N_{dat} \times N$ elements including all calculated $s_i(k_{on}, k_{off}, c, t)$. The regularized Tikhonov solution p_λ was obtained using the Matlab package Regularization Tools by Per Christian Hansen (Hansen, 2007), where for L the identity matrix was used and for p^* a null vector was used. Additionally, the L diagonal elements that correspond to (k_{on}, k_{off})-pairs with K_D beyond the range of applied concentrations were modified by setting them K_D/c_{max} for $K_D > c_{max}$ and c_{min}/K_D for $K_D < c_{min}$, where c_{min} and c_{max} are the lowest and highest concentration in the data set $b(c, t)$, respectively. This helps to stabilize the solution in a K_D range of applied concentrations. Finally, to obtain $P_i(k_{on}, k_{off})$ starting from the Tikhonov regularized solution p_λ an active set method (Landi & Zama, 2006) was applied to provide a nonnegative regularized solution with help of the conjugate gradient algorithm in the Matlab package

Regularization Tools (Hansen, 2007).

For the mushroom analysis the kinetic model describes only monolayer formation in agreement to experimental observation and the number of binding sites was reduced if the grafting distance g_{cNup} exceeded 10 nm (dimension of Kapβ1), i.e. the size of each binding site was set to $g_{cNup} \times g_{cNup}$. For Nup98, in the dense regime, the monolayer model was used as well, in agreement with experimental observation.

5.2.1.2 Evaluation of the kinetic analysis

In order to test the precision of the kinetic analysis in revealing individual kinetic species a model-sensogram is constructed that is more elaborate than simple 1:1 binding and subsequently the (k_{on}, k_{off})-pairs can be calculated assuming pseudo-first-order kinetics. The model considers two state binding and a transition in binding site affinity:

$$L \underset{k_{-tr}}{\overset{k_{tr}}{\rightleftarrows}} L*$$
(5.30)

$$L + A_s \underset{k_{-a1}}{\overset{k_{a1}}{\rightleftarrows}} LA_{s1} \underset{k_{-b1}}{\overset{k_{b1}}{\rightleftarrows}} LA_{s2}$$
(5.31)

$$L* + A_s \underset{k_{-a2}}{\overset{k_{a2}}{\rightleftarrows}} L*A_{s1} \underset{k_{-b2}}{\overset{k_{b2}}{\rightleftarrows}} L*A_{s2}$$
(5.32)

where the surface sites L can undergo transition into L^* with constant k_{tr} (k_{-tr}) that changes the set of kinetics from k_1 to k_2 for analyte (A_s) binding. This is shown in

Fig. 5.3, where we have initially only surface sites L and as the reaction progresses L^* is formed such that the composition of surface sites changes dynamically.
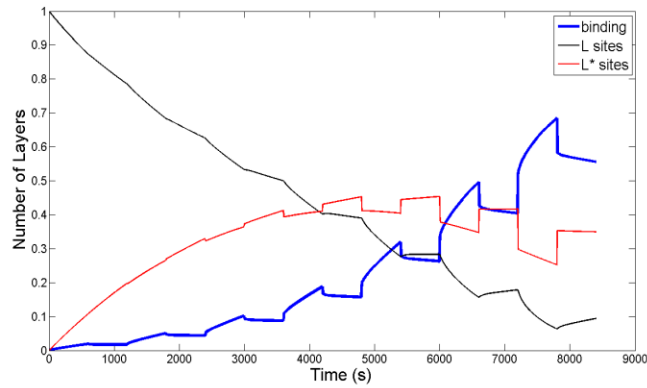
Fig. 5.3. Sensogram obtained from the kinetic model described by Eqs. 5.30 - 5.32. The binding of analyte is shown in blue, the free ligand sites of type L and L^* are shown in red and black respectively.

To obtain the binding sensogram in Fig. 5.3 the kinetic constants were set:

$k_{a1} = 1 \cdot 10^3 / k_{-a1} = 1 \cdot 10^{-2} \rightarrow K_{D1a} = 10\ \mu M$ $K_{D1.app} = 99\ nM$

$k_{b1} = 1 \cdot 10^{-2} / k_{-b1} = 1 \cdot 10^{-4}$

$k_{a2} = 1 \cdot 10^5 / k_{-a2} = 1 \cdot 10^0 \rightarrow K_{D2a} = 10\ \mu M$ $K_{D2.app} = 909\ nM$

$k_{b2} = 1 \cdot 10^{-3} / k_{-b2} = 1 \cdot 10^{-4}$

$k_{tr} = 2 \cdot 10^{-4} / k_{-tr} = 1 \cdot 10^{-4}$

where $K_{D,app}$ is calculated from

$$K_{D.app} = \frac{K_{Da}}{1+K_{Ab}} \tag{5.33}$$

The model was then decomposed into single (k_{on}, k_{off})-pairs as described above and shown in Fig. 5.4.
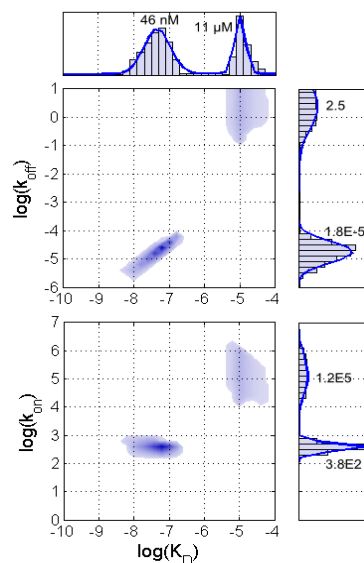
Fig. 5.4. Interaction map obtained for the model sensogram shown in Fig. 5.3 (blue). The map reveals a slow and a fast species with K_D of 46 nM and 11 μM respectively; the histograms are sums over the respective axes.

We can see from the interaction map that a fast and a slow phase are apparent. The fast phase agrees very well with the fast kinetics of the L^* phase k_{a2} and k_{-a2} and K_{D2a} for this phase (10^5 M^{-1}s^{-1}, 10^0 s^{-1}, and 10 μM respectively). The slow phase is distributed around a K_D of 46 nM that is similar, though lower, to $K_{D1.app} = 100\ nM$ and can be attributed to the limiting rates of the L phase k_{a1} and k_{-b1} that are given as 10^{-4} s^{-1} and 10^3 M^{-1}s^{-1} respectively. The divergence form $K_{D1.app}$ possibly arises from the inaccuracy of the solution at low concentrations (see Fig. 5.5), similarly as observed for many 'Kapβ1 - FG domain' binding solutions (see Fig. 5.7). The slow phase could additionally compromise other kinetic steps such as the "on rates" of the L and/or L^* phase given as 10^5 x 10^{-3} and 10^3 x 10^{-2}, respectively, that would influence the position of this distribution, and similar it would behave for the "off-

rates". Overall this model calculation shows that the technique provides the simplest distribution that is consistent with the data and as such minor phases could be incorporated into the shape and distribution of the major peaks in the map. An important point to consider is that the fast phase apparent at ~10 µM, the equilibrium constant of the first reaction step, whereas the second slow phase is apparent at $\sim K_{D1.app}$, the apparent constant of the overall reaction. Due to the dynamic transition in binding sites L/L^* the solution tends to deviate from the model at low concentrations, i.e. low K_D values.
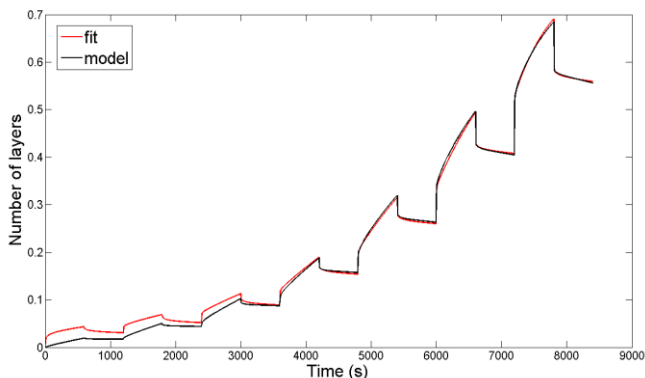
Fig. 5.5. Model sensogram obtained from Eqs. 5.30-5.32 (black) and respective solution (red) with RMSD = 0.0245.

5.2.2 Calculating average kinetic rates

The average k_{on} and k_{off} values for a range of concentrations c can be estimated from the interaction maps when considering the slope of the Langmuir isotherm (Eq. 4.6)

$$\frac{dR_{eq}}{dc} = \frac{K_D}{(c+K_D)^2} \tag{5.34}$$

where R_{max} was set to one. The average rate constant k_{av} is then calculated for summing over the entire interaction map for each point c defined on a suitable range of concentrations

$$k_{av}(c) = \sum_i \sum_j \left[\frac{\frac{K_D(i)}{(c+K_D(i))^2}}{\sum_i \frac{K_D(i)}{(c+K_D(i))^2}} \cdot \frac{k(j) \cdot M(j,i)}{\sum_j \sum_i M(j,i)} \right]$$

(5.35)

where $M(j, i)$ is the element of the interaction map with values $K_D(i)$ and $k(j)$. This analysis was applied to the fast phase and the slow phase via splitting the interaction map into two parts (see Fig. 5.13A). From Eq. 5.35 and neglecting the normalization terms as well as the rate constant k we have

$$p(c) = \sum_i \sum_j \left[\frac{K_D(i)}{(c+K_D(i))^2} \cdot M(j, i) \right]$$

(5.36)

such that

$$w_{fast} = \frac{p_{fast}}{p_{fast} + p_{slow}}$$

(5.37)

$$w_{slow} = \frac{p_{slow}}{p_{fast} + p_{slow}}$$

(5.38)

are the relative weightings w of the fast and slow phase, respectively. Notice that this is a simplified description as the Langmuir isotherm does not mimic the sequential binding constraint for multilayer formation used in the kinetic model.

5.2.3 Diffusion model for Kapβ1 kinetics

In order to investigate alternatively the characteristics of Kapβ1 binding to the FG layer, a simple model of diffusion in a potential was constructed. Here, the potential $U(r)$ has the following form:

$$U(r) = A \cdot exp(-((x - C)^2)/E) + B \cdot exp(-((x - D)^2)/F) - f(R) \cdot G \\ \cdot exp(-x/H) + I \cdot exp(-x/J)$$

(5.39)

As shown in Fig. 5.6 the potential $U(r)$ consist of two exponentials representing attraction due to the FG layer and hard wall repulsion near the grafting surface. Additionally, two Gaussian functions overlay the exponentials in order to generate a double-well potential. The function $f(R)$ accounts for the entropic penalty upon particle binding. Thus the function $f(R)$ manipulates the attractive exponential term and imposes a constraint on particle binding with particle loading R. This constraint mimics the finite capacity and conformational constraints of a molecular brush in agreement with polymer theory (see section 5.1.1). In our analysis we consider the following form of $f(R)$:

$$f(R) = 1 - R^2/R_{max}^2$$

(5.40)

where R_{max} is the maximal capacity of the brush. Importantly, the potential $U(r)$ is considered a potential of mean force (PFM) (see section 5.1.3.2) and thus comprises enthalpic as well as entropic contributions in a single dimension with the reaction coordinate normal to the grafting plane at $z = 0$. According to Kramers theory in the height friction limit (see Eq. 5.18) the reaction rate depends on the barrier height $U_b - U_a$ separating the reactant well a from the transition state b, as well as the shape

of the potential and the friction coefficient γ. In this model we consider the manipulation $f(R)$ to act on shifting U_b and U_a with only marginal influence on the shape of the potential. The friction coefficient γ and the shape of the potential ω, when comparing Eqs. 5.7 and 5.18, can be considered of entropical origin as well, and due to the arbitrary choice of γ and ω the potential hence has only qualitative character. The friction coefficient γ was treated as a constant over the entire potential and was set using the temperature dependent viscosity of water η_{H_2O} multiplied by a factor 100. The friction coefficient γ is involved in the simulation via the Stokes-Einstein relation for the diffusion coefficient D_{diff} and using a simple updating formula for particle movement in the potential (Gillespie & Seitaridou, 2013)

$$x(t + \Delta t) \approx x(t) + \frac{1}{\gamma} F_e\big(x(t)\big)\Delta t + \sqrt{2D_{diff}\Delta t}\, n_x \tag{5.41}$$

where $F_e(x) = -dU(x)/dx$ is the force acting on the particle derived from the potential energy function and n_x is a normal random variable $N(0,1)$ of mean $\mu = 0$ and variance $\sigma^2 = 1$. The above updating formula is physically accurate only for the non-ballistic regime $\Delta t \gg \tau \equiv m/\gamma$ (see section 5.1.3.3).
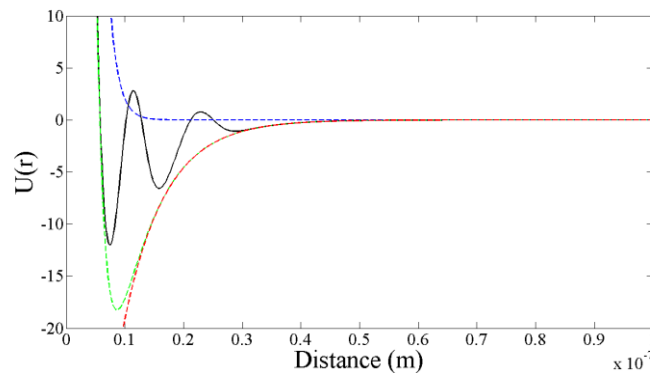

Fig. 5.6. The potential used for Brownian dynamics (solid line) is constructed from a repulsive exponential function (green dashed) and an attractive exponential function (red dashed), overlayed by two Gaussian functions to mimic the biphasic binding behavior observed experimentally.

5.3 Materials & Methods

SPR Measurement Protocol

All SPR measurements were performed at either 10°C or 37°C, respectively, in a four flow cell Biacore T100 instrument (GE Healthcare) where two flow cells were used as reference and the remaining two flow cells as sample cells. SPR bare gold sensor chips 'SIA Kit Au' were from GE Healthcare. Upon removal from storage in an argon atmosphere, gold sensor surfaces were ultra-sonicated in acetone and high purity ethanol (Merck) for 15 min respectively and dried in a nitrogen gas stream followed by 60 min UVO cleaning (Jelight Company Inc., Model 42A-220). The gold sensor surfaces were then ultra-sonicated for another 15 min in ethanol, dried in a nitrogen gas stream and mounted on the sample holder for immediate SPR usage. The clean gold sensor surface was incubated with cNup in PBS in flow cell 3-4. The incubation time was varied from 10 min up to 1 h at a flow rate of 2 μl/min to obtain different cNup grafting distances g_{cNup} (i.e., surface density). This was followed by a 120 s exposure to 1 mM $C_{17}H_{36}O_4S$ (nanoScience Instruments, US) to prevent unspecific binding to gold. Flow cell 1-2 was incubated with 1 mM $C_{17}H_{36}O_4S$ for 30 min at a flow rate of 2 μl/min. BSA titrations (3 x 30 sec with 60 s interval) after each Kapβ1 concentration followed at a flow rate of 10 μl/min with each injection passing all cells sequentially (6 min after each Kapβ1 injection). Average R_1 and R_2 values were measured at the end of each BSA injection cycle relative to the PBS baseline obtained 30 s later. The PBS running buffer was filtered and degassed using filterware (Techno Plastic Products AG) of 0.2 μm pore size. Kapβ1 was injected for 10 min at a flow rate of 10 μl/min at concentrations of 0.0001/ 0.0005/ 0.001/ 0.01/ 0.02/ 0.03/ 0.04/ 0.0625/ 0.125/ 0.25/ 0.5/ 1/ 2/ 4/ 8/ 13.4 μM although this could vary for different experiments.

5.4 Kinetic analysis

5.4.1 Binding to close-packed FG domains

To obtain a parsimonious distribution of kinetic constants, the analysis introduced by Svitel *et al* is applied (Svitel et al., 2003; Svitel et al., 2007) that uses a two-dimensional distribution of association and dissociation rate constants $\left(k_{on,i}, k_{off,i}\right)$ to describe Kapβ1-FG domain binding as a superposition of pseudo-first order reactions (see section 5.2.1.1). Briefly, this circumvents difficulties associated with analyzing heterogeneous interfacial interactions that are often encountered in multivalent systems (Peleg & Lim, 2010; Bright et al., 2001). In the present context, Kapβ1 binding depends on the FG domain surface density and the number of Kapβ1 molecules already bound. Here, k_{on} describes how quickly a Kapβ1 molecule locates and binds to FG repeats within a FG domain layer, while k_{off} correlates to Kapβ1-FG domain binding strength and stability. As already introduced in section 5.2.1.1, each surface site is "sticky" (in analogy to containing FG domains), and allows for analyte (Kapβ1) molecules to bind as kinetically modeled by

$$L + A_s \underset{k_{off,i}}{\overset{k_{on,i}}{\rightleftarrows}} LA_1 + A_s \underset{k_{off,i}}{\overset{k_{on,i}}{\rightleftarrows}} LA_2 + A_s \underset{k_{off,i}}{\overset{k_{on,i}}{\rightleftarrows}} \ldots \underset{k_{off,i}}{\overset{k_{on,i}}{\rightleftarrows}} LA_n \tag{5.42}$$
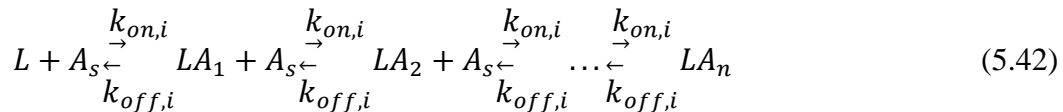
where L denotes the empty surface sites, A_s is the analyte concentration in solution, and LA_1 to LA_n correspond to surface sites where n represents the number of analytes that can bind per surface site. Here, we define $n = 3, 3, 1$ and 3 for cNup214, cNup62, cNup98 and cNup153, respectively. This imposes a sequential binding constraint that mimics the "multilayered" Kapβ1-FG domain binding characteristics observed experimentally (Fig. 5.7A).
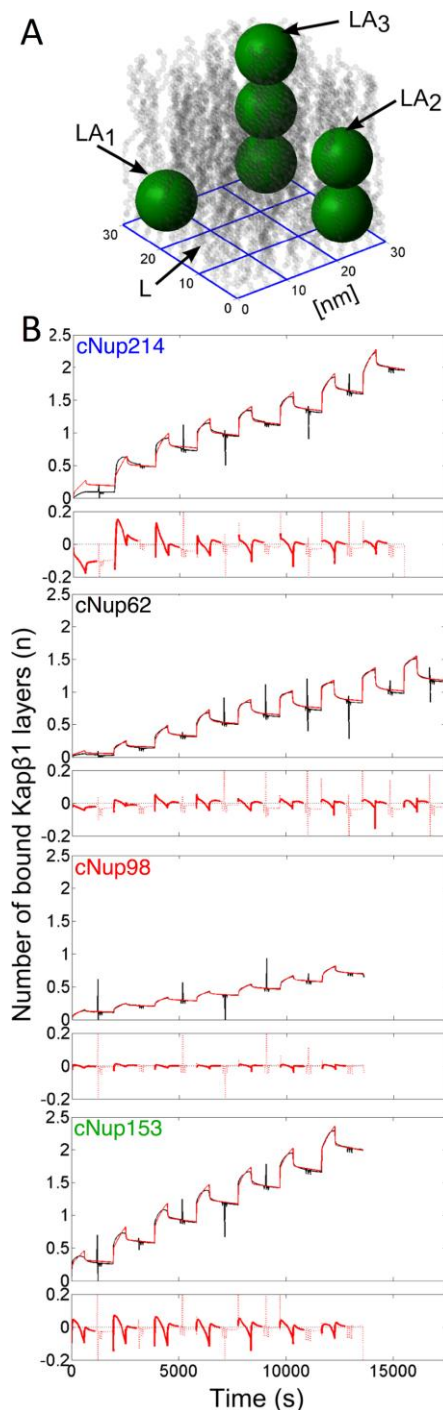
Fig. 5.7. Kinetic analysis of Kapβ1-FG domain binding. **(A)** Schematic representation of FG domain layer occupancy for $n = 1,2,3$. The model considers a two dimensional lattice of 10 x 10 nm^2 binding sites (based on the size of Kapβ1). L denotes the empty surface sites (i.e., FG domains) and LA_n corresponds to n number of analyte molecules bound per surface site. **(B)** Representative fits (gray) to SPR sensograms (black) for Kapβ1 binding to molecular brushes of cNup214, cNup62, cNup98, and cNup153 respectively. The residuals of the fits are included below the curves. Neglecting the SPR signals from BSA injections, the RMSD values (bold residuals) are: 0.13 (cNup214) > 0.094 (cNup153) > 0.063 (cNup62) > 0.026 (cNup98) (in terms of bound Kapβ1 layers). Note: Fitting errors may arise from structural changes that occur in the FG domain layer as Kapβ1 binding progresses (e.g., layer extension).

Fitting the SPR sensograms with this method (Fig. 5.7B) provides a constellation of k_{on} and k_{off} values in the interaction maps shown for each FG domain (Fig. 5.8A-D). Distribution analysis reveals distinct populations of k_{on} and k_{off} that can be grouped into slow (low k_{off}) and fast (high k_{off}) kinetic phases irrespective of the FG domain (Fig. 5.8E). The slow phase is manifested as a band with intense peaks for $k_{off} < 10^{-3}\ s^{-1}$ and $k_{on} < 10^6\ M^{-1}s^{-1}$ whereas the fast phase has a speckled distribution around $k_{off} \sim 10^0\ s^{-1}$ and $k_{on} \sim 10^6\ M^{-1}s^{-1}$ with a lower overall population as seen from the accompanying histograms. This fast phase accounts for about 10% of bound Kapβ1 molecules that exhibit a quick dissociation. An interesting feature of the slow phase for all FG domains is the occurrence of 2-3 peaks in k_{on} that decrease from $\sim 10^5\ M^{-1}s^{-1}$ at low K_D (i.e. high affinity) to $\sim 10^1\ M^{-1}s^{-1}$ at high K_D (i.e., low affinity). This likely denotes the transition from a moderate rate of penetration into a largely vacant FG domain layer at low Kapβ1 concentrations, to a slower rate of entry at higher concentrations due to a reduction of accessible binding sites within the layer and other effects such as layer extension and steric hindrance caused by increasing Kapβ1 occupancy. A slow release then follows in both cases once a stable complex is formed due to binding avidity. Importantly, this is accompanied by the emergence of the fast phase that becomes more prominent at higher Kapβ1 concentrations (i.e., high K_D), which can be correlated to limited binding at the periphery of the FG domain layer due to the onset of saturation inside it.

Interestingly, we find that k_{on} and k_{off} provide a broad range of K_D values. The maxima in the distributions as seen from the histograms on the top of each map correlates well with $K_{D1} \sim 100\ nM$ from equilibrium analysis (Fig. 4.10). In addition we find high K_D distributions with peaks at ~1 μM, 3.4 μM, 8.5 μM, 2.3 μM and for cNup214, cNup62, cNup98, and Nup153, respectively. Nevertheless, we note that the observed high K_D values have contributions from both slow and fast binding species with respective short or long half-lives (defined from k_{off}). Yet, in kinetic terms, the

vast Kapβ1 majority that interacts with an already saturated FG domain layer is in the fast phase. This is because they bind and unbind in a dynamic fashion with much higher attempt frequencies. Here, the fraction of interactions that lead into the slow phase can be estimated from $k_{on}(\text{slow})/k_{on}(\text{fast})$ (i.e., $10^1/10^6$), which corresponds to 0.001% at high Kapβ1 concentrations.
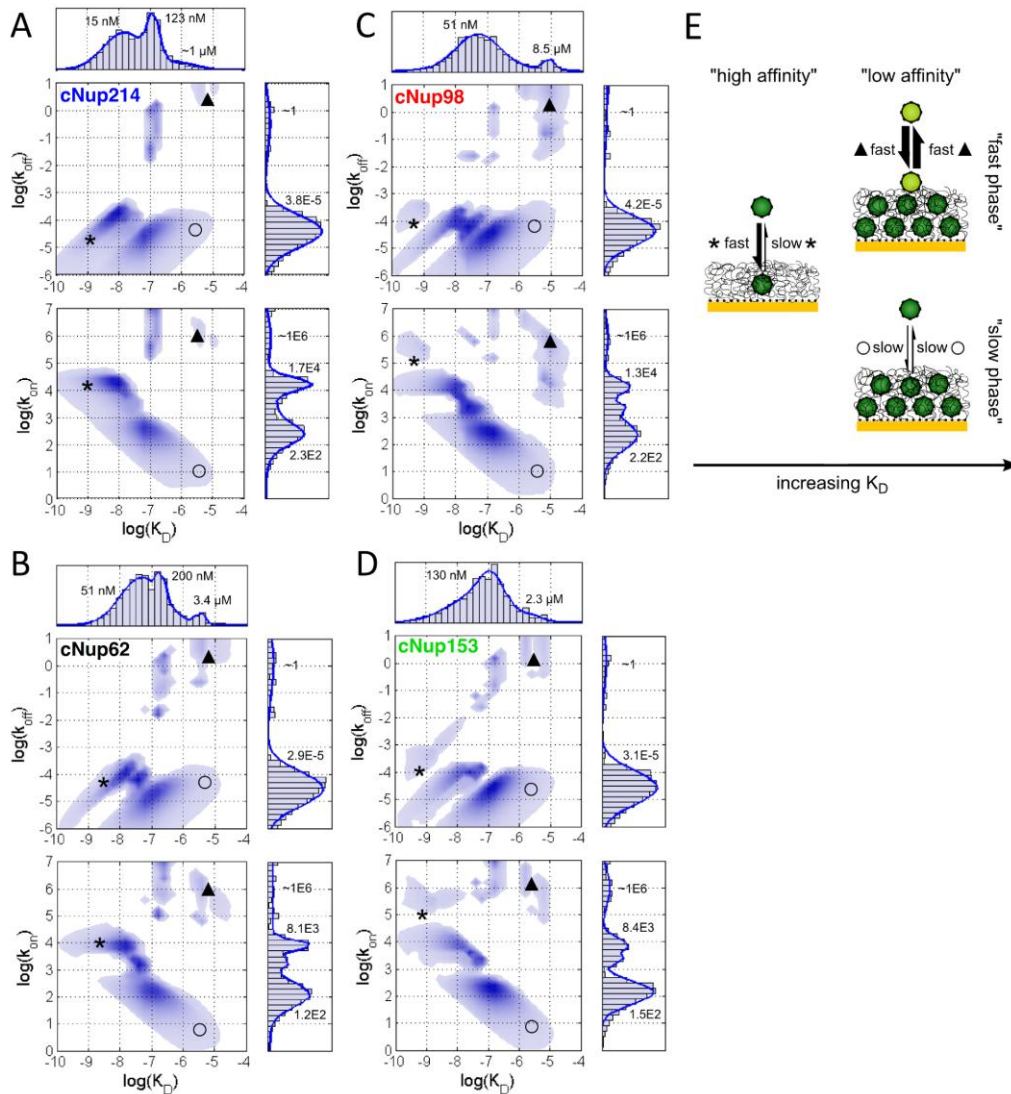
Fig. 5.8. Kinetic maps for Kapβ1 binding to close-packed **(A)** cNup214, **(B)** cNup62, **(C)** cNup98, and **(D)** cNup153. Each interaction map is averaged over four sensograms for each FG domain. The color intensity indicates the fractional abundance of a kinetic state. The accompanying histograms (top and right panels) sum over all values in a given axis. **(E)** State diagrams separating slow (dark; low k_{off}) and fast (light; high k_{off}) kinetic phases of Kapβ1 binding. Moderate to fast k_{on} into a largely vacant FG domain layer and slow k_{off} due to stable multivalent interactions results in high affinity binding (*). Two low affinity phases emerge due to FG domain layer saturation: a fast phase characterized by high (k_{on}/k_{off})-pairs due to limited binding at the layer periphery (▲); and a slow phase characterized by low (k_{on}/k_{off})-pairs due to slow penetration into a preoccupied layer (o).

5.4.2 Binding to sparse FG domains

The K_D distribution in the sparse FG domain regime is narrow in agreement with equilibrium Langmuir isotherm analysis (Fig. 4.10). Here, the fast phase is still present but reduced in population, i.e., a lower fraction of complexes with high $k_{off} \geq 0.001$ is observed. It is also striking that the slow k_{on} phase is well defined with a single dominant peak that is of similar magnitude to saturated close-packed FG domain layers, i.e. $10^1 - 10^3$ $M^{-1}s^{-1}$. Nonetheless, the reduction in k_{on} that is correlated to the level of Kapβ1 occupancy in the close-packed regime does not feature in the sparse regime.
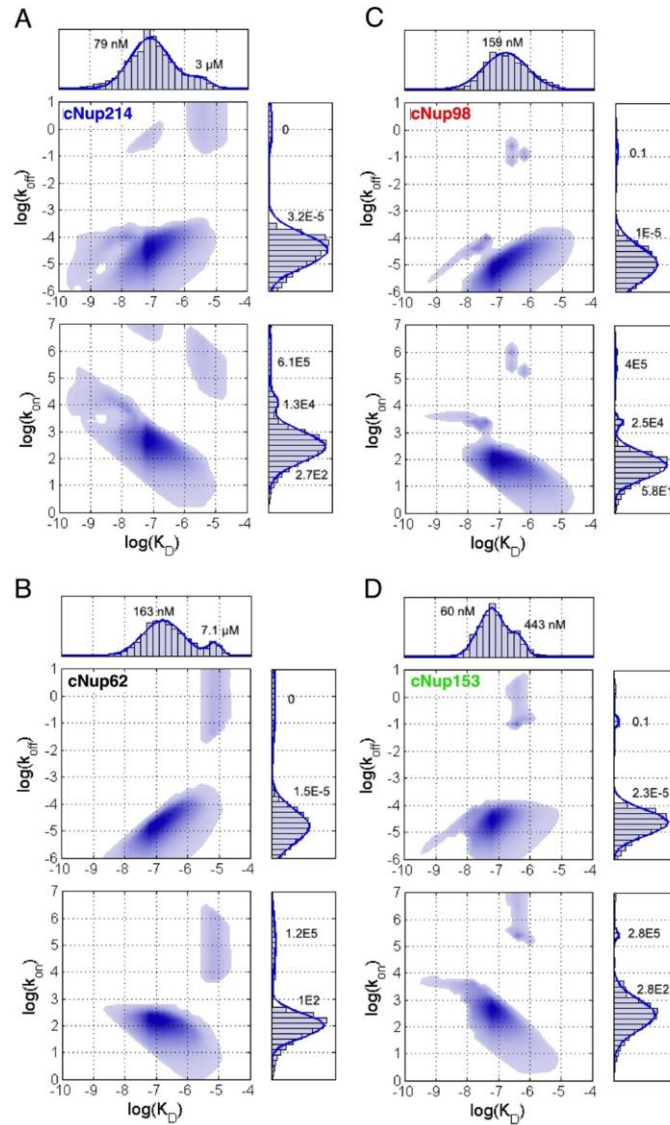
Fig. 5.9. Global kinetic analysis of the Kapβ1 binding to the sparse layers of cNup214 **(A)**, cNup62 **(B)**, cNup98 **(C)** and cNup153 **(D)**. Histograms on the right side of the interaction map are showing a probability of the different kinetic species with certain k_{on} and k_{off} rate constants. The histograms on the top of the plots are representing affinities weighted distribution.

5.4.3 Diffusion model

In order to investigate the binding of Kapβ1 to the FG layer a Brownian dynamics simulation was performed for particles moving in a two well potential (see section 5.2.3). This is closely related to the concept of a time dependent binding potential for

brush-particle interactions (Szleifer, 1997) (see section 5.1.1).The aim of this simulation is to reproduce the main characteristics of Kapβ1 binding qualitatively:

(i) Biphasic binding, i.e. slow and fast binding phases.

(ii) Fast establishment of a binding equilibrium while maintaining slow dissociation.

The time steps in the simulation were chosen as $\Delta t = 100\ ns$. The friction coefficient γ is $8.3922 \times 10^{-9}\ Nsm^{-1}$ at 25°C. This value is 100 times higher than the value for H_2O in order to mimic the high γ-limit. Using the mass of Kapβ1 (100 kDa) we get $\tau = 1.9787 \times 10^{-11}$ and thus the condition $\Delta t \gg \tau$ is maintained (see section 5.1.3.3). The diffusion coefficient is then given as $D_{diff} = 4.9050 \times 10^{-11} m^2 s^{-1}$ when using the Stokes-Einstein relation and a protein radius $r = 5\ nm$ for Kapβ1. In the simulation the number of particles in the bulk was maintained constant at 10 particles while the average number of particles in the first and second pocket were averaged at each time-point of the simulation with spacing $\Delta t = 0.05\ s$.
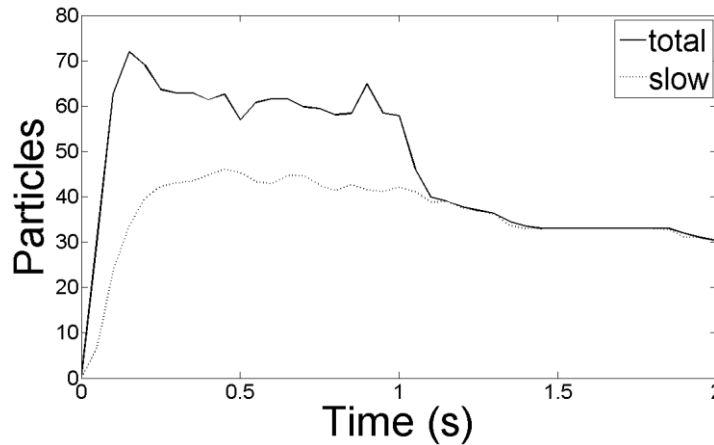
Fig. 5.10. Simulated binding curve for $T = 25°C$ using the double-well potential and the binding constraint $f(R) = 1 - R^2/R^2_{max}$.

Fig. 5.10 shows a binding curve obtained in the double-well potential at $T = 25°C$ and for a binding constraint $f(R) = 1 - R^2/R^2_{max}$ (see Eq. 5.40). The slow phase corresponds to particles in the first well close to the grafting surface. The total

binding curve clearly reveals a biphasic behavior with fast and slow dissociating species. However, only due to the manipulation $f(R) = 1 - R^2/R_{max}^2$ this leads to a fast saturation of the slow phase, as particle loading R leads to a contraction of the attractive potential term G in a time dependent manner. How does this contraction modify the potential? Fig. 5.11 introduces the main measures that define the kinetics and equilibrium of binding, i.e. the potential energy of a particle in binding well (2) is $U(a)$, at the transition state is $U(b)$ and in binding well (1) is $U(c)$, respectively. The kinetic rate for entering the first well $k_{on,1}$ is proportional to $\exp[-(U(b) - U(a))]$, whereas the kinetic rate for leaving the first well $k_{\text{off,w1}}$ is proportional to $\exp[-(U(b) - U(c))]$. The binding equilibrium constant of the first well $K_{D,w1}$ is proportional to $\exp[-U(c)]$ whereas the binding equilibrium of the second well $K_{D,w2}$ is proportional to $\exp[-U(a)]$. The contraction of the attractive potential (red dashed) with particle loading R will obviously shift the equilibrium $K_{D,w1}$ and $K_{D,w2}$ to higher concentrations. In agreement with this the kinetics are changing as well. Due to the exponential character of the attractive potential the absolute change of the potential will manifest as follows: $\Delta U_c > \Delta U_b > \Delta U_a$, such that upon particle loading, $k_{on,w1}$ is decreasing, while $k_{off,w1}$ is increasing ($w1$ for well 1). Thus the manipulation $f(R) = 1 - R^2/R_{max}^2$ enforces a fast binding equilibrium in binding well 1. The potential before (blue) and at the end of the association phase (red dashed), i.e. when the brush is loaded, is shown in Fig. 5.12, respectively.
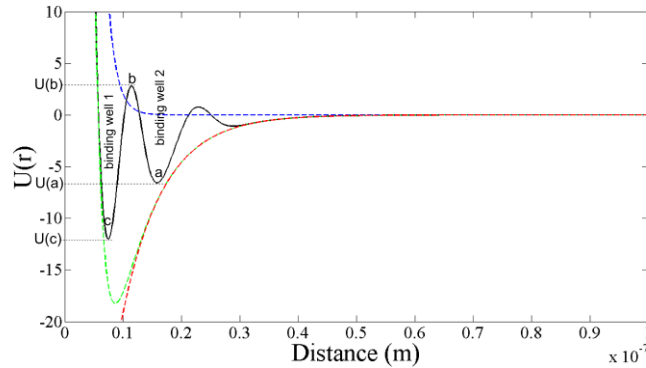
Fig. 5.11. The starting potential used for Brownian dynamics has two binding wells. The potential energy at well 2 is $U(a)$, at well 1 is $U(c)$ and for the barrier between the wells is $U(b)$, respectively. The red attractive potential G is contracting with particle loading R due to the constraint $f(R)$. The potential has only qualitative character.
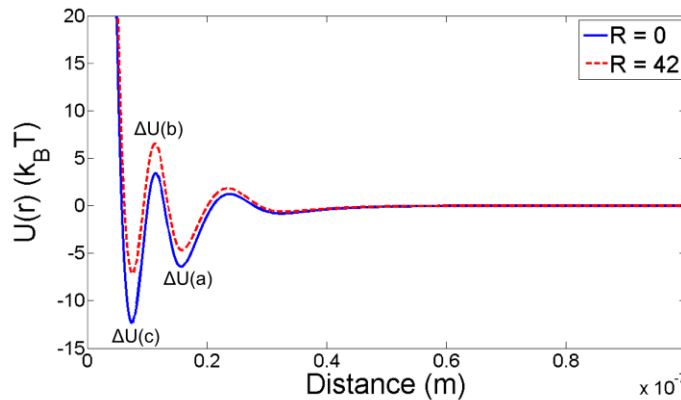
Fig. 5.12. Potential before ($R = 0$) and after particle binding ($R = 42$). The potential changes due to the manipulation $f(R)$ that leads to a contraction of the attractive potential G. This enforces a fast binding equilibrium in well 1 as $\Delta U(c) > \Delta U(b)$. However also well 2 is influenced by this manipulation.

5.5 Discussion

Importantly, the two equilibrium phases detected in the last chapter do not correspond directly to the fast and slow phases revealed from the kinetic maps, rather it seems that both of those kinetic phases respond to the occupancy of the FG layer. This is nicely depicted in Fig. 5.13, that is based on splitting the interaction map for Nup62

into two parts for achieving phase separation. The average k_{on} and k_{off} values in Fig. 5.13 are derived from reconstructing Langmuir isotherms (see section 5.2.2). The black line represents the fast phase, whereas the blue line represents the slow phase. The thickness of the line is the weighting that indicates the contribution of each phase to surface binding. Fig. 5.13 shows that the fast phase contribution to surface binding increases with Kapβ1 concentration $c_{Kapβ1}$, whereas the slow phase contribution moderately decreases. This goes together with an increase in the fast k_{off} rate as well as a decrease in the slow k_{on} rate. Interestingly this transition takes place in the low μM range of Kapβ1 bulk concentration.
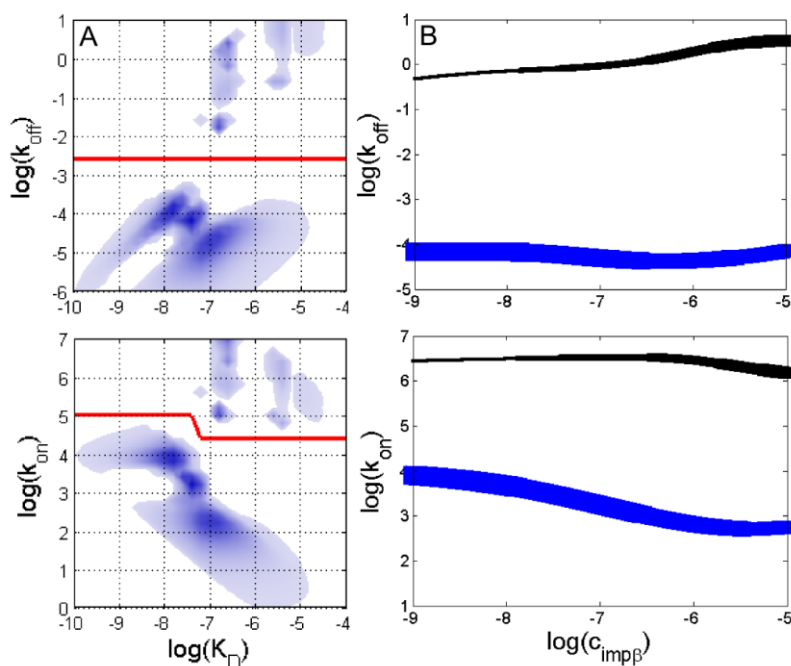
Fig. 5.13. (A) Splitting of the interaction map for cNup62 into two parts for separating the fast from the slow phase. **(B)** Average k_{on} and k_{off} for the fast (black) and slow (blue) phase with Kapβ1 concentration. The thickness of the lines represents the contribution of each phase to surface binding.

This is reminiscent of a "highway" effect, where Kap transport at the channel walls is slow but fast near the center (Fig. 5.14). The "highway" effect might explain how *in vivo* NPC transport is fast despite strong binding avidity measured *in vitro* thus far. The kinetic analysis shows that over time only an estimated 0.001 % of the total interactions would lead to the slow phase at physiological concentrations. Thus, in the scenario of a preoccupied NPC most Kapβ1 molecules entering the central channel

would remain in the fast phase. Meanwhile, cNup98 is able to promote fast transport because of intra-layer cohesion that makes it the least penetrable to Kapβ1. With their fast off-rates ($k_{off} \sim 1 s^{-1}$) and short half-lives (< 100 ms), these species would dominate fast transport through the NPC at physiological Kap concentrations. Nevertheless, this would require an unobstructed path in order to support transport by the fast phase, such as a single central channel that would be surrounded by the peripheries of Kap-occupied FG domain layers. The tightly bound slow phase Kapβ1 molecules thus likely serve as an integral, possibly regulatory component of the NPC.
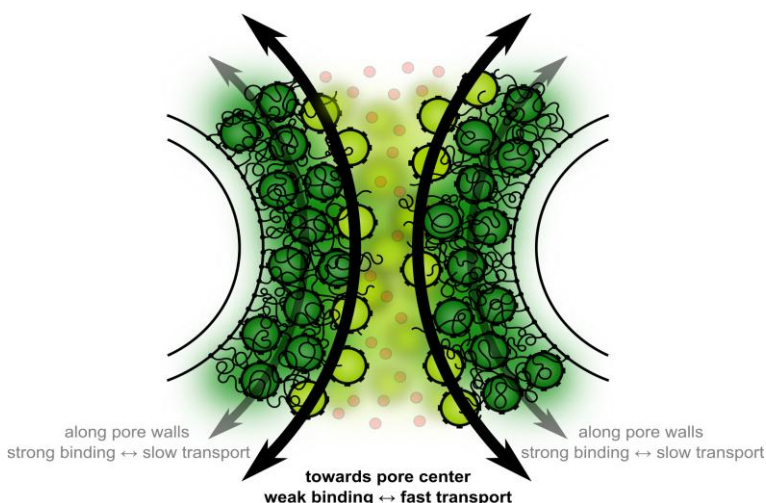
Fig. 5.14. The Nuclear Pore Complex Transport Highway. Model of the NPC "highway" where Kapβ1 traffic can proceed via at least two "lanes" at physiological concentrations. Slow transport is anticipated for strongly bound Kapβ1 molecules (dark green) that saturate semi-collapsed FG domains around the pore walls. Fast transport occurs nearer the pore center where Kapβ1 binds weakly to unoccupied FG domain protrusions (light green). Small passive molecules (red watermarked) may diffuse freely through the pore center.

Transportin molecules accumulate to the nucleus with a Michaelis-Menten constant $K_M = 4 \, \mu M$, whereas at higher transportin concentrations the transport rates do not saturate, apparently due to cooperativity in NPC passage (Ribbeck & Görlich, 2001). If the translocation of transportin molecules follows the highway effect, this is in agreement with a cooperative change of the fast phase with occupancy of slow phase binding sites. Similar, the transport times of import complexes consisting of NLS-2xGFP, Kapβ1, and Kapα1 was dropping from 8.6 ± 0.4 ms to 1.4 ± 0.1 ms as the

Kapβ1 concentration was increased from 0.1 nM to 15 μM at a fixed cargo concentration of 0.1 nM, thereby improving import efficiency (Yang & Musser, 2006). Akin the highway model, the fast phase is not diminished at low Kapβ1 concentrations but is getting more pronounced at high Kapβ1 concentrations due to limited access to FG domain protrusions at the layer periphery. Similarities can be found with Ma *et. al.* in terms of the preferred localization of Kapβ1 in the NPC (Ma & Yang, 2010) where translocation occurs (Ma et al., 2012), and the open pore center for passive diffusion. FG domain protrusions towards close to the center may certainly contribute to the inhomogeneous, viscous characteristics of the central channel (Ma et al., 2010). The tightly bound slow phase is in well agreement with the observation of ~100 Kapβ1 molecules that populate the NPC at steady state (Tokunga et al., 2008).

The NPC transport highway reconciles key features postulated by different NPC models. While entropic exclusion rejects non-binding molecules, rapid and reversible binding to FG domain protrusions would promote fast diffusional exchange between the two faces of the NPC (Rout et al., 2000). Fast phase interactions of the NTR's with the FG domains resembles reduction of dimensionality (Peters, 2005). However, reduction of dimensionality in context of the NPC transport highway may resemble spatial diffusion with preferential localization of the NTR's near the NPC wall (Ma & Yang, 2010). The actual residence time of the NTR's inside the NPC would then depend on the fast phase k_{off} and the number of binding events during NPC passage (Berezhkovskii et al., 2002 & 2005). The open channel configuration has important consequences not only in that it would guarantee the transport of big cargo's, an open channel would necessitate molecular crowding of fast phase transport receptors to out-compete passive diffusion (Kowalczyk et al., 2011). Thus the highway model supports a view where crowding is not only important for selectivity (Zilman et al., 2007), but also in promoting fast NTR transport trough the NPC. Finally, it is possible that in the confined geometry of the NPC the structural response upon Kapβ1 binding is modified, e.g. favoring condensation of the FG domains (Ma et al., 2012),

whereas steric and entropic constraints promoting the fast phase already apply at lower grades of re-extension.

In analogy with polymer theory (Szleifer, 1997; Kim & O'Shaughnessy, 2006), Kapβ1 entering the slow phase has to overcome a steric barrier due to protein – FG domain osmotic repulsion. Moreover, the average entropic degrees of freedom of the chains are modified with protein adsorption. Thus, as proteins adsorb, the effective interaction potential changes and there will be an additional protein-protein repulsion. As a result the effective potential of Kapβ1 – FG domain interactions is time dependent. This is clearly reproduced in the kinetic maps as we observe a decrease in the slow phase k_{on} for entering the FG layer with increasing Kapβ1 occupancy. Due to the time dependence of the effective potential it is difficult to establish a meaningful kinetic model. The binding curves in particular reveal fast saturation while remaining slow dissociation. Any model with a static set of binding sites (i.e. the sites do not evolve cooperatively) will fail to reproduce the peculiar shape of the binding curves. Using distribution of binding sites nevertheless helps to identify the kinetic species involved in the reaction despite its static character. It is therefore not surprising that the rmsd of the regularized solutions have the same scaling as the extensibilities, namely, cNup214 > cNup153 > cNup62 > cNup98, supporting the notion of conformational changes affecting the Kapβ1 – FG domain interactions progressively.

The Brownian dynamics simulation exemplifies the principle of Kapβ1 – FG domain binding. The entropic penalty for particle binding was directly applied to the two well potential, that is considered a PMF (see section 5.1.3.2), via the modification $f(R)$. The energy required to stretch an ideal chain is purely entropic and is quadratic in extension, i.e. the retracting force is proportional to extension and thus follows Hooke's law (Dill & Bromberg, 2002). At already moderate Kapβ1 concentrations the FG domains start to extend and thus cause an entropic penalty to the end-tethered FG domains. This simple analysis shows that the characteristic binding curves obtained

for Kapβ1 binding are strongly influenced by surface tethering effects of the FG domains and entropic constraints of chain stretching. The kinetics of Kapβ1 binding, in agreement with polymer theory (Szleifer, 1997), can only be described considering a time dependent potential as a function of adsorbed protein. Using a time dependent manipulation of the attractive potential, the fast binding equilibrium and slow dissociation of Kapβ1 binding can be reproduced. However, an exact description of Kapβ1 binding kinetics using Brownian dynamics is not straight forward due to the complexity of the system. It is very likely, that in such a description the capacity of the brush is a dynamic quantity as well, depending on bulk Kapβ1 concentration due to the cooperative mechanism of FG bundle distortion.

5.6 Error analysis

SPR comes with several limitations concerning the measurement of fast kinetics, one of them is restricted mass transport due to limited translational diffusion in laminar flow cell systems (see section 5.1.2). The diffusion coefficient D can be estimated from the Stokes-Einstein relation. Using $r = 4.95\ nm$ for the hydrodynamic radius of Kapβ1 and the viscosity of water $\eta = 0.891 \cdot 10^{-3}\ Pa \cdot s$ at 25°C we get $D = 4.95 \cdot 10^{-11}\ m^2/s$. For the flow cell dimensions we use $w = 5 \cdot 10^{-4}\ m$, $h = 5 \cdot 10^{-5}\ m$ and $l = 0.24 \cdot 10^{-2}\ m$ as the width, height and length, respectively (Myszka et al, 1997). This yields a diffusion limited rate constant $k_{tr} = 7.55 \cdot 10^{-6}\ m/s$. The relation $k_a\ R_T/k_{tr} \geq 1$ (see section 5.1.2) for transport limited surface binding, using a receptor concentration of $R_T = 1.66 \cdot 10^{-11} M \cdot m$ for Kapβ1 binding, which is obtained for a regular lattice with Kapβ1 sized binding sites (i.e. $\sigma_{Kap\beta1} = 10\ nm$), is fulfilled if $k_a \geq 4.55 \cdot 10^5 M^{-1}s^{-1}$. In case of the nucleoporins we need to consider that there is no single type of binding site, such that even though there are binding states with k_{on} around 10^6 M^{-1} s^{-1} they do appear in lower number than $R_T = 1.66 \cdot 10^{-11} M \cdot m$. If we assume 10% of RT to appear as fast binding sites, as expected from the interaction maps, we get mass transport limitations only for $k_a \geq 4.55 \cdot 10^6 M^{-1}s^{-1}$. For a distribution of binding sites and affinities it is not straight forward

to implement the two compartment model (see section 5.1.2) due to the competition of all sites for the analyte in the compartment close to the surface. In the distribution analysis the theoretical binding curves s_i (see section 5.2.1.1) are independent which is not the case if Eqs. 5.4 and 5.5 are used. However, for states with $k_a > 10^6$ it should be kept in mind that these states might be mass transport limited. Another limitation is the data collection rate of the SPR instrument. Even though data can be collected at 10 Hz, the amount of data is getting large for long running experiments. In order to make data analysis computationally feasible, the time resolution was reduced to 1 Hz for the singular value decomposition. This implies that off rates $k_{off} > 1 \, s^{-1}$ are not to be determined with accuracy.

The two compartment model (Eqs. 5.4 and 5.5) can however be applied to determine qualitatively the effect of mass transport limitation. This is shown in Fig. 5.15 for using $k_{tr} = 7.55 \times 10^{-6} \, m/s$, $s_{max} = 1.66 \times 10^{-11} \, M \cdot m$ and $h_i = 1 \times 10^{-6} \, m$. Severe mass transport limitation is observed only if k_{on} is fast and thus rebinding is fast (Fig. 5.15). This suggests that the fast phase kinetics that we measure are lower limits.
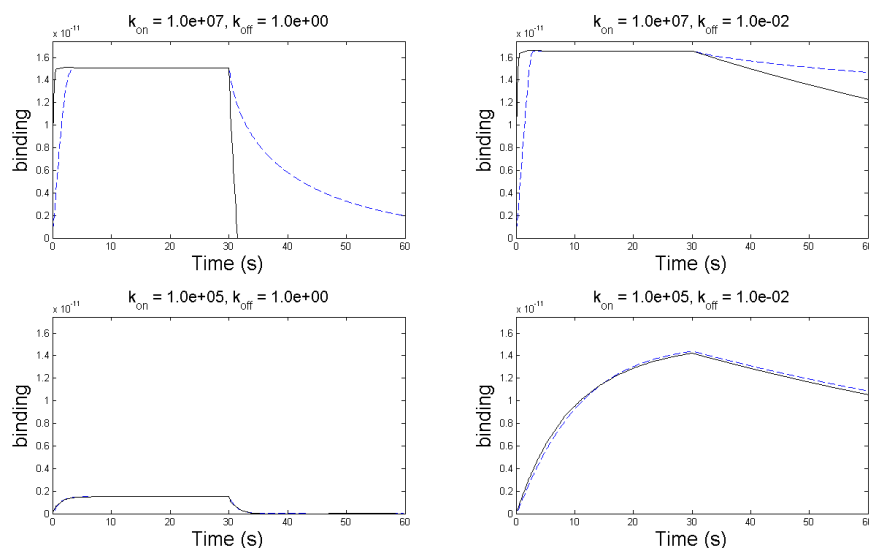
Fig. 5.15. Two compartment model (see section 5.1.2) applied for several cases of (k_{on}, k_{off})-pairs. Mass transport is only observed if k_{on} is fast.

Chapter 6

Model of Kap-centric NPC control

This chapter was published in Kapinos & Schoch et al., 2014.

6.1 Discussion

A major consequence of the findings is that at physiological concentrations the tightly bound, slow phase Kapβ1 molecules likely form an essential *barrier* component of the NPC that acts against non-specific cargo's. This represents a shift in paradigm with respect to FG-centric barrier models (e.g., brush, meshwork) because this highlights the role of both the FG domains and Kaps, and not the FG domains alone. Apparently, the FG domains act as a flexible "velcro"-like scaffold that can extend and contract with increasing or decreasing Kap occupancy, as explained by the ability of infiltrating nanoparticles to control molecular brush morphology (Opferman et al., 2013). However, beyond this, the findings predict that Kap occupancy dictates NPC barrier conformation, transport selectivity and speed in the NPC.

Such a Kap-centric barrier model is shown in Fig. 6.1. At physiological concentration, the NPC mechanism consists of a majority of slow phase Kapβ1 molecules that are incorporated within extended FXFG domains that line the central channel towards the NPC periphery with the exception of Nup98 (i.e., GLFG) that forms a cohesive annular ring around the central plane. Together, the Kaps and the engorged FG domains surround a narrow aqueous channel along the NPC axis that enforces the passive size limit while remaining selective to fast phase Kapβ1 molecules that bind weakly enough to diffuse along peripheral regions of the FG domains e.g., by a reduction of dimensionality (Peters, 2005; Peters, 2009). Any perturbation that reduces Kapβ1 occupancy would lead to a retraction of the barrier and a decrease in

selectivity (i.e., the pore would become more leaky) because of a widening of the aqueous channel. Consequently, this leads to a slow down of subsequent Kapβ1 transport given the increase of free FG repeats. However, the re-population of the NPC by slow Kapβ1 species would provide a feedback mechanism that reinstates Kap-occupancy, self-heals FG domain conformation, and thereafter normalizes transport selectivity and speed control. This may explain how the mechanistic (occupancy) and kinetic (FG repeat availability) characteristics of the barrier are balanced to accommodate local perturbations in the NPC (i.e., higher Kapβ1 occupancy => higher selectivity/less leaky and fast Kapβ1 transport; lower Kapβ1 occupancy => lower selectivity/more leaky and slow Kapβ1 transport).

Importantly, the proposed molecular view directly agrees with the preferential binding of Kapβ1 along the NPC walls due to FG domain binding and may further embody the interactions that underlie the NPC transport pathway as a "self-regulated viscous channel" (Ma et al., 2012; Ma & Yang; 2010). Further validations can be found from the inverse correlation between (decreasing) Kapβ1 interaction time and (increasing) import efficiency with increasing Kapβ1 concentrations where efficient nuclear transport only commenced at sufficiently high Kapβ1 concentrations (> 1.5 μM) (Yang & Musser, 2006). This work also predicts that a continuum of different transport rates can exist depending on local NPC Kap concentrations. This scenario explains why the NPC cannot be devoid of Kaps because any Kap that encounters an FG domain-only barrier would suffer from high FG binding avidity and slow down. A final provocative consequence of a Kap-centric barrier mechanism is that a reduction of Kaps rather than FG domains (Strawn et al., 2004) would result in NPC "leakiness". As a case in point, an increased presence of Kaps seems to "tighten" barrier functionality in both FG domain gels (Frey & Görlich, 2009) and artificial NPC's (Jovanovic-Talisman et al., 2009).

Physiological Kap concentration:
optimal selectivity, fast transport

Reduced Kap concentration:
decreased selectivity, slow transport
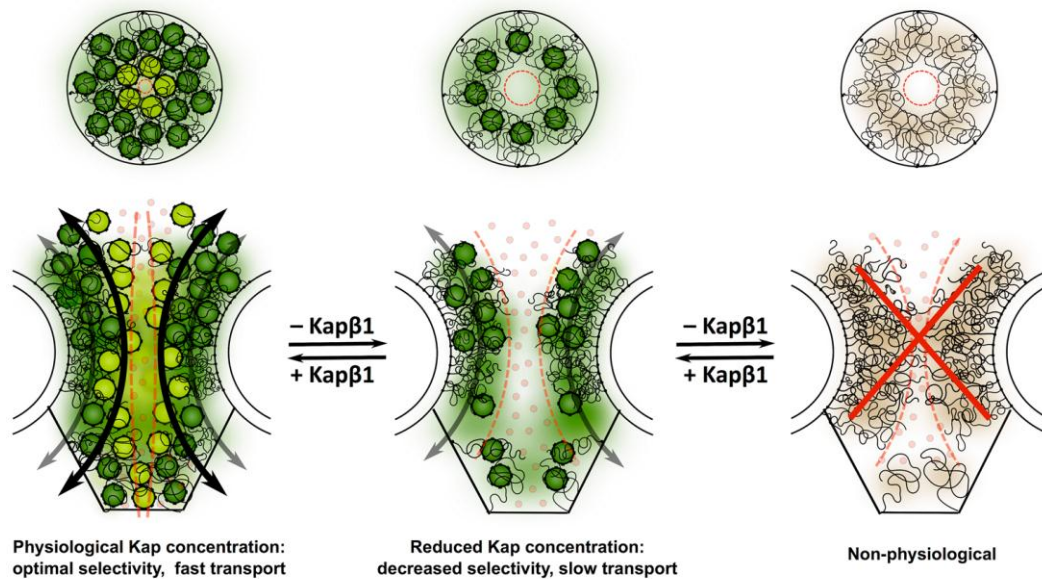
Non-physiological

Fig. 6.1. Kap-centric control in NPC's. Kapβ1 is an integral constituent of the NPC at physiological steady state conditions. Selective barrier functionality against non-specific cargoes is provided by slow phase Kapβ1 molecules (dark) that saturate and engorge peripheral FG domains (e.g. Nup214 and Nup153). Fast phase Kapβ1 molecules (light) promote fast transport through a narrow central channel (e.g., Nup62) due to the limited availability of FG repeats. Nup98 coheres into a narrow annular ring or "bottleneck" at the central plane of the NPC. Kapβ1 reduction leads to barrier contraction and a decrease in selectivity because of a widening of the aqueous channel. The availability of free FG repeats slows down the transport of Kapβ1 molecules, which eventually re-populate the FG domains to reinstate normal Kap-occupancy, and thereafter selectivity and speed control. NPC's devoid of Kapβ1 are likely unphysiological.

Chapter 7

Outlook & Conclusions

7.1 Conclusions

I have successfully converted a fundamental biological problem into a tractable biophysical question which I have evaluated using a SPR method that I have innovated. My findings clearly show that FG domain conformation is directly impacted by Karyopherin binding. This is moreover influenced by the surface density of FG domains. The conformational changes also influence multivalent binding in a significant way. Unlike current FG centric models we predict that Kapβ1 forms a key component of the NPC. However, a mature limitation is that SPR is done on an infinite plane and not on a pore geometry. The geometrical confinement of FG domains needs to be studied in the future (see Outlook).

This thesis is considered to reveal insight into the molecular mechanisms of nucleo-cytoplasmic transport (NCT) based on the structure – function relationship of phenylalanine-glycine (FG) nucleoporins *in situ*. Surface plasmon resonance (SPR) is the most sensitive technique for probing molecular affinities, however, persistent challenges in determining molecular structure anticipated the development of a novel technique appropriate in this context:

Non-interacting molecules can be used to determine the thickness of surface-tethered molecular brushes using SPR.

The technique revisits the fundamental aspect of molecular brushes to entropically hinder proteins from surface adsorption as shown for polyethylene glycol (PEG). Applied to surface-tethered FG domains, that are considered intrinsically disordered, this technique reveals that:

Close-packed, end-tethered FXFG domains behave similar to polymer brushes regarding their ability to extend away from the surface and their protein repellant properties.

Further, the FG domain layers can be probed structurally by stepwise titration of increasing nuclear transport receptor (NTR) concentrations and using non-interacting molecules, as in case of Karyopherin-β1 (Kapβ1):

The FXFG domains extend with increasing Kapβ1 concentration in order to accommodate high numbers of Kapβ1.

Interestingly the extensibilities of the vertebrate FG domains scale with their putative localization towards the nuclear pore periphery: Nup214 > Nup153 > Nup62 > Nup98. In analogy to polymer theory the brush – particle binding potential is time dependent with a binding capacity governed by polymer stretching:

FG domain surface-tethering causes entropic regulation of the binding capacity and binding affinity of slow phase Kapβ1, respectively.

The Kapβ1 molecules that are getting trapped inside the FG domain layer reveal low

off-rates k_{off} due to avidity (i.e. multivalent binding). They are therefore considered to form a slow phase that can not account for the rapid *in vivo* dwell times. However, for titrating Kapβ1 to physiological concentrations, the Kapβ1 – FG domain interaction reveals a range of affinities. Thus, avidity does not hinder fast transport *per se*. Moreover, the kinetic analysis of the Kapβ1 – FG domain interaction reveals a biphasic population including slow and fast binding species. The rates of those phases evolve upon layer filling:

FG domain layer saturation and extension promotes a fast phase with high off-rates k_{off}.

Layer saturation can therefore be considered a cooperative process that influences succeeding binding events. Regarding the nuclear pore complex (NPC) the above mentioned findings indicate that:

The tightly bound slow phase Kapβ1 molecules likely serve as an integral, possibly regulatory component of the NPC.

Nevertheless, this would require an unobstructed path in order to support transport by the fast phase, such as a single central channel that would be surrounded by the peripheries of Kapβ1-occupied FG domain layers. Nucleo-cytoplasmic transport from this perspective might likely work on the principles of competition and crowding based selectivity (Zilman et al., 2007) as well as reduction of dimensionality (Peters, 2005), where Kapβ1-occupied FG domain layers define the pore boundary and tune interaction strength.

7.2 Outlook

7.2.1 Lateral diffusion of slow phase Kapβ1

In order to complete the *in vitro* based approach to the molecular mechanism of NCT, some important controls need to be done in the near future. Even though the results from SPR are in good agreement with *in vivo* studies on nucleo-cytoplasmic transport (see section 1.2.4.1), SPR is lacking lateral resolution. The slow phase determined by SPR is defined by the low off rates k_{off} of the Kapβ1 molecules to leave the FG domain layer. However, it would be important to determine the lateral diffusion of the molecules inside the layer as well. This could be addressed optimally by using fluorescent recovery after photobleaching (FRAP) in combination with total internal reflection fluorescence microscopy (TIRF) as shown in Fig. 7.1. A layer of FG domains on a glass slide is incubated with fluorescently labeled Kapβ1 molecules and the fast phase is washed away, such that only the slow phase remains. A spot on the surface is then bleached and the repopulation of this spot is observed using TIRF. This could be done at different levels of FG layer saturation.
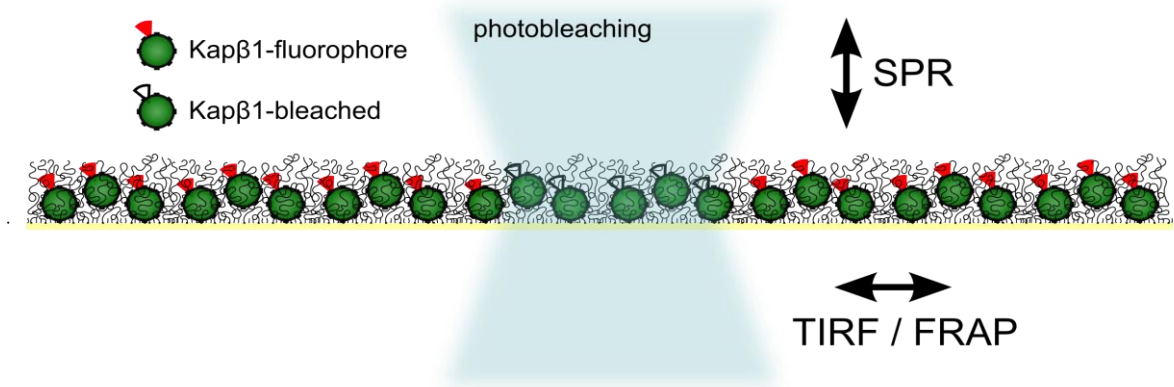
Fig. 7.1. Suggested experiment to investigate on the lateral motion of slow phase Kapβ1 molecules. Common SPR has no lateral resolution, whereas by using fluorescent recovery after photobleaching (FRAP) in combination with total internal reflection fluorescence microscopy (TIRF) the lateral motion of Kapβ1 molecules could be determined.

7.2.2 The Nanopore Project

It is important to validate our findings on planar surfaces for FG domains confined within a nanopore. The conformational responses of nucleoporins inside a nanopore may be modified, however, this is difficult to quantify. More meaningful is to record the affinities and kinetics of such modified nanopores upon exposure to Kapβ1 and draw comparison to the planar system. We expect the fast and slow phases to be conserved for the FG domains confined within the nanopore.

Due to advances in nanofabrication the optical properties of plasmonic nanostructures have received particular attention in science and engineering (Sannomiya et al., 2011). For us the aim is to mimic the NPC in solid state nanopores that are plasmonically active. Therefore a novel construct of nanohole membranes is provided by the group of Prof. Andreas Dahlin (Chalmers University of Technology, Göteborg, Sweden), that enables for selective modification of the inner pores (see Fig. 7.2) as the membranes are constructed from two different materials, i.e. Si_3N_4 and Au. The selective functionalization with site specific chemistry has been tested. FG domains of nucleoporins are tethered inside the pores to Si_3N_4 using an APTES linker, whereas the outside Au surface is passivated using polyethylene glycol (PEG) via direct thiol coupling. The aim of the project is to detect and quantify the binding of transport receptors to the nucleoporins located inside the pore.
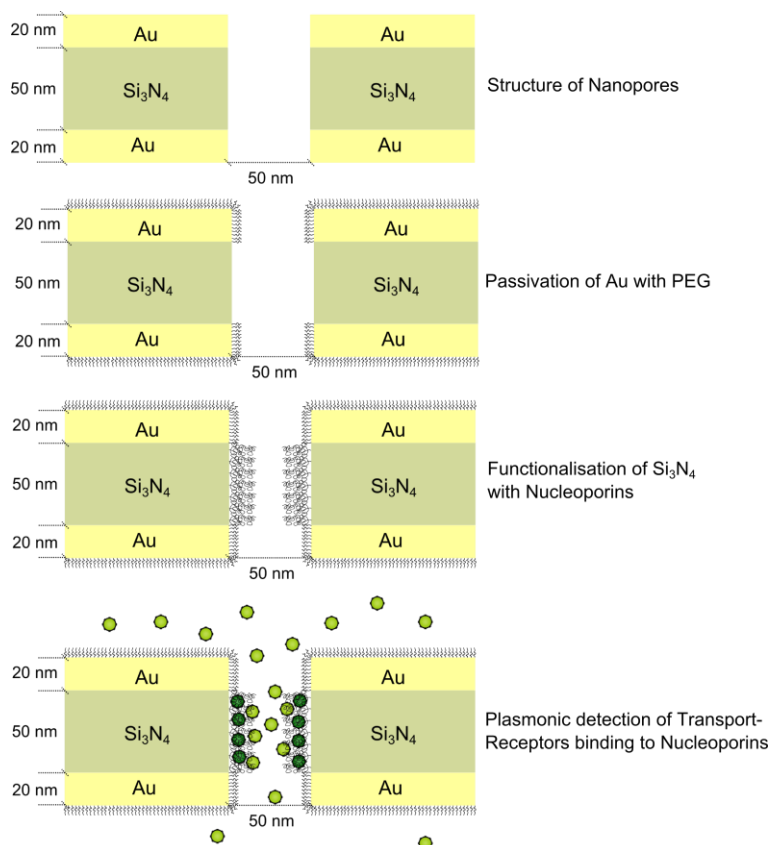
Fig. 7.2. Site specific modification of the nanopore sample and subsequent binding of transport-receptors. The setup mimics the nuclear pore complex and allows for real time plasmonic quantification of receptor binding to the nucleoporins inside the pore.

Initially the chemistry was established using a Si_3N_4 QCM-D sensor and an Au SPR sensor. For both types of surfaces the entire protocol for nanopore functionalization was applied (see end of section for the protocol). Briefly, the protocol comprises following steps: 1) SH-PEG, 2) APTES, 3) SMCC, 4) Nucleoporins. At this stage, the protocol was still slightly different from the protocol in the appendix, using 'acidic piranha' and UVO (instead of 'basic piranha' and O_2 plasma) for sample cleaning as well as toluene (instead of methanol) for APTES immobilization, respectively. Fig. 7.3 shows the QCM-D calculated thicknesses for Nup62 immobilization to the Si_3N_4 sensor surface. Using a rigid Sauerbrey model we obtain a final layer height $d = 19$ nm and for a viscoelastic Voigt model $d = 23\ nm$, respectively. These values are upper limits due to a fixed layer density of 1000 kg/m^3 in the fitting model. However, the cNup62 layer can be regarded as viscoelastic due to the difference in Voigt and

Sauerbrey calculated thicknesses, respectively (see Appendix for QCM theory). On the other hand, the Au surface was checked for the passivating properties of PEG, i.e. to protect the gold surface from protein adsorption. According to the protocol, the PEG layer needs to withstand the APTES treatment. As shown in Fig. 7.4 injecting cNup62 on the gold SPR sensor surface reveals no binding and similarly subsequent injections of BSA and Kapβ1 only reveal minor binding for Kapβ1, probably due to a residual cNup62 presence on the surface. However, injecting anti-PEG antibody reveals significant binding and thus indicates the presence of a PEG layer on the Au surface. Thus the PEG layer on the Au surface endures the chemical modification steps needed for nucleoporin attachment to the Si_3N_4 surface.
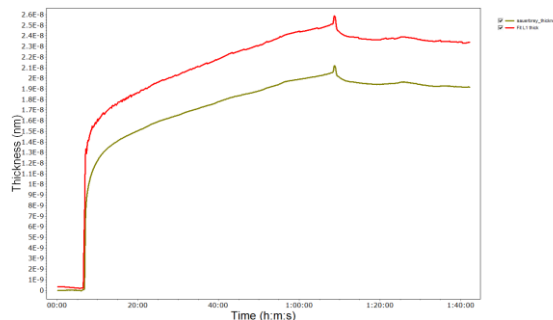
Fig. 7.3. Thickness determined using QCM-D for the immobilization of cNup62. The Si_3N_4 sensor surface was first modified according the 'nanopore' functionalization protocol and mounted to the QCM-D flow cells for final immobilization of cNup62. The rigid Sauerbrey model (green) gives a final height of $d = 19\ nm$, whereas the viscoelastic Voigt model (red) gives a final thickness $d = 23\ nm$, respectively. These are upper limits for the brush height due to a fixed layer density of 1000 kg/m^3 in the fitting model.
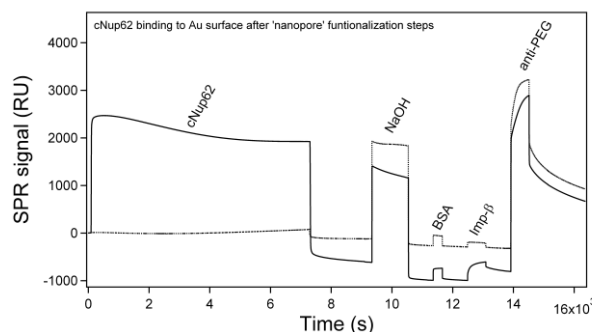
Fig. 7.4. Injection of cNup62, NaOH, BSA, Kapβ1, and anti-PEG IgG using SPR. The Au sensor surface was first modified according the 'nanopore' functionalization protocol and mounted to the SPR flow cells for final immobilization of cNup62. The surface is passivating for cNup62, BSA, and Kapβ1 adsorption. The binding of anti-PEG IgG indicates the presence of a PEG layer on the Au surface that withstands the APTES functionalization steps.

The functionalization of the nanopore sample for electron microscopy (EM) was then performed using PDMS flow cells and an automated syringe pump for solution injection (see Fig. 7.5). The flow cell system was used for all functionalization steps with the aim of Kapβ1 colloid localization to the pores.
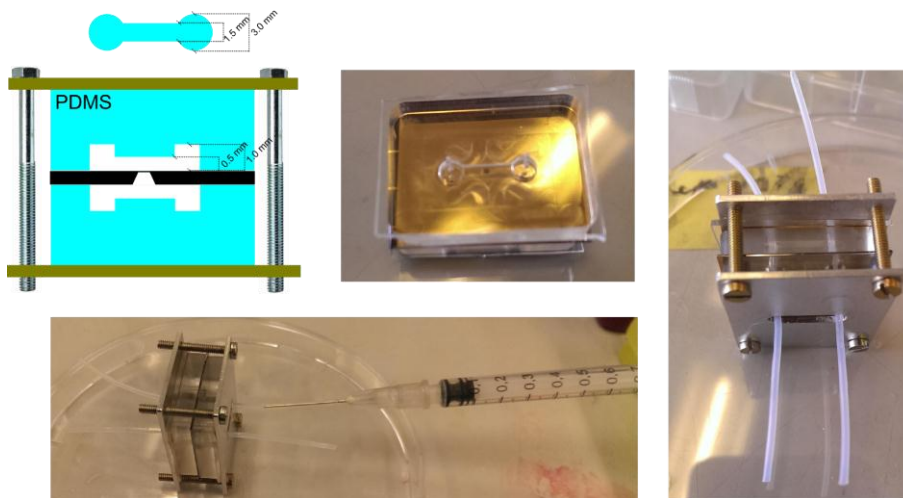
Fig. 7.5. Flow cell system used to functionalize the nanopore sample. Two PDMS masks are mounted on both sides of the nanopore sample and the resulting chambers can be accessed using tubings as inlets. The injections were performed by using a syringe pump (not shown).

Kapβ1 colloids were obtained with direct electrostatic adsorption of Kapβ1 to the negatively charged Au colloids (see end of section for the methods). Fig. 7.6 shows a scanning electron microscopy (SEM) image after fixation of the colloids using NHS/EDC. The SEM image clearly shows colloids that localize inside the nanopores.
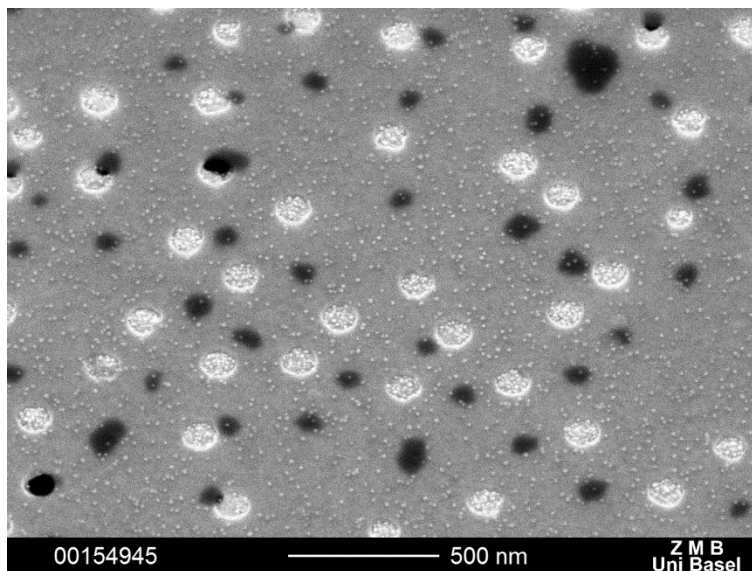
Fig. 7.6. Scanning electron microscopy image of functionalized nanopores (~100 nm diameter). Gold colloids tagged with transport receptors localize to the inside of the cNsp1 functionalized pores.

The binding of Kapβ1 to cNsp1 functionalized pores was recorded in the Lab of Prof. Andreas Dahlin (Chalmers University of Technology, Göteborg, Sweden). The functionalization protocol was very similar to the functionalization for the EM studies except that methanol was used instead of ethanol for APTES treatment and that larger flow cells were used compatible with the microscopy setup. However the flow cells were only used from the SMCC step whereas the APTES and PEG treatment were done using bulk immersion of the sample (see end of section for the protocol).
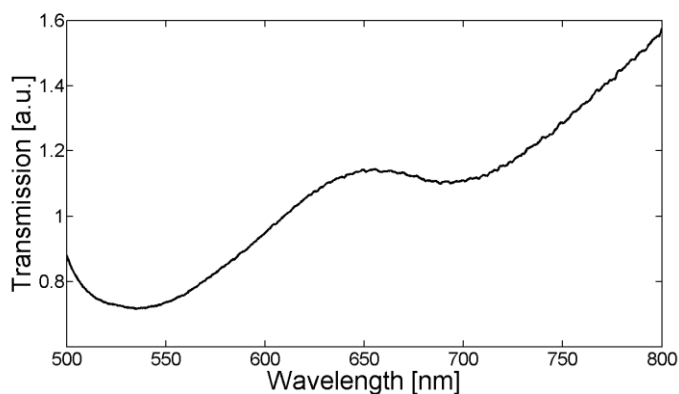
Fig. 7.7. Transmission spectra for the 50 nm diameter nanopore sample after functionalization. The spectra shows a shallow peak at $\lambda \sim 650\ nm$ and dip at $\lambda \sim 690\ nm$, respectively.

A wavelength spectra for the 50 nm pore sample (obtained at the end of the measurement) is shown in Fig. 7.7. The spectra reveals a shallow peak at $\lambda \sim 650 \ nm$ as well as a shallow dip at $\lambda \sim 690 \ nm$, respectively, that can both be tracked during the binding of Nsp1 and Kapβ1, respectively. For the 50 nm pore samples the peak and dip are more shallow as compared to the 100 nm pore samples (not shown) such that there is significantly more noise in determining their position, however, with respect to the NPC dimension it is more reasonable to work with the 50 nm samples. For the 50 nm pores we find that there is no shift in the peak position for the adsorption of cNsp1 and Kapβ1, respectively, such that we show only the shift in the dip position in Fig. 7.8. This is to be expected as the peak position is rather related to the surface plasmon modes, whereas the dip position is rather related to the cavity plasmonic modes. The relative contributions of the two modes for detecting surface and pore binding, however, depends on the exact pore geometry.
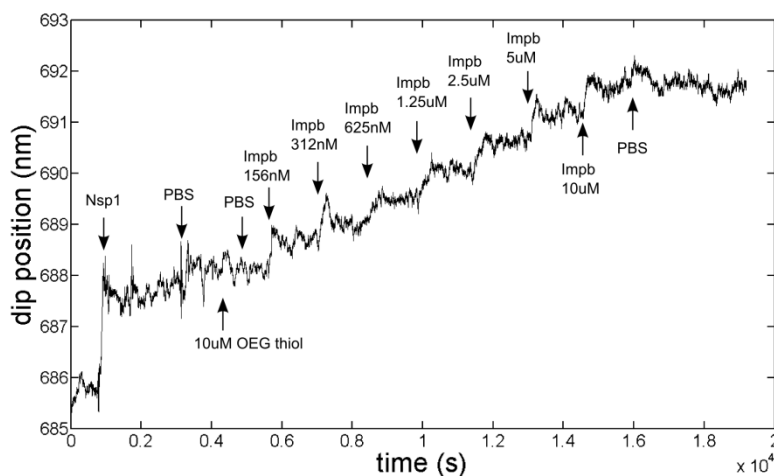
Fig. 7.8. Dip position over time for Nsp1 and Kapβ1 binding, respectively. The injections of the different molecules are indicated in the figure.

The dip position for the experiment with the 50 nm pores is shown in Fig. 7.8. Initially the injection of Nsp1 leads to a pronounced shift in the dip position, the remaining activated APTES groups are then quenched using a diluted OEG thiol solution (i.e. $C_{17}H_{36}O_4S$). This is followed by increasing concentrations of Kapβ1, and finally rinsing with PBS without any detectable dissociation of Kapβ1. The noise

level is quite high such that the determination of the kinetics is not feasible. The determination of kinetics would anyway be difficult as the setup is not based on microfluidics that would allow for a fast switching of the solvent. However, the data allows for the construction of a Langmuir isotherm as shown in Fig. 7.9.
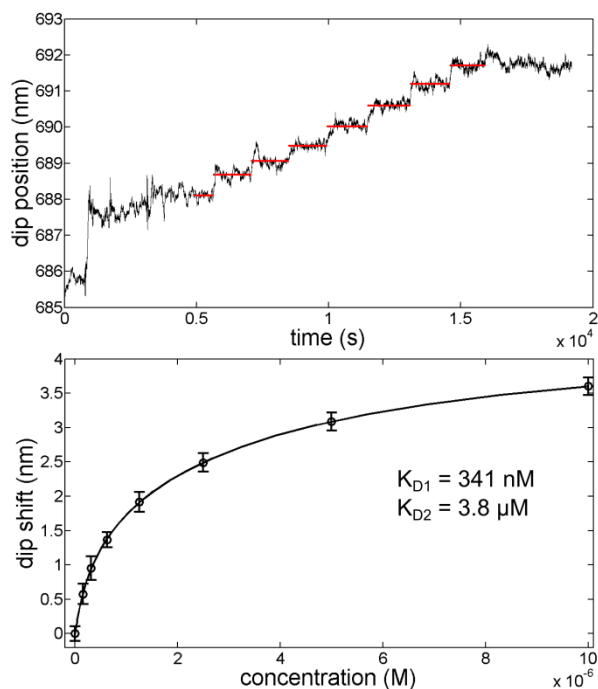
Fig. 7.9. Construction of a Langmuir isotherm from the Kapβ1 binding response. **(A)** Line fits (red) to obtain the Kapβ1 binding reponse (i.e. dip position) for each injection. **(B)** Resulting two component Langmuir isotherm from the dip shift relative to the PBS baseline. The errorbars show the standard deviations for the line fits. The obtained equilibrium binding constants are $K_{D1} = 341\,nM$ and $K_{D2} = 3.8\,\mu M$, respectively.

The obtained equilibrium binding constants $K_{D1} = 341\,nM$ and $K_{D2} = 3.8\,\mu M$ from the two component Langmuir isotherm are in well agreement with the constants obtained from conventional SPR (see section 4.5.2). This suggests that the Kapβ1 - FG layer binding affinities obtained from conventional SPR are meaningful also in the context of Kapβ1 binding to FG nups in a pore geometry.

Methods:

Kapβ1 colloids:

The coating of gold nanoparticles (10 nm, Sigma Aldrich) follows the procedure explained in David Hughes, 2005, where the protein binding is by straightforward electrostatic absorption relying on the negative charge of the gold particles. Unbound gold is unstable and changes color from red to blue in the presence of salts, which can be used to find the amount of protein required to coat the particles. Therefore 5 ml of gold colloids were mixed with 125 μl of 1% PEG 8'000 Da solution in MilliQ H_2O and adjusted to pH 5.2 (i.e. 0.5 points above the pI of Kapβ1). A 1:2 dilution series of 20 μl Kapβ1 was then mixed with 0.5 ml of gold particles, each, and the lowest concentration was selected where there was no blue shift after the addition of 100 μl of 10% NaCl, i.e. $c_{Kapβ1} = 100$ nM. For bulk production of colloids, 7.5 ml of gold colloids were mixed with 250 μl of 1% PEG 3'350 Da solution in MilliQ H_2O and adjusted to pH 5.2. Subsequently, the colloids were added to Kapβ1 to obtain a 200 nM Kapβ1 suspension and stabilized after 2 min by adding 1 ml of   1% PEG in MilliQ H_2O.

Nanopore experiments:

Nanopore samples were provided by the group of Prof. Andreas Dahlin, Chalmers University of Technology, Göteborg, Sweden. The samples were rinsed with milliQ H_2O, aceton and ethanol before „basic piranha" (1:1:5 of NH_3, H_2O_2, and H_2O) treatment at 80°C for 10 min. The samples were then immersed in milliQ H_2O for 10 min, rinsed with ethanol and dried using a N_2 gas stream. They were then further cleaned using O_2 plasma cleaning at low power. The samples were then immersed over night in 0.1 mM SH-PEG 5'000 kDa (Laysan Bio, Inc) in PBS at RT. The samples were then rinsed with H_2O, and methanol, respectively. Next, the samples were immersed in 1% APTES (Sigma) in methanol for 30 min followed by rinsing with methanol and H_2O. Then the sample was mounted to the flow cells with inlets on

either side of the membrane. 2 mg of sulfo-SMCC were dissolved in 1 ml warm H2O, mixed with 2 ml of PBS and the sample was incubated for 30 min at RT. All sample solutions were degased using a vacuum pump while stirring with a magnetic stirrer. The flow cell was rinsed with PBS and incubated for ~40 min with cNsp1 in PBS 2mM TCEP (Sigma), while recording the transmission spectra in real time. The cells were then rinsed with PBS and 10 μM of $C_{17}H_{36}O_4S$ (Nanoscience) in PBS for ~10 min to quench active APTES sites. Finally the cells were incubated with increasing concentrations of Kapβ1 in PBS (156 nM – 10 μM) for 25 min each and the sample was rinsed with PBS.

Nanopore functionalization EM:

Nanopore samples were provided by the group of Prof. Andreas Dahlin, Chalmers University of Technology, Göteborg, Sweden. The samples were rinsed with milliQ H_2O, aceton and ethanol before „basic piranha" (1:1:5 of NH_3, H_2O_2, and H_2O) treatment at 80°C for 10 min. The samples were then immersed in milliQ H_2O for 10 min, rinsed with ethanol and dried using a N_2 gas stream. They were then further cleaned using O_2 plasma cleaning (12.5 W, 0.3 mbar, 10 min). Meanwhile the PDMS flow cells were prepared by punching the inlets and sonicating the flow cells in aceton, isopropanol, and ethanol for 5 min, respectively. The flow cells were then mounted on both sides of the nanopore sample, fixated using an aluminium holder, and the tubings were inserted into the inlets (see Fig. 7.5). The tubings were additionally glued with epoxy. All sample solutions were degased using a vacuum pump while stirring with a magnetic stirrer. The flow cells were initially filled with PBS using a syringe. The inlets were then connected to a syrenge pump operated at 5-10 μl/min and the flow cells were filled with 1 mM SH-PEG 5'000 kDa (Laysan Bio, Inc) in PBS and incubated for 2h at RT. The flow cells were then rinsed with PBS, H_2O, and ethanol, respectively. Next, the flow cells were filled with 1% APTES in ethanol for 30 min followed by rinsing with ethanol, PBS, H_2O and leaving them over night at RT using 5 μl/min flow. Then, 2 mg of sulfo-SMCC were dissolved in 1 ml warm H2O, mixed with 2 ml of PBS and the sample was incubated for 2h at RT. The

flow cell was rinsed with PBS and incubated for 2h with cNsp1 in PBS 2mM TCEP. The cells were then rinsed with PBS and 10 µM of $C_{17}H_{36}O_4S$ in PBS for 20 min to quench active APTES sites. Finally the cells were incubated with Au-PEG-Kapβ1 colloids in PBS for 1h and proteins were cross-linked using 200 mM EDC, 400 mM NHS in 20 mM MES buffer pH 6.0, 100 mM NaCl, for 1h. The sample was rinsed with PBS, H20, dried using a N2 gas stream, and mounted for SEM imaging.

7.2.3 Cloud point grafting

This project is related to polymer brushes rather than the NPC, and is a collaboration with Prof. Andreas Dahlin (Chalmers University of Technology, Göteborg, Sweden). As introduced in section 3.1.2.2 the phase diagram is divided into a single phase region and a two phase region, where near the „cloud point" the polymer undergoes the phase change due to marginal solvent conditions (Rubinstein & Colby, 2002). For PEG in water, increasing the temperature and/or increasing the salt concentration leads to a reduction in hydration and thus a reduction of the effective radius of gyration, such that a denser packing of grafted chains is possible (Kingshott et al., 2002). Here we are using a grafting-to method for PEG brushes which is based on a high salt concentration (0.9 M Na2SO4) in water and suitable concentrations to approach the cloud point of PEG. The heights were subsequently determined using AFM as shown in Fig. 7.10.
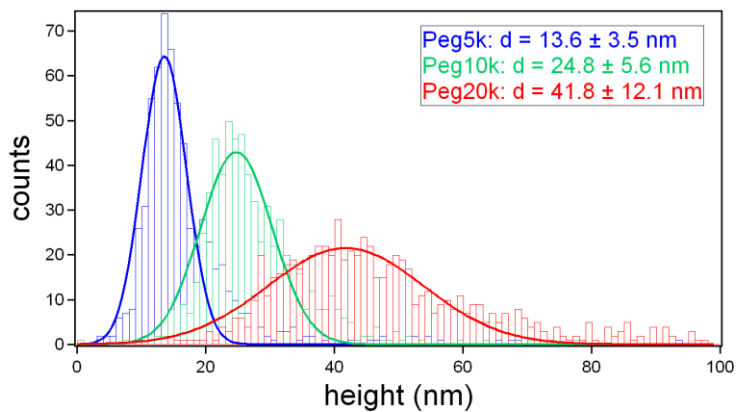
Fig. 7.10. Gaussian analysis of PEG brush heights for different molecular weights M_w using „cloud point grafting". PEG brush heights were obtained from AFM force-distance curves (1 pN threshold).

The concentrations used for cloud point grafting for PEG 5 kDa, PEG 10 kDa and PEG 20 kDa are 0.6 mg/ml, 0.33 mg/ml and 0.12 mg/ml, respectively, that corresponds to 120 nM, 33 nM, and 6 nM, respectively. These concentrations are obviously much lower than the 1 mM concentrations used for the grafting-to approach in PBS (see chapter 2), nevertheless the measured brush heights are higher in case of the cloud point grafting. Remarkably, the brush heights are in agreement with calculations based on a simple model similar to the de Gennes „strongly stretched" brush, were the height is proportional to molecular weight (Emilsson et al., 2015).

The cloud point grafting was also applied to nanostructures. The samples consist of a glass slide with a 30 nm top gold layer perforated with nanopores of 85, 100, and 150 nm diameter, respectively. The samples were manufactured in the lab of Prof. Andreas Dahlin. Fig. 7.11A shows the topography from the z-piezo movement as the force map was recorded, whereas Fig. 7.11B shows the respective brush heights from the contact point evaluation.
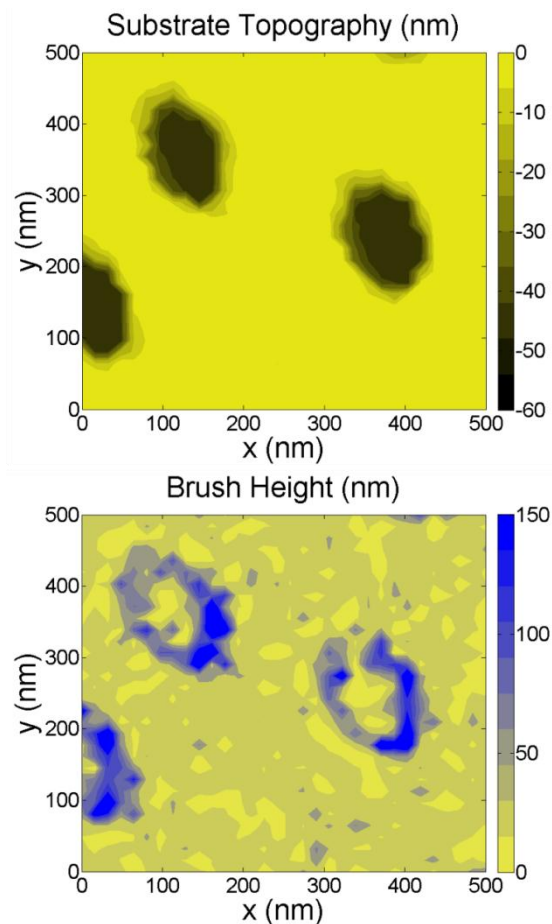
Fig. 7.11. (A) Substrate topography image reconstructed from the z-piezo movement for a 150 nm pore sample. The dark wells correspond to nanopores of roughly 30 nm depth. **(B)** Corresponding spatial mapping of PEG brush heights measured from AFM force-distance curves (1 pN threshold). The blue areas of extended brush height colocalize with the dark wells in substrate topography.

The topography image was flattened once using line fits. The blue shaded areas coincide in position with the dark wells in topography. The force curves at the pore edges are not always well defined as the tip is often slipping at the edge of the pore. Therefore the force curves were fit using two exponentials and additionally selected for curves where there are no jumps in the distance. The contact points were the calculated by subtracting the topography from the brush height (1 pN treshold). The average contact points for pore diameter 85 nm, 100 nm, and 150 nm are shown in Fig. 7.12 for pore and flat states, where the pore states were defined for topography values $z \leq -5\ nm$ and flat states otherwise, respectively.
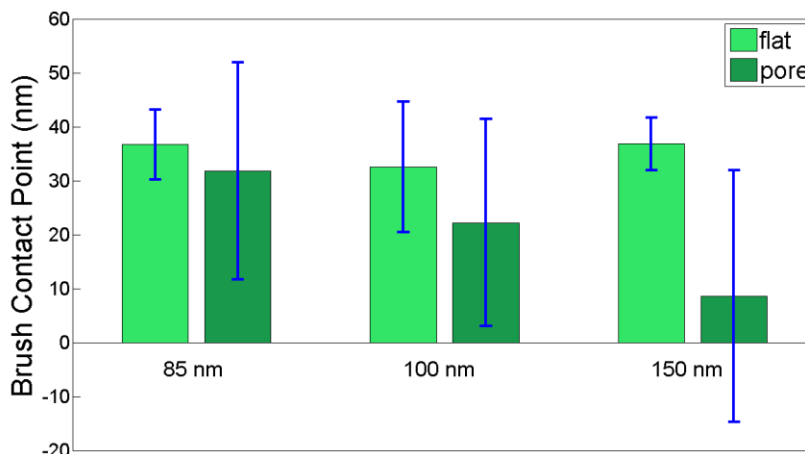
Fig. 7.12. Brush contact point for SH-PEG 20kDa relative to the substrate topography (i.e. $z = 0$ for the gold surface, see Fig. 7.11A). For the 85 nm pores the contact points over the pores (dark green) are well above $z = 0$, indicating that the pores are covered by PEG. For the 150 nm pores the contact points may fall below $z = 0$, indicating that the pores are not entirely covered. Pore states where defined for a topography $z \leq -5\ nm$.

7.2.4 Temperature induced changes in FG domains

In this chapter the focus is on thermodynamic aspects of NTR binding (mainly Kapβ1) to FG domains using surface plasmon resonance (SPR) and isothermal titration calorimetry (ITC). Our results indicate that the layer height of surface-tethered FG domains decreases with increasing temperature being consistent with a phase separation that occurs in lower critical solution temperature (LCST) polymers. These temperature-induced height changes stem largely from FG domain cohesion, and considerably impact NTR binding. The cystein-modified FG domain construct used in this chapter is Nsp1p-12FF (for details see „Materials & Methods"), termed cNsp1 for clarity (*this project is so far unpublished*).

For surface-tethered Nsp1 (Nsp1p, residues 262–492) as well as Nup62 (cNup62) FG domains the height was measured using BSA, while ramping the temperature from 4°C to 45°C. This is shown in Fig. 7.13, that shows a decrease in height with temperature. For cNup62, starting at $T = 4°C$ and $d_2 \approx 16.5\ nm$, the layer height

decreases stepwise until $d_2 \approx 12\ nm$ at $T = 45°C$. This equals a decrease in height of about 30 %, considerably more than estimated for the temperature influence on the decay length l_d alone (see section 3.2). When the temperature is reset to $T = 4°C$ the layer height is partially recovering to $d_2 \approx 16\ nm$. Similar for Nsp1p, where however the recovery is less at 4°C. The temperature-induced height change indicates FG domain cohesion. FG domain cohesion could be related to bundle formation as recently reported in a computer simulation (see Fig. 1.6; Gamini et al., 2014).
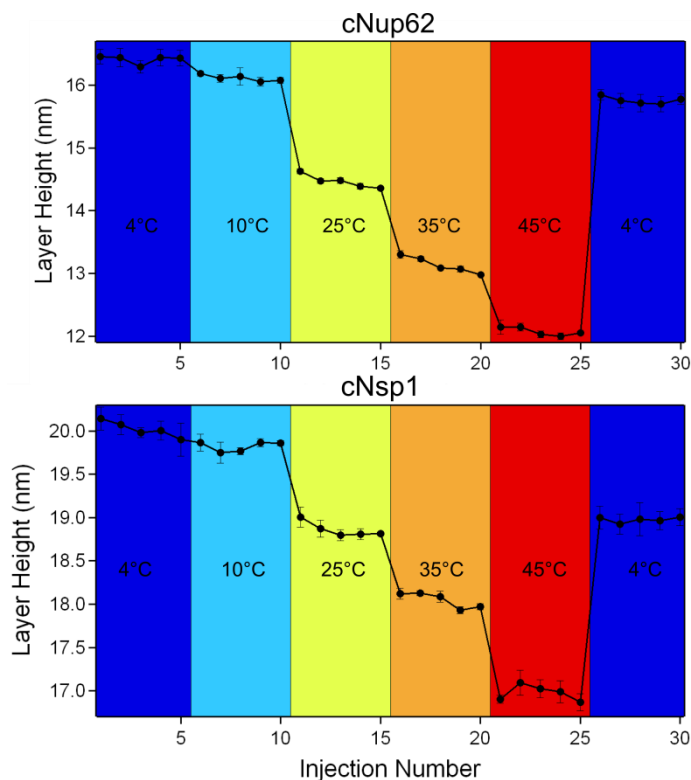
Fig. 7.13. Height dependence on temperature for surface-tethered cNup62 **(A)** and Nsp1p FG domains **(B)**, respectively. Using non-interacting BSA molecules the height of cNsp1 was accessed for temperatures ranging from $T = 4°C$ to $45°C$. The initial layer height of $d_2 \approx 16.5\ nm$ at $T = 4°C$ decreases in a stepwise manner to a final layer height $d_2 \approx 12\ nm$ at $T = 45°C$ for cNup62. When resetting the temperature to 4°C the layer is partially recovering to $d_2 \approx 16\ nm$. Similar for Nsp1p, where however the recovery is less at 4°C.

The influence of Nsp1p and cNup62 structural changes on NTR binding was investigated by performing SPR binding assays at 10°C as well as 37°C. Binding of the nuclear transport receptor Kapβ1 to cNup62 and Nsp1p is shown in Fig. 7.14 and Fig. 7.15, respectively. The procedure of the experiments is the same as already

introduced in chapter 4, where BSA injections are used to determine the FG domain layer thickness before and after each Kapβ1 injection. The same procedure was also applied for NTF2 binding to Nsp1p (not shown). For Kapβ1 the highest concentrations were approximately 14 - 17 μM and for NTF2 approximately 300 μM.
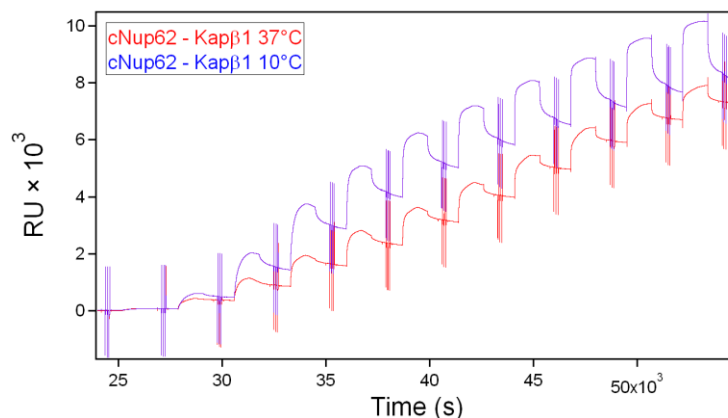
Fig. 7.14. SPR sensograms for Kapβ1 binding to surface-tethered Nup62 FG domains (cNup62). BSA injections are used to determine stepwise height changes in cNup62 upon Kapβ1 binding. The experiments were performed at 10°C (blue) and 37°C (red) respectively.
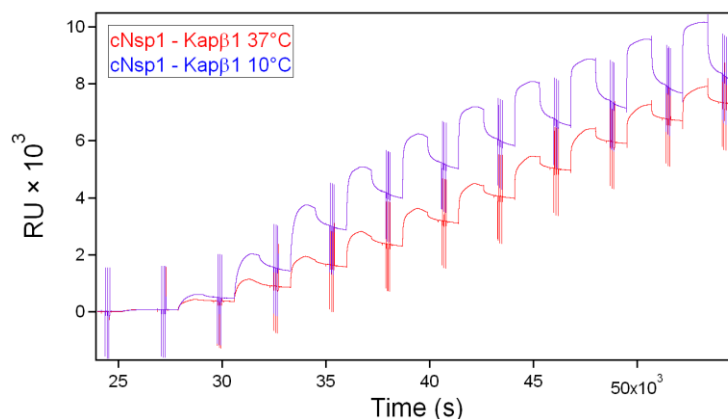
Fig. 7.15. SPR sensograms for Kapβ1 binding to surface-tethered Nsp1 FG domains (Nsp1p). BSA injections are used to determine stepwise height changes in cNsp1 upon Kapβ1 binding. The experiments were performed at 10°C (blue) and 37°C (red) respectively.

The relative changes in layer thickness ($\Delta\, d_{cNsp1\cdot Kap\beta1}/d_{cNsp1}$ and $\Delta\, d_{cNsp1\cdot NTF2}/d_{cNsp1}$) are shown as a function of surface density (Da/nm^2) of bound Kapβ1 ($\rho_{Kap\beta1}$) and bound NTF2 (ρ_{NTF2}) in Fig. 7.16 and Fig. 7.17 respectively. For Kapβ1, the relative extension increases at 37°C in order to accommodate the same

receptor surface density $\rho_{Kap\beta1}$. However, this is not surprising as the initial layer height d_{cNsp1} is lower at 37°C. The extension of the layer is about 50% at the highest concentrations used. Further, the initial compaction is more pronounced at 37°C and shifted towards lower surface densities $\rho_{Kap\beta1}$. For NTF2 the surface density ρ_{NTF2} of stable complexes is much lower and the layer height monotonically decreases with binding, such that there is no re-extension as seen for Kapβ1. The NTF2 homodimer has a molecular weight of 34 kDa and two binding sites for FG motifs (Bayliss et al., 2002), whereas Kapβ1 has a molecular weight of 97 kDa and ~10 hydrophobic grooves serving as potential FG binding sites (Isgro & Schulten, 2005). The higher valency and size of Kapβ1 thus enables the extension of the Nsp1 layer, whereas layer extension is lacking for NTF2 binding.
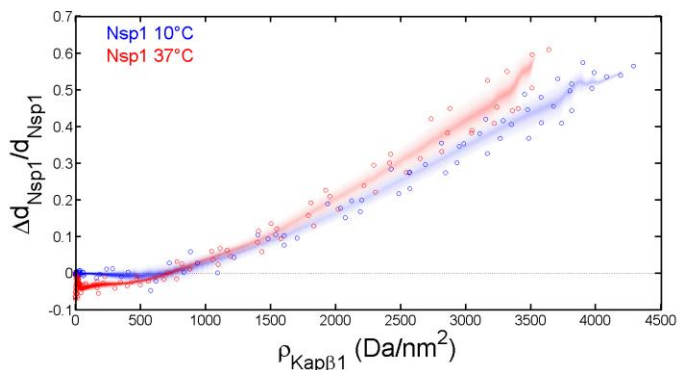
Fig. 7.16. Relative change in cNsp1 layer height ($\Delta d_{cNsp1\cdot Kap\beta1}/d_{cNsp1}$) plotted as a function of Kapβ1 surface density ($\rho_{Kap\beta1}$), for 10°C (blue) and 37°C (red), respectively.
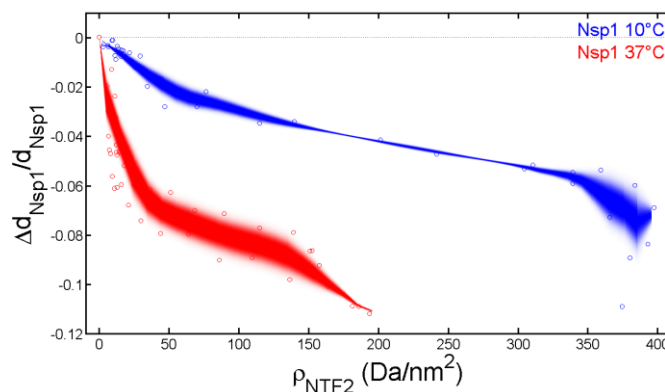
Fig. 7.17. Relative change in cNsp1 layer height ($\Delta d_{cNsp1 \cdot NTF2}/d_{cNsp1}$) plotted as a function of NTF2 surface density (ρ_{NTF2}), for 10°C (blue) and 37°C (red), respectively.

The interaction maps (see section 5.2.1) for Kapβ1 are shown in Fig. 7.18 and 7.19 for cNup62 and Nsp1p, respectively. For Kapβ1 the K_D values at 10°C are very similar to the K_D values at 37°C, and this is consistent with a Langmuir isotherm analysis (not shown). We find that the fast phase (i.e., high k_{on} and k_{off}) is more populated at 10°C and consists of two populations, whereas only one fast phase population is present at 37°C. Also, the slow phase (i.e., low k_{on} and k_{off}) is shifted towards lower values at 37°C indicating slower entry and exit of the layer.
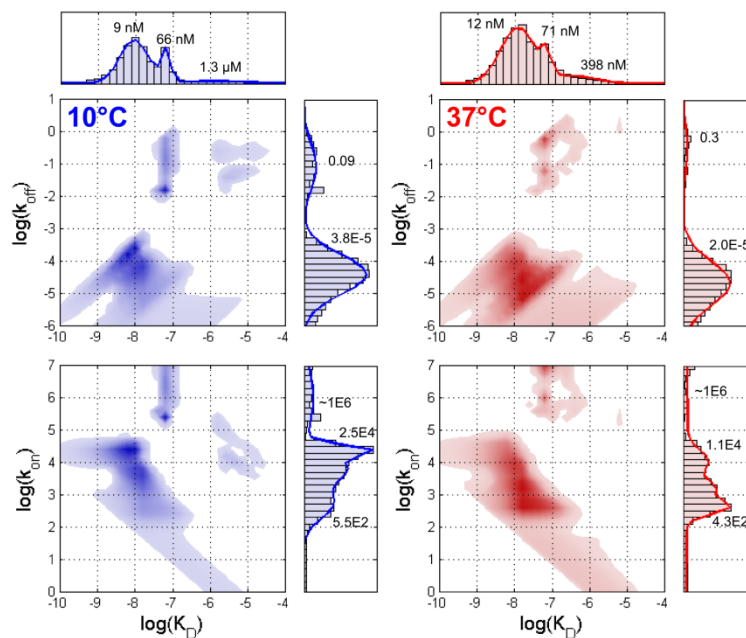
Fig. 7.18. Interaction maps for Kapβ1 binding to surface-tethered FG domains of Nup62 (cNup62) at 10°C (blue) and 37°C (red), respectively.
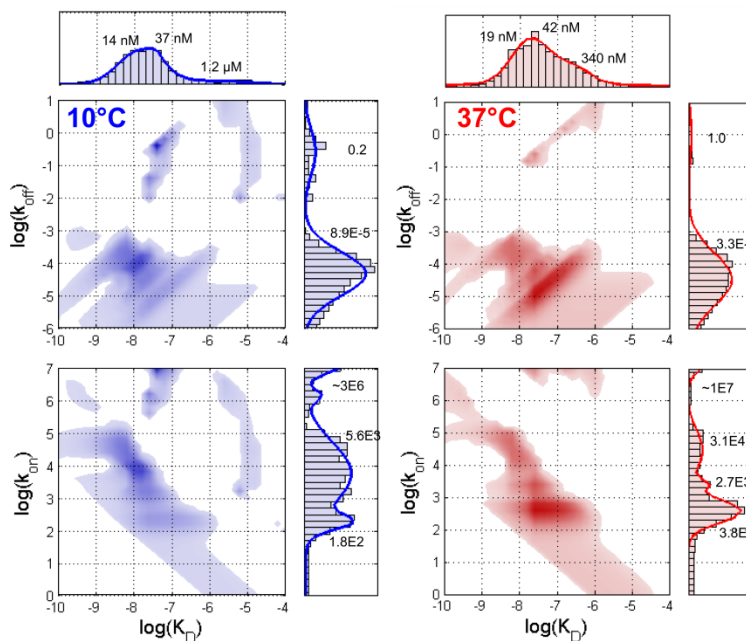
Fig. 7.19. Interaction maps for Kapβ1 binding to surface-tethered FG domains of Nsp1 (cNsp1) at 10°C (blue) and 37°C (red), respectively.

Isothermal titration calorimetry (ITC) was used to determine the heat exchange for NTR binding to surface-tethered Nsp1 FG domains (cNsp1) by the means of gold nano-colloids. Therefore cNsp1 functionalized nano-colloids of 20 nm diameter were titrated into a solution containing high µM concentrations of NTR's, aiming to saturate the FG domain layer. The heat of the interaction was measured at 10°C, 25°C and 37°C as shown in Fig. 7.20 for Kapβ1 and NTF2, respectively. From SPR measurements we expect similar fractions of the dominant slow phase species of Kapβ1 to interact with the surface tethered FG domain layer (see Fig. 7.16), such that a qualitative comparison of the heat of reaction is feasible. From Fig. 7.20 it can be seen that the change in enthalpy ΔH is positive with temperature, i.e. the change in enthalpy ΔH is getting less negative. Thus Kapβ1 binding causes a positive heat capacity change ΔC_p, and this infers that the change in entropy ΔS is positive as well (see Appendix A1). For NTF2 direct comparison of the change in enthalpy ΔH is more problematic as SPR reveals highly temperature dependent surface bound fractions of fast and slow phase NTF2 molecules, respectively (see Fig. 7.17). Nevertheless, the reaction is endothermic at all temperatures and given that fewer receptors interact with the layer at 37°C, the reaction seems to carry a positive heat capacity signature ΔC_p as well. However, for NTF2 the fast phase is the dominant kinetic species.
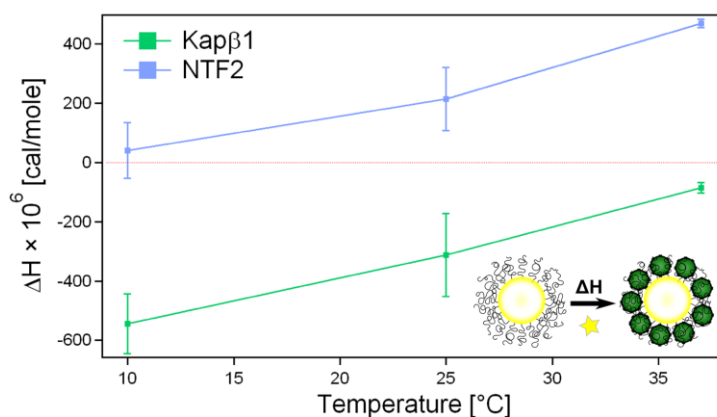
Fig. 7.20. ITC measurements for cNsp1 – Kapβ1 (green) and cNsp1 – NTF2 (blue) interaction, respectively, showing ΔH at various temperatures. Inset: ΔH is measured by titrating gold nano-colloids functionalized with surface-tethered cNsp1 into a solution of high µM NTR concentration. The change in enthalpy ΔH consequently results from saturating the FG domain layer with NTR's.

The temperature induced changes in FG domain cohesion have considerable impact on NTR binding. Structural changes are due to a decrease in solvent quality with temperature as predicted for the rupture of polymer – water hydrogen bonds (Dormidontova, 2002), and may be related to other phenomena such as the aggregation of unfolded proteins or cold denaturation of folded proteins (Cooper, 2005). Indeed, in molecular dynamic simulation it was found that hydrogen bonding is the most important structural determinant in FG domain aggregates (Dölker et al., 2010) and the FG motifs are not particularly critical for Nsp1 bundle formation (Gamini et al., 2014). The ITC measurements further reveal a positive ΔC_p and thus positive changes in ΔH with temperature for cNsp1 – Kapβ1 binding. This is surprising as the hydrophobic burial inherent to FG cores interacting with the hydrophobic pockets on Kapβ1 (Bayliss et al., 2000) is expected to associate with a negative ΔC_p signature, as commonly observed in protein – protein and protein - ligand interactions (Cooper, 2005) (see Appendix A1). A reasonable explanation for the positive ΔC_p in our experiments is that the thermodynamic signature of the cNsp1 – Kapβ1 interaction is dominated by conformational changes in the FG domains rather than hydrophobic burial of binding sites. As illustrated in Fig. 7.21, a negative ΔC_p for the cohesion of FG domains, in agreement with the aggregation of unfolded proteins (Cooper, 2005), may account for the positive ΔC_p measured upon Kapβ1 binding. Step 2 and 3 are the ones that we monitor in SPR and ITC, respectively. From SPR we assume that $\Delta G_2 \approx \Delta G_3$ (i.e. similar K_D values) and from ITC we know that $\Delta H_2 < \Delta H_3$ and we can therefore expect that $\Delta S_2 < \Delta S_3$ for the interaction. The positive heat capacity ΔC_p in step 4 is therefore considered a direct consequence of bundle distortion, i.e. in step 4 we are reversing the hidden thermodynamic profile related to step 1. The exothermic heat profile of the cNsp1 - Kapβ1 interaction further indicates that slow phase binding is a cooperative process including a multiplicity of weak interactions (Cooper et al., 2001), in agreement with Kapβ1 having an estimated 10 FG binding sites (Isgro & Schulten, 2005). However, as Kapβ1 binding can compensate for the enthalpy gain of bundle formation, its seems that FG domain linker regions are involved in slow phase binding as well. The endothermic profile of NTF2 binding on the other hand, that has hydrophobic pockets similar to Kapβ1

(Bayliss et al., 2002), indicates that single (or non-multivalent) FG interactions are consistent with the persistent view of the entropic nature of the hydrophobic effect (Snyder et al., 2014). From ΔC_p we expect bundle unfolding for NTF2 as well, however, NTF2 binding does not feature enthalpic compensation of bundle formation.
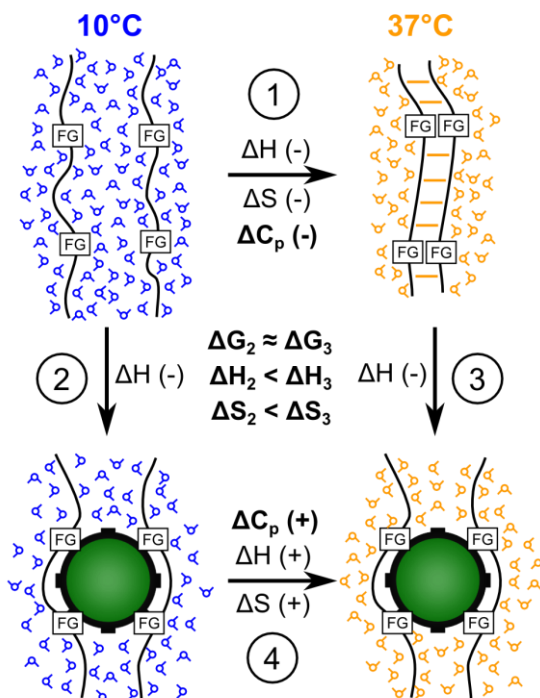
Fig. 7.21. Postulated mechanism for FG domain dominated binding energetics. In step 1 heat induces bundle formation in cNsp1 FG domains. Step 2 and 3 are monitored by ITC and SPR, respectively. From SPR we know that $\Delta G_2 \approx \Delta G_3$ and from ITC we know that $\Delta H_2 < \Delta H_3$, which implies that $\Delta S_2 < \Delta S_3$. The positive heat capacity change ΔC_p in step 4 is therefore a direct consequence of the hidden negative change ΔC_p for bundle formation in step 1.

A closer look at the K_D values for Kapβ1 binding reveals that the slow phase peaks at higher k_{on} values for 10°C. At higher loadings, however, brush stretching is getting more expensive, i.e. the entropy scales with the square of polymer end-to-end displacement (Rubinstein & Colby, 2003), and brush filling slows down. What might therefore be the consequences of bundle formation? Whenever the bulk Kapβ1 concentration is increased, the brush is forced to stretch and frees additional binding capacity. This is the main reason for the broad range in K_D values other than multivalency. Bundle unfolding on the other hand is expected to occur rather at a

specific threshold concentration of cooperatively acting Kapβ1 molecules, however, unfolding causes entropic compensation to layer stretching. Thus a direct consequence of bundle formation might be that layer extension is most sensitive to Kapβ1 concentrations in the near physiological μM range. As an additional consequence of the cooperative nature of bundle distortion, FG domain bundles trigger biphasic binding with two clearly separated species of fast (monovalent) and slow phase (multivalent) interactions, respectively (see Fig. 7.22). The formation of bundles is further supported by circular dichroism (CD) measurements that reveal β-sheet formation with increasing temperature (data not shown).
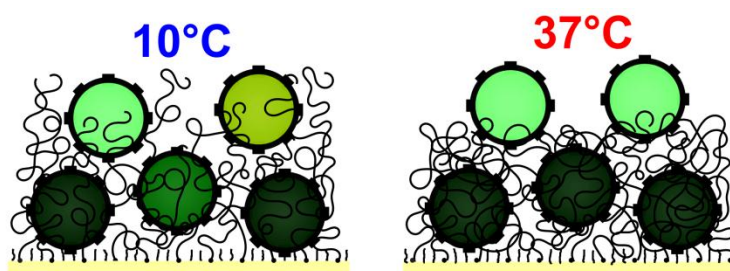
Fig. 7.22. Emerging picture for Kapβ1 – cNsp1 interaction. At 37°C the binding is rather biphasic (on top vs inside), whereas at 10°C the binding of Kapβ1 is rather multiphasic (many binding states). At 37°C the binding strength inside the layer is high (dark green), while enabling a well defined fast phase with a minimal coordination number (light green).

Methods:

Nsp1 colloids

Gold nanoparticles (20 nm in PBS, Sigma) were coated with Nsp1 for ITC studies. Therefore 4 ml of gold nanoparticles in PBS (as purchased) were mixed with 1 ml of Nsp1 12 FF (~ 170 μM) in PBS and incubated for 3h at RT. The suspension was then thoroughly dialyzed two times into 500 ml of 8 M urea, 100 mM Na_2HPO_4, 2 mM TCEP and 10 mM Tris-HCl, pH 8.5 at RT using a 300 kDa MWCO cellulose ester (CE) membrane (spectrumlabs). This was followed by a thorough dialysis (three times) into PBS first at RT then at 4°C using a 50 MWCO regenerated cellulose (RC) membrane (spectrumlabs). The concentration of the particles was determined using a

spectra-photometer according the protocol by Haiss et al., 2007. Coating and monodispersity of the particles was validated using DLS (Zetasizer Nano, Malvern).

ITC measurements

Isothermal titration calorimetry (MicroCal VP-ITC, Malvern) was used to measure the heat of reaction by titrating Nsp1 coated gold colloids into high concentrations of NTR's. Therefore, 3 x 30 µl of about 1.2 nM functionalized gold colloids in PBS were titrated into a cell containing around 40 µM of Kapβ1 or around 400 µM of NTF2 in PBS, respectively. This was performed at 10°C, 25°C, and 37°C, respectively, and the heat of dilution for Nsp1 coated gold colloids titrated into PBS was subtracted.

Appendix

A1 Thermodynamics of biomolecular interactions

The heat capacity C_p is most intuitively defined as the increase in enthalpy (due to small volume changes in protein reactions the internal energy U and the enthalpy H may be considered equivalent) with temperature and relates to other thermodynamic quantities as (Prabhu & Sharp, 2005)

$$C_p = \frac{dH}{dT} = T\frac{dS}{dT} = -T^2\frac{d^2G}{dT^2} = \frac{\langle \delta H^2 \rangle}{kT^2} \tag{A1}$$

Because $G = H - TS$ and entropy and enthalpy change in the same direction, the free energy G has a much weaker dependence on temperature than either of its components. Heat capacity expressed as the curvature of the free energy means that a positive (negative) change in heat capacity yields a downward (upward) curvature to ΔG where at the extremum the entropy change is zero. The downward curvature also explains the phenomenon of cold protein denaturation. The fourth expression of C_p is the mean square fluctuation in energy. Major heat capacity related features in biomolecular reactions are the positive and negative ΔC_p of burial for nonpolar (-) and polar (+) groups, respectively. For the burial of polar surface in model compounds the contribution to ΔC_p is about 60 % as large as the contribution from nonpolar surface (per solvated area) and has opposite sign (Spolar et al., 1992). More challenging is the quantification of changes in ΔS and ΔH in a biomolecular reaction. The hydrophobic effect (nonpolar burial) is mainly entropic in nature due to the release of „structured" water (Snyder et al., 2014), whereas small nonpolar model compounds reveal only small changes in van der Waals (VdW) interaction energies when transferred into either water or into their neat phase (Baldwin, 2007). The burial

of polar residues is strongly connected to the formation of protein-protein H-bonds in exchange to H-bonds that are formed between polar protein groups and water molecules. Considering that the polar carbonyl oxygen and the amide nitrogen participate in more H-bonds in the denatured state, it was argued that hydrogen bonding may favor protein unfolding (Spolar et al., 1992; Dill, 1990). However, titration experiments show that peptide helix formation is enthalpy-driven in water (Baldwin, 2007). This paradox was addressed using following explanations: 1) the extent of peptide solvation in the unfolded state decreases when considering backbone conformation and neighboring side-chains, 2) there is cooperativity in forming a network of H-bonds that leads to an increase in H-bond energy. It was further argued that the close-packing due to van der Waals interaction could strengthen peptide H-bonds (Baldwin, 2007). Similarly, the close-packing of nonpolar side chains in a protein may lead to substantially stronger VdW interaction energies as compared to an organic liquid. Coulombic interactions are mainly entropic in nature due to the release of counter-ions into the bulk (Becker et al., 2011) but may also contribute to the stabilization of proteins (Baldwin, 2007).

Therefore, positive heat capacities changes ΔC_p are commonly related the exposure of hydrophobic residues such as observed in the process of protein unfolding (except for helix unfolding that reveals a negative ΔC_p) (Prabhu & Sharp, 2005), whereas aggregation of unfolded proteins commonly shows a negative ΔC_p (Cooper, 2005). More generally, positive heat capacity anomalies were attributed to cooperative order – disorder reactions involving a multiplicity of weak interactions (including hydrophobic interactions and H-bond lattices), examples are protein dissociation, protein unfolding and ice melting (Cooper et al., 2001). It was shown in a computer simulation that a large component of ΔC_p upon protein unfolding comes from fluctuations of non-bonded interactions within the protein (Lazaridis & Karplus, 1999), and both the hydration and the protein term depend on the relative compactness of the folded and unfolded states (Prabhu & Sharp, 2005). Model calculations on solute hydration reveal changes in water H-bond distribution angles

that either increase water energy fluctuations (nonpolar solute) or decrease water energy fluctuations (polar solvent) (which can be related to ΔC_p via Eq. A1), whereas both types of solvation decrease the entropy of water molecules. In this model the low-angle water molecules promoted by hydrophobic groups have a larger interaction energy. As the temperature is lowered, the entropic penalty for hydrating nonpolar groups is reduced and this could lead to cold denaturation of proteins (Prabhu & Sharp, 2005). The aspects discussed here on biomolecular thermodynamics are summarized in table 5.1.

For proteins in solution (RT):	ΔH	ΔS	ΔC_p
polar burial (VdW, H-bond)	(+, -)	+	+
nonpolar burial (VdW)	(+, -)	+	-
Coulombic interactions	(+, -)	+	?
order – disorder transition	+	+	+

Table A1. Positive and negative contribution of physical interactions on the thermodynamic signature of biomolecular reactions: $\Delta H, \Delta S, \Delta C_p$. The terms in brackets may be negative in the context of cooperativity, such as also implied via the positive ΔH in an order – disorder transition.

A2 Isothermal titration calorimetry (ITC)

Isothermal Titration Calorimetry (ITC) is a technique that directly measures the heat exchange accompanying a chemical or biochemical reaction (Martinez et al., 2013). It provides a complete thermodynamic characterization of a macromolecule-ligand interaction, and as such enables the determination of the binding affinity as well as the changes in enthalpy and entropy of the interaction. Additionally the heat capacity of binding may be determined by titrating the ligand at different temperatures.

In ITC the measured heat during the titration corresponds to the enthalpy of the

interaction. To measure the heat of the reaction, a sample and a reference cell are kept at constant temperature via heating the sample cell (if the reaction is endothermic) or the reference cell (if exothermic) with power $W(t)$. The final thermogram Q is obtained by the integration of the individual peaks for each injection relative to the baseline:

$$Q = \int_{t_i}^{t_f} W(t) \cdot dt \tag{A2}$$

The temperature derivative (at constant pressure) of the enthalpy, i.e., the heat capacity change in the process (association or dissociation), ΔC_p, can be determined by performing the same experiment at several temperatures. The slope of an enthalpy versus temperature plot gives the heat capacity of the reaction. The estimation of the heat capacity change allows the determination of the thermodynamic parameters (affinity, Gibbs energy, enthalpy, and entropy) at any temperature. The Gibbs free energy change, ΔG, of an association reaction is temperature dependent and is described by (Jelesarov & Bosshard, 1999)

$$\Delta G(T) = \Delta H(T_R) + \int_{T_R}^{T} \Delta C_p dT - T\Delta S(T_R) - T \int_{T_R}^{T} \Delta C_p \ln T \tag{A3}$$

ΔH and ΔS are the change in enthalpy and entropy, respectively, ΔC_p is the heat capacity change, and T_R is an appropriate reference temperature. To characterize the thermodynamics of a binding reaction means to determine ΔG, ΔH and ΔS at a given reference temperature and to obtain ΔC_p to predict the change of the above three parameters with temperature.

A3 Plasmonic Nanoholes

For three-dimensional (3D) cavities of finite dimension $d_c \ll \lambda_0$ made in a metal film the resonances are mainly transverse cavity modes (Wurtz et al., 2011). A general understanding of such resonances can be obtained by invoking the principle of complementarity between the optical response of ellipsoidal particles and voids supporting localized surface plasmon resonances

$$\omega_p^2 = \omega_{particle}^2 + \omega_{void}^2 \tag{A4}$$

where ω_p is the bulk plasmon frequency, and $\omega_{particle}$ and ω_{void} are the transverse localized resonance of the particle and the void, respectively. In the electrostatic approximation, and for a lossless Drude metal, the resonant wavelength of the lowest-order surface plasmon modes (dipolar) for an ellipsoidal particle in a field polarized along one of the principle axis j takes the form

$$\lambda_{particle} = \frac{2\pi c}{\omega_p} \sqrt{1 - \epsilon_d \left(1 - \frac{1}{L_j}\right)}, j = 1,2,3 \tag{A5}$$

where L is the geometrical or depolarization factor that reflects the shape of the particle, c is the speed of light in vacuum, and ϵ_d denotes the dielectric constant of the embedding medium. The resonance condition for the void can then be expressed as follows:

$$\lambda_{void} = \frac{2\pi c}{\omega_p} \frac{1}{\sqrt{1 - \frac{1}{1 - \epsilon_d\left(1 - 1/L_j\right)}}}, \quad j = 1,2,3 \tag{A6}$$

A4 Quartz crystal microbalance (QCM)

In the quartz crystal microbalance technique (QCM) an applied voltage is inducing a shear strain in a quartz crystal (Höök et al. 2007). The linear change in resonance frequency of the QCM-sensor upon added mass is expressed in the Sauerbrey relation:

$$\Delta m = \frac{C}{n} \Delta f \qquad\qquad\qquad (A7)$$

where C is the sensitivity factor ($C \propto 1/f_0$) and n (=1,2, ...) is the overtone number. However, for many liquid-phase applications such as biomolecule and polymer adsorption to the sensor surface the simple linear relation between Δf and Δm is no longer valid. This is due to the non-rigid character of many molecular layers that induces frictional (viscous) losses and thus a damping of the sensor oscillation. The QCM-D response is obtained via determining the dissipation D and frequency f of output voltage of the freely decaying sensor-oscillation at multiple harmonics. In viscoelastic representations these additional information about energy dissipation are included to describe the adsorbed film characterized by a complex shear modulus:

$$G = G' + iG'' = \mu_f + i2\pi f \nu_f = \mu_f(1 + i2\pi f\tau) \qquad\qquad (A8)$$

where μ_f is the elastic shear (storage) modulus, η_f is the shear viscosity (loss modulus) and τ ($= \eta_f/\mu_f$) is the characteristic relaxation time. The film is further represented by a uniform hydrodynamic thickness, δ_f, ans a density, ρ_f. In the Voigt model changes in ΔD and Δf are expressed in form of the respective hydrodynamic and viscoelastic parameter, where ρ_l and η_l in addition describe density and viscosity of the bulk liquid.

A5 Determination of concentration of gold nanoparticles

The concentration of gold nanoparticles can be determined directly from UV-vis spectra (Haiss et al., 2007). The number density of particles N (particles/ml) can be calculated from the absorbance A_{450} at $\lambda = 450\ nm$ (1 cm path length) according to

$$N = \frac{A_{450} \times 10^{14}}{d^2 \left[-0.295 + 1.36\, exp\left(-\left(\frac{d-96.8}{78.2} \right)^2 \right) \right]} \tag{A9}$$

where d is the particle diameter that can be determined from DLS or more accurately from TEM. However, the authors also show that the particle diameter can be determined from the UV-vis spectra as well. One should also be aware that Eq. A9 is only accurate in case of uncoated gold nanoparticles.

A6 Additional Materials & Methods:

Cloning and expression of recombinant Kapβ1:

Full-length human Kapβ1 was amplified by PCR and inserted into a *Nco*I–*Bam*HI digested pETM-11 expression vector (EMBL Protein Expression and Purification Facility). N-terminal His$_6$-tagged Kapβ1 was expressed in *E. coli* BL21 (DE3) cells at 30 °C overnight and purified on a Ni-NTA column (50 mM TrisHCl, pH 8, 100 mM NaCl, 1 mM DTT; eluted with 80–300 mM imidazole) followed by gel-filtration using a Superdex 200 column (GE Healthcare). Purified protein was analysed by SDS–PAGE and selected fractions containing Kapβ1 were pooled, dialysed against PBS and concentrated.

Cloning and expression of recombinant cNup153, cNup98, cNup62 and
cNup214:

The 601aa C-terminal FG-repeat domain of human Nup153 (aa 874–1,475, Nup153-
C) was PCR-cloned into bacterial expression vector pGEX 6P-1 (GE Healthcare),
which contains a N-terminal glutathione-*S*-transferase (GST) and C-terminal His-tag.
The nucleotide sequence encoding the FG-domains of human nucleoporin Nup98 (aa
1–505) was cloned into pPEP-TEV vector at the *Bam*HI and *Eco*RI restriction sites
using the prokaryotic expression vector pPEP-TEV. This construct contains a N-
terminal His-tag followed by 36 residues of a short laminin linker and a TEV protease
cleavage site. To allow attachment of the recombinant Nup153 or Nup98 fragments to
the gold surfaces, three cysteines were added to the N-terminus in both cases. The
recombinant Cys-Nup153 and Cys-Nup98 were expressed in *Escherichia coli* BL21
(DE3) competent cells (Novagen). The N-terminal FG repeat domain of human
Nup62 (amino acids 1–240) was subcloned by GenScript Inc. into pPEP-TEV vector
at the BamHI and SalI restriction sites. One cysteine was added to its C terminus
(Cys-Nup62) as a covalent tether to Au. A construct containing the FG domain of
cNup214 in pETM-11 was kindly provided by B. Fahrenkrog. To allow attachment of
cNup214 to the Au surface, the first amino acid preceding the fragment's original
sequence was mutated into cysteine by site-directed mutagenesis using primers. The
expressed FG-domains were purified under denaturing conditions (8 M urea, 100 mM
Na_2HPO_4, 10 mM DTT and 10 mM Tris-HCl, pH 8.5) using a Ni-NTA column. A
PreScision protease (GE Healthcare) was used to cleave both the N-terminal
glutathione-*S*-transferase (GST) and C-terminal His-tag from Cys-Nup153-C after
purification. TEV protease was used to remove the His-tag from Cys-Nup98. After
cleavage, the recombinant fragments of Nup98 carry a pre-sequence of GlyGlySer
before the three cysteines at the N-terminus. Some additional residues were also
present in the Cys-Nup153-C construct at both termini after cleavage. Cleavage of
Nup62 using TEV protease is facilitated using 0.5 M urea. Subsequently, all FG-
domains were purified under denaturing conditions. The His-tag-free protein
fragments were than eluted with a buffer containing 8 M urea, 100 mM Na_2HPO_4,

10 mM DTT and 10 mM Tris-HCl, pH 8.5. The final protein purity was analysed by 12% PAGE at 0.1% SDS. The protein concentration was determined by Bradford assay and verified by estimation of protein amounts on Commassie Brilliant Blue-stained SDS-PAGE (12% acryl amide). Alternatively, the protein concentration was also calculated from the absorption at 280 nm. An extinction coefficient of the protein fragment was calculated using the ProtParam program.

Intrinsic properties of the FG domain constructs:

*If this value <<0.5 then the sequence is cohesive and if this value >> 0.5 then it is considered to be repulsive.

Protein (total # of aa)	aa range:	Net charge		Charged aa, %	Charged/ Hydrophobic*	% of length	Conformation
cNup214 (281 aa) pI=9.71	1809-1892	0 (-) 1 (+)	3 (-) 9 (+)	5.6	0.041	30	Cohesive
	1893-2020	3 (-) 7 (+)	—— 6 (+)		0.25	10	Cohesive
	2021-2090	0 (-) 1 (+)			0.09	25	Cohesive
cNup62 (240 aa) pI=9.31	1-240	0 (-) 2 (+)	2 (+)	0.8	0.026	100	Cohesive
cNup98 (498 aa) pI=8.89	1-160	0 (-) 3 (+)	12 (-) 16 (+)	5.6	0.081	32	Cohesive
	161-226	9 (-) 8 (+)	—— 4 (+)		1.066	13	Repulsive
	227-498	3 (-) 5 (+)			0.117	55	Cohesive
cNup153 (602 aa) pI=9.10	874-1270	37 (-) 34 (+)	43 (-) 47 (+)	15	0.681	66	Repulsive
	1271-1475	6 (-) 13 (+)	5 (+)		0.005	34	Cohesive

A7 Matlab scripts

The most convenient matlab scripts and functions that were used for scientific analysis throughout the thesis are shown here. The programs (i) - (viii) are in context of the decay length l_d evaluation as introduced in sections 2.1.1.5 and 2.2.2. The programs (ix) - (xii) are in context of the kinetic analysis as introduced in section 5.2.1. Programs (xiii) - (xiv) are the SPR diffusion model introduced in section 5.2.3. Program (xv) evaluates adlayer thickness from BSA injections, program (xvi) is a visualization tool used for the SPR adlayer thickness plots, and programs (xvi) – (xxii) are to calculate BSA penetration and the SPR response for strongly stretched polymer brushes according to sections 3.2 and 3.3.

(i) l_d_calc.m

```
function[l_d]=l_d_calc(d_a,n_a)
%% Program description
%This function returns the optimal decay length l_d for input values of the
%adlayer in the measuring cell (adlayer thickness: d_a, adlayer refractive
%index: n_a)
%
%Total SPR layer structure: prism / metal / adlayer / solvent
%
%Dependencies: f_calc3,cauchy2,cauchy,K_calc
%
%Written by: Rafael L. Schoch, Basel, 2015

%% Parameter settings
n_pbs=sqrt(1.77985);
n_bsa=sqrt(1.78193);
t=25;
lambda=589;
n_h2o=cauchy(t,lambda);
dn1=n_pbs-n_h2o;
dn2=n_bsa-n_h2o;


%% Parameter settings
T=[25]; %temperatures
lambda=760; %wavelength used in SPR instrument in [nm]
n_t_bsa=cauchy(T,lambda)+dn2;
n_t_pbs=cauchy(T,lambda)+dn1;
n_pri=cauchy2(T,lambda*10^-3);
e_prism=cauchy2(T,lambda*10^-3).^2;%prism dielectric constant
e_sol=(n_t_pbs).^2; %solvent dielectric constant
e_par=(n_t_bsa).^2; %non-interacting particles in solvent dielectric constant
[e_met,n_met,k_met]=K_calc(T+273.15); %metal dielectric constant
d_met=50; %metal thickness in [nm]
n1=1.45; %reference layer refractive index
d1=2; %reference layer thickness in [nm]

t1=64; %lower limit incidence angle in [deg]
t2=74; %upper limit incidence angle in [deg]

%% Main Program
```

```
e_d=e_sol;
dip2_sol = f_calc3_fit(t1,t2,e_pri,e_d,e_met,n_a^2,d_met,d_a,lambda);

e_d=e_par;
dip2_par = f_calc3_fit(t1,t2,e_pri,e_d,e_met,n_a^2,d_met,d_a,lambda);

e_d=e_sol;
dip1_sol = f_calc3_fit(t1,t2,e_pri,e_d,e_met,n1^2,d_met,d1,lambda);

e_d=e_par;
dip1_par = f_calc3_fit(t1,t2,e_pri,e_d,e_met,n1^2,d_met,d1,lambda);

dip1=dip1_par-dip1_sol;
dip2=dip2_par-dip2_sol;

d2=320/2*log(dip1/dip2)+d1;
l_d=((d_a-d1)/(d2-d1))*320;

end
```

(ii) fresnel.m

```
%% Program description
%This function returns the optimal decay lengths l_d in a map for an input
%adlayer range in the measuring cell (adlayer thickness: d_a, adlayer
refractive %index: n_a)
%
%Total SPR layer structure: prism / metal / adlayer / solvent
%
%Dependencies: f_calc3_fit
%
%Written by: Rafael L. Schoch, Basel, 2015

%% Parameter settings
lambda=760; %wavelength used in SPR instrument in [nm]
e_p=2.3104; %prism dielectric constant
e_d=1.77985; %solvent dielectric constant
e_lay=[-20.224+1.440j,0]; %metal dielectric constant / (adlayer dielectric constant)
d_lay=[50,0]; %metal thickness in [nm] / (adlayer thickness in [nm])
t1=64; %lower limit incidence angle in [deg]
t2=74; %upper limit incidence angle in [deg]
d_a=[2:1:40]; %range of adlayer thickness in [nm]
n_a=[1.35:0.01:1.45]; %range of adlayer refractive index in [nm]
n1=1.45; %reference layer refractive index
d1=2; %reference layer thickness in [nm]

%% Main program
matrix1=zeros(length(n_a),length(d_a));
matrix2=zeros(length(n_a),length(d_a));
matrix=zeros(length(n_a),length(d_a));

z=0;

for kk=1:length(d_a)
    for pp=1:length(n_a)

e_d=1.77985;

d_lay(1,2)=d_a(kk);
e_lay(1,2)=(n_a(pp))^2;
dip = f_calc3_fit(t1,t2,e_p,e_d,e_lay,d_lay,lambda);
matrix1(pp,kk)=dip;

e_d=1.78401;

dip = f_calc3_fit(t1,t2,e_p,e_d,e_lay,d_lay,lambda);
matrix2(pp,kk)=dip;
```

```
    end
end

d_lay(1,2)=d1;
e_lay(1,2)=n1^2;

e_d=1.77985;
dip = f_calc3_fit(t1,t2,e_p,e_d,e_lay,d_lay,lambda);
put1=dip;

e_d=1.78401;
dip = f_calc3_fit(t1,t2,e_p,e_d,e_lay,d_lay,lambda);
put2=dip;

put=put2-put1;
matrix=matrix2-matrix1;

d2=320/2*log(put./matrix)+d1;

dmat=zeros(size(matrix));
decay=zeros(size(matrix));

for pp=1:length(n_a)
dmat(pp,:)=d_a;
end

decay=((dmat-d1)./(d2-d1))*320;

decay=((decay-min(min(decay)))./(max(max(decay))-min(min(decay)))).*256;

zlefs=[0:(256*0.53380783)/8:256*0.53380783,256];

contourf(d_a,n_a,decay,zlefs);
set(gca,'YDir','normal')
set(gca,'position',[0.2 0.2 0.6 0.6])
colormap jet(9)
cbar_axes = colorbar
set(cbar_axes,'YTick',[0:256/16.9:256],'YTickLabel',{'0' '100'
'200','300','400','500','600','700','800','900+'})
```

(iii) l_d_opt.m

```
function [fin] = l_d_opt()
%% Program description
%This function returns the optimal decay length l_d_fin, the adlayer
%refractive index n_a_fin and the adlayer thickness d_a_fin for an
%individual SPR experiment.
%
%The input values are the immobilisation response [RU], the initial layer
%thickness [d_init] and the initial decay length used therefor [l_d_init].
%
%The function calculates the adlayer refractive index based on experimentally
%obtained refractive index increments for PEG in PBS (0.1203 cm3/g) and
%proteins in PBS (0.1554 cm3/g), respectively. This function can thus be
%used for either protein or PEG layers, by using either n_prot (default)
%or n_peg when calling the function l_d_calc.m (line 40), respectively.
%
%Dependencies: l_d_calc,f_calc3_fit
%(The settings in the dependencies need to be consistent with the experiment
%as well.)
%
%Written by: Rafael L. Schoch, Basel, 2015

%% Parameter settings
RU=6300; %SPR immobilisation response for adlayer in [RU]
d_init=[50]; %caluated initial height in [nm]
l_d_init=350; %initial decay length in [nm]

n_pbs=sqrt(1.77985);
```

```
n_bsa=sqrt(1.78193);
t=25;
lambda=589;
n_h2o=cauchy(t,lambda);
dn1=n_pbs-n_h2o;
dn2=n_bsa-n_h2o;
T=25;
lambda2=760;

n_s=cauchy(T,lambda2)+dn1

l_d_range=[300:2:450]; %sampled decay length range

%% Main program
frac=exp((d_init-2).*2./l_d_init);
l_d_fin=zeros(1,length(d_init));

for j=1:length(d_init)
    xx=100;
for i=1:length(l_d_range)

    d_in=l_d_range(1,i)./2.*log(frac(1,j))+2;
    n_prot=RU*0.1554./(1300*d_in)+n_s;
    n_peg=RU*0.12./(1000*d_in)+n_s;
    l_d =l_d_calc(d_in,n_peg); %use either n_prot or n_peg as input
    diff=abs(l_d - l_d_range(1,i));

    if  diff <= xx
    l_d_fin(1,j)=l_d_range(1,i);
    xx = diff;
    n_a_fin=n_peg; %use either n_prot or n_peg as input
    d_a_fin=d_in;
    end

end
end
fin=[l_d_fin,n_a_fin,d_a_fin];
end
```

(iv) f_calc3_fit.m

```
function [dip] = f_calc3(t1,t2,e_pri,e_d,e_met,e_n,d_met,d,lambda)
%% Program description
% This function calculates the SPR reflectivity as a function of angle of incidence
and
% returns the minimum position [dip]. The equations for the Fresnel reflection
coefficients
% are taken from Ekgasit et al., 2004.
%
% Written by: Rafael L. Schoch, Basel, 2013

format longE
step=0.001; %angular resolution [deg]
z=0;

for theta2 = t1:step:t2

theta=theta2/(360)*2*pi;
z=z+1;

k_xp=(2*pi/lambda)*(e_pri*sin(theta)^2)^0.5;
k_z1=(((2*pi/lambda))^2.*e_met-k_xp^2).^0.5;
k_z2=(((2*pi/lambda))^2.*e_n-k_xp^2).^0.5;

q1=k_z1./e_met;
q2=k_z2./e_n;

M=([cos(k_z1*d_met),-j/q1*sin(k_z1*d_met);-j*q1*sin(k_z1*d_met),cos(k_z1*d_met)])...
*([cos(k_z2*d),-j/q2*sin(k_z2*d);-j*q2*sin(k_z2*d),cos(k_z2*d)]);
```

```
q_d=((((2*pi/lambda))^2.*e_d-k_xp^2).^0.5)/e_d;
q_p=((((2*pi/lambda))^2.*e_pri-k_xp^2).^0.5)/e_pri;

r(1,z)=((M(1,1)+M(1,2)*q_d)*q_p-
(M(2,1)+M(2,2)*q_d))/((M(1,1)+M(1,2)*q_d)*q_p+(M(2,1)+M(2,2)*q_d));
end

Ref=abs(r).^2;

[deg,pos]=min(Ref);

delta=100;
dip_in=t1+pos*step;
angl=t1+pos*step-delta*step:step:t1+pos*step+delta*step;
myfun=inline('p(1)+p(3)*((x-p(2)).^2)','p','x');
p=lsqcurvefit(myfun,[Ref(pos),dip_in,1],angl,Ref(pos-delta:pos+delta),[Ref(pos)-
0.1,t1+pos*step-delta*step,0],[Ref(pos)+0.1,t1+pos*step+delta*step,5]);
dip=p(2);

end
```

(v) l_d_calc_temp.m

```
function[]=l_d_calc_temp()
%% Program description
%This function returns the optimal decay length for given input values of the
%layer structure of the reference cell (adlayer: d1,n1) and the measuring cell
(adlayer: d2,n2)
%over a range of temperatures T.
%
%layer structure: prism / metal / adlayer / solvent
%
%Dependencies: cauchy.m, cauchy2.m, K_calc, f_calc3, f_calc3
%
%written by Rafael L. Schoch, Basel 2015

close all
clear all

lambda=760; %wavelength used in SPR instrument in [nm]
d_met=50; %metal thickness in [nm]
n1=1.45; %reference layer refractive index
d1=2; %reference layer thickness in [nm]
t1=64; %lower limit incidence angle in [deg]
t2=74; %upper limit incidence angle in [deg]
e_lay=1.36^2; %approx layer refractive index at z=0! av. is n=1.35 for peg20k

n_pbs=sqrt(1.77985);
%n_bsa=sqrt(1.78401);
n_bsa=sqrt(1.78193);
t=25;
lambda2=589;
n_h2o=cauchy(t,lambda2);
dn1=n_pbs-n_h2o;
dn2=n_bsa-n_h2o;
T2=25+273.15;
kb=1.38065e-23;
n=300; %number of d_a (nm) layers considered for brush
d_a=0.2;
R=[6.25]/2*10^-9;
m=2;


%% Parameter settings
T=[5:1:35]; %temperatures
e_pri=cauchy2(T,lambda*10^-3).^2;
n_t_bsa=cauchy(T,lambda)+dn2;
n_t_pbs=cauchy(T,lambda)+dn1;
```

```matlab
e_sol=(n_t_pbs).^2; %solvent dielectric constant
e_par=(n_t_bsa).^2; %non-interacting particles in solvent dielectric constant
[e_met,n_met,k_met]=K_calc(T+273.15); %metal dielectric constant
T2=25+273.15;

%% Main program
for i=1:length(T)

B=40*10^-9;
A=(999)*10^25;

x=([d_a:d_a:d_a*n]-d_a/2)*10^(-9);

ss=size(x);
F_osm=zeros(1,ss(2));
F_ins=zeros(1,ss(2));
boltz_bsa=zeros(1,n);

for tt=1:ss(2)
clear myfun
z0=x(tt);
if z0 <= R
    z0=R;
end

if z0-R < B && z0+R <= B
    F_osm(1,tt)=insertion2(z0,R,A,B,m,T2,z0-R,z0+R);
elseif z0-R< B && z0+R > B
    F_osm(1,tt)=insertion2(z0,R,A,B,m,T2,z0-R,B);
else
    F_osm(1,tt)=0;
end
end

F_ins=F_osm;

boltz_bsa=exp(-(F_ins)/(kb*T2));

chi_peg=zeros(1,n);
chi_peg2=zeros(1,n);
chi_peg2=(1-x.^2/B^2).^(m-1);

for k=1:length(x)
    if x(1,k) <= B
    chi_peg(1,k)=chi_peg2(1,k);
    end
end

e_peg_par=chi_peg*e_lay+(1-chi_peg)*e_sol(1,i)+boltz_bsa*(e_par(1,i)-e_sol(1,i));
e_peg_sol=chi_peg*e_lay+(1-chi_peg)*e_sol(1,i);

e_d=e_sol(1,i);
dip2_sol = fmulti(t1,t2,e_pri(1,i),e_d,e_met(1,i),e_peg_sol,d_met,d_a,lambda);

e_d=e_par(1,i);
dip2_par = fmulti(t1,t2,e_pri(1,i),e_d,e_met(1,i),e_peg_par,d_met,d_a,lambda);

e_d=e_sol(1,i);
dip1_sol = f_calc3_fit(t1,t2,e_pri(1,i),e_d,e_met(1,i),n1^2,d_met,d1,lambda);

e_d=e_par(1,i);
dip1_par = f_calc3_fit(t1,t2,e_pri(1,i),e_d,e_met(1,i),n1^2,d_met,d1,lambda);

dip1(1,i)=dip1_par-dip1_sol;
dip2(1,i)=dip2_par-dip2_sol;
end

d2=40;
d=300/2*log(dip1./dip2)+2;
l_d=((d2-d1)./(d-d1))*300;
```

```matlab
myfun = inline('p(1)+p(2)*T.^2', 'p', 'T');
p = lsqcurvefit(myfun,[300,1],T,l_d,[0,0],[1000,1000])

plot(T,l_d,'*k')
hold on
plot(T,p(1)+p(2)*T.^2,'b-')

end
```

(vi) cauchy.m

```matlab
function [n] = cauchy(t,lambda)
%This function returns the refractive index of water for input
%lambda (wavelength) and temperature (t)
%(according Bashkatov & Genina, 2003);
%lambda in nm;
%
%written by Rafael L. Schoch, Basel 2015

A=1.3208-1.2325*10^(-5)*t-1.8674*10^(-6)*t.^2+5.0233*10^(-9)*t.^3;
B=5208.2413-0.5179.*t-2.284*10^(-2)*t.^2+6.9608*10^(-5)*t.^3;
C=-2.5551*10^8-18341.336*t-917.2319*t.^2+2.7729*t.^3;
D=9.3495+1.7855*10^(-3)*t+3.6733*10^(-5)*t.^2-1.2932*10^(-7)*t.^3;


n=A+B/lambda^2+C/lambda^4+D/lambda^6;

end
```

(vii) cauchy2.m

```matlab
function [n] = cauchy2(t,lambda)
%% Program description
%This function returns the refractive index of the prism for input
%lambda (wavelength) and temperature (t)
%for prism: N-BK7 glass (Schott, Optical Glass Data Sheet,2013);
%lambda in um;
%
%written by Rafael L. Schoch, Basel 2015

format longE
B1=1.03961212;
B2=0.231792344;
B3=1.01046945;
C1=0.00600069867;
C2=0.0200179144;
C3=103.560653;

n_lambda=sqrt(B1*lambda^2/(lambda^2-C1)+B2*lambda^2/(lambda^2-
C2)+B3*lambda^2/(lambda^2-C3)+1);

t0=20;
D0=1.86*10^-6;
D1=1.31*10^-8;
D2=-1.37*10^(-11);
E0=4.34*10^-7;
E1=6.27*10^(-10);

lambda_tk=0.17;

delta_t=t-t0;

fun = @(x) (n_lambda^2-1)/(2*n_lambda)*(D0+2*D1.*(x-t0)+3*D2.*(x-t0).^2+(E0+2*E1.*(x-
t0).^2)/(lambda^2-lambda_tk^2));

for i=1:length(t)
delta_n(i) = integral(fun,t0,t(i));
end
n=n_lambda+delta_n;
```

```
end
```

(viii) K_calc.m

```
function [eps,n,k] = K_calc(T)

%This function returns the dielectric constant and refractive index of
%gold as a function of temperature (T); based onthe drude model
%
%(according Ujihara, 1972; Johnson & Christy, 1972);
%
%written by Rafael L. Schoch, Basel 2015

w_c0=1.1843*10^14;
td=164;
t0=273.15+25;
wp=1.3634*10^16;
w=2.48*10^15;
eps25=-20.224+1.440j;

fun = @(x) x.^4./(exp(x)-1);
int0=integral(fun,0,td/t0);


K=w_c0*(t0^5*int0)^-1;

eps_t0=1-wp^2/(w^2+w_c0^2)+1i*wp^2*w_c0/((w^2+w_c0^2)*w);
delta_eps = eps25 -eps_t0;

for i=1:length(T)
int1(1,i)=integral(fun,0,td/T(i));
w_c(1,i)=K*T(i)^5*int1(1,i);

eps(1,i)=1-wp^2/(w^2+w_c(1,i)^2)+1i*wp^2*w_c(1,i)/((w^2+w_c(1,i)^2)*w)+delta_eps;
eps1(1,i)=1-wp^2/(w^2+w_c(1,i)^2)+real(delta_eps);
eps2(1,i)=wp^2*w_c(1,i)/((w^2+w_c(1,i)^2)*w)+imag(delta_eps);

n=(0.5*(eps1+(eps1.^2+eps2.^2).^0.5)).^0.5;
k=(0.5*((eps1.^2+eps2.^2).^0.5-eps1)).^0.5;
end

end
```

(ix) kinetic_analysis.m

```
%% Program description
%This Matlab script performs a singular value decomposition of SPR data %following the
idea of surface heterogeneity (Svitel et al., 2003)and using the
%Matlab package "Regularization Tools" (RT) by Per Christian Hansen.
%Non-negativity of the regularized solution is achieved using an active set %method
(Landi & Zama., 2005). For further explanations see: Kapinos & Schoch et %al.,
Biophysical J. 2014.
%
%Dependencies: kinfitF15.m, cgsvd.m (RT), l_curve.m (RT), tikhonov.m (RT), %cgls.m
(RT), l_corner.m (RT), lcfun.m (RT), round_X.m
%
%The function kinfitF15.m is the kinetic model that is solved numerically using %the
Matlab function ode15s.m and can be replaced by any other pseudo first %order model if
the "kinetic species" are adjusted also inside this script. All %other dependencies
(except for round_X.m) are functions taken from the Matlab %package "Regularization
Tools".
%
%The resulting matrices and arrays are stored and may be further processed
for %Gaussian fitting using the script interaction_map.m.
%
%Written by: Rafael L. Schoch, Basel, 2015
```

```matlab
clear all
close all

global k1 km1;

%% Parameter settings
options = odeset('AbsTol',1e-03,'RelTol',1e-06);

%"kinetic species" in agreement with kinetic model
L1=[0.0625, 0.125, 0.25, 0.5, 1, 2, 4, 8, 13.6]*10^-6; %applied analyte concentrations
in [mol/l]
R1=(1*10^10); %initial surface receptor concentration in [sites/mm2]
RL1=0; %initial complex1 concentration in [sites/mm2] (standard =0)
RLL1=0; %initial complex2 concentration in [sites/mm2] (standard =0)
RLLL1=0; %initial complex3 concentration in [sites/mm2] (standard =0)

k11=logspace(0, 7, 36); %range and number of on-rates sampled (standard =(0, 7, 36))
km11=logspace(-6, 1, 36); %range and number of off-rates sampled (standard =(-6, 1,
36))

xa=[L1(1);R1;RL1;RLL1;RLLL1]; %vector of initial "kinetic species" concentrations
ta=600; %time of association phases in SPR data in [s], determine accurately!
td=1343; %time of dissociation phases in SPR data in [s], determine accurately!
startpnt=140455; %starting point of first injection of analyte in SPR data, determine
accurately!
td1=500; %time of initial dissociation phases in SPR data (to be stronger weighted) in
[s], i.e. if there are BSA injections after td1

ru_layer = 2200; %this is an important factor! For a multi-layer kinetic model it
determines how many biacore [RU] equals 1 layer

data=dlmread('Nup62_2.txt'); %read in SPR data as txt file column vector

save_curves='Nup62_senso.txt'; %filename for saving (time, fit, sensogram, residuals)
save_matrix1='Nup62_matrix1.txt'; %filename for saving kon-koff matrix
save_matrix2='Nup62_kon_matrix.txt'; %filename for saving KD-kon matrix
save_matrix3='Nup62_koff_matrix.txt'; %filename for saving KD-koff matrix

non_negativity=2000; %number of steps in non-negativity algorithm (standard =2000)

fprintf('part(1/2): % 3d %%',0)
sd=size(data);
points=sd(1)-startpnt-1;
save('save.mat','data')
load('save.mat')

s1=size(k11);
s1m=size(km11);
s=size(L1);
columns_tot=s1(2)*s1m(2);

%% Construction of "senso" from "data". The number of points is reduced from 10 Hz to
1 Hz
pp=0;
countj=startpnt;

for j=1:s(1,2)
for i=countj:10:countj+ta*10-1
    pp=pp+1;
    senso(1,pp)=data(i,1);
end
countj=countj+ta*10;
for i=countj:10:countj+(td1)*10-1
    pp=pp+1;
    senso(1,pp)=data(i,1);
end
countj=countj+(td1)*10;
for i=countj:100:countj+(td-td1)*10-1
    pp=pp+1;
    senso(1,pp)=data(i,1);
end
```

```
countj=countj+(td-td1)*10;
end

%% Generation of empty binding curves for each "kinetic species"
curveL0=zeros(1,length(senso));
curveR=zeros(1,length(senso));
curveRL=zeros(1,length(senso));
curveRLL=zeros(1,length(senso));
curveRLLL=zeros(1,length(senso));

%% Senso preparation
senso=senso./ru_layer;
save('save1.mat','senso')
load('save1.mat')

%% Generation of empty matrix "A"
A=zeros((length(senso)),s1(2)*s1m(2));

%% Filling of matrix "A" columns with nummerical binding curves for each kon/koff pair
per_i=0;
columns=0;
for h=1:s1(2)
    k1=k11(h);
    for j=1:s1m(2)
        km1=km11(j);

for i=1:s(1,2)

xa(1)=L1(i);

tstart=(i-1)*(ta+td);
t1=[tstart:1:tstart+ta-1];
t2=[tstart+ta:1:tstart+ta+td1-1,tstart+ta+td1:10:tstart+ta+td-1];
start=(length(t1)+length(t2))*(i-1)+1;
tend=(length(t1)+length(t2))*i;
fity=zeros(1, s(2)*(length(t1)+length(t2)));

%% Numerical association curves
[T,M]=ode15s('kinfitF15',t1,xa,options);
L0=M(:,1);
R=M(:,2);
RLa=M(:,3);
RLLa=M(:,4);
RLLLa=M(:,5);

% "kinetic species" for dissociation:
xd=[0;R(end);RLa(end);RLLa(end);RLLLa(end)];

%% Numerical dissociation curves
[T,M]=ode15s('kinfitF15',t2,xd,options);
L0d=M(:,1);
Rd=M(:,2);
RLad=M(:,3);
RLLad=M(:,4);
RLLLad=M(:,5);

%% Curve assembly
curveL0(start:tend)=[L0.',L0d.'];
curveR(start:tend)=[R.',Rd.'];
curveRL(start:tend)=[RLa.',RLad.'];
curveRLL(start:tend)=[RLLa.',RLLad.'];
curveRLLL(start:tend)=[RLLLa.',RLLLad.'];

%"kinetic species" for association:
xa=[L1(i);Rd(end);RLad(end);RLLad(end);RLLLad(end)];
end

%initial "kinetic species" for association:
xa=[L1(1);R1;RL1;RLL1;RLLL1];

%% Matrix "A" assembly
```

```matlab
A(:,((h-1)*s1(2)+j))=(curveRL+2*curveRLL+3*curveRLLL)./(R1);

%% Progress display
columns=columns+1;
per_1=round((columns/columns_tot)*100);
if per_1 > per_i
fprintf('\b\b\b\b\b\b % 3d %%',per_1)
per_i=per_1;
end

end
end

fprintf('\n')
fprintf('part(2/2): % 3d %%',0)

%% Generation of matrix "L" for regularization
n=size(A,2);
L=eye(n);
z=0;
b=senso';
za=0;

for h=1:s1(2)
    k1=k11(h);
    for j=1:s1m(2)
        km1=km11(j);
        za=za+1;
K_d=km11(j)/k11(h);
if K_d <= L1(1)
    L(za,za)=L1(1)/K_d;
end
if K_d >= L1(end)
    L(za,za)=K_d/L1(end);
end
end
end

%% Singular value decomposition and choosing a regularization parameter lambda
[U,sm,X,V]=cgsvd(A,L);
lambda=l_curve(U,sm,b,'Tikh');

%% Tikhonov regularized solution x_lambda
[x_lambda]=tikhonov(U,sm,X,b,lambda);

%% Active set method for non-negativity
for i=1:size(x_lambda)
if x_lambda(i)<=0
x_lambda(i)=0.0001;
end
end
x_lambda2=x_lambda;

    g =-A'*b+(A'*A+lambda*L)*x_lambda;

    index=find(g~=0);
    index_W=find(g==0);
    g_red = g(index);
    Q = (A'*A+lambda*L);
    Q_red = Q(index,index);
    per_i=0;

for k=1:non_negativity
    per_1=round((k/non_negativity)*100);
    if per_1 > per_i
    fprintf('\b\b\b\b\b\b % 3d %%',per_1) %progress display
    end
    per_i=per_1;
    if z==0;
    iter=200;
```

```matlab
if length(g_red)== 1
    d_red = -g_red/Q_red;
else
d_red = cgls(Q_red,-g_red,iter);
d_red = d_red(:,iter);
end
d=zeros(n,1);
alpha_min = 1;
I=0;
lagran=zeros(n,1);
lagran_neg=zeros(n,1);
d(index) = d_red;
d=round_X(d,1e-12);

if any(d)== 1

    for i=1:length(d)
    if d(i)< 0
    alpha = (-x_lambda(i))./d(i);
    if alpha < alpha_min && alpha > 1e-16
    alpha_min=alpha;
    I=i;
    end
    end
    end

    x_lambda = x_lambda+alpha_min.*d;

    g =-A'*b+(A'*A+lambda*L)*x_lambda;

    g_red = g(index);

    if any(I)==1

    index(index==I)=[];
    index_W=[index_W;I];
    index_W=sort(index_W);

    g_red = g(index);
    Q_red = Q(index,index);
    end

else

    g =-A'*b+(A'*A+lambda*L)*x_lambda;
    g_red_W = g(index_W);
    Q_red_W = Q(index_W,index_W);
    d_red_W = cgls(Q_red_W,-g_red_W,iter);
    d_red_W = d_red_W(:,iter);
    b0_W=-g_red_W-Q_red_W*d_red_W;
    lagran(index_W)=b0_W;

    for i=1:length(lagran)
    if lagran(i)< 0
    lagran_neg(i)= lagran(i);
    end
    end

    [lagran_min,I] = min(lagran_neg);
    if lagran_min < 0

       index=[index;I];
       index=sort(index);
       index_W(index_W==I)=[];

       for i=1:size(x_lambda)
       if x_lambda(i)<=0
       x_lambda(i)=0.0001;
       end
       end
       g_red = g(index);
```

```matlab
            Q_red = Q(index,index);
            lagran_min=lagran_min;
        else
            z=1;

        end

    end
    end
end

fprintf('\n')

%% kon-koff matrix1 assembly
matrix1=zeros(s1(2),s1m(2));

for h=1:s1(2)

    for j=1:s1m(2)

        matrix1(h,j) = matrix1(h,j) + x_lambda((h-1)*s1(2)+j)*1000;

    end
end

%% kon-KD matrix2 assembly
matrix2=zeros(s1(2),s1(2)+s1m(2)-1);

for i=s1(2):-1:1
    zal=0;
    for j=i:1:s1(2)
        zal=zal+1;
    matrix2(j,abs(i-s1(2))+1)=matrix2(j,abs(i-s1(2))+1)+matrix1(j,zal);
    end
end

for i=1:1:s1(2)-1
    zal=s1(2)+1;
    for j=i:-1:1;
        zal=zal-1;
    matrix2(j,2*s1(2)-i)=matrix2(j,2*s1(2)-i)+matrix1(j,zal);
    end
end

%% koff-KD matrix3 assembly
matrix3=zeros(s1(2),s1(2)+s1m(2)-1);

for i=s1(2):-1:1
    zal=0;
    for j=i:1:s1(2)
        zal=zal+1;
    matrix3(zal,abs(i-s1(2))+1)=matrix3(zal,abs(i-s1(2))+1)+matrix1(j,zal);
    end
end

for i=1:1:s1(2)-1
    zal=s1(2)+1;
    for j=i:-1:1;
        zal=zal-1;
    matrix3(zal,2*s1(2)-i)=matrix3(zal,2*s1(2)-i)+matrix1(j,zal);
    end
end

%% KD-values array assembly
KD=zeros(1,s1(2)+s1m(2)-1);

zal=0;
for i=s1(2):-1:1
    zal=zal+1;
    KD(1,zal)=km11(1)/k11(i);
end
```

```matlab
for i=s1(2):-1:2
    KD(1,s1(2)+i-1)=km11(i)/k11(1);
end

%% Save matrices 1-3 to txt file
format longE
save(save_matrix1, 'matrix1', '-ASCII')
save(save_matrix2, 'matrix2', '-ASCII')
save(save_matrix3, 'matrix3', '-ASCII')

%% Interaction maps (contour and bar plots)
sm2=size(matrix2);
k_on_sum=zeros(1,sm2(1,1));
for i = 1:sm2(1,1)
    k_on_sum(1,i)=sum(matrix2(i,:));
end

sm3=size(matrix3);
k_off_sum=zeros(1,sm2(1,1));
for i = 1:sm2(1,1)
    k_off_sum(1,i)=sum(matrix3(i,:));
end

sm2=size(matrix2);
k_d_on_sum=zeros(1,sm2(1,2));
for i = 1:sm2(1,2)
    k_d_on_sum(1,i)=sum(matrix2(:,i));
end

sm3=size(matrix3);
k_d_off_sum=zeros(1,sm2(1,2));
for i = 1:sm2(1,2)
    k_d_off_sum(1,i)=sum(matrix3(:,i));
end

figure(1)
hold on
axis off
axis square

cc3=[0.85:-0.008:0.058]';
cc4=[0.95:-0.002:0.752]';

colormap([cc3 cc3 cc4])

axes('position',[.2  .22  .28  .28]);
contour(log10(KD),log10(k11),matrix2,[0.1:0.1:10],'LevelStep',0.1,'fill','on')

xlabel('log(K_{D})','fontsize',14);
ylabel('log(k_{on})','fontsize',14);
axis([-10 -4 log10(k11(1)) log10(k11(end))])
axis square
grid on
set(gca,'XTick',-10:1:-4)

axes('position',[.43  .22  .05  .28]); barh(log10(k11),k_on_sum,1)
set(gca,'XTickLabel','')
set(gca,'YTickLabel','')
set(gca,'YLim',[log10(k11(1)) log10(k11(end))])
set(gca,'XTick',[])
grid on

axes('position',[.2  .55  .28  .28]);
contour(log10(KD),log10(km11),matrix3,[0.1:0.1:10],'LevelStep',100,'fill','on')
ylabel('log(k_{off})','fontsize',14);
axis([-10 -4 log10(km11(1)) log10(km11(end))])
axis square
grid on
set(gca,'XTick',-10:1:-4)
```

```matlab
axes('position',[.43  .55  .05  .28]); barh(log10(km11),k_off_sum,1)
set(gca,'XTickLabel','')
set(gca,'YTickLabel','')
set(gca,'YLim',[log10(km11(1)) log10(km11(end))])
set(gca,'XTick',[])
grid on

axes('position',[.2625  .85  .155  .09]); bar(log10(KD),k_d_on_sum,1)
set(gca,'XTickLabel','','XLim',[-10 -4])
set(gca,'YTickLabel','')
set(gca,'XTick',-10:1:-4,'fontsize',12)
set(gca,'YTick',[])
grid on

%% Plotting sensogram, fit and residuals
Mcurve=A*x_lambda;

t=zeros(1,length(senso));
size(t);
countj=0;
pp=0;

for j=1:s(1,2)
for i=countj:10:countj+ta*10-1
    pp=pp+1;

    t(1,pp)=i/10;
end
    countj=countj+ta*10;
for i=countj:10:countj+td1*10-1
    pp=pp+1;

    t(1,pp)=i/10;
end
    countj=countj+td1*10;
for i=countj:100:countj+(td-td1)*10-1
    pp=pp+1;

    t(1,pp)=i/10;
end
    countj=countj+(td-td1)*10;
end

Mc=Mcurve';
bb=b';
residu=b-Mcurve;

figure(2);
c=s(2);
axes('position',[0.2 , 0.4  ,0.6  .5]);
plot(t,bb,'k','linewidth',2)
hold on
plot(t,Mc,'r','linewidth',2)
set(gca,'XLim',[0 t(1,end)])
ylabel('Number of analyte layers','fontsize',20);
axes('position',[0.2,  .16,  .6,  .2])
plot(t,bb-Mc,':r','linewidth',2)
t1=1;
for i = 1:c
t2=t1+ta+td1;
hold on
plot(t(1,t1+2:t2),bb(1,t1+2:t2)-Mc(1,t1+2:t2),'-r','linewidth',3)
t1=t1+ta+td1+length(1:10:td-td1);
end
plot([0,t(1,end)],[0,0],':k','linewidth',2)
set(gca,'XLim',[0 t(1,end)],'YLim',[-0.2 0.2])
xlabel('Time (s)','fontsize',20);

%% Save the curves (time, fit, sensogram, residuals)
res=residu';
save(save_curves, 't', 'Mc', 'bb', 'res','-ASCII')
```

(x) kinfitF15.m

```matlab
function dx=kinfitF15(t,x)
%% Program description
%Differential equations of kinetic model for Kapb1 - FG domain interaction
%(3 layer model).
%% Main program
global k1 km1;
dx=zeros(5,1);
dx(1)=0;
dx(2)=-k1*x(2)*x(1)+km1*x(3);
dx(3)=k1*x(2)*x(1)-km1*x(3)-k1*x(3)*x(1)+km1*x(4);
dx(4)=k1*x(3)*x(1)-km1*x(4)-k1*x(4)*x(1)+km1*x(5);
dx(5)=k1*x(4)*x(1)-km1*x(5);
```

(xi) round_X.m

```matlab
function [gnew] = round_X(g,prec)

s_g = size(g);
    for j = 1:s_g(1)
    for i = 1:s_g(2)
    if (g(j,i) < prec) && (g(j,i) > -prec)
    g(j,i) = 0;
    end
    end
    end
    gnew=g;

end
```

(xii) interaction_map.m

```matlab
%% Program description
%This Matlab script can be used to generate interaction maps together with
%Gaussian fitted bar-plots for the interaction matrices 2 & 3 generated in the %script
kinetic_analysis.m.
%
%Written by Rafael L. Schoch, Basel 2015

%% Parameter settings
k11=logspace(0, 7, 36); %range and number of on-rates sampled (standard =(0, 7, 36))
km11=logspace(-6, 1, 36); %range and number of off-rates sampled (standard =(-6, 1,
36))
s1=size(k11);
s1m=size(km11);

%% Read in interaction matrices; for averaging more than one pair of matrices may be
read in.
mat1on=dlmread('Nup62_kon_matrix.txt'); %read in KD-kon matrix
mat1off=dlmread('Nup62_koff_matrix.txt'); %read in KD-koff matrix
%mat2on=dlmread('Nup62_2_matrix2.txt'); %%read in KD-kon matrix; may be deactivated
using '%' sign
%mat2off=dlmread('Nup62_2_matrix3.txt'); %read in KD-koff matrix; may be deactivated
using '%' sign
%mat3on=dlmread('Nup62_3_matrix2.txt'); %read in KD-kon matrix; may be deactivated
using '%' sign
%mat3off=dlmread('Nup62_3_matrix3.txt'); %read in KD-koff matrix; may be deactivated
using '%' sign
%mat4on=dlmread('Nup62_4_matrix2.txt'); %read in KD-kon matrix; may be deactivated
using '%' sign
%mat4off=dlmread('Nup62_4_matrix3.txt'); %read in KD-koff matrix; may be deactivated
using '%' sign

matrix2=mat1on;%+mat2on+mat3on+mat4on; %forming sum of matrices; adjust to effectively
```

```
used KD-kon matrices
matrix3=mat1off;%+mat2off+mat3off+mat4off; %frming sum of matrices; adjust to
effectively used KD-koff matrices

%% Normalizing on and off matrices
hval2=max(max(matrix2));
hval3=max(max(matrix3));
matrix2=matrix2/hval2*10;
matrix3=matrix3/hval3*10;


%% Generating sums for bar plots
KD=zeros(1,s1(2)+s1m(2)-1);
zal=0;

for i=s1(2):-1:1
    zal=zal+1;
    KD(1,zal)=km11(1)/k11(i);
end

for i=s1(2):-1:2
    KD(1,s1(2)+i-1)=km11(i)/k11(1);
end

sm2=size(matrix2);
k_on_sum=zeros(1,sm2(1,1));
for i = 1:sm2(1,1)
    k_on_sum(1,i)=sum(matrix2(i,:));
end

sm3=size(matrix3);
k_off_sum=zeros(1,sm2(1,1));
for i = 1:sm2(1,1)
    k_off_sum(1,i)=sum(matrix3(i,:));
end

sm2=size(matrix2);
k_d_on_sum=zeros(1,sm2(1,2));
for i = 1:sm2(1,2)
    k_d_on_sum(1,i)=sum(matrix2(:,i));
end

%% Fitting Gaussians to the sums of kon, koff and KD
xx=log10(KD)';
yy=k_d_on_sum';
yy2=k_on_sum';
xx2=log10(k11)';
yy3=k_off_sum';
xx3=log10(km11)';

%% Definition of the Gaussian functions with parameters p(1)...p(9) for KD,
pp(1)....pp(12) for kon, ppp(1)...ppp(9) for koff, ADJUST!!!
myfun1 = inline('p(1)*exp(-((xx-p(2)).^2)/(2*p(3)^2))+p(4)*exp(-((xx-
p(5)).^2)/(2*p(6)^2))+p(7)*exp(-((xx-p(8)).^2)/(2*p(9)^2))', 'p', 'xx');
myfun2 = inline('pp(1)*exp(-((xx2-pp(2)).^2)/(2*pp(3)^2))+pp(4)*exp(-((xx2-
pp(5)).^2)/(2*pp(6)^2))+pp(7)*exp(-((xx2-pp(8)).^2)/(2*pp(9)^2))+pp(10)*exp(-((xx2-
pp(11)).^2)/(2*pp(12)^2))', 'pp', 'xx2');
myfun3 = inline('ppp(1)*exp(-((xx3-ppp(2)).^2)/(2*ppp(3)^2))+ppp(4)*exp(-((xx3-
ppp(5)).^2)/(2*ppp(6)^2))+ppp(7)*exp(-((xx3-ppp(8)).^2)/(2*ppp(9)^2))', 'ppp', 'xx3');

%% Fitting myfun to the data for the startvalues of p(1)...p(9) etc.
lsqcurvefit(function,startvalues,xdata,ydata,lower_bounds,upper_bounds), ADJUST!!!
p = lsqcurvefit(myfun1,[40,-7.6,1,50,-6.9,0.5,10,-5.5,0.5],xx,yy,[0,-8,0,0,-7.2,0,0,-
6.2,0],[1000,-7,10,1000,-6,10,1000,-5,10]); %KD
pp =
lsqcurvefit(myfun2,[10,6,2,60,4,0.5,20,3,0.5,40,2,1],xx2,yy2,[0,5,0,0,3.5,0,0,2.5,0,0,
1,0],[1000,6.5,10,1000,4.5,10,1000,3.5,10,1000,2.8,10]); %kon
ppp = lsqcurvefit(myfun3,[10,0,2,60,-4,0.8,20,-5,0.8],xx3,yy3,[0,-2,0,0,-4.8,0,0,-
6,0],[1000,0.8,10,1000,-3.5,10,1000,-4.6,10]); %koff

%% Interaction maps (contour, bars and gaussians)
```

```
figure(1)
hold on
axis off
axis square
cc=[0.85:-0.005:0.355]';
cc3=[0.85:-0.008:0.058]';
cc4=[0.95:-0.002:0.752]';
cc1=ones(100,1)*0;
cc2=ones(100,1)*0.8;
size(cc);
size(cc2);
colormap([cc3 cc3 cc4]);

axes('position',[.2  .22  .28  .28]);
contour(log10(KD),log10(k11),matrix2,[0.1:0.1:10],'LevelStep',0.1,'fill','on')

xlabel('log(K_{D})','fontsize',14);
ylabel('log(k_{on})','fontsize',14);
axis([-10 -4 log10(k11(1)) log10(k11(end))])
axis square
grid on
set(gca,'XTick',-10:1:-4)
axes('position',[.43  .22  .05  .28]); barh(log10(k11),k_on_sum,1)
hold on
plot(myfun2(pp,xx2),xx2,'-','LineWidth',2)
set(gca,'XTickLabel','')
set(gca,'YTickLabel','')
set(gca,'YLim',[log10(k11(1)) log10(k11(end))])
set(gca,'XTick',[])
grid on

axes('position',[.2  .55  .28  .28]);
contour(log10(KD),log10(km11),matrix3,[0.1:0.1:10],'LevelStep',100,'fill','on')
ylabel('log(k_{off})','fontsize',14);
axis([-10 -4 log10(km11(1)) log10(km11(end))])
axis square
grid on
set(gca,'XTick',-10:1:-4)

axes('position',[.43  .55  .05  .28]); barh(log10(km11),k_off_sum,1)
hold on
plot(myfun3(ppp,xx3),xx3,'-','LineWidth',2)
set(gca,'XTickLabel','')
set(gca,'YTickLabel','')
set(gca,'YLim',[log10(km11(1)) log10(km11(end))])
set(gca,'XTick',[])
grid on

axes('position',[.2625  .85  .155  .09]); bar(log10(KD),k_d_on_sum,1)
hold on
plot(xx,myfun1(p,xx),'-','LineWidth',2)
set(gca,'XTickLabel','','XLim',[-10 -4])
set(gca,'YTickLabel','')
set(gca,'XTick',-10:1:-4,'fontsize',12)
set(gca,'YTick',[])
grid on

%% Display Gaussian values
zal=1;
for i=1:3:length(p)
    amplitude_KD(1,zal)=p(i);
    zal=zal+1;
end

zal=1;
for i=1:3:length(pp)
    amplitude_kon(1,zal)=pp(i);
    zal=zal+1;
end

zal=1;
```

```
for i=1:3:length(ppp)
    amplitude_koff(1,zal)=ppp(i);
    zal=zal+1;
end

zal=1;
for i=2:3:length(p)
    position_KD(1,zal)=p(i);
    zal=zal+1;
end

zal=1;
for i=2:3:length(pp)
    position_kon(1,zal)=pp(i);
    zal=zal+1;
end

zal=1;
for i=2:3:length(ppp)
    position_koff(1,zal)=ppp(i);
    zal=zal+1;
end


zal=1;
for i=3:3:length(p)
    width_KD(1,zal)=p(i);
    zal=zal+1;
end

zal=1;
for i=3:3:length(pp)
    width_kon(1,zal)=pp(i);
    zal=zal+1;
end

zal=1;
for i=3:3:length(ppp)
    width_koff(1,zal)=ppp(i);
    zal=zal+1;
end


format shortE
results_kon=['For kon: positions: ',num2str(10.^position_kon),' amplitudes:
',num2str(amplitude_kon),' widths: ',num2str(10.^width_kon)];
fprintf('kon positions: ')
fprintf('% .2E',10.^position_kon)
fprintf('\nkon amplitudes: ')
fprintf('% .1f',amplitude_kon)
fprintf('\nkon widths: ')
fprintf('% .2f',width_kon)

fprintf('\nkoff positions: ')
fprintf('% .2E',10.^position_koff)
fprintf('\nkoff amplitudes: ')
fprintf('% .1f',amplitude_koff)
fprintf('\nkoff widths: ')
fprintf('% .2f',width_koff)

fprintf('\nKD positions: ')
fprintf('% .2E',10.^position_KD)
fprintf('\nKD amplitudes: ')
fprintf('% .1f',amplitude_KD)
fprintf('\nKD widths: ')
fprintf('% .2f',width_KD)
fprintf('\n')
```

(xiii) diffusion.m

```matlab
%% Program description
%brownian diffusion in a two well potential
%Dependencies: Fe2.m
%Written by Rafael L. Schoch, Basel, 2015

close all
clear all

%% Parameter settings
T=273.15+25; %simulation temperature
TT=273.15+25; %temperature for potential construction (default = 25°C)
kb=1.3806488*10^(-23); %boltzmann constant
nu=2.414*10^(-5)*10^(247.8/(T-140)); %viscosity of water
nu2=2.414*10^(-3)*10^(247.8/(T-140)); %viscosity in simulation
D_dif=kb*T/(6*pi*nu*5*10^-9) %diffusion constant in water
D_visc=kb*T/(6*pi*nu2*5*10^-9) %diffusion constant in simulation
simulation_steps = 1*10^3; %number of simulation steps
dt=1*10^-7; %time per simulation step
drag=kb*T/D_visc
m=1.66053892*10^(-24)*100*10^3;
tau=m/drag
A=20*kb*T;%Gaussian heights
B=5*kb*T;
C=11*10^-9;    %Gaussian positions
D=22*10^-9;
E=(3*10^-9)^2; %Gaussian widths
F=(6*10^-9)^2;
G=80*kb*T;   %attractive exponential magnitude
H=7.5*10^-9;  %exp decay
I=1300*kb*T; %repulsive exponential magnitude
J=1.6*10^-9;    %exp decay
len1=100; %height of cell in nm
len=len1*10^-9;
bulk_particles=10; %constant number of bulk particles at association
time_bins=500; %how often simulation_steps * dt is analyzed (resolution of plot)
time_bins2=20; %how often simulation_steps * dt * time_bins is analyzed
time_plot=[1:1:time_bins2]*simulation_steps*dt*time_bins;
time_plot_d=[1:1:time_bins2]*simulation_steps*dt*time_bins+time_plot(end);
part_count=zeros(1,time_bins);
part_count_slow=zeros(1,time_bins);
part_count2=zeros(1,time_bins2);
part_count_slow2=zeros(1,time_bins2);
part_count_slow_Fe=0; %number ot particles in slow first potential well
p_max=100; %capacity of brush in number of particles


%% Main program association
number_particles=bulk_particles;

v=zeros(number_particles,simulation_steps);
x=zeros(number_particles,simulation_steps);

v(:,1)=randn(number_particles,1)*sqrt(kb*T/m);
x(:,1)=rand(number_particles,1)*(len-D)+D; %initial distributing particles randomly
down to 3rd well
x_start=x(:,1);
disti=zeros(1,len1);
per_i=0;
fprintf('\n % 3d %%', 0)

for h = 1:time_bins2;

% Progress display
per_1=round((h/(2*time_bins2))*100);
if per_1 > per_i
fprintf('\b\b\b\b\b\b % 3d %%',per_1)
per_i=per_1;
end
```

```
part_count=zeros(1,time_bins);
part_count_slow=zeros(1,time_bins);
for m = 1:time_bins;

for j=1:number_particles
for i=1:simulation_steps-1   %updating algorithm
    troll=randn;
    x(j,i+1) = x(j,i)-
D_visc/(kb*T)*Fe2(x(j,i),A,B,C,D,E,F,G,H,I,J,part_count_slow_Fe,p_max)*dt+sqrt(2*D_vis
c*dt)*troll;

    if x(j,i+1) > len   %boundary condition
        x(j,i+1)=2*len-x(j,i)-(-
D_visc/(kb*T)*Fe2(x(j,i),A,B,C,D,E,F,G,H,I,J,part_count_slow_Fe,p_max)*dt+sqrt(2*D_vis
c*dt)*troll);
    end

    if x(j,i+1) < 0   %boundary condition
        x(j,i+1)=-x(j,i)-(-
D_visc/(kb*T)*Fe2(x(j,i),A,B,C,D,E,F,G,H,I,J,part_count_slow_Fe,p_max)*dt+sqrt(2*D_vis
c*dt)*troll);
    end


end
end


for j=1:number_particles %count bound particles, i.e. for position lower second hill
if x(j,end)< D
part_count(1,m)=part_count(1,m)+1;
end

if x(j,end)< C
part_count_slow(1,m)=part_count_slow(1,m)+1;
end
end

part_count_slow_Fe=part_count_slow(1,m);

v_end=v(:,end);
x_end=x(:,end);

if h < time_bins2 && m < time_bins

new_part=bulk_particles-(number_particles-part_count(1,m)); %number of particles in
bulk kept constant
number_particles=number_particles+new_part;


v=zeros(number_particles,simulation_steps);
x=zeros(number_particles,simulation_steps);

if new_part == 0;
v(:,1)=[v_end];
x(:,1)=[x_end];
end

if new_part > 0
v(:,1)=[v_end;randn(new_part,1)*sqrt(kb*T/m)]; %take old particles end values add new
random particles to maintian constant bulk conc
x(:,1)=[x_end;rand(new_part,1)*(len-2*D)+2*D];
end

if new_part < 0 %remove particles from bulk

   while length(x_end) > number_particles
   [cc]=find(x_end > D);
   x_end(cc(1))=[];
   v_end(cc(1))=[];
```

```matlab
        end
    v(:,1)=[v_end];
    x(:,1)=[x_end];
end
end


end


part_count2(1,h)=mean(part_count);
part_count_slow2(1,h)=mean(part_count_slow);
end

for j = 1:number_particles
    for i = 1:simulation_steps
    for jj=1:1:len1 % 1 nm bins for particle distribution
        if x(j,i) <= jj*10^-9 && x(j,i) > (jj-1)*10^-9
        disti(1,jj)=disti(1,jj)+1/(simulation_steps*number_particles);
        end
    end
    end
end

save('parameter_constrained.txt', 'p_max','part_count_slow_Fe','-ASCII')

Z=[0.5:1:99.5]*10^-9;
Gf=(A*exp(-((Z-C).^2)/E)+B*exp(-((Z-D).^2)/F)- (G*(1-
part_count_slow_Fe^2/p_max^2))*exp(-Z/H)+I*exp(-Z/J));
boltz=(exp(-Gf/(kb*T)))/(sum(exp(-Gf/(kb*T))));

%% Main program dissociation
[dd]=find(x_end > D);
part_count_d=zeros(1,time_bins);
part_count2_d=zeros(1,time_bins2);
part_count_slow_d=zeros(1,time_bins);
part_count_slow2_d=zeros(1,time_bins2);
x_end(dd)=[];
v_end(dd)=[];
number_particles = length(x_end);
v=zeros(number_particles,simulation_steps);
x=zeros(number_particles,simulation_steps);
v(:,1)=[v_end];
x(:,1)=[x_end];

for h = 1:time_bins2;

% Progress display
per_1=round((h/(2*time_bins2))*100)+50;
if per_1 > per_i
fprintf('\b\b\b\b\b\b % 3d %%',per_1)
per_i=per_1;
end

part_count_d=zeros(1,time_bins);
part_count_slow_d=zeros(1,time_bins);
for m = 1:time_bins;

for j=1:number_particles
for i=1:simulation_steps-1  %updating algorithm

    troll=randn;
    x(j,i+1) = x(j,i)-
D_visc/(kb*T)*Fe2(x(j,i),A,B,C,D,E,F,G,H,I,J,part_count_slow_Fe,p_max)*dt+sqrt(2*D_vis
c*dt)*troll;

    if x(j,i+1) < 0  %boundary condition
        x(j,i+1)=-x(j,i)-(-
D_visc/(kb*T)*Fe2(x(j,i),A,B,C,D,E,F,G,H,I,J,part_count_slow_Fe,p_max)*dt+sqrt(2*D_vis
c*dt)*troll);
    end

end
```

```
end

for j=1:number_particles %count bound particles, i.e. for position lower second hill
if x(j,end)< D
part_count_d(1,m)=part_count_d(1,m)+1;
end

if x(j,end)< C
part_count_slow_d(1,m)=part_count_slow_d(1,m)+1;
end
end

part_count_slow_Fe=part_count_slow_d(1,m);

v_end=v(:,end);
x_end=x(:,end);

[dd]=find(x_end > D);

x_end(dd)=[];
v_end(dd)=[];

number_particles = length(x_end);

v=zeros(number_particles,simulation_steps);
x=zeros(number_particles,simulation_steps);

if number_particles > 0
v(:,1)=[v_end];
x(:,1)=[x_end];
end

end
part_count2_d(1,h)=mean(part_count_d);
part_count_slow2_d(1,h)=mean(part_count_slow_d);
end

figure(1)
plot([0,time_plot,time_plot_d],[0,part_count2,part_count2_d],'-
k',[0,time_plot,time_plot_d],[0,part_count_slow2,part_count_slow2_d],'--k')

figure(2)
plot(Z,disti,'-b',Z,boltz,':k')
```

(xiv) Fe2.m

```
function [ y ] = Fe2( x,A,B,C,D,E,F,G,H,I,J,part_count_slow,p_max)
%% Program description
% This function returns the force on a particle given the position "x" and
% the parameters of the potential function "A-J", as well as the number of
% particles in the first binding well "part_count" and the capacity of this
% binding well "p_max".
% written by Rafael L. Schoch, Basel, 2015

y=2*A/E*(C-x).*exp(-(C-x).^2/E)+2*B/F*(D-x).*exp(-(D-x).^2/F)+(G*(1-
part_count_slow^2/p_max^2))/H*exp(-x/H)-I/J*exp(-x/J);
end
```

(xv) evaluation2.m

```
function []=evaluation2()
%% Program description
% This function returns the mean thickness values and standard deviation for    % each
BSA injection bundle in an SPR sensogram.
%
% Dependencies: readColData.m
% (http://web.cecs.pdx.edu/~gerry/MATLAB/plotting/examples/readColData.m)
```

```matlab
clear all
close all

%% parameters settings
cells=3; %number of flow cells used
inject=63; %number of injections of phosphate buffer and bsa together
phb=0; %number of phosphate buffer injections (before bsa injections)
diff=60; %jump in resonance signal for recognition of bsa/phb peak (sensitivity)
bundle=3; %number of bsa injections in a bundle per analyte concentration;
caliboff=0; %set to zero if calibration factor should be neglected (eg. for biacore
sensors)
ld=350; %Decay length in [nm]

%loads the sensograms Fc1-Fc4 from the same folder as the matlab function
%[labels,t(:,1),ru(:,1)] = readColData('Nsp1_10_1p.txt',2,0,1);  %flow cell 1
(reference cell)
%[labels,t(:,2),ru(:,2)] = readColData('Nsp1_10_1n.txt',2,0,1);  %flow cell 2
%[labels,t(:,3),ru(:,3)] = readColData('Nsp1_10_2n.txt',2,0,1);  %flow cell 3

[labels,ru(:,1)] = readColData('Nsp1_37_5p.txt',1,0,1);  %flow cell 1 (reference cell)
[labels,ru(:,2)] = readColData('Nsp1_37_5n.txt',1,0,1);  %flow cell 2
[labels,ru(:,3)] = readColData('Nsp1_37_6n.txt',1,0,1);  %flow cell 3

height=zeros(cells,inject);
bound=zeros(cells,inject);
const=0;

for ii=1:cells
dim=size(ru);
dim(1,1);
numb=1;
za=1; %starting point of sensogram evaluation
test=10;
for i=za:1:dim(1,1)-5000
    za=za+1;
    if ru(za-1,ii)-ru(za,ii)>=diff
        for z=2:1:5
            if abs(ru(za-z+1,ii)-ru(za-z,ii))<=1
                if test==10
                if numb<=inject
                peak=ru(za-z+1-const,ii);
                height(ii,numb)=peak-(ru(za-z+1+300,ii));
                bound(ii,numb)=ru(za-z+1+300,ii);
                numb=numb+1;
                za=za+4;
                test=5;
                end
                end
            end
        end
      test=10;
    end

end

end
height;
calib1=zeros(1,phb);
calib2=zeros(1,phb);
refcalib=0;

for i=1:phb
refcalib=refcalib+height(1,i);
end

for k=2:cells
    for i=1:phb
    calib2(1,k-1)=calib2(1,k-1)+(height(k,i));
    end
end
```

```matlab
calib=refcalib./calib2;

if caliboff==0
    calib=ones(1,cells-1);
end

for k=2:cells
for i=1:(inject-phb)
ratio(k-1,i)=height(1,phb+i)/height(k,phb+i);
end
end

for k=1:(cells-1)
    for i=1:(inject-phb)
thickness(k,i)=ld/2*log(ratio(k,i)./calib(1,k));
end
end

thickness2=thickness+2;
bound2=zeros(cells-1,inject-phb);

for k=2:cells
for i=1:(inject-phb)
bound2(k-1,i)=bound(k,i);
end
end

schnitt3=zeros(cells-1,(inject-phb)/bundle);
bound3=zeros(cells-1,(inject-phb)/bundle);

for k=1:(cells-1)
for i=1:((inject-phb)/bundle)

p=i*bundle-(bundle-1);

for z=1:bundle
schnitt3(k,i)=schnitt3(k,i)+(thickness2(k,p+z-1));
bound3(k,i)=bound3(k,i)+(bound2(k,p+z-1));
end
schnitt3(k,i)=schnitt3(k,i)/bundle;
bound3(k,i)=bound3(k,i)/bundle;

end

end

stdev3=zeros(cells-1,(inject-phb)/bundle);

for k=1:(cells-1)
for i=1:((inject-phb)/bundle)

p=i*bundle-(bundle-1);

for z=1:bundle
stdev3(k,i)=stdev3(k,i)+(thickness2(k,p+z-1)-schnitt3(k,i))^2;
end
stdev3(k,i)=sqrt(stdev3(k,i))/bundle;
end

end

Mw=100000;
rholayer=1000;
dh=10;

na=6.02214129*10^23;
thickness=schnitt3
stdev=stdev3

size(thickness)
```

```
deltad=(thickness-
thickness(:,1)*ones(1,size(thickness,2)))./(thickness(:,1)*ones(1,size(thickness,2)))

ruimp=bound3-bound3(:,1)*ones(1,size(bound3,2));

gimp=((1300*Mw*10^21)./(na*ruimp)).^0.5;
rhoimp=dh^2*rholayer./(gimp.^2)

plot(rhoimp',deltad','ks-')
xlabel('rho');
ylabel('delta d');
A=[rhoimp(1,:)',deltad(1,:)',rhoimp(2,:)',deltad(2,:)'];
save my_data.txt A -ASCII
```

(xvi) extension2.m

```
function[]=extension2()
%% Programm description
% This function plots average curves weighted by the width of the standard
% deviation and chroma according the density of points. It is applied to a
% set of data recorded over a similar x-range, such as NTR surface density
% vs thickness plots from SPR.
%
% Written by Rafael Schoch, Basel, 2015

clear all
close all


for zz=1:2
clear tt pp array_spline_x array_spline_y
data=0;
ee={'nsp1_data_10C.txt' 'nsp1_data_37C.txt'}
eee={'Nsp1 10°C' 'Nsp1 37°C'}
data=dlmread(ee{1,zz});
size(ee)
size(eee)
size(data)
colormap([0 0 1;
     1 0 0;
     0 0 1;
     1 0 0]);

sd=size(data);
zahl=0;
za=0;

for i=1:2:sd(1,2)
    for j=1:sd(1,1)
    if j==1
        zahl=zahl+1;
    data2(zahl,:)=[data(j,i+1),data(j,i)];
    else if data(j,i+1)~=0
            zahl=zahl+1;
            data2(zahl,:)=[data(j,i+1),data(j,i)];

    end
    end
    end
    za=za+1;
array_d(1,i)=zahl;
zahl=0;
end

zahl=0;
nn=1000;
yy=zeros(nn,sd(1,2)/2);
xx=zeros(nn,sd(1,2)/2);
```

```matlab
hold on

for i = 1:2:sd(1,2)
xx=linspace(data(1,i),max(data(:,i)),array_d(1,i));
tt=[data(1:array_d(1,i),i)';data(1:array_d(1,i),i+1)'];
pp=spline(xx,tt);
yy = ppval(pp, linspace(data(1,i),max(data(:,i)),nn));
zahl=zahl+1;
array_spline_x(:,zahl)=yy(1,:);
array_spline_y(:,zahl)=yy(2,:);
end
array_d

binwidth=10;
bins=ceil(max(max(data))/binwidth);
i_bin=zeros(bins,size(array_spline_x,2),size(array_spline_x,1));

for i=1:bins
    for j=1:size(array_spline_x,2)
    for h=1:size(array_spline_x,1)
        if array_spline_x(h,j) >= (i-1)*binwidth && array_spline_x(h,j) < i*binwidth
        i_bin(i,j,h)=h;
        end
    end
    end
end

aver=zeros(bins,size(array_spline_y,2));
stdev=zeros(bins,size(array_spline_y,2));

for i=1:bins
   for j=1:size(array_spline_y,2)
        if isempty(array_spline_y(nonzeros(i_bin(i,j,:)),j)) ==  0
        aver(i,j)=mean(array_spline_y(nonzeros(i_bin(i,j,:)),j));
        stdev(i,j)=std(array_spline_y(nonzeros(i_bin(i,j,:)),j));

        end
   end

end

bin_aver=zeros(bins+1,1);
for i=1:bins
bin_aver(i+1,1)=binwidth/2+(i-1)*binwidth;
end

tot_aver=zeros(bins+1,1);
for i=1:bins
tot_aver(i+1,1)=mean(nonzeros(aver(i,:)));

end

bin_data=zeros(1,bins);
for i=1:bins
    for k=1:sd(1)
    for j=1:sd(2)
    if data(k,j) > (i-1)*binwidth && data(k,j) <= i*binwidth
    bin_data(1,i)=bin_data(1,i)+1;
    end
    end
    end
end

bin_weight_1d=zeros(1,bins);

lat_weighting=80;

for i=1:bins
    if i>200
```

```
                g=200;
        else
                g=i;
        end
        if i<bins-200
                k=200;
        else
                k=bins-i;
        end
        for j=1:g
        bin_weight_1d(1,i)=bin_weight_1d(1,i)+((bin_data(1,i-j+1)*exp(-((-
j+1)/lat_weighting)^2))/g);
        end
        for h=1:k
        bin_weight_1d(1,i)=bin_weight_1d(1,i)+((bin_data(1,i+h-1)*exp(-((k-
1)/lat_weighting)^2))/k);
        end
end
bin_weight_1d=bin_weight_1d/max(bin_weight_1d);


tot_aver=smooth(tot_aver);
tot_stdev2=zeros(bins+1,1);
for i=1:bins
tot_stdev2(i+1,1)=sqrt(sum(stdev(i,:).^2))/(length(nonzeros(stdev(i,:))));
end

tot_stdev=zeros(bins+1,1);
for i=1:bins
tot_stdev(i+1,1)=std(nonzeros(aver(i,:)));
end

for i=1:bins+1
    if tot_stdev(i) == 0 && i>1
tot_stdev(i)=tot_stdev2(i);
    end
end
tot_stdev=smooth(tot_stdev);


grad=40;
upper=zeros(grad,length(tot_aver));
lower=zeros(grad,length(tot_aver));
numb_stdev=1;

for i=1:grad
upper(i,:)=[tot_aver+numb_stdev*i/grad*tot_stdev];
lower(i,:)=[tot_aver-numb_stdev*i/grad*tot_stdev];
end
alpha_scale=exp(-((linspace(0,0.3,grad+1)).^2)/0.015);
X=zeros(bins,4);
Y=zeros(grad,4);
cmap=colormap
for k=1:bins
for i=1:grad
X(k,:)=[[bin_aver(k),bin_aver(k+1)],[bin_aver(k+1),bin_aver(k)]];
Y(i,:)=[[lower(i,k),lower(i,k+1)],[upper(i,k+1),upper(i,k)]];
h=fill(X(k,:),Y(i,:),cmap(zz,:),'edgecolor','none');
set(h,'facealpha',alpha_scale(i)*bin_weight_1d(1,k)^0.7,'edgealpha',alpha_scale(i)*bin
_weight_1d(1,k)^0.7);
end
end


aa=zz+2;

for i=1:2:size(data,2)
plot(data(:,i),data(:,i+1),'Marker','o','Markersize',6,'Linewidth',1.2,'MarkerFaceColo
r','none','MarkerEdgeColor',cmap(aa,:),'Linestyle','none')
end


end
```

```matlab
y0line=zeros(1,100);
x0line=linspace(0,4500,100);
plot(x0line,y0line,':k')
axis([0 4500 -0.1 0.7])


xlabel('\rho_{Kap\beta1}','FontSize',36)
ylabel('\Deltad_{Nsp1}/d_{Nsp1}','FontSize',36)

set(gca,'box','on','Linewidth',2,'Fontsize',20)


h_leg=legend(eee{1,1},'location','Northwest',eee{1,2},'location','Northwest')
set(h_leg,'Fontsize',26)
h2 = get(h_leg,'children') ; % the symbol and the text are children of the legend
object

delete(h2(1),h2(3))%,h2(5),h2(7))
hh=findobj(h_leg,'Type','Text')


set(hh,'HorizontalAlignment','left')

set(hh(1),'Color',cmap(2,:))

set(hh(2),'Color',cmap(1,:))

leg_pos = get(h_leg,'position')


legend boxoff
```

(xvii) force_eval_script.m

```matlab
%% Program description
%This script evaluates a binary force map and returns the topography values "t_h",
%the brush heights "b_h", the brush surface "b_s" and the residuals "r_a" for the
%force curve fitting. The force curves are fit using a double exponential
%and the contact point is evaluated at treshold "tresh".
%
%Written by: Rafael L. Schoch, Basel, 2015

close all;
clear all;

fid = fopen('peg20_25C.003'); % Open the binary file for reading with file pointer fid
fseek(fid,43008,-1);
[data,count] = fread(fid,[1,2*4096*1024],'int16'); % Scan the data into a vector, in
this case called data
fclose(fid); % Close the file

defl_der=1.05;
zsens=101.8000*defl_der;  %\@Sens. Zsens: (nm/V)
zscansize=2.946955 ; %\@4:Ramp size: (V)
samples=4096; %4096

z=linspace(0,zsens*zscansize,samples);

VperLSB=0.0003750000; %\@4:Z scale: V [Sens. DeflSens] (V/LSB)
chi= 9.200000   ; %\@Sens. DeflSens: (nm/V)
force=0.0107348; %\Spring Constant (nN/nm)
ss=size(data);
ss2=ss(2)/(2*4096);
brushheights=zeros(1,ss2);
resall=zeros(1,ss2);

deflpn=zeros(ss2,samples);
```

```matlab
distance=zeros(ss2,samples);
deflsens=zeros(1,ss2);

for j=1:ss2;

%calculate deflection in V
deflV=data(1,(j-1)*2*4096+4097:j*2*4096)*VperLSB;

%baselinefit and substraction
deflbase=deflV(1,2000:4000);
zbase=z(1,2000:4000);
myfun1=inline('p(1)+p(2)*x','p','x');
p=lsqcurvefit(myfun1,[-40,0.1],zbase,deflbase,[-100,-1],[100,1]);
deflcor=deflV-p(2)*z-p(1);

%fit deflection sensitivity & recalculate spring constant
deflstart=deflcor(1,20:300);
zstart=z(1,20:300);
myfun3=inline('ppp(1)+ppp(2)*xxx','ppp','xxx');
ppp=lsqcurvefit(myfun3,[1000,-10],zstart,deflstart,[0,-100],[2000,1]);
deflsens(1,j)=-1/ppp(2);
springconst=(force*chi^2)/deflsens(1,j)^2;
deflnm=deflcor*deflsens(1,j);

%calculate tip-sample distance and deflection in pN
distance(j,:)=z+deflnm;
deflpn(j,:)=deflnm*springconst*1000;

%shift hard wall contact to zero in distance
val=min(distance(j,:));
distance(j,:)=distance(j,:)-val;

%make expfit starting from distance where deflpn = xpn over distance range
zz=999;
pos=1;
xpn=500;

for i = 1:samples
    if abs(deflpn(j,i)-xpn) < zz
    pos=i;
    zz=abs(deflpn(j,i)-xpn);
    end
end

if pos >= 3000
pos=2000;
end
if pos <= 100
pos=2000;
end

range=4096-pos-20;

myfun2=inline('pp(1)*exp(-(xx-pp(2))/pp(3))+pp(4)*exp(-(xx-pp(5))/pp(6))','pp','xx');
[pp,resnorm]=lsqcurvefit(myfun2,[xpn,distance(j,pos),20,xpn,distance(j,pos),2],distanc
e(j,pos:pos+range),deflpn(j,pos:pos+range),[0.001,distance(j,pos)-
50,0.001,0.001,distance(j,pos)-
5,0.001],[1000,distance(j,pos)+5,100,1000,distance(j,pos)+5,10])
resall(1,j)=resnorm/range;

dist=distance(j,pos:pos+range);
yexp=(pp(1)*exp(-(dist-pp(2))/pp(3))+pp(4)*exp(-(dist-pp(5))/pp(6)));
dist2(j,:)=distance(j,pos:pos+2000);
yexp2(j,:)=(pp(1)*exp(-(dist2(j,:)-pp(2))/pp(3))+pp(4)*exp(-(dist2(j,:)-
pp(5))/pp(6)));


%find contact point (1pN treshold)
zz=999;
pos2=0;
tresh=1;
```

```matlab
s=size(yexp);
for i = 1:s(2)
    if abs(yexp(i)-tresh) < zz
    pos2=i;
    zz=abs(yexp(i)-tresh);
    end
end

brushheights(1,j)=distance(j,pos2+pos-1);

end

xbar=0:1:100;
xs=size(xbar);
ybar=zeros(1,xs(2)-1);
xb=size(brushheights);

for i=1:xs(2)-1
    for j=1:xb(2)
        if brushheights(j) > xbar(i) && brushheights(j) <= xbar(i+1)
        ybar(i)=ybar(i)+1;
        end
    end
end

B=reshape(brushheights,[32,32]);

figure(1) %map of brush heights
xd=linspace(0,500,32);
yd=linspace(0,500,32);
contourf(xd,yd,B,10,'Linecolor','none')

cc1=[0.9:-0.1:0.0]';
cc2=[0.9:-0.1:0.0]';
cc3=[0.28:0.08:1]';

colormap([cc1 cc2 cc3])
caxis([0 150])
colorbar
axis([0 500 0 500])

xbar2=0.5:1:99.5;

figure(2) %brush height histogram
bar(xbar2,ybar,1)

figure(3) %plot last force-distance curve and expfit
plot(distance(j,:),deflpn(j,:),'k-',distance(j,pos:pos+range),yexp,'b-')

figure(4) %map of residuals
C=reshape(resall,[32,32])
for i=1:32
    for j=1:32
    if C(i,j) >= 2*10^5
        C(i,j) = 0;
    end
    end
end
xd=linspace(0,500,32);
yd=linspace(0,500,32);
contourf(xd,yd,C)

cc1=[0.9:-0.1:0.0]';
cc2=[0.9:-0.1:0.0]';
cc3=[0.28:0.08:1]';

colormap([cc1 cc2 cc3])
colorbar
axis([0 500 0 500])

figure(5) %map of contact point surface
```

```
sb=size(B);
brush_surf=zeros(sb);
for i=1:sb(2)
    brush_surf(:,i)=B(:,i)+topo_eval(i);
end
xd=linspace(0,500,32);
yd=linspace(0,500,32);
contourf(xd,yd,brush_surf,10,'Linecolor','none')

cc1=[0.9:-0.1:0.0]';
cc2=[0.9:-0.1:0.0]';
cc3=[0.28:0.08:1]';

colormap([cc1 cc2 cc3])
caxis([0 60])
colorbar
axis([0 500 0 500])

figure(6) %map of z-piezo topography
sb=size(B);
topo_surf=zeros(sb);
for i=1:sb(2)
    topo_surf(:,i)=topo_eval(i);
end
xd=linspace(0,500,32);
yd=linspace(0,500,32);
contourf(xd,yd,topo_surf,10,'Linecolor','none')

cc1=[0.0:0.1:0.9]';
cc2=[0.0:0.1:0.9]';
cc3=[0.0:0.01:0.09]';

colormap([cc1 cc2 cc3])
caxis([-60 0])
colorbar
axis([0 500 0 500])

figure(7) %3D brush surface
surf(xd,yd,brush_surf)


sb=size(B);
topo_height=zeros(1,1024);
brush_height=zeros(1,1024);
brush_surf_a=zeros(1,1024);
zzz=0;

pnt1=500;
pnt2=1500;

for i=1:sb(2)
    topo_array=topo_eval(i);
    for j=1:sb(1)

    if distance((i-1)*sb(2)+j,pnt2) <= 500 && distance((i-1)*sb(2)+j,pnt1) <= 500
%removing force curves where tip is slipping (optional)
    zzz=zzz+1;
    zak2(1,zzz)=(i-1)*sb(2)+j;
    topo_height(1,zzz)=topo_array(j);
    brush_height(1,zzz)=B(j,i);
    brush_surf_a(1,zzz)=brush_surf(j,i);
    end
    end
end

t_h=topo_height;
b_h=brush_height;
b_s=brush_surf_a;
r_a=resall;
save_curves='topo_brush_20k_150nm_003_r.txt';
save_curves2='topo_brush_20k_150nm_003_r_distance.txt';
```

```
save_curves3='topo_brush_20k_150nm_003_r_deflpn.txt';
save_curves4='topo_brush_20k_150nm_003_r_dist2.txt';
save_curves5='topo_brush_20k_150nm_003_r_yexp2.txt';

save(save_curves, 't_h', 'b_h','b_s','r_a','-ASCII')
save(save_curves2, 'distance','-ASCII')
save(save_curves3, 'deflpn','-ASCII')
save(save_curves4, 'dist2','-ASCII')
save(save_curves5, 'yexp2','-ASCII')
```

(xviii) density_parfor_int.m

```
%% Program description
%This script calculates the SPR response for BSA injection and a polymer
%brush with analytical SCF theory density profile. The profile can be
%defined using "A" for the osmotic pressure at z=0 and "B" for the brush height
%as well as "m" for the solvent quality. The osmotic scaling for BSA
%partitioning is defined in the script insertion2.m. The output is the
%calculated thickness from BSA monomer and BSA dimer partitioning,
%respectively, using an evanescent field decay length ld = 300 nm.
%
%Dependencies: cauchy2.m, cauchy.m, K_calc.m, insertion2.m, fmulti.m, f_calc3_fit.m
%
%Written by: Rafael L. Schoch, Basel, 2015.

if matlabpool('size') == 0 % checking to see if my pool is already open
    matlabpool open 8
end
clear all
close all

lambda=760; %wavelength used in SPR instrument in [nm]
d_met=50; %metal thickness in [nm]
n1=1.45; %reference layer refractive index
d1=2; %reference layer thickness in [nm]
t1=64; %lower limit incidence angle in [deg]
t2=74; %upper limit incidence angle in [deg]
e_lay=1.36^2; %approx layer refrective index at z=0! av. is n=1.35 for peg20k

n_pbs=sqrt(1.77985);
n_bsa=sqrt(1.78193);
t=25;
lambda2=589;
n_h2o=cauchy(t,lambda2);
dn1=n_pbs-n_h2o;
dn2=n_bsa-n_h2o;

kb=1.38065e-23;
T=[5,15,25,35];
T2=[5,15,25,35]+273.15;
n=300; %number of d_a (nm) layers considered for brush
d_a=0.2;
R=[6.25,8.26]/2*10^-9;
kmax=120;
hmax=25;
log_val=zeros(2*length(T2)*(kmax)*(hmax),6);
th=[38,37,35,33]; %approx height for calculation start
m=2; %parameter that defines solvent quality

for sel=1:2;
for j=1:length(T2)

e_pri=cauchy2(T(j),lambda*10^-3).^2;
n_t_bsa=cauchy(T(j),lambda)+dn2;
n_t_pbs=cauchy(T(j),lambda)+dn1;
e_sol=(n_t_pbs).^2; %solvent dielectric constant
e_par=(n_t_bsa).^2; %non-interacting particles in solvent dielectric constant
[e_met,n_met,k_met]=K_calc(T(j)+273.15); %metal dielectric constant
```

```matlab
log_val_d=zeros(kmax,hmax);
log_val_T=zeros(kmax,hmax);
log_val_A=zeros(kmax,hmax);
log_val_B=zeros(kmax,hmax);
log_val_m=zeros(kmax,hmax);
log_val_sel=zeros(kmax,hmax);

parfor k=1:kmax;
A=(2*k)*10^25;
for h=1:hmax
B=(th(j)+(h-1)/2)*10^-9;


x=([d_a:d_a:d_a*n]-d_a/2)*10^(-9);

ss=size(x);
F_ins=zeros(1,ss(2));
boltz_bsa=zeros(1,n);

for tt=1:ss(2)
clear myfun
z0=x(tt);
if z0 <= R(sel)
    z0=R(sel);
end

if z0-R(sel) < B && z0+R(sel) <= B
    F_ins(1,tt)=insertion2(z0,R(sel),A,B,m,T2(j),z0-R(sel),z0+R(sel));
elseif z0-R(sel)< B && z0+R(sel) > B
    F_ins(1,tt)=insertion2(z0,R(sel),A,B,m,T2(j),z0-R(sel),B);
else
    F_ins(1,tt)=0;
end
end

boltz_bsa=exp(-(F_ins)/(kb*T2(j)));

chi_peg=zeros(1,n);
chi_peg2=zeros(1,n);
chi_peg2=(1-x.^2/B^2).^(m-1);

for i=1:length(x)
    if x(1,i) <= B
    chi_peg(1,i)=chi_peg2(1,i);
    end
end

e_peg_par=chi_peg*e_lay+(1-chi_peg)*e_sol+boltz_bsa*(e_par-e_sol);
e_peg_sol=chi_peg*e_lay+(1-chi_peg)*e_sol;

%% Main Program
e_d=e_sol;
dip2_sol = fmulti(t1,t2,e_pri,e_d,e_met,e_peg_sol,d_met,d_a,lambda);

e_d=e_par;
dip2_par = fmulti(t1,t2,e_pri,e_d,e_met,e_peg_par,d_met,d_a,lambda);

e_d=e_sol;
dip1_sol = f_calc3_fit(t1,t2,e_pri,e_d,e_met,n1^2,d_met,d1,lambda);

e_d=e_par;
dip1_par = f_calc3_fit(t1,t2,e_pri,e_d,e_met,n1^2,d_met,d1,lambda);

dip1=dip1_par-dip1_sol;

dip2=dip2_par-dip2_sol;

d2=300/2*log(dip1/dip2)+d1;

log_val_d(k,h)=d2; %does not work with j or sel as index anymore in parfor
```

```
log_val_T(k,h)=T(j);
log_val_A(k,h)=A;
log_val_B(k,h)=B;
log_val_m(k,h)=m;
log_val_sel(k,h)=sel;

end
end

for k2=1:kmax
    for h2=1:hmax

zz=(sel-1)*length(T2)*kmax*hmax+(j-1)*kmax*hmax+(k2-1)*hmax+h2;
log_val(zz,:)=[log_val_T(k2,h2),log_val_d(k2,h2),log_val_A(k2,h2),log_val_B(k2,h2),log
_val_m(k2,h2),log_val_sel(k2,h2)];

    end
end

end
end
save('log_file_pi_2_mfix_good.txt','log_val','-ASCII')

matlabpool close
```

(xix) density_parfor_int_bind.m

```
%% Program description
%This script calculates the SPR response for BSA injection and a polymer
%brush with analytical SCF theory density profile. The profile can be
%defined using "A" for the osmotic pressure at z=0 and "B" for the brush height
%as well as "m" for the solvent quality. The osmotic scaling for BSA
%partitioning is defined in the script insertion2.m. The attractive term is
%defined from per monomer in contact with BSA "eps" in kBT in the script
%insertion_area.m.
%The output is the calculated thickness from BSA monomer and BSA dimer partitioning,
%respectively, using an evanescent field decay length ld = 300 nm.
%
%Dependencies: cauchy2.m, cauchy.m, K_calc.m, insertion2.m, fmulti.m, f_calc3_fit.m,
%insertion_area.m
%
%Written by: Rafael L. Schoch, Basel, 2015.

if matlabpool('size') == 0 % checking to see if my pool is already open
    matlabpool open 8
end
clear all
close all

lambda=760; %wavelength used in SPR instrument in [nm]
d_met=50; %metal thickness in [nm]
n1=1.45; %reference layer refractive index
d1=2; %reference layer thickness in [nm]
t1=64; %lower limit incidence angle in [deg]
t2=74; %upper limit incidence angle in [deg]
e_lay=1.36^2; %approx layer refractive index at z=0! av. is n=1.35 for peg20k

n_pbs=sqrt(1.77985);
%n_bsa=sqrt(1.78401);
n_bsa=sqrt(1.78193);
t=25;
lambda2=589;
n_h2o=cauchy(t,lambda2);
dn1=n_pbs-n_h2o;
dn2=n_bsa-n_h2o;

kb=1.38065e-23;
T=[5,15,25,35];
T2=[5,15,25,35]+273.15;
```

```matlab
n=300; %number of d_a (nm) layers considered for brush
d_a=0.2;
R=[6.25,8.26]/2*10^-9;
epsmax=30;
hmax=30;
log_val=zeros(2*length(T2)*(epsmax)*(hmax),6);
th=[38,37,35,33]; %approx height for calculation start
m=2;

for sel=1:2;
for j=1:length(T2)

e_pri=cauchy2(T(j),lambda*10^-3).^2;
n_t_bsa=cauchy(T(j),lambda)+dn2;
n_t_pbs=cauchy(T(j),lambda)+dn1;
e_sol=(n_t_pbs).^2; %solvent dielectric constant
e_par=(n_t_bsa).^2; %non-interacting particles in solvent dielectric constant
[e_met,n_met,k_met]=K_calc(T(j)+273.15); %metal dielectric constant

log_val_d=zeros(epsmax,hmax);
log_val_T=zeros(epsmax,hmax);
log_val_eps=zeros(epsmax,hmax);
log_val_B=zeros(epsmax,hmax);
log_val_m=zeros(epsmax,hmax);
log_val_sel=zeros(epsmax,hmax);
A=(70)*10^25;

parfor k=1:epsmax;
eps=(k-1)*0.002;

for h=1:hmax
B=(th(j)+(h-1)/2)*10^-9;

x=([d_a:d_a:d_a*n]-d_a/2)*10^(-9);

ss=size(x);
F_osm=zeros(1,ss(2));
boltz_bsa=zeros(1,n);

for tt=1:ss(2)
clear myfun
z0=x(tt);
if z0 <= R(sel)
    z0=R(sel);
end

if z0-R(sel) < B && z0+R(sel) <= B
    F_osm(1,tt)=insertion2(z0,R(sel),A,B,m,T2(j),z0-R(sel),z0+R(sel));
elseif z0-R(sel)< B && z0+R(sel) > B
    F_osm(1,tt)=insertion2(z0,R(sel),A,B,m,T2(j),z0-R(sel),B);
else
    F_osm(1,tt)=0;
end
end

F_ads=zeros(1,ss(2));

for tt=1:ss(2)
clear myfun
z0=x(tt);
if z0 <= R(sel)
    z0=R(sel);
end

if z0-R(sel) < B && z0+R(sel) <= B
    F_ads(1,tt)=insertion_area(z0,R(sel),A,B,m-1,T2(j),z0-R(sel),z0+R(sel),eps);
elseif z0-R(sel)< B && z0+R(sel) > B
    F_ads(1,tt)=insertion_area(z0,R(sel),A,B,m-1,T2(j),z0-R(sel),B,eps);
else
    F_ads(1,tt)=0;
end
```

```
end

F_ins=F_osm+F_ads;

boltz_bsa=exp(-(F_ins)/(kb*T2(j)));

chi_peg=zeros(1,n);
chi_peg2=zeros(1,n);
chi_peg2=(1-x.^2/B^2).^(m-1);

for i=1:length(x)
    if x(1,i) <= B
    chi_peg(1,i)=chi_peg2(1,i);
    end
end

e_peg_par=chi_peg*e_lay+(1-chi_peg)*e_sol+boltz_bsa*(e_par-e_sol);
e_peg_sol=chi_peg*e_lay+(1-chi_peg)*e_sol;

%% Main Program
e_d=e_sol;
dip2_sol = fmulti(t1,t2,e_pri,e_d,e_met,e_peg_sol,d_met,d_a,lambda);

e_d=e_par;
dip2_par = fmulti(t1,t2,e_pri,e_d,e_met,e_peg_par,d_met,d_a,lambda);

e_d=e_sol;
dip1_sol = f_calc3_fit(t1,t2,e_pri,e_d,e_met,n1^2,d_met,d1,lambda);

e_d=e_par;
dip1_par = f_calc3_fit(t1,t2,e_pri,e_d,e_met,n1^2,d_met,d1,lambda);

dip1=dip1_par-dip1_sol;

dip2=dip2_par-dip2_sol;

d2=300/2*log(dip1/dip2)+d1;

log_val_d(k,h)=d2; %does not work with j or sel as index anymore in parfor
log_val_T(k,h)=T(j);
log_val_eps(k,h)=eps;
log_val_B(k,h)=B;
log_val_m(k,h)=m;
log_val_sel(k,h)=sel;

end
end

for k2=1:epsmax
    for h2=1:hmax

zz=(sel-1)*length(T2)*epsmax*hmax+(j-1)*epsmax*hmax+(k2-1)*hmax+h2;
log_val(zz,:)=[log_val_T(k2,h2),log_val_d(k2,h2),log_val_eps(k2,h2),log_val_B(k2,h2),l
og_val_m(k2,h2),log_val_sel(k2,h2)];

    end
end

end
end
save('log_file_pi_3_phi_eps_good.txt','log_val','-ASCII')

matlabpool close
```

(xx) insertion_area.m

```
function [ F_ins] = insertion(z0,R,A,B,m,T2,int_s,int_e,eps)
%% Program description
%This function returns the attractive energy for BSA in contact with the
```

```
%PEG polymer brush.
clear myfun
a=0.41*10^-9;
phi0=0.23;
kb=1.38065e-23;
myfun=@(z) (-a^(-2)*eps*(kb*T2)*phi0*(1-z.^2/B^2).^m)*2*pi.*abs(z-z0).*sqrt(R^2./(R^2-
(abs(z-z0)).^2));
F_ins=integral(myfun,int_s,int_e);
end
```

(xxi) insertion2.m

```
function [ F_ins] = insertion(z0,R,A,B,m,T2,int_s,int_e)
%% Program description
%This function returns the energy for particle insertion due to the osmotic penalty.
clear myfun
kb=1.38065e-23;
myfun= @(z)(A*(kb*T2)*(1-z.^2/B^2).^m)*pi*R^2.*sin(acos(abs((z-z0)/R))).^2;
F_ins=integral(myfun,int_s,int_e);
end
```

(xxii) fmulti.m

```
function [dip] = fmulti(t1,t2,e_pri,e_d,e_met,e_n,d_met,d,lambda)
%% Program description
% This function calculates the SPR reflectivity as a function of angle of incidence
and
% returns the minimum position [dip]. The equations for the Fresnel reflection
coefficients
% are taken from Ekgasit et al., 2004. Here, e_n is a vector of n
% elements representing the dielectric constant of the n first d=1nm slices.
%
% Written by: Rafael L. Schoch, Basel, 2013

format longE
step=0.001; %angular resolution [deg]
z=0;

for theta2 = t1:step:t2

theta=theta2/(360)*2*pi;
z=z+1;

k_xp=(2*pi/lambda)*(e_pri*sin(theta)^2)^0.5;
k_z1=(((2*pi/lambda))^2.*e_met-k_xp^2).^0.5;
k_z2=(((2*pi/lambda))^2.*e_n-k_xp^2).^0.5;

q1=k_z1./e_met;
q2=k_z2./e_n;

M=([cos(k_z1*d_met),-j/q1*sin(k_z1*d_met);-j*q1*sin(k_z1*d_met),cos(k_z1*d_met)]);

for i=1:length(k_z2)
M=M*([cos(k_z2(i)*d),-j/q2(i)*sin(k_z2(i)*d);-j*q2(i)*sin(k_z2(i)*d),cos(k_z2(i)*d)]);
end

q_d=((((2*pi/lambda))^2.*e_d-k_xp^2).^0.5)/e_d;
q_p=((((2*pi/lambda))^2.*e_pri-k_xp^2).^0.5)/e_pri;

r(1,z)=((M(1,1)+M(1,2)*q_d)*q_p-
(M(2,1)+M(2,2)*q_d))/((M(1,1)+M(1,2)*q_d)*q_p+(M(2,1)+M(2,2)*q_d));
end

Ref=abs(r).^2;
[deg,pos]=min(Ref);

delta=100;
dip_in=t1+pos*step;
```

```
angl=t1+pos*step-delta*step:step:t1+pos*step+delta*step;
myfun=inline('p(1)+p(3)*((x-p(2)).^2)','p','x');
p=lsqcurvefit(myfun,[Ref(pos),dip_in,1],angl,Ref(pos-delta:pos+delta),[Ref(pos)-
0.1,t1+pos*step-delta*step,0],[Ref(pos)+0.1,t1+pos*step+delta*step,5]);
dip=p(2);

end
```

(1)   Abbott, N. L.; Blankschtein, D.; Hatton, T. A. Protein Partitioning in Two-Phase
        Aqueous Polymer Systems. 1. Novel Physical Pictures and a Scaling Thermodynamic
        Formulation. *Macromolecules* **1991**, *24* (15), 4334–4348.

(2)   Abbott, N. L.; Blankschtein, D.; Hatton, T. A. Protein Partitioning in Two-Phase
        Aqueous Polymer Systems. 2. On the Free Energy of Mixing Globular Colloids and
        Flexible Polymers. *Macromolecules* **1992**, *25* (15), 3917–3931.

(3)   Abbott, N. L.; Blankschtein, D.; Hatton, T. A. Protein Partitioning in Two-Phase
        Aqueous Polymer Systems. 3. A Neutron Scattering Investigation of the Polymer
        Solution Structure and Protein-Polymer Interactions. *Macromolecules* **1992**, *25* (15),
        3932–3941.

(4)   Adam, E. J. Identification of Cytosolic Factors Required for Nuclear Location
        Sequence-Mediated Binding to the Nuclear Envelope. *J. Cell Biol.* **1994**, *125* (3), 547–
        555.

(5)   Adam, S. A.; Geracet, L. Cytosolic Proteins That Specifically Bind Nuclear Location
        Signals Are Receptors for Nuclear Import. *Cell* **1991**, *66* (5), 837–847.

(6)   Akey, C. W. Protein Import through the Nuclear Pore Complex Is a Multistep Process.
        J. Cell Biol. **1989**, *109* (3), 971–982.

(7)   Akey, C. W. Interactions and Structure of the Nuclear Pore Complex Revealed by
        Cryo- Electron Microscopy. *J. Cell Biol.* **1989**, *109* (3), 955–970.

(8)   Arwin, H. Application of Ellipsometry Techniques to Biological Materials. *Thin Solid
        Films* **2011**, *519* (9), 2589–2592.

(9)   Atkinson, C. E.; Mattheyses, A. L.; Kampmann, M.; Simon, S. M. Conserved Spatial
        Organization of FG Domains in the Nuclear Pore Complex. *Biophys. J.* **2013**, *104* (1),
        37–50.

(10)   Bae, Y. C.; Lambert, S. M.; Soane, D. S.; Prausnitz, J. M. Cloud-Point Curves of Polymer
        Solutions from Thermooptical Measurements. *Macromolecules* **1991**, *24* (15), 4403–
        4407.

(11)   Baldwin, R. L. Energetics of Protein Folding. *J. Mol. Biol.* **2007**, *371* (2), 283–301.

(12)   Bashkatov, A. N.; Genina, E. a. Water Refractive Index in Dependence on
        Temperature and Wavelength: A Simple Approximation. *Proc. SPIE 5068, Saratov Fall
        Meet. 2002 Opt. Technol. Biophys. Med. IV, 393 (October 14, 2003)* **2003**, *5068*, 393–
        395.

(13)   Baskir, J. N.; Hatton, T. A.; Suter, U. W. Thermodynamics of the Partitioning of
        Biomaterials in Two-Phase Aqueous Polymer Systems: Comparison of Lattice Model
        to Experimental Data. *J. Phys. Chem.* **1989**, *93* (5), 2111–2122.

(14)   Baulin, V. A.; Halperin, A. Signatures of a Concentration-Dependent Flory χ
        Parameter: Swelling and Collapse of Coils and Brushes. *Macromol. Theory
        Simulations* **2003**, *12* (8), 549–559.

(15)   Baulin, V. A.; Zhulina, E. B.; Halperin, A. Self-Consistent Field Theory of Brushes of Neutral Water-Soluble Polymers. *J. Chem. Phys.* **2003**, *119* (20), 10977.

(16)   Bayliss, R.; Leung, S. W.; Baker, R. P.; Quimby, B. B.; Corbett, A. H.; Stewart, M. Structural Basis for the Interaction between NTF2 and Nucleoporin FxFG Repeats. *EMBO J.* **2002**, *21* (12), 2843–2853.

(17)   Bayliss, R.; Littlewood, T.; Stewart, M. Structural Basis for the Interaction between FxFG Nucleoporin Repeats and Importin-β in Nuclear Trafficking. *Cell* **2000**, *102* (1), 99–108.

(18)   Bayliss, R.; Littlewood, T.; Strawn, L. A.; Wente, S. R.; Stewart, M. GLFG and FxFG Nucleoporins Bind to Overlapping Sites on Importin-Beta. *J. Biol. Chem.* **2002**, *277* (52), 50597–50606.

(19)   Beck, M.; Lucić, V.; Förster, F.; Baumeister, W.; Medalia, O. Snapshots of Nuclear Pore Complexes in Action Captured by Cryo-Electron Tomography. *Nature* **2007**, *449* (7162), 611–615.

(20)   Becker, A. L.; Welsch, N.; Schneider, C.; Ballauff, M. Adsorption of RNase A on Cationic Polyelectrolyte Brushes: A Study by Isothermal Titration Calorimetry. *Biomacromolecules* **2011**, *12* (11), 3936–3944.

(21)   Bednenko, J.; Cingolani, G.; Gerace, L. Importin Beta Contains a COOH-Terminal Nucleoporin Binding Region Important for Nuclear Transport. *J. Cell Biol.* **2003**, *162* (3), 391–401.

(22)   Bekiranov, S.; Bruinsma, R.; Pincus, P. Solution Behavior of Polyethylene Oxide in Water as a Function of Temperature and Pressure. *Phys. Rev. E* **1997**, *55* (1), 577–585.

(23)   Ben-Efraim, I.; Gerace, L. Gradient of Increasing Affinity of Importin   for Nucleoporins along the Pathway of Nuclear Import. *J. Cell Biol.* **2001**, *152* (2), 411–418.

(24)   Berezhkovskii, A. M.; Bezrukov, S. M. Channel-Facilitated Membrane Transport: Constructive Role of Particle Attraction to the Channel Pore. *Chem. Phys.* **2005**, *319* (1–3), 342–349.

(25)   Berezhkovskii, A. M.; Pustovoit, M. A.; Bezrukov, S. M. Channel-Facilitated Membrane Transport: Transit Probability and Interaction with the Channel. *J. Chem. Phys.* **2002**, *116* (22), 9952.

(26)   Binnig, G.; Quate, C. F. Atomic Force Microscope. *Phys. Rev. Lett.* **1986**, *56* (9), 930–933.

(27)   Bright, J. N.; Woolf, T. B.; Hoh, J. H. Predicting Properties of Intrinsically Unstructured Proteins. *Prog. Biophys. Mol. Biol.* **2001**, *76* (3), 131–173.

(28)   Burada, P. S.; Hänggi, P.; Marchesoni, F.; Schmid, G.; Talkner, P. Diffusion in Confined Geometries. *Chemphyschem* **2009**, *10* (1), 45–54.

(29)   Butt, H.-J.; Cappella, B.; Kappl, M. Force Measurements with the Atomic Force
        Microscope: Technique, Interpretation and Applications. *Surf. Sci. Rep.* **2005**, *59* (1–
        6), 1–152.

(30)   Cai, L.-H.; Panyukov, S.; Rubinstein, M. Mobility of Spherical Probe Objects in Polymer
        Liquids. *Macromolecules* **2011**, *44* (19), 7853–7863.

(31)   Carignano, M. A.; Szleifer, I. Statistical Thermodynamic Theory of Grafted Polymeric
        Layers. *J. Chem. Phys.* **1993**, *98* (6), 5006.

(32)   Chatel, G.; Desai, S. H.; Mattheyses, A. L.; Powers, M. A.; Fahrenkrog, B. Domain
        Topology of Nucleoporin Nup98 within the Nuclear Pore Complex. *J. Struct. Biol.*
        2012, *177* (1), 81–89.

(33)   Chen, Y.; Chen, J. Z. Y. Absorption and Engulfing Transitions in Nanoparticle
        Infiltration into a Polymer Brush: A Monte Carlo Simulation. *J. Polym. Sci. Part B
        Polym. Phys.* **2012**, *50* (1), 21–26.

(34)   Cingolani, G.; Petosa, C.; Weis, K.; Muller, C. Structure of Importin-Beta Bound to the
        IBB Domain of Importin-Alpha. *Nature* **1999**, *399* (6733), 221–229.

(35)   Colwell, L. J.; Brenner, M. P.; Ribbeck, K. Charge as a Selection Criterion for
        Translocation through the Nuclear Pore Complex. *PLoS Comput. Biol.* **2010**, *6* (4),
        e1000747.

(36)   Cooper, A. Heat Capacity Effects in Protein Folding and Ligand Binding: A Re-
        Evaluation of the Role of Water in Biomolecular Thermodynamics. *Biophys. Chem.*
        2005, *115* (2–3), 89–97.

(37)   Cooper, A.; Johnson, C. M.; Lakey, J. H.; Nöllmann, M. Heat Does Not Come in
        Different Colours: Entropy–enthalpy Compensation, Free Energy Windows, Quantum
        Confinement, Pressure Perturbation Calorimetry, Solvation and the Multiple Causes
        of Heat Capacity Effects in Biomolecular Interactions. *Biophys. Chem.* **2001**, *93* (2–3),
        215–230.

(38)   Cronshaw, J. M.; Krutchinsky, A. N.; Zhang, W.; Chait, B. T.; Matunis, M. J. Proteomic
        Analysis of the Mammalian Nuclear Pore Complex. *J. Cell Biol.* **2002**, *158* (5), 915–
        927.

(39)   Currie, E. P. K.; Van der Gucht, J.; Borisov, O. V.; Stuart, M. A. C. Stuffed Brushes:
        Theory and Experiment. *Pure Appl. Chem.* **1999**, *71* (7), 1227–1241.

(40)   Currie, E. P. K.; Norde, W.; Cohen Stuart, M. A. Tethered Polymer Chains: Surface
        Chemistry and Their Impact on Colloidal and Surface Properties. *Adv. Colloid
        Interface Sci.* **2003**, *100–102*, 205–265.

(41)   Dange, T.; Grünwald, D.; Grünwald, A.; Peters, R.; Kubitscheck, U. Autonomy and
        Robustness of Translocation through the Nuclear Pore Complex: A Single-Molecule
        Study. *J. Cell Biol.* **2008**, *183* (1), 77–86.

(42)   de Bruijn, H. E.; Altenburg, B. S. F.; Kooyman, R. P. H.; Greve, J. Determination of

Thickness and Dielectric Constant of Thin Transparent Dielectric Layers Using Surface Plasmon Resonance. *Opt. Commun.* **1991**, *82* (5–6), 425–432.

(43)   De Feijter, J. A.; Benjamins, J.; Veer, F. A. Ellipsometry as a Tool to Study the Adsorption Behavior of Synthetic and Biopolymers at the Air-Water Interface. *Biopolymers* **1978**, *17* (7), 1759–1772.

(44)   de Gennes, P. G. Conformations of Polymers Attached to an Interface. *Macromolecules* **1980**, *13* (5), 1069–1075.

(45)   de Gennes, P. A Second Type of Phase Separation in Polymer Solutions. *Comptes Rendus l'Académie des Sci. - Ser. II* **1991**, *313* (10), 1117–1122.

(46)   Denning, D. P.; Patel, S. S.; Uversky, V.; Fink, A. L.; Rexach, M. Disorder in the Nuclear Pore Complex: The FG Repeat Regions of Nucleoporins Are Natively Unfolded. *Proc. Natl. Acad. Sci. U. S. A.* **2003**, *100* (5), 2450–2455.

(47)   Dill, K. A. Dominant Forces in Protein Folding. *Biochemistry* **1990**, *29* (31), 7133–7155.

(48)   Dill, K.; Bromberg, S. *Molecular Driving Forces: Statistical Thermodynamics in Chemistry & Biology*; Garland Science, 2002.

(49)   Dimitrov, D.; Milchev, A.; Binder, K. Polymer Brushes on Flat and Curved Substrates: Scaling Concepts and Computer Simulations. *Macromol. Symp.* **2007**, *252* (1), 47–57.

(50)   Dölker, N.; Zachariae, U.; Grubmüller, H. Hydrophilic Linkers and Polar Contacts Affect Aggregation of FG Repeat Peptides. *Biophys. J.* **2010**, *98* (11), 2653–2661.

(51)   Dormidontova, E. E. Role of Competitive PEO–Water and Water–Water Hydrogen Bonding in Aqueous Solution PEO Behavior. *Macromolecules* **2002**, *35* (3), 987–1001.

(52)   Eck, W.; Craig, G.; Sigdel, A.; Ritter, G.; Old, L. J.; Tang, L.; Brennan, M. F.; Allen, P. J.; Mason, M. D. PEGylated Gold Nanoparticles Conjugated to Monoclonal F19 Antibodies as Targeted Labeling Agents for Human Pancreatic Carcinoma Tissue. *ACS Nano* **2008**, *2* (11), 2263–2272.

(53)   Edmond, E.; Ogston, A. An Approach to the Study of Phase Separation in Ternary Aqueous Systems. *Biochem. J.* **1968**, *109* (4), 569-.

(54)   Egorov, S. A. Insertion of Nanoparticles into Polymer Brush under Variable Solvent Conditions. *J. Chem. Phys.* **2012**, *137* (13), 134905.

(55)   Einstein, A. Über Die von Der Molekularkinetischen Theorie Der Wärme Geforderte Bewegung von in Ruhenden Flüssigkeiten Suspendierten Teilchen. *Ann. Phys.* **1905**, *322* (8), 549–560.

(56)   Eisele, N. B.; Andersson, F. I.; Frey, S.; Richter, R. P. Viscoelasticity of Thin Biomolecular Films: A Case Study on Nucleoporin Phenylalanine-Glycine Repeats Grafted to a Histidine-Tag Capturing QCM-D Sensor. *Biomacromolecules* **2012**, *13* (8), 2322–2332.

(57)   Eisele, N. B.; Frey, S.; Piehler, J.; Görlich, D.; Richter, R. P. Ultrathin Nucleoporin

Phenylalanine-Glycine Repeat Films and Their Interaction with Nuclear Transport Receptors. *EMBO Rep.* **2010**, *11* (5), 366–372.

(58)   Ekgasit, S.; Thammacharoen, C.; Knoll, W. Surface Plasmon Resonance Spectroscopy Based on Evanescent Field Treatment. *Anal. Chem.* **2004**, *76* (3), 561–568.

(59)   Eliassi, A.; Modarress, H.; Mansoori, G. A. Measurement of Activity of Water in Aqueous Poly(ethylene Glycol) Solutions (Effect of Excess Volume on the Flory–Huggins χ-Parameter). *J. Chem. Eng. Data* **1999**, *44* (1), 52–55.

(60)   Elliott, L. C. C.; Jing, B.; Akgun, B.; Zhu, Y.; Bohn, P. W.; Fullerton-Shirey, S. K. Loading and Distribution of a Model Small Molecule Drug in Poly(N -Isopropylacrylamide) Brushes: A Neutron Reflectometry and AFM Study. *Langmuir* **2013**, *29* (10), 3259–3268.

(61)   Emilsson, G.; Schoch, R. L.; Feuz, L.; Höök, F.; Lim, R. Y. H.; Dahlin, A. B. Strongly Stretched Protein Resistant Poly(ethylene Glycol) Brushes Prepared by Grafting-To. *ACS Appl. Mater. Interfaces* **2015**, *7* (14), 7505–7515.

(62)   Ermilov, V.; Lazutin, A.; Halperin, A. Colloids in Brushes: The Insertion Free Energy via Monte Carlo Simulation with Umbrella Sampling. *Macromolecules* **2010**, *43* (7), 3511–3520.

(63)   Fahrenkrog, B.; Maco, B.; Fager, A. M.; Köser, J.; Sauder, U.; Ullman, K. S.; Aebi, U. Domain-Specific Antibodies Reveal Multiple-Site Topology of Nup153 within the Nuclear Pore Complex. *J. Struct. Biol.* **2002**, *140* (1–3), 254–267.

(64)   Feigin, L. A.; Svergun, D. I. *Structure Analysis by Small-Angle X-Ray and Neutron Scattering*; Taylor, G. W., Ed.; Springer US: Boston, MA, 1987.

(65)   Feldherr, C. M. Movement of a Karyophilic Protein through the Nuclear Pores of Oocytes. *J. Cell Biol.* **1984**, *99* (6), 2216–2222.

(66)   Filippidi, E.; Michailidou, V.; Loppinet, B.; Rühe, J.; Fytas, G. Brownian Diffusion close to a Polymer Brush. *Langmuir* **2007**, *23* (9), 5139–5142.

(67)   Forbes, D. J. Structure and Function of the Nuclear Pore Complex. *Annu. Rev. Cell Biol.* **1992**, *8*, 495–527.

(68)   Forwood, J. K.; Lange, A.; Zachariae, U.; Marfori, M.; Preast, C.; Grubmüller, H.; Stewart, M.; Corbett, A. H.; Kobe, B. Quantitative Structural Analysis of Importin-β Flexibility: Paradigm for Solenoid Protein Structures. *Structure* **2010**, *18* (9), 1171–1183.

(69)   Franke, W. W. Structure and Biochemistry of the Nuclear Envelope. *Philos. Trans. R. Soc. B Biol. Sci.* **1974**, *268* (891), 67–93.

(70)   Frey, S.; Görlich, D. FG/FxFG as Well as GLFG Repeats Form a Selective Permeability Barrier with Self-Healing Properties. *EMBO J.* **2009**, *28* (17), 2554–2567.

(71)   Fukuhara, N.; Fernandez, E.; Ebert, J.; Conti, E.; Svergun, D. Conformational

Variability of Nucleo-Cytoplasmic Transport Factors. *J. Biol. Chem.* **2004**, *279* (3), 2176–2181.

(72)   Gamini, R.; Han, W.; Stone, J. E.; Schulten, K. Assembly of Nsp1 Nucleoporins Provides Insight into Nuclear Pore Complex Gating. *PLoS Comput. Biol.* **2014**, *10* (3), e1003488.

(73)   Ghavami, A.; Veenhoff, L. M.; van der Giessen, E.; Onck, P. R. Probing the Disordered Domain of the Nuclear Pore Complex through Coarse-Grained Molecular Dynamics Simulations. *Biophys. J.* **2014**, *107* (6), 1393–1402.

(74)   Gil, E.; Hudson, S. Stimuli-Reponsive Polymers and Their Bioconjugates. *Prog. Polym. Sci.* **2004**, *29* (12), 1173–1222.

(75)   Gillespie, D.; Seitaridou, E. *Simple Brownian Diffusion: An Introduction to the Standard Theoretical Models*; Oxford University Press, USA, 2012.

(76)   Gorlich, D.; Pante, N.; Kutay, U.; Aebi, U.; Bischoff, F. Identification of Different Roles for RanGDP and RanGTP in Nuclear Protein Import. *EMBO J.* **1996**, *15* (20), 5584–5594.

(77)   Haiss, W.; Thanh, N. T. K.; Aveyard, J.; Fernig, D. G. Determination of Size and Concentration of Gold Nanoparticles from UV-Vis Spectra. *Anal. Chem.* **2007**, *79* (11), 4215–4221.

(78)   Halperin, A. Compression Induced Phase Transitions in PEO Brushes: The N-Cluster Model. *Eur. Phys. J. B* **1998**, *3* (3), 359–364.

(79)   Halperin, A. Polymer Brushes That Resist Adsorption of Model Proteins: Design Parameters. *Langmuir* **1999**, *15* (7), 2525–2533.

(80)   Halperin, A.; Kröger, M. Collapse of Thermoresponsive Brushes and the Tuning of Protein Adsorption. *Macromolecules* **2011**, *44* (17), 6986–7005.

(81)   Halperin, A.; Kröger, M.; Zhulina, E. B. Colloid-Brush Interactions: The Effect of Solvent Quality. *Macromolecules* **2011**, *44* (9), 3622–3638.

(82)   Halperin, A.; Fragneto, G.; Schollier, A.; Sferrazza, M. Primary versus Ternary Adsorption of Proteins onto PEG Brushes. *Langmuir* **2007**, *23* (21), 10603–10617.

(83)   Halperin, A.; Kröger, M. Ternary Protein Adsorption onto Brushes: Strong versus Weak. *Langmuir* **2009**, *25* (19), 11621–11634.

(84)   Halperin, A.; Zhulina, E. B. Atomic Force Microscopy of Polymer Brushes: Colloidal versus Sharp Tips. *Langmuir* **2010**, *26* (11), 8933–8940.

(85)   Hammouda, B.; Ho, D. L. Insight into Chain Dimensions in PEO/water Solutions. *J. Polym. Sci. Part B Polym. Phys.* **2007**, *45* (16), 2196–2200.

(86)   Hansen, P. C. Regularization Tools Version 4.0 for Matlab 7.3. *Numer. Algorithms* **2007**, *46* (2), 189–194.

(87)   Hansen, P.; Cohen, J.; Podgornik, R.; Parsegian, V. Osmotic Properties of Poly(ethylene Glycols): Quantitative Features of Brush and Bulk Scaling Laws. *Biophys. J.* **2003**, *84* (1), 350–355.

(88)   Harder, P.; Grunze, M.; Dahint, R.; Whitesides, G. M.; Laibinis, P. E. Molecular Conformation in Oligo(ethylene Glycol)-Terminated Self-Assembled Monolayers on Gold and Silver Surfaces Determines Their Ability To Resist Protein Adsorption. *J. Phys. Chem. B* **1998**, *102* (2), 426–436.

(89)   Haynes, C. A.; Benitez, F. J.; Blanch, H. W.; Prausnitz, J. M. Application of Integral-Equation Theory to Aqueous Two-Phase Partitioning Systems. *AIChE J.* **1993**, *39* (9), 1539–1557.

(90)   Henriksen, N.; Hansen, F. *Theories of Molecular Reaction Dynamics: The Microscopic Foundation of Chemical Kinetics (Oxford Graduate Texts)*; Oxford University Press, USA, 2008.

(91)   Heuberger, M.; Drobek, T.; Spencer, N. D. Interaction Forces and Morphology of a Protein-Resistant Poly(ethylene Glycol) Layer. *Biophys. J.* **2005**, *88* (1), 495–504.

(92)   Homola, J. *Surface Plasmon Resonance Based Sensors*; Homola, J., Ed.; Springer Series on Chemical Sensors and Biosensors; Springer Berlin Heidelberg: Berlin, Heidelberg, 2006; Vol. 4.

(93)   Höök, F.; Kasemo, B. *Piezoelectric Sensors*; Steinem, C., Janshoff, A., Eds.; Springer Series on Chemical Sensors and Biosensors; Springer Berlin Heidelberg, 2007; Vol. 5.

(94)   Höök, F.; Kasemo, B.; Nylander, T.; Fant, C.; Sott, K.; Elwing, H. Variations in Coupled Water, Viscoelastic Properties, and Film Thickness of a Mefp-1 Protein Film during Adsorption and Cross-Linking: A Quartz Crystal Microbalance with Dissipation Monitoring, Ellipsometry, and Surface Plasmon Resonance Study. *Anal. Chem.* **2001**, *73* (24), 5796–5804.

(95)   Hu, T.; Wu, C. Clustering Induced Collapse of a Polymer Brush. *Phys. Rev. Lett.* **1999**, *83* (20), 4105–4107.

(96)   Hughes, D. Preparation of Colloidal Gold Probes. *Methods Mol. Biol.* **2005**, *295*, 155–172.

(97)   Hülsmann, B. B.; Labokha, A. A.; Görlich, D. The Permeability of Reconstituted Nuclear Pores Provides Direct Evidence for the Selective Phase Model. *Cell* **2012**, *150* (4), 738–751.

(98)   Hyotyla, J. T.; Deng, J.; Lim, R. Y. H. Synthetic Protein Targeting by the Intrinsic Biorecognition Functionality of Poly(ethylene Glycol) Using PEG Antibodies as Biohybrid Molecular Adaptors. *ACS Nano* **2011**, *5* (6), 5180–5187.

(99)   Isgro, T. A.; Schulten, K. Binding Dynamics of Isolated Nucleoporin Repeat Regions to Importin-Beta. *Structure* **2005**, *13* (12), 1869–1879.

(100) Jarnik, M. Toward a More Complete 3-D Structure of the Nuclear Pore Complex. *J.*

Struct. Biol. **1991**, *107* (3), 291–308.

(101)   Jelesarov, I.; Bosshard, H. Isothermal Titration Calorimetry and Differential Scanning Calorimetry as Complementary Tools to Investigate the Energetics of Biomolecular Recognition. *J. Mol. Recognit. 12* (1), 3–18.

(102)   Jeon, S. I.; Lee, J. H.; Andrade, J. D.; De Gennes, P. G. Protein—surface Interactions in the Presence of Polyethylene Oxide. *J. Colloid Interface Sci.* **1991**, *142* (1), 149–158.

(103)   Jeon, S. .; Andrade, J. . Protein—surface Interactions in the Presence of Polyethylene Oxide. *J. Colloid Interface Sci.* **1991**, *142* (1), 159–166.

(104)   Johnson, P. B.; Christy, R. W. Optical Constants of the Noble Metals. *Phys. Rev. B* **1972**, *6* (12), 4370–4379.

(105)   Jönsson, M.; Johansson, H.-O. Effect of Surface Grafted Polymers on the Adsorption of Different Model Proteins. *Colloids Surf. B. Biointerfaces* **2004**, *37* (3–4), 71–81.

(106)   Jovanovic-Talisman, T.; Tetenbaum-Novatt, J.; McKenney, A. S.; Zilman, A.; Peters, R.; Rout, M. P.; Chait, B. T. Artificial Nanopores That Mimic the Transport Selectivity of the Nuclear Pore Complex. *Nature* **2009**, *457* (7232), 1023–1027.

(107)   Jung, L. S.; Campbell, C. T.; Chinowsky, T. M.; Mar, M. N.; Yee, S. S. Quantitative Interpretation of the Response of Surface Plasmon Resonance Sensors to Adsorbed Films. *Langmuir* **1998**, *14* (19), 5636–5648.

(108)   Kankate, L.; Werner, U.; Turchanin, A.; Gölzhäuser, A.; Grossmann, H.; Tampé, R. Protein Resistant Oligo(ethylene Glycol) Terminated Self-Assembled Monolayers of Thiols on Gold by Vapor Deposition in Vacuum. *Biointerphases* **2010**, *5* (2), 30–36.

(109)   Kapinos, L. E.; Schoch, R. L.; Wagner, R. S.; Schleicher, K. D.; Lim, R. Y. H. Karyopherin-Centric Control of Nuclear Pores Based on Molecular Occupancy and Kinetic Analysis of Multivalent Binding with FG Nucleoporins. *Biophys. J.* **2014**, *106* (8), 1751–1762.

(110)   Karim, A.; Satija, S.; Douglas, J.; Ankner, J.; Fetters, L. Neutron Reflectivity Study of the Density Profile of a Model End-Grafted Polymer Brush: Influence of Solvent Quality. *Phys. Rev. Lett.* **1994**, *73* (25), 3407–3410.

(111)   Karlstroem, G. A New Model for Upper and Lower Critical Solution Temperatures in Poly(ethylene Oxide) Solutions. *J. Phys. Chem.* **1985**, *89* (23), 4962–4964.

(112)   Kawakatsu, T. *Statistical Physics of Polymers*; Springer, 2004.

(113)   Kim, J. U.; O'Shaughnessy, B. Morphology Selection of Nanoparticle Dispersions by Polymer Media. *Phys. Rev. Lett.* **2002**, *89* (23), 238301.

(114)   Kim, J. U.; O'Shaughnessy, B. Nanoinclusions in Dry Polymer Brushes. *Macromolecules* **2006**, *39* (1), 413–425.

(115)   Kingshott, P.; Thissen, H.; Griesser, H. J. Effects of Cloud-Point Grafting, Chain Length, and Density of PEG Layers on Competitive Adsorption of Ocular Proteins. *Biomaterials* **2002**, *23* (9), 2043–2056.

(116)   Knoll, W. Interfaces and Thin Films as Seen by Bound Electromagnetic Waves. *Annu. Rev. Phys. Chem.* **1998**, *49*, 569–638.

(117)   Koutsioubas, A. G.; Spiliopoulos, N.; Anastassopoulos, D. L.; Vradis, A. A.; Priftis, G. D. Surface Plasmon Resonance as a Tool for the Estimation of Adsorbed Polymeric Layer Characteristics: Theoretical Considerations and Experiment. *J. Polym. Sci. Part B Polym. Phys.* **2007**, *45* (15), 2060–2070.

(118)   Koutsioubas, A. G.; Spiliopoulos, N.; Anastassopoulos, D. L.; Vradis, A. A.; Toprakcioglu, C. Formation of Polymer Brushes inside Cylindrical Pores: A Computer Simulation Study. *J. Chem. Phys.* **2009**, *131* (4), 44901.

(119)   Kowalczyk, S. W.; Kapinos, L.; Blosser, T. R.; Magalhães, T.; van Nies, P.; Lim, R. Y. H.; Dekker, C. Single-Molecule Transport across an Individual Biomimetic Nuclear Pore Complex. *Nat. Nanotechnol.* **2011**, *6* (7), 433–438.

(120)   Krull, S.; Thyberg, J.; Björkroth, B.; Rackwitz, H.-R.; Cordes, V. C. Nucleoporins as Components of the Nuclear Pore Complex Core Structure and Tpr as the Architectural Element of the Nuclear Basket. *Mol. Biol. Cell* **2004**, *15* (9), 4261–4277.

(121)   Kubitscheck, U.; Grünwald, D.; Hoekstra, A.; Rohleder, D.; Kues, T.; Siebrasse, J. P.; Peters, R. Nuclear Transport of Single Molecules: Dwell Times at the Nuclear Pore Complex. *J. Cell Biol.* **2005**, *168* (2), 233–243.

(122)   Labokha, A. A.; Gradmann, S.; Frey, S.; Hülsmann, B. B.; Urlaub, H.; Baldus, M.; Görlich, D. Systematic Analysis of Barrier-Forming FG Hydrogels from Xenopus Nuclear Pore Complexes. *EMBO J.* **2013**, *32* (2), 204–218.

(123)   Landi, G.; Zama, F. The Active-Set Method for Nonnegative Regularization of Linear Ill-Posed Problems. *Appl. Math. Comput.* **2006**, *175* (1), 715–729.

(124)   Lazaridis, T.; Karplus, M. Heat Capacity and Compactness of Denatured Proteins. *Biophys. Chem.* **1999**, *78* (1–2), 207–217.

(125)   Lee, H.; Kim, D. H.; Witte, K. N.; Ohn, K.; Choi, J.; Akgun, B.; Satija, S.; Won, Y.-Y. Water Is a Poor Solvent for Densely Grafted Poly(ethylene Oxide) Chains: A Conclusion Drawn from a Self-Consistent Field Theory-Based Analysis of Neutron Reflectivity and Surface Pressure-Area Isotherm Data. *J. Phys. Chem. B* **2012**, *116* (24), 7367–7378.

(126)   Lee, H.-S.; Penn, L. S. Evidence for Relative Radius of Gyration as the Criterion for Selective Diffusion Behavior of Polymer Brushes. *Langmuir* **2009**, *25* (14), 7983–7989.

(127)   Levicky, R.; Herne, T. M.; Tarlov, M. J.; Satija, S. K. Using Self-Assembly To Control the Structure of DNA Monolayers on Gold: A Neutron Reflectivity Study. *J. Am. Chem. Soc.* **1998**, *120* (38), 9787–9792.

(128)   Liedberg, B.; Lundström, I.; Stenberg, E. Principles of Biosensing with an Extended Coupling Matrix and Surface Plasmon Resonance. *Sensors Actuators B Chem.* **1993**, *11* (1–3), 63–72.

(129) Lim, R. Y. H.; Fahrenkrog, B.; Köser, J.; Schwarz-Herion, K.; Deng, J.; Aebi, U. Nanomechanical Basis of Selective Gating by the Nuclear Pore Complex. *Science* **2007**, *318* (5850), 640–643.

(130) Lim, R. Y. H.; Huang, N.-P.; Köser, J.; Deng, J.; Lau, K. H. A.; Schwarz-Herion, K.; Fahrenkrog, B.; Aebi, U. Flexible Phenylalanine-Glycine Nucleoporins as Entropic Barriers to Nucleocytoplasmic Transport. *Proc. Natl. Acad. Sci. U. S. A.* **2006**, *103* (25), 9512–9517.

(131) Liu, S. M.; Stewart, M. Structural Basis for the High-Affinity Binding of Nucleoporin Nup1p to the Saccharomyces Cerevisiae Importin-Beta Homologue, Kap95p. *J. Mol. Biol.* **2005**, *349* (3), 515–525.

(132) Löfås, S.; Malmqvist, M.; Rönnberg, I.; Stenberg, E.; Liedberg, B.; Lundström, I. Bioanalysis with Surface Plasmon Resonance. *Sensors Actuators B Chem.* **1991**, *5* (1–4), 79–84.

(133) Lok, B. K.; Cheng, Y.-L.; Robertson, C. R. Protein Adsorption on Crosslinked Polydimethylsiloxane Using Total Internal Reflection Fluorescence. *J. Colloid Interface Sci.* **1983**, *91* (1), 104–116.

(134) Lott, K.; Bhardwaj, A.; Mitrousis, G.; Pante, N.; Cingolani, G. The Importin Beta Binding Domain Modulates the Avidity of Importin Beta for the Nuclear Pore Complex. *J. Biol. Chem.* **2010**, *285* (18), 13769–13780.

(135) Lowe, A. R.; Siegel, J. J.; Kalab, P.; Siu, M.; Weis, K.; Liphardt, J. T. Selectivity Mechanism of the Nuclear Pore Complex Characterized by Single Cargo Tracking. *Nature* **2010**, *467* (7315), 600–603.

(136) Lukosz, W. Integrated-Optical and Surface-Plasmon Sensors for Direct Affinity Sensing. Part II: Anisotropy of Adsorbed or Bound Protein Adlayers. *Biosens. Bioelectron.* **1997**, *12* (3), 175–184.

(137) Ma, J.; Goryaynov, A.; Sarma, A.; Yang, W. Self-Regulated Viscous Channel in the Nuclear Pore Complex. *Proc. Natl. Acad. Sci. U. S. A.* **2012**, *109* (19), 7326–7331.

(138) Ma, J.; Yang, W. Three-Dimensional Distribution of Transient Interactions in the Nuclear Pore Complex Obtained from Single-Molecule Snapshots. *Proc. Natl. Acad. Sci. U. S. A.* **2010**, *107* (16), 7305–7310.

(139) Macara, I. G. Transport into and out of the Nucleus. *Microbiol. Mol. Biol. Rev.* **2001**, *65* (4), 570–594.

(140) Maimon, T.; Elad, N.; Dahan, I.; Medalia, O. The Human Nuclear Pore Complex as Revealed by Cryo-Electron Tomography. *Structure* **2012**, *20* (6), 998–1006.

(141) Manghi, M.; Aubouy, M.; Gay, C.; Ligoure, C. Inwardly Curved Polymer Brushes: Concave Is Not like Convex. *Eur. Phys. J. E* **2001**, *5* (5), 519–530.

(142) Martinez, J. C.; Murciano-Calles, J.; S., E.; Iglesias-Bexiga, M.; Luque, I.; Ruiz-Sanz, J. Isothermal Titration Calorimetry: Thermodynamic Analysis of the Binding

Thermograms of Molecular Recognition Events by Using Equilibrium Models. In *Applications of Calorimetry in a Wide Context - Differential Scanning Calorimetry, Isothermal Titration Calorimetry and Microcalorimetry*; InTech, 2013; pp 73–104.

(143)   Matsuyama, A.; Tanaka, F. Theory of Solvation-Induced Reentrant Phase Separation in Polymer Solutions. *Phys. Rev. Lett.* **1990**, *65* (3), 341–344.

(144)   Mattaj, I. W.; Englmeier, L. Nucleocytoplasmic Transport: The Soluble Phase. *Annu. Rev. Biochem.* **1998**, *67*, 265–306.

(145)   Melzak, K. A.; Moreno-Flores, S.; Yu, K.; Kizhakkedathu, J.; Toca-Herrera, J. L. Rationalized Approach to the Determination of Contact Point in Force-Distance Curves: Application to Polymer Brushes in Salt Solutions and in Water. *Microsc. Res. Tech.* **2010**, *73* (10), 959–964.

(146)   Merlitz, H.; Wu, C.-X.; Sommer, J.-U. Inclusion Free Energy of Nanoparticles in Polymer Brushes. *Macromolecules* **2012**, *45* (20), 8494–8501.

(147)   Miao, L.; Schulten, K. Transport-Related Structures and Processes of the Nuclear Pore Complex Studied through Molecular Dynamics. *Structure* **2009**, *17* (3), 449–459.

(148)   Milchev, A.; Dimitrov, D. I.; Binder, K. Excess Free Energy of Nanoparticles in a Polymer Brush. *Polymer (Guildf).* **2008**, *49* (17), 3611–3618.

(149)   Milner, S. T.; Witten, T. A.; Cates, M. E. Theory of the Grafted Polymer Brush. *Macromolecules* **1988**, *21* (8), 2610–2619.

(150)   Milner, S. T.; Witten, T. A.; Cates, M. E. Theory of the Grafted Polymer Brush. *Macromolecules* **1988**, *21* (8), 2610–2619.

(151)   Mock, J. J.; Hill, R. T.; Tsai, Y.-J.; Chilkoti, A.; Smith, D. R. Probing Dynamically Tunable Localized Surface Plasmon Resonances of Film-Coupled Nanoparticles by Evanescent Wave Excitation. *Nano Lett.* **2012**, *12* (4), 1757–1764.

(152)   Mon, K. K.; Percus, J. K. Self-Diffusion of Fluids in Narrow Cylindrical Pores. *J. Chem. Phys.* **2002**, *117* (5), 2289.

(153)   Moore, M. S.; Blobel, G. The GTP-Binding Protein Ran/TC4 Is Required for Protein Import into the Nucleus. *Nature* **1993**, *365* (6447), 661–663.

(154)   Moore, M. S.; Blobel, G. The Two Steps of Nuclear Import, Targeting to the Nuclear Envelope and Translocation through the Nuclear Pore, Require Different Cytosolic Factors. *Cell* **1992**, *69* (6), 939–950.

(155)   Moussavi-Baygi, R.; Jamali, Y.; Karimi, R.; Mofrad, M. R. K. Biophysical Coarse-Grained Modeling Provides Insights into Transport through the Nuclear Pore Complex. *Biophys. J.* **2011**, *100* (6), 1410–1419.

(156)   Moussavi-Baygi, R.; Jamali, Y.; Karimi, R.; Mofrad, M. R. K. Brownian Dynamics Simulation of Nucleocytoplasmic Transport: A Coarse-Grained Model for the Functional State of the Nuclear Pore Complex. *PLoS Comput. Biol.* **2011**, *7* (6),

e1002049.

(157) Myszka, D.; He, X.; Dembo, M.; Morton, T.; Goldstein, B. Extending the Range of Rate Constants Available from BIACORE: Interpreting Mass Transport-Influenced Binding Data. *Biophys. J.* **1998**, *75* (2), 583–594.

(158) Nachury, M. V.; Weis, K. The Direction of Transport through the Nuclear Pore Can Be Inverted. *Proc. Natl. Acad. Sci.* **1999**, *96* (17), 9622–9627.

(159) Naim, B.; Zbaida, D.; Dagan, S.; Kapon, R.; Reich, Z. Cargo Surface Hydrophobicity Is Sufficient to Overcome the Nuclear Pore Complex Selectivity Barrier. *EMBO J.* **2009**, *28* (18), 2697–2705.

(160) Norde, W. My Voyage of Discovery to Proteins in Flatland ...and Beyond. *Colloids Surf. B. Biointerfaces* **2008**, *61* (1), 1–9.

(161) Norde, W.; Gage, D. Interaction of Bovine Serum Albumin and Human Blood Plasma with PEO-Tethered Surfaces: Influence of PEO Chain Length, Grafting Density, and Temperature. *Langmuir* **2004**, *20* (10), 4162–4167.

(162) Opferman, M. G.; Coalson, R. D.; Jasnow, D.; Zilman, A. Morphological Control of Grafted Polymer Films via Attraction to Small Nanoparticle Inclusions. *Phys. Rev. E* **2012**, *86* (3), 31806.

(163) Opferman, M. G.; Coalson, R. D.; Jasnow, D.; Zilman, A. Morphology of Polymer Brushes Infiltrated by Attractive Nanoinclusions of Various Sizes. *Langmuir* **2013**, *29* (27), 8584–8591.

(164) Pale-Grosdemange, C.; Simon, E. S.; Prime, K. L.; Whitesides, G. M. Formation of Self-Assembled Monolayers by Chemisorption of Derivatives of Oligo(ethylene Glycol) of Structure HS(CH2)11(OCH2CH2)mOH on Gold. *J. Am. Chem. Soc.* **1991**, *113* (1), 12–20.

(165) Paradise, A.; Levin, M. K.; Korza, G.; Carson, J. H. Significant Proportions of Nuclear Transport Proteins with Reduced Intracellular Mobilities Resolved by Fluorescence Correlation Spectroscopy. *J. Mol. Biol.* **2007**, *365* (1), 50–65.

(166) Patel, S. S.; Belmont, B. J.; Sante, J. M.; Rexach, M. F. Natively Unfolded Nucleoporins Gate Protein Diffusion across the Nuclear Pore Complex. *Cell* **2007**, *129* (1), 83–96.

(167) Paulillo, S. M.; Phillips, E. M.; Köser, J.; Sauder, U.; Ullman, K. S.; Powers, M. A.; Fahrenkrog, B. Nucleoporin Domain Topology Is Linked to the Transport Status of the Nuclear Pore Complex. *J. Mol. Biol.* **2005**, *351* (4), 784–798.

(168) Peleg, O.; Lim, R. Y. H. Converging on the Function of Intrinsically Disordered Nucleoporins in the Nuclear Pore Complex. *Biol. Chem.* **2010**, *391* (7), 719–730.

(169) Peterlinz, K. A.; Georgiadis, R. Two-Color Approach for Determination of Thickness and Dielectric Constant of Thin Films Using Surface Plasmon Resonance Spectroscopy. *Opt. Commun.* **1996**, *130* (4–6), 260–266.

(170)   Peters, R. Translocation through the Nuclear Pore Complex: Selectivity and Speed by Reduction-of-Dimensionality. *Traffic* **2005**, *6* (5), 421–427.

(171)   Peters, R. Translocation through the Nuclear Pore: Kaps Pave the Way. *BioEssays* **2009**, *31* (August 2008), 466–477.

(172)   Pincus, P. Colloid Stabilization with Grafted Polyelectrolytes. *Macromolecules* **1991**, *24* (10), 2912–2919.

(173)   Plunkett, K. N.; Zhu, X.; Moore, J. S.; Leckband, D. E. PNIPAM Chain Collapse Depends on the Molecular Weight and Grafting Density. *Langmuir* **2006**, *22* (9), 4259–4266.

(174)   Prabhu, N. V; Sharp, K. A. Heat Capacity in Proteins. *Annu. Rev. Phys. Chem.* **2005**, *56*, 521–548.

(175)   Pyhtila, B.; Rexach, M. A Gradient of Affinity for the Karyopherin Kap95p along the Yeast Nuclear Pore Complex. *J. Biol. Chem.* **2003**, *278* (43), 42699–42709.

(176)   Radu, A.; Blobel, G.; Moore, M. S. Identification of a Protein Complex That Is Required for Nuclear Protein Import and Mediates Docking of Import Substrate to Distinct Nucleoporins. *Proc. Natl. Acad. Sci.* **1995**, *92* (5), 1769–1773.

(177)   Radu, A.; Moore, M. S.; Blobel, G. The Peptide Repeat Domain of Nucleoporin Nup98 Functions as a Docking Site in Transport across the Nuclear Pore Complex. *Cell* **1995**, *81* (2), 215–222.

(178)   Reichelt, R. Correlation between Structure and Mass Distribution of the Nuclear Pore Complex and of Distinct Pore Complex Components. *J. Cell Biol.* **1990**, *110* (4), 883–894.

(179)   Rexach, M.; Blobel, G. Protein Import into Nuclei: Association and Dissociation Reactions Involving Transport Substrate, Transport Factors, and Nucleoporins. *Cell* **1995**, *83* (5), 683–692.

(180)   Reznik, C.; Landes, C. F. Transport in Supported Polyelectrolyte Brushes. *Acc. Chem. Res.* **2012**, *45* (11), 1927–1935.

(181)   Ribbeck, K.; Görlich, D. Kinetic Analysis of Translocation through Nuclear Pore Complexes. *EMBO J.* **2001**, *20* (6), 1320–1330.

(182)   Ribbeck, K.; Lipowsky, G.; Kent, H. M.; Stewart, M.; Görlich, D. NTF2 Mediates Nuclear Import of Ran. *EMBO J.* **1998**, *17* (22), 6587–6598.

(183)   Richardson, W. D.; Mills, A. D.; Dilworth, S. M.; Laskey, R. A.; Dingwall, C. Nuclear Protein Migration Involves Two Steps: Rapid Binding at the Nuclear Envelope Followed by Slower Translocation through Nuclear Pores. *Cell* **1988**, *52* (5), 655–664.

(184)   Rogers, J.; Tam, T. Solution Behavior of Polyethylene Glycols in Water Using Vapor Pressure Osmometry. *Can. J. Pharm. Sci.* **1977**, *12* (3), 65–70.

(185)   Rout, M. P. The Yeast Nuclear Pore Complex: Composition, Architecture, and Transport Mechanism. *J. Cell Biol.* **2000**, *148* (4), 635–652.

(186)   Rubinstein, M.; Colby, R. *Polymer Physics (Chemistry)*; Oxford University Press, USA, 2003.

(187)   Saeki, S.; Kuwahara, N.; Nakata, M.; Kaneko, M. Upper and Lower Critical Solution Temperatures in Poly (Ethylene Glycol) Solutions. *Polymer (Guildf).* **1976**, *17* (8), 685–689.

(188)   Salamon, Z.; Macleod, H. A.; Tollin, G. Surface Plasmon Resonance Spectroscopy as a Tool for Investigating the Biochemical and Biophysical Properties of Membrane Protein Systems. II: Applications to Biological Systems. *Biochim. Biophys. Acta - Rev. Biomembr.* **1997**, *1331* (2), 131–152.

(189)   Salamon, Z.; Macleod, H. A.; Tollin, G. Surface Plasmon Resonance Spectroscopy as a Tool for Investigating the Biochemical and Biophysical Properties of Membrane Protein Systems. I: Theoretical Principles. *Biochim. Biophys. Acta - Rev. Biomembr.* **1997**, *1331* (2), 117–129.

(190)   Sannomiya, T.; Scholder, O.; Jefimovs, K.; Hafner, C.; Dahlin, A. B. Investigation of Plasmon Resonances in Metal Films with Nanohole Arrays for Biosensing Applications. *Small* **2011**, *7* (12), 1653–1663.

(191)   Sarid, D.; Challener, W. *Modern Introduction to Surface Plasmons: Theory, Mathematica Modeling, and Applications*; Cambridge University Press, 2010.

(192)   Satulovsky, J.; Carignano, M. A.; Szleifer, I. Kinetic and Thermodynamic Control of Protein Adsorption. *Proc. Natl. Acad. Sci. U. S. A.* **2000**, *97* (16), 9037–9041.

(193)   Saxton, M. J. A Biological Interpretation of Transient Anomalous Subdiffusion. I. Qualitative Model. *Biophys. J.* **2007**, *92* (4), 1178–1191.

(194)   Schneck, E.; Berts, I.; Halperin, A.; Daillant, J.; Fragneto, G. Neutron Reflectometry from Poly (Ethylene-Glycol) Brushes Binding Anti-PEG Antibodies: Evidence of Ternary Adsorption. *Biomaterials* **2015**, *46*, 95–104.

(195)   Schneck, E.; Schollier, A.; Halperin, A.; Moulin, M.; Haertlein, M.; Sferrazza, M.; Fragneto, G. Neutron Reflectometry Elucidates Density Profiles of Deuterated Proteins Adsorbed onto Surfaces Displaying Poly(ethylene Glycol) Brushes: Evidence for Primary Adsorption. *Langmuir* **2013**, *29* (46), 14178–14187.

(196)   Schoch, R. L.; Kapinos, L. E.; Lim, R. Y. H. Nuclear Transport Receptor Binding Avidity Triggers a Self-Healing Collapse Transition in FG-Nucleoporin Molecular Brushes. *Proc. Natl. Acad. Sci. U. S. A.* **2012**, *109* (42), 16911–16916.

(197)   Schoch, R. L.; Lim, R. Y. H. Non-Interacting Molecules as Innate Structural Probes in Surface Plasmon Resonance. *Langmuir* **2013**, *29* (12), 4068–4076.

(198)   Schulz, L. G. The Optical Constants of Silver, Gold, Copper, and Aluminum I The Absorption Coefficient K. *J. Opt. Soc. Am.* **1954**, *44* (5), 357.

(199)   Schulz, L. G.; Tangherlini, F. R. Optical Constants of Silver, Gold, Copper, and Aluminum II The Index of Refraction N. *J. Opt. Soc. Am.* **1954**, *44* (5), 362.

(200) Schwarz-Herion, K.; Maco, B.; Sauder, U.; Fahrenkrog, B. Domain Topology of the p62 Complex within the 3-D Architecture of the Nuclear Pore Complex. *J. Mol. Biol.* **2007**, *370* (4), 796–806.

(201) Schwendel, D.; Dahint, R.; Herrwerth, S.; Schloerholz, M.; Eck, W.; Grunze, M. Temperature Dependence of the Protein Resistance of Poly- and Oligo(ethylene Glycol)-Terminated Alkanethiolate Monolayers. *Langmuir* **2001**, *17* (19), 5717–5720.

(202) Siebrasse, J. P.; Kaminski, T.; Kubitscheck, U. Nuclear Export of Single Native mRNA Molecules Observed by Light Sheet Fluorescence Microscopy. *Proc. Natl. Acad. Sci. U. S. A.* **2012**, *109* (24), 9426–9431.

(203) Sjolander, S.; Urbaniczky, C. Integrated Fluid Handling System for Biomolecular Interaction Analysis. *Anal. Chem.* **1991**, *63* (20), 2338–2345.

(204) Skoda, M. W. A.; Schreiber, F.; Jacobs, R. M. J.; Webster, J. R. P.; Wolff, M.; Dahint, R.; Schwendel, D.; Grunze, M. Protein Density Profile at the Interface of Water with Oligo(ethylene Glycol) Self-Assembled Monolayers. *Langmuir* **2009**, *25* (7), 4056–4064.

(205) Smith, A.; Brownawell, A.; Macara, I. G. Nuclear Import of Ran Is Mediated by the Transport Factor NTF2. *Curr. Biol.* **1998**, *8* (25), 1403-S1.

(206) Snyder, P. W.; Lockett, M. R.; Moustakas, D. T.; Whitesides, G. M. Is It the Shape of the Cavity, or the Shape of the Water in the Cavity? *Eur. Phys. J. Spec. Top.* **2013**, *223* (5), 853–891.

(207) Solmaz, S. R.; Chauhan, R.; Blobel, G.; Melčák, I. Molecular Architecture of the Transport Channel of the Nuclear Pore Complex. *Cell* **2011**, *147* (3), 590–602.

(208) Spolar, R. S.; Livingstone, J. R.; Record, M. T. Use of Liquid Hydrocarbon and Amide Transfer Data to Estimate Contributions to Thermodynamic Functions of Protein Folding from the Removal of Nonpolar and Polar Surface from Water. *Biochemistry* **1992**, *31* (16), 3947–3955.

(209) Steels, B. M.; Koska, J.; Haynes, C. A. Analysis of Brush-Particle Interactions Using Self-Consistent-Field Theory. *J. Chromatogr. B Biomed. Sci. Appl.* **2000**, *743* (1–2), 41–56.

(210) Stenberg, E.; Persson, B.; Roos, H.; Urbaniczky, C. Quantitative Determination of Surface Concentration of Protein with Surface Plasmon Resonance Using Radiolabeled Proteins. *J. Colloid Interface Sci.* **1991**, *143* (2), 513–526.

(211) Stepanek, J.; Vaisocherova, H.; Piliarik, M. *Surface Plasmon Resonance Based Sensors*; Homola, J., Ed.; Springer Series on Chemical Sensors and Biosensors; Springer Berlin Heidelberg: Berlin, Heidelberg, 2006; Vol. 4.

(212) Stewart, M. Molecular Mechanism of the Nuclear Protein Import Cycle. *Nat. Rev. Mol. Cell Biol.* **2007**, *8* (3), 195–208.

(213) Strawn, L. A.; Shen, T.; Shulga, N.; Goldfarb, D. S.; Wente, S. R. Minimal Nuclear Pore

Complexes Define FG Repeat Domains Essential for Transport. *Nat. Cell Biol.* **2004**, *6* (3), 197–206.

(214) Sundberg, E.; Andersen, P.; Gorshkova, I.; Schuck, P. *Protein Interactions*; Schuck, P., Ed.; Springer US: Boston, MA, 2007.

(215) Svitel, J.; Balbo, A.; Mariuzza, R.; Gonzales, N.; Schuck, P. Combined Affinity and Rate Constant Distributions of Ligand Populations from Experimental Surface Binding Kinetics and Equilibria. *Biophys. J.* **2003**, *84* (6), 4062–4077.

(216) Svitel, J.; Boukari, H.; Van Ryk, D.; Willson, R. C.; Schuck, P. Probing the Functional Heterogeneity of Surface Binding Sites by Analysis of Experimental Binding Traces and the Effect of Mass Transport Limitation. *Biophys. J.* **2007**, *92* (5), 1742–1758.

(217) Szleifer, I. Protein Adsorption on Surfaces with Grafted Polymers: A Theoretical Approach. *Biophys. J.* **1997**, *72* (2), 595–612.

(218) Terry, L. J.; Shows, E. B.; Wente, S. R. Crossing the Nuclear Envelope: Hierarchical Regulation of Nucleocytoplasmic Transport. *Science* **2007**, *318* (2000), 1412–1416.

(219) Tetenbaum-Novatt, J.; Hough, L. E.; Mironska, R.; McKenney, A. S.; Rout, M. P. Nucleocytoplasmic Transport: A Role for Nonspecific Competition in Karyopherin-Nucleoporin Interactions. *Mol. Cell. Proteomics* **2012**, *11* (5), 31–46.

(220) Tokunaga, M.; Imamoto, N.; Sakata-Sogawa, K. Highly Inclined Thin Illumination Enables Clear Single-Molecule Imaging in Cells. *Nat. Methods* **2008**, *5* (2), 159–161.

(221) Tran, Y.; Auroy, P.; Lee, L.-T. Determination of the Structure of Polyelectrolyte Brushes. *Macromolecules* **1999**, *32* (26), 8952–8964.

(222) Tu, L.-C.; Fu, G.; Zilman, A.; Musser, S. M. Large Cargo Transport by Nuclear Pores: Implications for the Spatial Organization of FG-Nucleoporins. *EMBO J.* **2013**, *32* (24), 3220–3230.

(223) Ujihara, K. Reflectivity of Metals at High Temperatures. *J. Appl. Phys.* **1972**, *43* (5), 2376.

(224) Venohr, H.; Fraaije, V.; Strunk, H.; Borchard, W. Static and Dynamic Light Scattering from Aqueous Poly(ethylene Oxide) Solutions. *Eur. Polym. J. 34* (5–6), 723–732.

(225) Vetter, I. R.; Arndt, A.; Kutay, U.; Görlich, D.; Wittinghofer, A. Structural View of the Ran–Importin β Interaction at 2.3 Å Resolution. *Cell* **1999**, *97* (5), 635–646.

(226) Voinova, M. V.; Jonson, M.; Kasemo, B. "Missing Mass" Effect in Biosensor's QCM Applications. *Biosens. Bioelectron.* **2002**, *17* (10), 835–841.

(227) Vörös, J. The Density and Refractive Index of Adsorbing Protein Layers. *Biophys. J.* **2004**, *87* (1), 553–561.

(228) Wang, S.; van Dijk, J. A. P. P.; Odijk, T.; Smit, J. A. M. Depletion-Induced Demixing in Aqueous Protein–Polysaccharide Solutions. *Biomacromolecules* **2001**, *2* (4), 1080–1088.

(229) Wang, S.; Zhu, Y. Molecular Diffusion on Surface Tethered Polymer Layers: Coupling of Molecular Thermal Fluctuation and Polymer Chain Dynamics. *Soft Matter* **2010**, *6* (19), 4661.

(230) Wurtz, G. A.; Pollard, R. J.; Zayats, A. V. Optics of Metallic Nanostructures. *Compr. Nanosci. Technol. Vol 3 Nanostructured Surfaces* 135–186.

(231) Xu, S.; Powers, M. A. In Vivo Analysis of Human Nucleoporin Repeat Domain Interactions. *Mol. Biol. Cell* **2013**, *24* (8), 1222–1231.

(232) Yamada, J.; Phillips, J. L.; Patel, S.; Goldfien, G.; Calestagne-Morelli, A.; Huang, H.; Reza, R.; Acheson, J.; Krishnan, V. V; Newsam, S.; et al. A Bimodal Distribution of Two Distinct Categories of Intrinsically Disordered Structures with Separate Functions in FG Nucleoporins. *Mol. Cell. Proteomics* **2010**, *9* (10), 2205–2224.

(233) Yaneva, J.; Dimitrov, D. I.; Milchev, A.; Binder, K. Nanoinclusions in Polymer Brushes with Explicit Solvent – A Molecular Dynamics Investigation. *J. Colloid Interface Sci.* **2009**, *336* (1), 51–58.

(234) Yang, Q.; Rout, M. P.; Akey, C. W. Three-Dimensional Architecture of the Isolated Yeast Nuclear Pore Complex: Functional and Evolutionary Implications. *Mol. Cell* **1998**, *1* (2), 223–234.

(235) Yang, W.; Gelles, J.; Musser, S. M. Imaging of Single-Molecule Translocation through Nuclear Pore Complexes. *Proc. Natl. Acad. Sci. U. S. A.* **2004**, *101* (35), 12887–12892.

(236) Yang, W.; Musser, S. M. Nuclear Import Time and Transport Efficiency Depend on Importin Beta Concentration. *J. Cell Biol.* **2006**, *174* (7), 951–961.

(237) Yim, H.; Kent, M. S.; Mendez, S.; Balamurugan, S. S.; Balamurugan, S.; Lopez, G. P.; Satija, S. Temperature-Dependent Conformational Change of PNIPAM Grafted Chains at High Surface Density in Water. *Macromolecules* **2004**, *37* (5), 1994–1997.

(238) Yim, H.; Kent, M. S.; Satija, S.; Mendez, S.; Balamurugan, S. S.; Balamurugan, S.; Lopez, G. P. Study of the Conformational Change of poly(N-Isopropylacrylamide)-Grafted Chains in Water with Neutron Reflection: Molecular Weight Dependence at High Grafting Density. *J. Polym. Sci. Part B Polym. Phys.* **2004**, *42* (17), 3302–3310.

(239) Yim, H.; Kent, M. S.; Satija, S.; Mendez, S.; Balamurugan, S. S.; Balamurugan, S.; Lopez, G. P. Evidence for Vertical Phase Separation in Densely Grafted, High-Molecular-Weight Poly(N -Isopropylacrylamide) Brushes in Water. *Phys. Rev. E* **2005**, *72* (5), 51801.

(240) Zhang, Q. Y.; Xiang, X. Interaction between Polymer Brush and Nanoparticle: Brownian Dynamics Investigation. *ACTA Phys. Pol. A* **2013**, *123* (4), 642–646.

(241) Zhulina, E. B.; Borisov, O. V.; Pryamitsyn, V. A.; Birshtein, T. M. Coil-Globule Type Transitions in Polymers. 1. Collapse of Layers of Grafted Polymer Chains. *Macromolecules* **1991**, *24* (1), 140–149.

(242) Zilman, A.; Di Talia, S.; Chait, B. T.; Rout, M. P.; Magnasco, M. O. Efficiency,

Selectivity, and Robustness of Nucleocytoplasmic Transport. *PLoS Comput. Biol.* **2007**, *3* (7), e125.

Curriculum Vitae

Rafael L. Schoch, from Zurich CH
born in Basel CH, 16.02.1984

Bachelor in Nanosciences, University of Basel
October 2003 – July 2007

Master in Nanosciences, University of Basel,
September 2007 – April 2010

PhD in Nanosciences, Biozentrum, University of Basel
May 2010 – April 2015

Talks:

MRS spring meeting, San Francisco, US, 2012

Posters:

Rigi-Workshop, From biological machines to molecular devices of the future, Rigi, CH, 2011

Gordon Research Conference, Biointerface Science, Les Diablerets, CH, 2012

Biochemical Society Conference, Intrinsically Disordered Proteins, York, UK, 2012

FEBS Workshop, Biological Surfaces and Interfaces, Sant Feliu de Guixols, ES, 2013

Selective transport trough nanopores: physics meets biology, Lenzerheide, CH, 2015

Others:

MIT Short Programs, Multiscale Materials Design, Boston, US, 2014.

First author article in selection „Best of 2014" from Biophysical Journal.

Publication List

First author:

(1)   Schoch, R. L.; Kapinos, L. E.; Lim, R. Y. H. Nuclear Transport Receptor Binding Avidity Triggers a Self-Healing Collapse Transition in FG-Nucleoporin Molecular Brushes. *Proc. Natl. Acad. Sci. U. S. A.* **2012**, *109* (42), 16911–16916.

(2)   Schoch, R. L.; Lim, R. Y. H. Non-Interacting Molecules as Innate Structural Probes in Surface Plasmon Resonance. *Langmuir* **2013**, *29* (12), 4068–4076.

(3)   Kapinos, L. E.; Schoch, R. L.; Wagner, R. S.; Schleicher, K. D.; Lim, R. Y. H. Karyopherin-Centric Control of Nuclear Pores Based on Molecular Occupancy and Kinetic Analysis of Multivalent Binding with FG Nucleoporins. *Biophys. J.* **2014**, *106* (8), 1751–1762.

Co-author:

(4)   Marot, L.; Schoch, R. L.; Steiner, R.; Meyer, E. Rhodium and Silicon System: I. Glassy Metallic Alloy Formation. *Nanotechnology* **2010**, *21* (36), 365706.

(5)   Marot, L.; Schoch, R. L.; Steiner, R.; Thommen, V.; Mathys, D.; Meyer, E. Rhodium and Silicon System: II. Rhodium Silicide Formation. *Nanotechnology* **2010**, *21* (36), 365707.

(6)   Emilsson, G.; Schoch, R. L.; Feuz, L.; Höök, F.; Lim, R. Y. H.; Dahlin, A. B. Strongly Stretched Protein Resistant Poly(ethylene Glycol) Brushes Prepared by Grafting-To. *ACS Appl. Mater. Interfaces* **2015**, *7* (14), 7505–7515.

(7)   Emilsson, G.; Schoch, R. L.; Oertle, P.; Xiong, K.; Lim, R. Y. H.; Dahlin, A. B. Surface Plasmon Resonance Methodology for Monitoring Polymerization Kinetics and Morphology Changes of Brushes—evaluated with poly(N-Isopropylacrylamide). *Appl. Surf. Sci.* **2016**.